More than a Single Cell Gone Rogue: The Significance of Multiple Founders to Tumor Initiation, Growth, and Progression

By

Alyssa A. Leystra

A dissertation submitted in partial fulfillment of

the requirements for the degree of

Doctor of Philosophy

(Cancer Biology)

at the

UNIVERSITY OF WISCONSIN – MADISON

2016

Date of final oral examination: 07/14/2016

The dissertation is approved by the following members of the Final Oral Committee:
Richard B. Halberg, Associate Professor, Medicine
Caroline Alexander, Professor, Oncology
Paul F. Lambert, Howard M. Temin Professor, Chair of Oncology
Kristina A. Matkowskyj, Assistant Professor, Pathology and Laboratory Medicine
Shigeki Miyamoto, Professor, Oncology

Abstract

More than a Single Cell Gone Rogue: The Significance of Multiple Founders to Tumor Initiation, Growth, and Progression

Alyssa A. Leystra

Under the supervision of Richard B. Halberg

At the University of Wisconsin – Madison

High levels of intratumoral heterogeneity contributes to a poor clinical prognosis. Genetic diversity among tumor subclones within tumors might contribute to tumor adaptability through cell-autonomous and non-cell autonomous mechanisms throughout tumor initiation, growth, progression, and response to therapy. Therefore, understanding sources of intratumoral heterogeneity might help identify novel prevention and treatment strategies. Genetic diversity can arise after tumor initiation through a gradual accumulation or punctuated bursts of genomic changes resulting in heterogeneous tumors which are composed of multiple subclones. Interestingly, genetic diversity can also arise during tumor initiation through the contributions of multiple unique tumor-founding cells. The resulting tumors are not only heterogeneous but also multi-ancestral, and each one likely displays a greater degree of diversity between unique ancestral clones than would be observed among subclones in a uni-ancestral tumor.

During tumor evolution, multiple ancestral clones might go through selective competition or alternatively cooperate throughout tumor evolution. A driver mutation in one tumor-founding cell might cause the resulting progeny to sweep through a tumor mass, resulting in progression to a more homogenous uni-ancestral tumor. If multiple ancestral clones cooperate, however,

heterogeneity is likely to be maintained and contribute to tumor progression. We sought to determine whether expression of a gene which drives tumor progression within a tumor-founding cell would reduce intratumoral heterogeneity in colorectal cancer.

Activation of the PI3K signaling pathway is common in many cancers and is associated with cancer progression. We investigated the role of PI3K activation as a driver throughout the development of colorectal cancer. Constitutive PI3K signaling can initiate tumorigenesis independent of aberrant WNT signaling, and can increase the rate of tumor growth and progression by synergizing with aberrant WNT signaling. These findings indicate that PI3K is both an initiator and driver of tumor progression in the colon.

Using this newly established model with a high likelihood of progressing to cancer, individual ancestral tumor clones could be followed through tumor progression. Even in the setting of PI3K activation, the multi-ancestral structure is maintained. Moreover, these tumors are larger than other tumors, indicating that multiple clones might increase tumor growth rates. Finally, clones within multi-ancestral tumors are more frequently invasive and invade deeper than clones in less heterogeneous tumors with similar mutations. Multiple ancestral clones might therefore be cooperating to promote tumor progression in this model.

Early inter-clonal diversity increases the probability of randomly acquiring a mutation which provides a fitness advantage, while also increasing the opportunity for meaningful interactions to evolve among tumor cell populations. Our data indicate that multiple tumor-founding cells contribute to tumor initiation, and their progeny persist and can cooperate during tumor progression. Understanding the interactions between co-evolved clones might therefore lead to improved strategies to disrupt tumor growth and progression.

Acknowledgements

I would like to thank my thesis advisor, Richard Halberg, without whom this thesis would not have been possible, and moreover whose passion, curiosity, energy, and guidance shaped me into the scientist I am today.

I would like to additionally thank Drs. Caroline Alexander, Paul Lambert, Kristina Matkowskyj, Shigeki Miyamoto, Michael Newton, and Bill Sugden, whose ongoing support, guidance, and insight have shaped my research and the way I think about science.

I would also like to thank all past and present Halberg lab members who contributed to this research, especially Dr. Dustin Deming, Dr. Christopher Zahm, Chelsie Sievers, Dawn Albrecht, and Linda Clipson.

I would like to thank my friends and family for understanding that I love them even when I am busy, and for supporting and encouraging me in every aspect of life. In particular, I would like to thank my dearest friends: Matt and Kelle, Chris and Melissa, Martin and Jessie, Dan, Kris, Megan, and Bill; my new family: Vern, Ann, Toph, and Katie; my brother Isaac; and particularly my parents, Jim and Janine, whose guidance and support throughout my entire life shaped me into the person I am today.

Finally, I would like to dedicate this thesis to my husband, Josh, who supported and inspired me nearly every step of the way with his unique energy, humor, and passion for cooking.

Acknowledgements

I would like to thank my thesis advisor, Richard Halberg, without whom this thesis would not have been possible, and moreover whose passion, curiosity, energy, and guidance shaped me into the scientist I am today.

I would like to additionally thank Drs. Caroline Alexander, Paul Lambert, Kristina Matkowskyj, Shigeki Miyamoto, Michael Newton, and Bill Sugden, whose ongoing support, guidance, and insight have shaped my research and the way I think about science.

I would also like to thank all past and present Halberg lab members who contributed to this research, especially Dr. Dustin Deming, Dr. Christopher Zahm, Chelsie Sievers, Dawn Albrecht, and Linda Clipson.

I would like to thank my friends and family for understanding that I love them even when I am busy, and for supporting and encouraging me in every aspect of life. In particular, I would like to thank my dearest friends: Matt and Kelle, Chris and Melissa, Martin and Jessie, Dan, Kris, Megan, and Bill; my new family: Vern, Ann, Toph, and Katie; my brother Isaac; and particularly my parents, Jim and Janine, whose guidance and support throughout my entire life shaped me into the person I am today.

Finally, I would like to dedicate this thesis to my husband, Josh, who supported and inspired me nearly every step of the way with his unique energy, humor, and passion for cooking.

Table of Contents

Glossary

The following terms are either poorly and inconsistently defined in the field of tumor heterogeneity or else are being newly defined. The following definitions apply to any use of these terms throughout this thesis.

Clone	A group of cells which are all derived from a single tumor-founding cell
Driver gene	A gene which through mutation or irregular expression can contribute to tumor initiation, maintenance, or progression
Driver mutation	A heritable change in the DNA which which can contribute to tumor initiation, maintenance, or progression
Multi-ancestral tumor	An abnormal mass of cells which is derived from more than one tumor-founding cell
Subclone	A group of cells which are derived from a single ancestor cell which gained a driver mutation within a clone of interest
Transformation	The change that a normal cell undergoes to become a tumor-founding cell
Tumor-founding cell	A cell located within a normal tissue architecture whose immediate progeny form an abnormal mass of cells
Uni-ancestral tumor	An abnormal mass of cells which is derived from a single tumor-founding cell

CHAPTER 1

Introduction to intratumoral heterogeneity and multi-ancestral tumors.

Introduction

High intratumoral heterogeneity contributes to tumor growth, progression, and resistance to therapy. Heterogeneity can be defined either by phenotype including cell metabolism, differentiation and morphology, or by genotype including genetic, epigenetic, and copy number variations[1]. With the decreasing costs of sequencing and an increased interest in using mutational profiling to guide patient therapy, genetic heterogeneity is now the predominant measure of intratumoral heterogeneity[1-3]. In many cancer types, high intratumoral heterogeneity is associated with a worse clinical prognosis for patients[4-9].

Consequences of Genetic Heterogeneity

Increased genetic diversity among tumor cells results in increased tumor adaptability and resistance to a variety of insults, including immune surveillance, nutrient deprivation, and chemotherapy[10,11]. Some tumors contain minor subclones with pre-existing resistance to therapies[8,12-14]. Similarly, an effective targeted therapy can fail to provide a long-term benefit if only a subset of tumor cells carry the actionable mutation[14]. However, careful planning of treatment regimens can take advantage of heterogeneity in clonal response to therapy. Alternating between targeting rapidly growing clones which are susceptible to therapy and slower growing clones which are resistant to therapy can extend the length of time that therapy remains effective and thus extend the duration of response and quality of life[15,16].

In addition to increased tumor adaptability, genetically diverse clones can interact to the advantage of one or more clones within a single tumor[17]. Cooperation of co-evolved clones can result in increased tumor growth[18]. Additionally, minor tumor subclones can promote the invasion and metastasis of other subclones[19]. Diverse tumor populations might even mediate

chemotherapy resistance non-cell autonomously[20]. Thus, intratumoral heterogeneity can provide diversity which increases the chances that resistant populations exist within a tumor and furthermore can actively promote tumor growth, progression, and chemotherapy resistance through interclonal interactions.

Sources of Genetic Heterogeneity

Genomic instability contributes to a gradual accumulation of diversity (Figure 1-1A). Defects in DNA repair, telomere maintenance, and chromosome segregation can result in the accumulation of point mutations, larger scale genomic rearrangements, and copy number alterations[3]. Ongoing gradual evolution might allow numerous clones to arise and compete within a local environment, resulting in selection of the fittest clones[21]. However, while increased diversity might enhance tumor adaptability, too much diversity as a consequence of elevated mutation rates can result in decreased cell survival and enhanced response to immunotherapies and DNA damaging agents[22-24].

Alternatively, punctuated bursts of genomic alterations can rapidly create extensive diversity and then allow clones time to expand and co-evolve (Figure 1-1B). Mutational bursts can be mediated by single catastrophic events like chromothripsis, or by potent mutagens like DNA-damaging radiation and chemotherapies[25,26]. Since punctuated bursts of mutations do not confer a constant mutational burden upon cells, clones which survive mutational bursts do not contend with the stress of significant ongoing genomic changes.

Genetic diversity can also arise during tumor initiation when multiple cells become transformed over a short period of time. Multi-ancestral tumors which arise from distinct tumor-founding cells might contain as much or more diversity than their uni-ancestral counterparts at an

earlier time during tumor evolution (Figure 1-1C). Unfortunately, very little is known about how this early diversity might impact the tumor growth, progression, and response to therapy.

Detection of Multi-Ancestral Tumors

Early work in the field of cancer biology concluded that most tumors are clonally derived from a single tumor-founding cell[27,28]. Despite the small number of tumors and tumor types examined in these original studies, the erroneous idea that all tumors are clonally derived became a central dogma of the field of cancer biology. In fact, many cancers can be derived from multiple tumor-founding cells, including chronic lymphocytic leukemia[29], malignant mesothelioma[30], and colon cancers[31], among many others[32].

Differentially labeling normal cells prior to tumor initiation is required to identify multi-ancestral tumors. In humans, most studies relied on random X-chromosome inactivation (which occurs early in development, long before tumor initiation) to identify distinct cell lineages[27,28,30-32]. Unfortunately, random X-chromosome inactivation results in large patches of similarly labeled cells, resulting in insufficient power to detect multi-ancestral tumors without extremely large sample sizes[33]. To overcome this challenge, animal models in which reporter proteins are differentially expressed in neighboring cells can facilitate tracking multiple tumor-founding cells through initiation, growth, and progression. Using these models, multi-ancestral gliomas and colon tumors were observed at frequencies ranging from 10-100%[34-38]. Unfortunately, due to the challenges of detecting multi-ancestral tumors in humans, little is known about the true prevalence of this tumor structure, and the frequency with which this structure arises is likely underestimated[39].

Formation of Multi-Ancestral Tumors

Clues to how multi-ancestral tumors arise might be found by comparing the frequency with which these tumors arise in different biological contexts. Multi-ancestral tumors are common in the setting of familial adenomatous polyposis (FAP), a condition in which a germline mutation in the *APC* tumor suppressor gene predisposes patients to colon tumorigenesis[40]. Meanwhile, they are seldom observed in the setting of inflammatory bowel disease (IBD), another condition which predisposes patients to colon tumorigenesis[41]. Since FAP patients often develop hundreds to thousands more synchronous tumors throughout the length of the colon than IBD patients, one potential explanation is that independently arising uni-ancestral tumors randomly collide and coalesce into multi-ancestral masses in FAP patients.

While random collision might explain some multi-ancestral tumors in patients with a high tumor burden, it is unlikely to be the only mechanism by which multi-ancestral tumors arise. Multi-ancestral colon tumors were identified in non-inflammatory, low tumor multiplicity settings, both in sporadic human disease and in mouse models[36,42]. In fact, the frequency with which these heterotypic tumors are detected in low-tumor burden mouse models indicates that they likely arise as a consequence of short range interactions between tumor-founding cells[36,37].

One or more tumor-founding cells might transform other nearby cells and thus "recruit" them to form a tumor mass. Tumor-adjacent tissue is often hyperplastic, indicating that tumors can impact the phenotype of nearby cells[43]. Genetically unique tumors often arise within close proximity of one another, indicating that the original tumors might transform nearby cells[44]. Some secreted ligands including Wnt1 can even cause transformation *in vitro* and *in vivo*[18,45]. If tumor-founding cells can transform neighboring normal tissue, the lower frequency with which multi-ancestral tumors are identified in IBD patients compared to sporadic disease might

therefore indicate that inflammation disrupts the communication between potential tumor-founding cells. Understanding how tumor-founding cells recruit neighboring cells might therefore lead to therapies that prevent additional heterogeneity from arising within tumors. Furthermore, if recruited clones rely on continuous signals from recruiter clones, disruption of the signals might reduce heterogeneity within established tumors.

Multiple tumor-founding cells might become independently transformed in close physical and temporal proximity and then cooperate to facilitate tumor initiation. By cooperating, multiple tumor-founding cells might be able to share the burden of acquiring the hallmarks of cancer and remodeling the tissue into a tumor-promoting environment instead of requiring all of the transforming events to accumulate within a single cell[46]. If multiple tumor-founding cells can cooperate during tumor initiation, the lower frequency with which multi-ancestral tumors are identified in IBD patients compared to sporadic disease might therefore indicate that inflammation is sufficient to promote tumorigenesis without a cooperating partner. Just as anti-inflammatory compounds can prevent inflammation-dependent tumorigenesis, understanding how tumor-founding cells cooperate to promote tumorigenesis might therefore lead to novel tumor prevention strategies.

Ultimately, however, comparing frequencies of multi-ancestral tumors between different biological conditions remains challenging since it is currently impossible to know the true frequency of multi-ancestral tumors within a population. A homotypic tumor could be derived from two tumor-founding cells carrying the same marker or from a single tumor-founding cell. Therefore, the power to detect multi-ancestral tumors varies between biological contexts and detection methods[39]. Improved experimental models will be necessary to identify the mechanism by which multi-ancestral tumors arise.

Growth and Progression of Multi-Ancestral Tumors

Though the multi-ancestral tumor architecture was identified in many tumor and cancer types, colon tumors were studied the most thoroughly[31,32,35,36,38,40-42]. Unfortunately, due to a lack of colon cancer models, most studies of the multi-ancestral tumor architecture were performed upon adenomas which likely lacked mutations in common tumor driver genes, including *Tp53*, *Kras*, and *Pik3ca*.

While the reported frequency of multi-ancestral adenomas in mouse models are relatively high, ranging from from 10-100%, multiple ancestral clones might compete within the tumor resulting in a single clone which eventually dominates the tumor and drives progression[34-38] (Figure 1-1D). In these tumors, the multi-ancestral tumor structure might only remain biologically relevant early in tumor evolution. Determining the role of multiple ancestors in promoting transformation might lead to the development of improved tumor prevention strategies.

Alternatively, multiple clones might persist throughout the adenoma to carcinoma sequence (Figure 1-1C). While heterogeneous uni-ancestral tumor cells might all share one or two actionable mutations which were present in the initial tumor-founding cells, it is unlikely that multiple ancestral clones would share actionable mutations. Selecting appropriate therapy for multi-ancestral tumors therefore becomes more challenging than for other heterogeneous tumors and increases the likelihood that the tumor will not respond to therapy. Additionally, regardless of the mechanism by which multi-ancestral tumors form, interactions between the co-existing clones might continue to actively promote tumor growth, invasion, and metastasis, resulting in a worse clinical prognosis[18,19]. The multi-ancestral structure might therefore provide

a prognostic marker, and understanding the mechanism by which the co-existing clones interact might lead to the development of novel therapies.

Unfortunately, multi-ancestral tumors were historically difficult to detect within patients and thus received little attention. While the biological relevance of multi-ancestral tumors is therefore poorly understood, early tumor heterogeneity gained as a consequence of multiple co-existing ancestral clones might drive the progression of a tumor. Tumors must escape immune surveillance, contact inhibition, and other critical checkpoints to grow into a detectable mass[47]. Early interclonal diversity increases the number of chances to randomly acquire an enhancement to one of these tumor hallmarks, while also increasing the opportunity for meaningful interactions to evolve between tumor cell populations. It remains likely, therefore, that the heterogeneity inherent within multi-ancestral tumors will impact the growth, progression, and chemotherapy resistance of the tumor and the overall prognosis of the patient. The work presented within this thesis establishes the significance of multiple tumor-founding cells in tumor initiation, growth, and progression.

Thesis Overview

To determine whether multiple clones are maintained as a tumor progresses to cancer, a model with a high likelihood of progressing to cancer is required. In Chapter 2, we examine the role of activated PI3K signaling within the colon and small intestine. PI3K signaling can initiate tumorigenesis independent of aberrant WNT signaling (Chapter 2.1) as well as increase the rate of tumor growth and progression by synergizing with canonical WNT signaling (Chapter 2.2). Importantly, even when PI3K signaling is activated prior to tumor initiation in the context of canonical WNT signaling, tumors still go through the adenoma-to-carcinoma sequence (Chapter

2.3). Together with the prevalence of *PIK3CA* mutations in clinical colorectal cancers, these findings indicate that PI3K is driver of both colon tumor initiation and progression.

Using this newly established model with a high likelihood of progressing to cancer, individual tumor clones could be followed through the adenoma to carcinoma sequence. In Chapter 3, we examine the contribution of multiple tumor-founding cells to tumor initiation, growth, and invasion. Fluorescently labeling cells prior to tumor initiation makes it possible to follow individual tumor-founding cells throughout tumorigenesis (Chapter 3.1). Even in the setting of PI3K activation, the multi-ancestral structure is maintained (Chapter 3.2). Moreover, multiple ancestral clones might be coopering to promote tumor progression in this model. We might therefore be able to take advantage of interactions between co-evolved clones to disrupt tumor growth and progression.

To understand the mechanism by which tumor-founding cells interact to promote tumor initiation, growth, invasion, and resistance to therapy, better *in vitro* and *in vivo* models will be needed. In Chapter 4, we introduce improvements upon previous models and methods which can be used to pursue these important questions. Further refinement of these models might reveal the mechanism by which multi-ancestral tumors form. Furthermore, utilizing targeted therapies against PI3K will allow us to determine whether naturally resistant clones protect susceptible clones within multi-ancestral tumors.

Together, these models could be used to better understand the ramifications of tumor ancestry during tumor initiation, growth, progression, and response to therapy. Just as inter-cellular interactions are critical to angiogenesis and immune escape, interclonal interactions likely contribute to tumor malignancy and chemotherapy resistance[19,20,46]. Identifying and

understanding the biological mechanism and repercussions of these interclonal interactions might therefore lead to the design of effective prevention and treatment strategies.

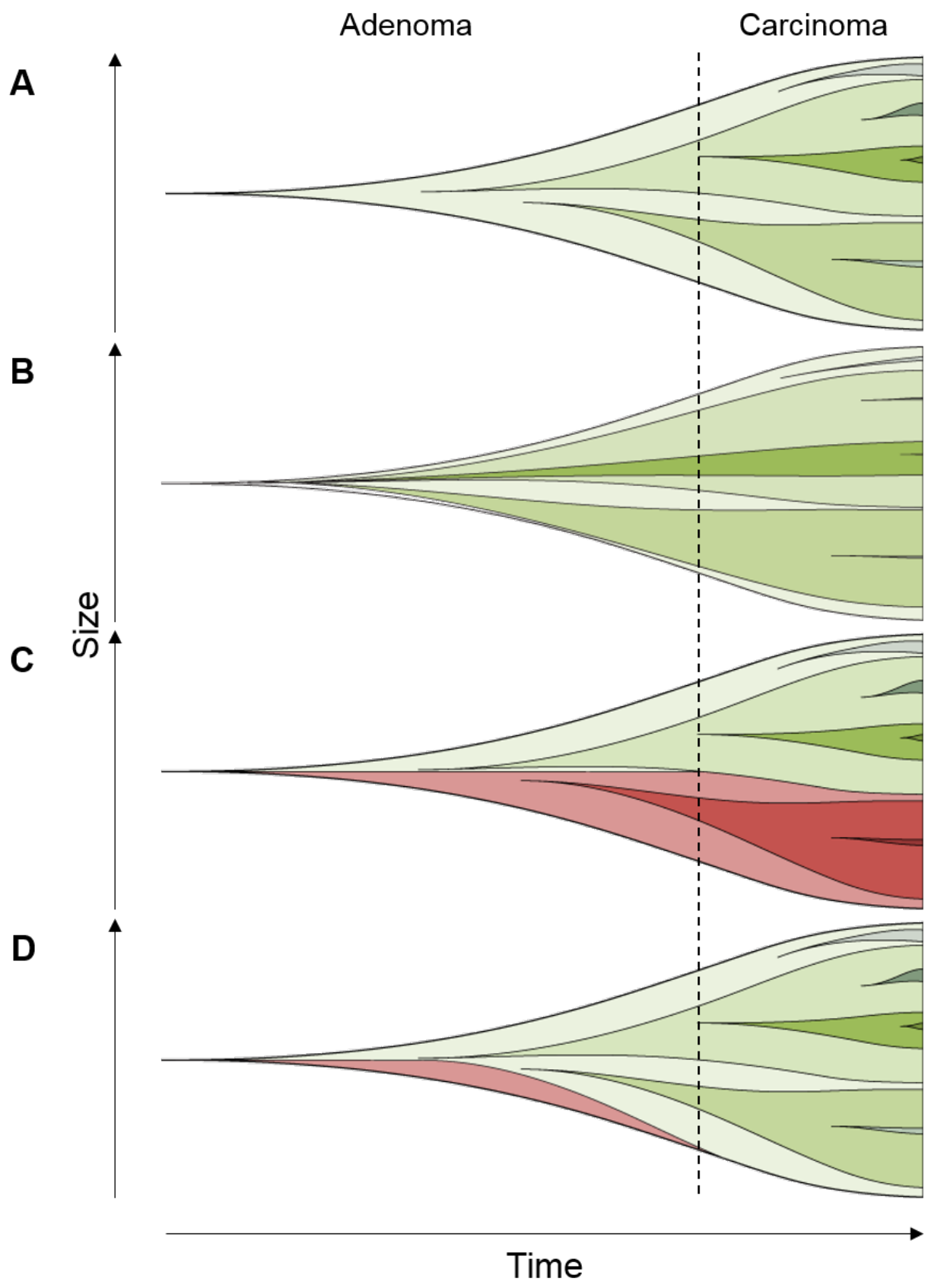
Adenoma
Carcinoma
A
B
C
D
Size
Time

Figure 1-1. Intratumoral heterogeneity can arise via multiple mechanisms. (A) A gradual accumulation of mutations results in constant clonal evolution and slow accumulation of tumor subclones. (B) Alternatively, mutational bursts result in the sudden accumulation of many tumor subclones. (C) Genetic diversity can also arise during tumor initiation if multiple cells become transformed over a short period of time. The clonal progeny of these multiple tumor-founding cells can then further evolve, resulting in the accumulation of many subclones within the resulting multi-ancestral tumor. Multiple ancestral clones might persist and even cooperate during multi-ancestral tumor progression. (D) Alternatively, one ancestral clone might gain a driver mutation which provides a competitive advantage, resulting in purification to a uni-ancestral tumor. Shades of green represent subclones within a green ancestral clones; shades of red represent subclones within a red ancestral clone.

References

1. Murugaesu, N., Chew, S. K. & Swanton, C. Adapting Clinical Paradigms to the Challenges of Cancer Clonal Evolution. *Am J Pathol* **182,** 1962–1971 (2013).
2. Navin, N. *et al.* Tumour evolution inferred by single-cell sequencing. *Nature* **472,** 90–94 (2011).
3. Burrell, R. A., McGranahan, N., Bartek, J. & Swanton, C. The causes and consequences of genetic heterogeneity in cancer evolution. *Nature* **501,** 338–345 (2013).
4. Suguro, M. *et al.* Clonal heterogeneity of lymphoid malignancies correlates with poor prognosis. *Cancer Sci* **105,** 897–904 (2014).
5. Medeiros, B. C., Othus, M., Fang, M., Appelbaum, F. R. & Erba, H. P. Cytogenetic heterogeneity negatively impacts outcomes in patients with acute myeloid leukemia. *Haematologica* **100,** 331–335 (2015).
6. Mengelbier, L. H. *et al.* Intratumoral genome diversity parallels progression and predicts outcome in pediatric cancer. *Nat Commun* **6,** 6125 (2015).
7. Mroz, E. A. *et al.* Intra-tumor genetic heterogeneity and mortality in head and neck cancer: analysis of data from the Cancer Genome Atlas. *PLoS Med* **12,** e1001786 (2015).
8. Landau, D. A. *et al.* Evolution and Impact of Subclonal Mutations in Chronic Lymphocytic Leukemia. *Cell* **152,** 714–726 (2013).
9. Anaka, M. *et al.* Intratumoral genetic heterogeneity in metastatic melanoma is accompanied by variation in malignant behaviors. *BMC Med Genomics* **6,** 40 (2013).
10. Merlo, L. M. F., Pepper, J. W., Reid, B. J. & Maley, C. C. Cancer as an evolutionary and ecological process. *Nat Rev Cancer* **6,** 924–935 (2006).
11. Greaves, M. & Maley, C. C. Clonal evolution in cancer. *Nature* **481,** 306–313 (2012).

12. Tougeron, D. *et al.* Effect of low-frequency *KRAS* mutations on the response to anti-EGFR therapy in metastatic colorectal cancer. *Ann Oncol* **24,** 1267–1273 (2013).

13. Gerlinger, M. *et al.* Intratumor Heterogeneity and Branched Evolution Revealed by Multiregion Sequencing. *N Engl J Med* **366,** 883–892 (2012).

14. Kosmidou, V. *et al.* Tumor Heterogeneity Revealed by *KRAS*, *BRAF*, and *PIK3CA* Pyrosequencing: *KRAS* and *PIK3CA* Intratumor Mutation Profile Differences and Their Therapeutic Implications. *Hum Mutat* **35,** 329–340 (2014).

15. Gatenby, R. A., Silva, A. S., Gillies, R. J. & Frieden, B. R. Adaptive Therapy. *Cancer Res* **69,** 4894–4903 (2009).

16. Sequist, L. V. *et al.* Genotypic and histological evolution of lung cancers acquiring resistance to EGFR inhibitors. *Sci Transl Med* **3,** 75ra26–75ra26 (2011).

17. Axelrod, R., Axelrod, D. E. & Pienta, K. J. Evolution of cooperation among tumor cells. *Proc Natl Acad Sci U S A* **103,** 13474–13479 (2006).

18. Cleary, A. S., Leonard, T. L., Gestl, S. A. & Gunther, E. J. Tumour cell heterogeneity maintained by cooperating subclones in Wnt-driven mammary cancers. *Nature* **508,** 113–117 (2014).

19. Marusyk, A. *et al.* Non-cell-autonomous driving of tumour growth supports sub-clonal heterogeneity. *Nature* **514,** 54–58 (2014).

20. Straussman, R. *et al.* Tumour micro-environment elicits innate resistance to RAF inhibitors through HGF secretion. *Nature* **487,** 500–504 (2012).

21. Waclaw, B. *et al.* A spatial model predicts that dispersal and cell turnover limit intratumour heterogeneity. *Nature* **525,** 261–264 (2015).

22. Swanton, C., McGranahan, N., Starrett, G. J. & Harris, R. S. APOBEC Enzymes:

Mutagenic Fuel for Cancer Evolution and Heterogeneity. *Cancer Discov* **5,** 704–712 (2015).

23. Le, D. T. *et al.* PD-1 Blockade in Tumors with Mismatch-Repair Deficiency. *N Engl J Med* **372,** 2509–2520 (2015).
24. Dhillon, K. K., Swisher, E. M. & Taniguchi, T. Secondary mutations of BRCA1/2 and drug resistance. *Cancer Sci* **102,** 663–669 (2011).
25. Stephens, P. J. *et al.* Massive Genomic Rearrangement Acquired in a Single Catastrophic Event during Cancer Development. *Cell* **144,** 27–40 (2011).
26. Sottoriva, A. *et al.* A Big Bang model of human colorectal tumor growth. *Nat Genet* **47,** 209–216 (2015).
27. Linder, D. & Gartler, S. M. Glucose-6-Phosphate Dehydrogenase Mosaicism: Utilization as a Cell Marker in the Study of Leiomyomas. *Science* **150,** 67–69 (1965).
28. Fialkow, P. J., Gartler, S. M. & Yoshida, A. Clonal origin of chronic myelocytic leukemia in man. *Proc Natl Acad Sci U S A* **58,** 1468 (1967).
29. Sanchez, M.-L. *et al.* Incidence and clinicobiologic characteristics of leukemic B-cell chronic lymphoproliferative disorders with more than one B-cell clone. *Blood* **102,** 2994–3002 (2003).
30. Comertpay, S. *et al.* Evaluation of clonal origin of malignant mesothelioma. *J Transl Med* **12,** 1 (2014).
31. Beutler, E., Collins, Z. & Irwin, L. E. Value of genetic variants of glucose-6-phosphate dehydrogenase in tracing the origin of malignant tumors. *N Engl J Med* **276,** 389–391 (1967).
32. Parsons, B. L. Many different tumor types have polyclonal tumor origin: Evidence and

implications. *Mutat Res Rev Mutat Res* **659,** 232–247 (2008).

33. Novelli, M. *et al.* X-inactivation patch size in human female tissue confounds the assessment of tumor clonality. *Proc Natl Acad Sci U S A* **100,** 3311–3314 (2003).

34. Fomchenko, E. I. *et al.* Recruited Cells Can Become Transformed and Overtake PDGF-Induced Murine Gliomas In Vivo during Tumor Progression. *PLoS ONE* **6,** e20605 (2011).

35. Thliveris, A. T. *et al.* Clonal Structure of Carcinogen-Induced Intestinal Tumors in Mice. *Cancer Prev Res* **4,** 916–923 (2011).

36. Thliveris, A. T. *et al.* Polyclonality of familial murine adenomas: Analyses of mouse chimeras with low tumor multiplicity suggest short-range interactions. *Proc Natl Acad Sci U S A* **102,** 6960–6965 (2005).

37. Newton, M. A., Clipson, L., Thliveris, A. T. & Halberg, R. B. A Statistical Test of the Hypothesis that Polyclonal Intestinal Tumors Arise by Random Collision of Initiated Clones. *Biometrics* **62,** 721–727 (2006).

38. Merritt, A. J., Gould, K. A. & Dove, W. F. Polyclonal structure of intestinal adenomas in $Apc^{Min/+}$ mice with concomitant loss of Apc^{+} from all tumor lineages. *Proc Natl Acad Sci U S A* **94,** 13927 (1997).

39. Newton, M. A. On estimating the polyclonal fraction in lineage-marker studies of tumor origin. *Biostat* **7,** 503–514 (2006).

40. Novelli, M. R. *et al.* Polyclonal Origin of Colonic Adenomas in an XO/XY Patient with FAP. *Science* **272,** 1187–1190 (1996).

41. Leedham, S. J. *et al.* Clonality, Founder Mutations, and Field Cancerization in Human Ulcerative Colitis–Associated Neoplasia. *Gastroenterology* **136,** 542–550.e6 (2009).

42. Thirlwell, C. *et al.* Clonality Assessment and Clonal Ordering of Individual Neoplastic Crypts Shows Polyclonality of Colorectal Adenomas. *Gastroenterology* **138,** 1441–1454.e7 (2010).

43. Matthew Bjerknes, H. C. Colossal Crypts Bordering Colon Adenomas in Apc^{Min} Mice Express Full-Length Apc. *Am J Pathol* **154,** 1831–1834 (1999).

44. Slaughter, D. P., Southwick, H. W. & Smejkal, W. Field cancerization in oral stratified squamous epithelium; clinical implications of multicentric origin. *Cancer* **6,** 963–968 (1953).

45. Jue, S. F., Bradley, R. S., Rudnicki, J. A., Varmus, H. E. & Brown, A. M. The mouse Wnt-1 gene can act via a paracrine mechanism in transformation of mammary epithelial cells. *Mol Cell Biol* **12,** 321–328 (1992).

46. Tabassum, D. P. & Polyak, K. Tumorigenesis: it takes a village. *Nat Rev Cancer* **15,** 473–483 (2015).

47. Hanahan, D. & Weinberg, R. A. The Hallmarks of Cancer. *Cell* **100,** 57–70 (2000).

CHAPTER 2

Early driver mutations can contribute to tumor initiation, growth, and progression.

Preface

When do driver mutations arise within heterogeneous tumors? *In silico* modeling predicts that heterogeneous mutations within cancers must have arisen when a tumor was too small to identify[1]. However, while *APC* mutations are thought to occur early during colorectal tumor evolution, many driver mutations including those in *KRAS* and *PIK3CA* which are often heterogeneous in colorectal cancers are thought to commonly arise later and contribute to tumor invasion and metastasis[2,3]. This notion is supported by the fact that while loss of *APC* does predispose intestinal epithelium to tumorigenesis, activating mutations in *KRAS* do not appear to do so in animal models[4]. The first part of this chapter demonstrates that constitutive activation of the protein product of *PIK3CA* (PI3K) predisposes the intestinal epithelium to tumorigenesis. The second part of the chapter extends the work by providing evidence that constitutive activation of PI3K synergizes with *APC* mutations to drive tumor growth and invasion. The final part of the chapter shows that early acquisition of *APC*, *KRAS*, and *PIK3CA* mutations (as predicted by *in silico* modeling of heterogeneous tumors) is insufficient to circumvent the adenoma-to-carcinoma transition. Together, these findings indicate that activation of PI3K in the normal intestinal mucosa can drive rapid tumor initiation and progression through the adenoma-to-carcinoma sequence.

2.1 Mice expressing activated PI3K rapidly develop advanced colon cancer

Alyssa A. Leystra, Dustin A. Deming, Christopher D. Zahm, Mohammad Farhoud, Terrah J. Paul Olson, Jamie N. Hadac, Laura A. Nettekoven, Dawn M. Albrecht, Linda Clipson, Ruth Sullivan, Mary Kay Washington, Jose R. Torrealba, Jamey P. Weichert, Richard B. Halberg.

Abstract

Aberrations in the phosphoinositide 3-kinase (PI3K) signaling pathway play a key role in the pathogenesis of numerous cancers by altering cellular growth, metabolism, proliferation, and apoptosis. Mutations in the catalytic domain of PI3K that generate a dominantly active kinase are commonly found in human colorectal cancers and have been thought to drive tumor progression but not initiation. However, the effects of constitutively activated PI3K upon the intestinal mucosa have not been previously studied in animal models. Here, we show that the expression of a dominantly active form of the PI3K protein in the mouse intestine results in hyperplasia and advanced neoplasia. Mice expressing constitutively active PI3K in the epithelial cells of the distal small bowel and colon rapidly developed invasive adenocarcinomas in the colon that spread into the mesentery and adjacent organs. The histologic characteristics of these tumors were strikingly similar to invasive mucinous colon cancers in humans. Interestingly, these tumors formed without a benign polypoid intermediary, consistent with the lack of aberrant WNT signaling observed. Together, our findings indicate a non-canonical mechanism of colon tumor initiation that is mediated through activation of PI3K. This unique model has the potential to further our understanding of human disease and facilitate the development of therapeutics through pharmacologic screening and biomarker identification.

Adapted from Cancer Res; 72(12); 2931–36. ©2012 AACR.

In addition to reformatting, the following changes were made for the sake of consistency:

- Figures and references were renumbered
- Minor words were changed to improve readability and clarity
- "*FC*$^{+}$" mice were renamed "Fabp1-Cre^{+}" mice

All animal models described in this paper are briefly defined in Appendix 1.

Authors' Contributions

A.A. Leystra and D.A. Deming contributed equally to this work.

A.A. Leystra, D.A. Deming, and R.B. Halberg were involved in all aspects of the research and preparation of the manuscript. C.D. Zahm assisted with animal husbandry, necropsy, and immunohistochemistry. M. Farhoud performed the PET/CT imaging and data analysis. J.R. Torrealba, R. Sullivan, and M.K. Washington assisted with IHC and interpretation of histopathology. J.N. Hadac performed the real-time PCR. T.J. Paul Olson, L.A. Nettekoven, and D.M. Albrecht provided technical support. J.P. Weichert provided reagents and oversaw PET/CT experiments. L. Clipson assisted with figure and manuscript preparation. All authors discussed results and edited the manuscript.

Introduction

Colorectal cancer remains a leading cause of cancer-related death, despite significant advances in treatment options. Targeting oncogenic pathways has been and continues to be a significant interest of many investigators. The PI3K/AKT signaling cascade has been identified as a promising target for drug development. Many new inhibitors of phosphoinositide 3-kinase (PI3K) and the downstream signaling molecules are currently in clinical development; however, their role in the clinical setting has yet to be well defined.

The PI3K/AKT pathway transmits signals from various transmembrane growth factor receptors through a kinase cascade to nuclear transcription factors[5]. PI3K initiates this signaling pathway through the phosphorylation of phosphatidylinositol 4,5-bisphosphate (PIP2) to phosphatidylinositol 3,4,5-trisphosphate (PIP3). PIP3 then activates the serine/threonine kinase AKT, which phosphorylates multiple downstream targets responsible for a wide variety of vital cellular functions. One of the prominent targets is mTOR, a serine/threonine kinase that is an important regulator of cell growth and metabolism. This kinase then mediates activation of the eukaryotic translation initiation factor 4E-binding protein (4E-BP1) and the p70S6 ribosomal kinase (S6) that are involved in protein synthesis.

Mutations of the *PIK3CA* gene, which encodes the p110 catalytic subunit of the PI3K kinase, are present in 20% to 30% of human colon cancers[6]. Three common mutations (E542K, E545K, and H1047R) result in a dominantly active form of the PI3K protein[7]. *PIK3CA* mutations have been investigated in numerous cancer cell lines; however, the effect of a dominant-active PI3K has not previously been investigated in the rodent intestine. We describe a novel mouse model designed to provide insight into the biologic effects of a dominantly active form of PI3K

in the colon and, once characterized, to further test new therapeutic agents and identify biomarkers.

Results

We sought to determine whether activation of the PI3K/AKT cascade affects homeostasis in the mammalian intestine. Mice carrying a transgene in which the fatty acid–binding protein promoter is fused to Cre recombinase (Fabp1-Cre) were crossed to mice carrying a transgene at the Rosa26 promoter which encodes a chimeric protein with the iSH2 domain of the p85 regulatory subunit fused to the N-terminus of p110 catalytic subunit (Pik3ca*; Appendix 2-1A)[8,9]. (FVB/J × C57Bl/6J)F1 progeny carrying both transgenes (Fabp1-Cre^{+} Pik3ca*$^{+}$) express this dominantly active form of p110 in epithelial cells of the distal small bowel and colon because the Cre recombinase excises a stop sequence upstream of the Pik3ca* transgene.

The majority of Fabp1-Cre^{+} Pik3ca*$^{+}$ mice became moribund between 40 and 60 days of age (Appendix 2-1B). These mice were imaged with a Siemens Dual Hybrid PET/CT scanner, revealing high avidity for fluorodeoxyglucose (^{18}F; FDG), and CLR1404[10] (^{124}I; a phospholipid ether analogue) in the proximal colon and low avidity for FDG in the distal small bowel and the remainder of the colon (Figure 2-1A and C). Mice were sacrificed and tissues were imaged *ex vivo* (data not shown). The high avidity in the proximal colon was due to the uptake of imaging agents by large tumors (Figure 2-1B and D). No signal was detected in any Fabp1-Cre^{0} Pik3ca*$^{+}$ littermates.

At necropsy, most Fabp1-Cre^{+} Pik3ca*$^{+}$ mice (15 of 17) were found to have severe obstruction of the proximal colon, resulting in marked dilation of the small bowel and cecum (Figure 2-2A). Obstructive enteropathy was always caused by the presence of a massive tumor in

the proximal colon. On gross examination, these colon tumors penetrated through the serosa and had an impressive enlargement of blood vessels and mesenteric lymphatic tissue (Figure 2-2A). In a group of 5 Fabp1-Cre^{+} Pik3ca*$^{+}$ mice, we sectioned *en bloc* the tumor and mesenteric lymphatic tissue. The lymphatic tissue was hyperplastic in all mice. Tumor deposits were identified within the mesenteric adipose tissue in 3 of 5 mice. In other Fabp1-Cre^{+} Pik3ca*$^{+}$ mice, the intestines were removed, split lengthwise, and splayed open, revealing large, flat, thickened rugal folds and plaque-like tumors in the proximal colon without a significant luminal exophytic component (Figure 2-2A).

Histologic examination of the proximal colon confirmed the presence of moderately differentiated, diffusely invasive mucinous adenocarcinomas with extension through the muscularis propria and serosa into the pericolonic adipose tissue (Figures 2-2B and -3A). These tumors exhibited mucinous differentiation with islands of malignant glands within mucin lakes (Figure 2-2B and 2-3B) as well as budding at the leading edge of invasion fronts. The masses elicited a desmoplastic reaction as well as inflammatory infiltration (Figure 2-2B). The neoplastic cells exhibited high-grade nuclear atypia, phosphorylation of AKT, and an increase in cellular proliferation, as compared with the normal colonic epithelium from Fabp1-Cre^{+} Pik3ca*$^{+}$ or Fabp1-Cre^{0} Pik3ca*$^{+}$ mice and adenomas from *Apc*$^{Min/+}$ mice (Figure 2-3B; Appendix 2-2 and -3). In addition, neoplastic cells were weakly positive for cytokeratin 20 and negative for cytokeratin 7, indicating that the transformed cells originated from the intestinal epithelium[11] (Appendix 2-4). Areas of invasion were covered by hyperplastic crypts with focal crypt dilatation and branching or at times a denuded epithelium.

Some of the Fabp1-Cre^{+} Pik3ca*$^{+}$ mice (6 of 17) also developed cecal tumors. Direct extension was observed of one tumor into the lymphatic, ovarian, uterine, and pancreatic tissue

(Figure 2-2C), which would be consistent with stage T4b invasion of human cancers. No gross evidence of liver or lung metastasis was identified.

The development of advanced cancers in this model is mediated by the expression of the dominantly active form of PI3K and consequently activation of several of its targets (Figures 2-3B and -4A; Appendix 2-5). The presence of the PI3K* protein was confirmed in the mucosa of the proximal and distal colon (Figure 2-4A). In addition, downstream activation of AKT and subsequent phosphorylation of S6 and 4E-BP1 were observed (Figure 2-4A). These observations confirm that the transgene was transcribed and translated in the colon of Fabp1-Cre^{+} Pik3ca*$^{+}$ mice and that its expression resulted in increased downstream activation of the PI3K/AKT/mTOR pathway. In contrast, phosphorylation of extracellular signal-regulated kinase (ERK)1/2 was not noted above baseline, indicating that activation of the RAF/MEK/ERK cascade is not involved in tumorigenesis in this model (Figure 2-4B).

Most human colorectal adenomas carry truncating mutations in *APC* and the loss of this gene is thought to be the tumor-initiating event[12]. These mutations result in translocation of β-catenin to the nucleus (Appendix 2-3) and consequently change the pattern of gene expression. β-catenin was examined in the invasive adenocarcinomas of Fabp1-Cre^{+} Pik3ca*$^{+}$ mice and found to be localized to the cell membrane and cytoplasm (Figure 2-3B). This pattern of localization indicates that tumor initiation in Fabp1-Cre^{+} Pik3ca*$^{+}$ mice is not mediated through aberrant WNT signaling. The lack of aberrant WNT signaling also correlates with the lack of an exophytic or polyp-like morphology in this model, as polyp formation would be expected in *Apc*-mutant tumors. Given the lack of other induced genetic abnormalities and the short time frame in which these tumors develop, the initiating event in Fabp1-Cre^{+} Pik3ca*$^{+}$ cancers appears to be PI3K-mediated.

With the goal of identifying precursor lesions or early tumors, Fabp1-Cre^{+} Pik3ca*$^{+}$ mice were sacrificed at fixed points in time. Cohorts of at least 4 mice were evaluated at 20, 30, 40, and 50 days of age. On histologic examination, the distal small bowel and colon were hyperplastic in all mice examined, and lesions similar to serrated sessile adenomas that are seen in humans were identified (Appendix 2-6). Invasive mucinous adenocarcinomas were first observed in the 40-day cohort.

To examine whether intestinal cell fate is altered before tumorigenesis, we assessed the four major epithelial cell lineages in the colon (Appendix 2-7). The relative number of absorptive cells, Paneth cells, and enteroendocrine cells in samples from Fabp1-Cre^{+} Pik3ca*$^{+}$ mice were similar to that observed in samples from controls. In contrast, goblet cells were slightly more abundant in the samples from experimental mice than in samples from controls.

Discussion

Animal models have led to significant advances in our understanding of the biology of many cancer types, including colorectal cancer. This study is the first to describe highly invasive mucinous adenocarcinomas in the mammalian intestine resulting from the expression of a dominantly active form of PI3K. These tumors are quite comparable with cancers in humans, especially those on the right side of the colon. Shared histologic characteristics include high-grade nuclear atypia, budding at the leading edge of the invasion fronts, and mucin lakes[13].

Recently, a model lacking the expression of PTEN in the intestine was described[14]. This model has a drastically different phenotype with only 19% of mice developing tumors in the small intestine by 12 months of age. Despite having activated AKT signaling, only one invasive adenocarcinoma was identified. We hypothesize that the primary difference between these two

models relates to the roles of PTEN and PI3K in the AKT signaling pathway (i.e., tumor suppressor gene vs. an oncogene). These models also have different genetic backgrounds, and Cre expression was controlled by different promoters.

Interestingly, in Fabp1-Cre^{+} Pik3ca*$^{+}$ mice, tumor initiation appears to be independent of WNT signaling and invasive cancers develop rapidly without a benign polypoid or exophytic precursor lesion. These tumors appear to develop through a novel non-canonical pathway to tumor initiation mediated by PI3K. Human tumor cell lines, including the commonly investigated RKO human colon cancer cell line, that possess activating mutations of *PIK3CA* but lack mutations of *APC* and *CTNNB1* have been described[14]. In addition, human colorectal tumors carrying activating mutations in *PIK3CA* often express normal levels of β-catenin[15]. Thus, non-polypoid tumors that arise quickly as a consequence of mutations in *PIK3CA* might explain the development of interval cancers that occur between screening colonoscopies. Further investigations need to examine this novel pathway to tumorigenesis described in this study.

This model will also aid in the development and testing of pharmacologic agents. Targeting oncogenic pathways has led to recent advances in the treatment of multiple cancers, including the use of vemurafenib to treat melanomas harboring *BRAF* mutations, erlotinib for lung cancers possessing *EGFR* mutations, and crizotinib to treat lung cancers harboring the *EML4-ALK* translocation. *PIK3CA* has been identified as an important oncogene in multiple cancers and thus modeling this mutation in the mammalian colon is important. This murine model with rapidly developing invasive colorectal cancers is an exciting model of human colon cancer that has the potential to be instrumental in the development of targeted therapeutics and biomarker identification.

Materials and Methods

Mouse husbandry

All animal studies were conducted under protocols approved by the Institutional Animal Care and Use Committee at the University of Wisconsin (Madison, WI) following the guidelines of the American Association for the Assessment and Accreditation of Laboratory Animal Care. Fabp1-Cre+ mice [FVB/N-Tg(Fabp1-Cre)1Jig; National Cancer Institute Mouse Repository; strain number - 01XD8] were maintained by backcrossing to FVB mice (FVB/J; The Jackson Laboratory; stock number - 001800). Pik3ca*$^{+}$ mice [C57BL/6-*Gt(ROSA)26Sor*$^{tm7(Pik3ca*,EGFP)Rsky}$/J; The Jackson Laboratory; stock Number - 012343] were maintained by crossing siblings for fewer than five generations. Fabp1-Cre^{+} Pik3ca*$^{+}$ and Fabp1-Cre^{0} Pik3ca*$^{+}$ littermates were generated by crossing Fabp1-Cre^{+} females with Pik3ca*$^{+}$ males. For comparison, F1 *Apc*$^{Min/+}$ hybrids were generated by crossing SWR females (SWR/J; The Jackson Laboratory; stock number - 00689) to C57BL/6 *Apc*$^{Min/+}$ males (C57BL/6J ApcMin/J; The Jackson Laboratory; stock number - 002020). Offspring carrying *Apc*$^{Min/+}$ were treated with drinking water containing 4% dextran sodium sulfate as described previously[16]. This treatment increases the multiplicity of tumors in the colon.

Genotyping

Mice were genotyped for Fabp1-Cre, Pik3ca*, and the *Min* allele of *Apc* as described previously[8,17,18].

Imaging

Animals were fasted for 6 hours before injection of ^{18}F-FDG (160 μCi; IBA Molecular). After injection, the animals were kept under anesthesia for 60 minutes and then prepared for dual hybrid microPET/CT colonography as described previously[19]. A 10-minute positron emission tomography (PET) acquisition was carried out and computed tomographic (CT) scan followed immediately. A similar approach was used to acquire images after injection of ^{124}I-CLR1404 (120 μCi; Novelos) except that the animals were not fasted before the injection of the imaging agent and PET scanning was conducted 98 hours after injection. In this case, the duration of the PET scan was set based on coincidence detection, which was 30 million counts or approximately 15 minutes. Maximum intensity projections were created in Siemens Inveon Research Workplace. The PET images were reconstructed using OSEM3D/MAP (OSEM3D, 2 iterations; MAP 18, iterations 16 subsets). Attenuation correction was carried out using the CT data. The CT images were reconstructed using standard conebeam reconstruction. Movies were created from 3-dimensional representations of the PET and CT data using AMIRA Version 5.2 software package (Visage Imaging Inc.).

Histology

Mice were euthanized by CO_2 asphyxiation. Small bowel and colon were removed, flushed with PBS, cut open lengthwise, splayed out, and fixed in 10% buffered formalin for 24 to 48 hours. Tissues were then stored in 70% ethanol. The duodenum, ileum, and colon were rolled, processed, embedded in paraffin, and cut into 5 μm sections. In some cases, tumors were isolated before rolling and then handled in the same manner. Sections were stained with either

hematoxylin and eosin (H&E) for histologic review or periodic acid-Schiff (PAS) stain to assess the goblet cells.

Immunohistochemistry

Immunohistochemistry was carried out using the Histomouse Max Broad Spectrum (DAB) Kit as instructed by the manufacturer (Invitrogen) except for the following modification: antigen unmasking was carried out by boiling the samples for 20 minutes in citrate buffer (pH 6.0) or treating samples with proteinase K for 5 minutes. The primary antibodies included rabbit anti-pAKT (Ser473, 1:100, Cell Signaling Technology), mouse anti-β-catenin (1:400, BD Biosciences—Clone 14), rabbit anti-cytokeratin 7 (clone SP52, Ventana,), rabbit anti-cytokeratin 20 (clone SP33, Ventana), rabbit anti-lysozyme (1:500, DAKO), rabbit anti-PCNA (1:1,000, Cell Signaling Technology), and rabbit anti-synaptophysin (1:500, Abcam).

Western blot analysis

Tissue samples were collected and flash frozen. After 24 hours, the samples were sonicated in T-PER tissue protein extraction reagent (Thermo Scientific), proteasome inhibitor cocktail (Sigma-Aldrich), and phenylmethylsulfonylfluoride (PMSF; Sigma-Aldrich). Extracted protein (30 μg) from experimental mice and controls was loaded onto precast 10% PAGE (Bio-Rad). The gels were run at 200 volts for 30 minutes and transferred to polyvinylidene difluoride (PVDF) Immobilon-P Membranes (Millipore) at 100 volts for 45 minutes. The membranes were blocked with 5% nonfat dry milk for 1 hour and then probed with primary antibodies against p110α, pAKT (Ser473), pS6 (Ser235/236), p4E-BP1 (Thr37/46), or pMAPK (Thr202/Tyr 204; Cell Signaling Technology) in bovine serum albumin (BSA; Sigma-Aldrich) at a 1:1,000 ratio

for 16 hours. Following this incubation, membranes were washed in TBS-T wash buffer (TBS, 0.05% Tween-20) before being probed with goat anti-rabbit horseradish peroxidase–labeled antibody (Millipore) in 5% nonfat dry milk or BSA at ratio of 1:10,000 for 1 to 2 hours. The membranes were then washed again with TBS-T. SuperSignal West Pico Chemiluminescent Substrate (Thermo Scientific) was added according to the manufacturer's instructions and incubated for 5 minutes. Following removal of the substrate, the membranes were placed in plastic sleeves and exposed to film. Anti-GAPDH (glyceraldehyde-3-phosphate dehydrogenase) antibody (Cell Signaling) was used as a loading control at a ratio of 1:5,000.

Real-time PCR

Tissue from mice was isolated and stored in RNAlater (Qiagen). Samples were disrupted in RLT buffer with a Kontes Pellet Grinder (Kimple & Chase). RNA was prepared using the RNeasy Mini Kit (Qiagen) following the manufacturer's instructions. The yield was quantified with a NanoDrop DU-800 (Thermo Scientific). cDNA was generated using the ImProm II Reverse Transcription System (Promega) from 500 ng RNA following the manufacturer's instructions. Quantitative PCR amplifications were prepared with 100 ng cDNA, Sso Advanced SYBR Green Supermix (Bio-Rad), and primers for mouse PI3K catalytic, alpha polypeptide (*PI3Kca*; NM008839) forward 5′-ATCATGCAAATCCAGTGCAA-3′ and reverse 5′-CAGCTGTCCGTCATCTTTCA-3′ and ribosomal protein L13A (*RPL13A*; NM_009438) forward 5′-TTCGGCTGAAGCCTACCAGAAAGT-3′ and reverse 5′-TCTTCCGATAGTGCATCTTGGCCT-3′. Real-time PCR was carried out with a CFX96 Real-Time PCR machine (Bio-Rad). Melt-curve analysis and serial dilution of cDNA confirmed

amplification of a single product with high efficiency. Gene expression was normalized to *RPL13A* and reactions were conducted in triplicate.

Disclosure of Potential Conflicts of Interest

The authors declare competing financial interests. J.P. Weichert is the founder of Cellectar, Inc., which holds the licensing rights to the CLR1404 technology, and therefore has a financial interest in this agent. J.P. Weichert is also employed as Director, CSO and has ownership interest (including patents) in Novelos. No potential conflicts of interests were disclosed by the other authors.

Acknowledgments

The authors thank Ella Ward and Jane Weeks in Experimental Pathology at the University of Wisconsin Carbone Cancer Center for technical assistance and Drs. Jeff Bacher, William F. Dove, Norman Drinkwater, Greg Kennedy, Paul Lambert, Mark Reichelderfer, H. Ian Robins, and William Schelman for critical review of the manuscript. The article is dedicated in the memory of Joseph E. Hoeger.

The project was supported by the Conquer Cancer Foundation of the American Society of Clinical Oncology through a Young Investigator Award (D.A. Deming), the National Cancer Institute of the U.S. NIH through P01 AI084853 (J.R. Torrealba), P30 CA014520 (Core Grant, University of Wisconsin Carbone Cancer Center), P50 CA095103 (Gastrointestinal Specialized Program of Research Excellence Grant, Vanderbilt-Ingram Cancer Center), R01 CA123438 (R.B. Halberg), T32 CA009614 (D.A. Deming), T32 CA009135 (J.N. Hadac and C.D. Zahm), and T32 CA090217 (T.J.P. Olson), and start-up funds (R.B. Halberg) from the Division of

Gastroenterology and Hepatology, the Department of Medicine, and the School of Medicine and Public Health at the University of Wisconsin.

2.2 *PIK3CA* and *APC* mutations are synergistic in the development of intestinal cancers

Dustin A. Deming, **Alyssa A. Leystra**, Laura Nettekoven, Chelsie Sievers, Devon Miller, Malisa Middlebrooks, Linda Clipson, Dawn Albrecht, Jeffrey Bacher, Mary Kay Washington, Jamey Weichert, and Richard B. Halberg.

Abstract

Human colorectal cancers are known to possess multiple mutations, though how these mutations interact in tumor development and progression has not been fully investigated. We have previously described the Fabp1-Cre^{+} Pik3ca*$^{+}$ murine colon cancer model, which expresses a constitutively activated phosphoinositide-3 kinase (PI3K) in the intestinal epithelium. The expression of this dominantly active form of PI3K results in hyperplasia and invasive mucinous adenocarcinomas. These cancers form via a non-canonical mechanism of tumor initiation that is mediated through activation of PI3K and not through aberrations in WNT signaling. Since the *Adenomatous Polyposis Coli* (*APC*) gene is mutated in the majority of human colon cancers and often occurs simultaneously with *PIK3CA* mutations, we sought to better understand the interaction between *APC* and *PIK3CA* mutations in the mammalian intestine. In this study, we have generated mice in which the expression of a constitutively active PI3K and the loss of APC occur simultaneously in the distal small intestine and colon. Here, we demonstrate that expression of a dominant active PI3K synergizes with loss of APC activity resulting in a dramatic change in tumor multiplicity, size, morphology and invasiveness. Activation of the PI3K pathway is not able to directly activate WNT signaling through the nuclear localization of CTNNB1 (β-catenin) in the absence of aberrant WNT signaling. Alterations at the transcriptional

level, including increased CCND1, may be the etiology of synergy between these activated pathways.

Adapted from Oncogene; 33, 2245–2254. ©2014 Deming *et al.*

In addition to reformatting, the following changes were made for the sake of consistency:

- Figures and references were renumbered
- Minor words were changed to improve readability and clarity
- "*FC*^{1}" mice were renamed "Fabp1-Cre^{+}" mice
- "*3K*^{1}" mice were renamed "Pik3ca*$^{+}$" mice

All animal models described in this paper are briefly defined in Appendix 1.

Authors' Contributions

D.A. Deming, A.A. Leystra, and R.B. Halberg were involved in all aspects of the research and preparation of the manuscript. C.K. Sievers assisted with IHC. J. Bacher assisted with MSI testing. L.A. Nettekoven, M. Middlebrooks, and D. Albrecht and D. Miller provided technical support. M.K. Washington assisted with interpretation of histopathology. J. Weichert provided reagents and oversaw experiments. L. Clipson assisted with figure and manuscript preparation. All authors discussed results and edited the manuscript.

Introduction

Colorectal adenocarcinoma continues to be a major etiology of morbidity and mortality despite significant advances in the understanding of tumor biology and treatment options[20]. The profile of mutations has now been characterized in multiple human cancers; however, the role of these mutations in tumorigenesis, progression and response to therapy has largely yet to be defined[21].

Adenomatous Polyposis Coli (*APC*) mutations have been well characterized as important mediators of colorectal tumorigenesis[22]. Germline mutations were discovered in patients with familial adenomatous polyposis, but somatic mutations are also present in 80–90% of sporadic colorectal polyps and cancers[23]. These mutations most often lead to truncation of the APC protein resulting in the loss of function of this tumor suppressor. Loss of APC function results in dysregulation of CTNNB1 (β-catenin), leading to increased WNT pathway signaling through MYC and CCND1 (cyclin D1), among others[24]. The $Apc^{Min/+}$ mouse carries a germline mutation in *Apc*, which results in these mice developing many adenomas along the length of intestinal tract[18]. This model has been widely used to study the biology of intestinal tumors and as a valuable tool for chemoprevention studies.

Genetic alterations in the phosphoinositide-3 kinase (PI3K) signaling pathway are the most common mutations found in cancer[6]. Oncogenic mutations of *PIK3CA* are important in multiple cancer types, including 20–30% of colorectal cancers[25]. Mutations of the *PIK3CA* gene encode for a dominant active form of the p110α catalytic subunit of PI3K and occur in three hotspots: E454K, E456K and H1047R[7]. *PIK3CA* mutations have been investigated in numerous cancer cell lines; however, until recently the effect of a dominant active PI3K in the mammalian intestine had not been investigated. Our laboratory has developed a murine model, Fabp1-Cre^{+}

Pik3ca*$^{+}$, that expresses a dominant active form of PI3K (p110*) in the distal small bowel and colon (Chapter 2.1). This model develops sessile large moderately differentiated invasive mucinous adenocarcinomas in the proximal colon through a non-canonical mechanism and without a polypoid luminal component.

APC and *PIK3CA* mutations are commonly identified together in human colorectal cancers, yet the interaction between these mutations remains to be investigated in rodent models[15]. The potential for cross-talk between these signaling cascades has been an area of interest. These pathways converge on glycogen synthase kinase 3 (GSK3) and potentially other mediators. Prior studies in cell culture models have had contradictory findings when examining the potential for an interaction between these signaling cascades[26-31]. To examine what effect mutations in *APC* and *PIK3CA* have on tumorigenesis, we have crossed the $Apc^{Min/+}$ mouse with the Fabp1-Cre^{+} Pik3ca*$^{+}$ mouse. This cross results in a murine model with the loss of one allele of *APC* throughout the intestinal epithelium and the expression of a dominant active PI3K (Pik3ca*$^{+}$) in the distal small intestine and colon due to the expression of Cre under the control of the fatty acid binding protein-1 promoter (Fabp1-Cre^{+}). Here, we demonstrate increased tumor multiplicity, size and a more aggressive and poorly differentiated phenotype as a consequence of synergy between *APC* and *PIK3CA* mutations.

Results

Expression of a dominantly active PI3K in the setting of allelic loss of Apc results in increased tumor multiplicity and increased tumor size

Fabp1-Cre^{+} Pik3ca*$^{+}$ $Apc^{Min/+}$ mice were dissected once moribund along with age-matched control littermates (Figure 2-5). The majority of mice developed massive proximal

colon cancers resulting in obstruction of the lumen (Figure 2-5A). These tumors were associated with an impressive vascular supply and hyperplastic lymphatic tissue (Figure 2-5C and D). Tumors are seen in the colon and distal small intestine (Figure 2-5E and F). In some instances, metastatic lesions were noted in the mesenteric lymphatic and adipose tissue (Figure 2-5G–J). No evidence of liver or lung metastases was identified.

A total of 61 mice were evaluated for the presence of intestinal tumors, including 18 Fabp1-Cre^{+} Pik3ca*$^{+}$ *Apc*$^{Min/+}$ mice, 17 Fabp1-Cre^{0} Pik3ca*$^{+}$ *Apc*$^{Min/+}$ mice, 6 Fabp1-Cre^{+} Pik3ca*^{0}*Apc*$^{Min/+}$ mice, 9 Fabp1-Cre^{0} Pik3ca*^{0}*Apc*$^{Min/+}$ mice and 11 Fabp1-Cre^{+} Pik3ca*$^{+}$ *Apc*$^{+/+}$ mice (Appendix 3-1). The average age of Fabp1-Cre^{+} Pik3ca*$^{+}$ *Apc*$^{Min/+}$ mice at necropsy was 52 days old. Mice appeared well until they became moribund from obstructive enteropathy relating to large obstructing colon cancers or secondary to anemia from bleeding intestinal tumors.

Tumor multiplicity was significantly increased in each section of the intestine where the activated PI3K was expressed in the setting of allelic loss of *Apc* (Figure 2-6). Overall, an average of 8.7 tumors were identified throughout the intestine in Fabp1-Cre^{+} Pik3ca*$^{+}$ *Apc*$^{Min/+}$ compared with 1.4 in Fabp1-Cre^{+} Pik3ca*$^{+}$ *Apc*$^{+/+}$ (P<0.001), and 1.4 in *Apc*$^{Min/+}$ controls (Fabp1-Cre^{0} Pik3ca*$^{+}$ *Apc*$^{Min/+}$, Fabp1-Cre^{+} Pik3ca*^{0} *Apc*$^{Min/+}$ or Fabp1-Cre^{0} Pik3ca*^{0}*Apc*$^{Min/+}$; P<0.001). Specifically, segment 4 and colon tumors were much more frequent in the Fabp1-Cre^{+} Pik3ca*$^{+}$ *Apc*$^{Min/+}$ mice. No increase in tumor multiplicity was noted in the proximal small intestinal sections, segments 1 and 2, which lack activated PI3K. This is useful as an internal control and indicates that the increase in tumor multiplicity is related to expression of constitutively active PI3K.

The intestinal sections from Fabp1-Cre^{+} Pik3ca*$^{+}$ *Apc*$^{Min/+}$ mice and associated controls were also evaluated for tumor size. Fixed tissues were examined under the dissecting

microscope. The maximum diameter of each tumor was determined using a measuring reticule. The flat Fabp1-Cre^{+} Pik3ca*$^{+}$ proximal colon tumors, as previously described (Chapter 2.1), were not measured as these tumors do not have discrete borders, which are required for reproducible measurements.

An increase in tumor size was noted in segment 4 and the colon (Figure 2-6B). In segment 4, a total of 66 tumors were measured (61 Fabp1-Cre^{+} Pik3ca*$^{+}$ *Apc*$^{Min/+}$ and 5 *Apc*$^{Min/+}$ controls). The Fabp1-Cre^{+} Pik3ca*$^{+}$ *Apc*$^{Min/+}$ segment 4 tumors averaged 2.8 mm (range 0.7–7;*P*=0.004), whereas the control tumors averaged <0.8 mm (range 0.4–2 mm) in diameter. These large tumors are forming by just 50 days of age or less. Tumors of this size would not be expected in *Min* mice until closer to 100 days of age or older. A total of 9 Fabp1-Cre^{+} Pik3ca*$^{+}$ *Apc*$^{Min/+}$ colon tumors were measured and the mean diameter was 4.3 mm (range 2–10 mm). Only one *Apc*$^{Min/+}$ control colon tumor was identified in 32 mice. This tumor measured 1.6 mm. A total of 14 tumors were identified in segments 1 and 2 of the small intestine (5 Fabp1-Cre^{+} Pik3ca*$^{+}$ *Apc*$^{Min/+}$ and 9 *Apc*$^{Min/+}$ controls). These tumors were not significantly different in size owing to the lack of constitutively active PI3K in this area (1.2 and 1.1, respectively, *P*=0.85).

Tumor development and progression are mediated by the expression of the dominant active form of PI3K

Expression of the constitutively active PI3K in the tumors of Fabp1-Cre^{+} Pik3ca*$^{+}$ mice has previously been shown to activate the PI3K signaling cascade (Chapter 2.1). In Fabp1-Cre^{+} Pik3ca*$^{+}$ *Apc*$^{Min/+}$ mice, all tumors in the distal small and large intestine, regardless of morphology, demonstrate the presence of p110* and activation of the PI3K signaling pathway (Figures 2-6, -7, and -8), including elevated phosphorylation of AKT compared with tumors

from *Apc*$^{Min/+}$ mice (Figure 2-6C). These observations confirm that the transgene was transcribed and translated in the colon of Fabp1-Cre^{+} Pik3ca*$^{+}$ *Apc*$^{Min/+}$ mice and that its expression resulted in increased downstream activation of the PI3K/AKT/mTOR pathway.

Differences in tumor morphology result from the expression of the dominant active form of PI3K in the setting of allelic loss of Apc in the intestine

Tumors with multiple distinct morphologies develop in the Fabp1-Cre^{+} Pik3ca*$^{+}$ *Apc*$^{Min/+}$ mice (Figure 2-7; Appendix 3-2 and 3). The flat lesions, previously described in the Fabp1-Cre^{+} Pik3ca*$^{+}$ mice, are present (Chapter 2.1; Figure 2-7A). These flat lesions are moderately differentiated invasive mucinous adenocarcinomas that arise in the setting of villous/serrated hyperplasia in the proximal colon. Extension of these cancers through the serosal layer is usually seen. These lesions are associated with a dramatic desmoplastic reaction and a high degree of tumor budding. No appreciable differences in tumor morphology were noted in the flat Fabp1-Cre^{+} Pik3ca*$^{+}$ *Apc*$^{Min/+}$ versus the Fabp1-Cre^{+} Pik3ca*$^{+}$ *Apc*$^{+/+}$ invasive mucinous adenocarcinomas of the proximal colon (Figure 2-7; Appendix 3-4). In all cases, these tumors formed without significant polypoid lesions extending into the lumen of the colon and invaded through the serosal surface.

In addition, polypoid tumors, which are not present in Fabp1-Cre^{+} Pik3ca*$^{+}$ mice (Chapter 2.1), are seen in the colon and distal small intestine. A total of 74 lesions were evaluated by a pathologist, and ranged from small adenomas to larger adenomas with high-grade dysplasia to invasive adenocarcinomas. While the flat tumors of the Fabp1-Cre^{+} Pik3ca*$^{+}$ *Apc*$^{Min/+}$ mice differ in morphology compared to *Apc*$^{Min/+}$ tumors, the polyploid tumors within these mice are more representative of *Apc*$^{Min/+}$ tumors, but display a greater degree of

architectural distortion. Compared with the *Apc*$^{Min/+}$ control colon tumor, these are much larger and less differentiated. The polyploid tumors of the Fabp1-Cre^{+} Pik3ca*$^{+}$ *Apc*$^{Min/+}$ mice demonstrate a high degree of nuclear CTNNB1 (β-catenin), KI67 and pAKT staining (Figure 2-7; Appendix 3-2). A marked difference in tumor morphology was also observed in the exophytic small bowel lesions (Figure 2-8). Large invasive adenocarcinomas were seen in the small intestine of Fabp1-Cre^{+} Pik3ca*$^{+}$ *Apc*$^{Min/+}$ mice, whereas only a limited number of small adenomas were seen in control littermates. The lesions of both the small and large intestine exhibited uptake of a novel near-infrared phospholipid ether analog, CLR1502, that selectively accumulates in advanced tumors (Appendix 3-5).

Fabp1-Cre^{+} Pik3ca*$^{+}$ Apc$^{Min/+}$ mice develop tumors with and without nuclear localization of CTNNB1

Immunohistochemistry (IHC) analysis of CTNNB1 has been used for many years as a marker of activated WNT signaling. When functional APC is no longer expressed, CTNNB1 accumulates and translocates to the nucleus. Here, we have examined CTNNB1 staining in tumor tissues of Fabp1-Cre^{+} Pik3ca*$^{+}$ *Apc*$^{Min/+}$ and their control littermates. Similar to what was demonstrated previously, the flat proximal colon mucinous invasive adenocarcinomas of the Fabp1-Cre^{+} Pik3ca*$^{+}$ *Apc*$^{+/+}$ and Fabp1-Cre^{+} Pik3ca*$^{+}$ *Apc*$^{Min/+}$ mice largely did not demonstrate nuclear CTNNB1 staining (Figure 2-8 and 9; Appendix 3-4). However, the polypoid lesions of the colon did demonstrate a high degree of nuclear CTNNB1. Microscopic adenomas can even be identified in the colon due to their high degree of nuclear CTNNB1 staining (Appendix 3-6).

These data indicate that tumors in the Fabp1-Cre^{+} Pik3ca*$^{+}$ *Apc*$^{Min/+}$ mice are developing via different mechanisms. In the flat proximal invasive colon adenocarcinomas, the lack of

nuclear CTNNB1 indicates that these tumors are not initiated by aberrant WNT signaling. Their non-canonical mechanism of tumorigenesis needs to be further clarified. In the polypoid colon lesions, where CTNNB1 is nuclear, these tumors are likely initiated by loss of APC and their more aggressive phenotype driven by the presence of the dominantly active PI3K. Interestingly, in two flat mucinous proximal colon cancers, thought to be initiated by PI3K, small foci of nuclear CTNNB1 were identified (Figure 2-10). The morphology of the cells in these regions also changed. This indicates that the cells with nuclear CTNNB1 likely lost the other allele of *Apc* after tumor initiation by activated PI3K. The change in morphology indicates that important phenotypic changes in the tumor might occur even if APC is lost after tumor initiation and not just as the initiator of tumorigenesis.

Fabp1-Cre^{+} Pik3ca^{+} Apc$^{Min/+}$ and Fabp1-Cre^{+} Pik3ca*$^{+}$ Apc $^{+/+}$ tumors are microsatellite stable*

Microsatellite instability (MSI) has been demonstrated to be an important marker for prognosis and response to treatment in humans[32]. MSI analysis of intestinal tumors from mice with Fabp1-Cre^{+} Pik3ca*$^{+}$ *Apc$^{Min/+}$* and Fabp1-Cre^{+} Pik3ca*$^{+}$ *Apc$^{+/+}$* mice was performed using mononucleotide repeats, which have been previously shown to be very sensitive for detection of MSI in mouse tumors[33] (Appendix 3-7). The microsatellite allelic patterns of 18 out of 22 tumor samples and matching normal samples were identical and therefore were considered as microsatellite stable. Four tumors contained a novel allele at the *mBat-66* locus that was not present in wild-type C57BL/6 mice. However, this novel allele was the same in all four tumors and is, therefore, likely due to a polymorphism in these F1 mice. Thus, MSI does not appear to

have a role in intestinal tumorigenesis in Fabp1-Cre^{+} Pik3ca*$^{+}$ *Apc*$^{Min/+}$ and Fabp1-Cre^{+} Pik3ca*$^{+}$ *Apc*$^{+/+}$ mice.

Similar tumor multiplicity and phenotypes are seen when Apc is lost only in the epithelial cells of the intestine in the setting of a constitutively active PI3K

In the *Apc*$^{Min/+}$ mouse, one allele of *Apc* is lost in all cells. Prior investigations have indicated that the loss of APC in stromal tissue may be important for tumorigenesis[34]. To investigate this further, we used a transgenic mouse with a Cre recombinase conditional knockout of *Apc* (*Apc*$^{fl/+}$)[35]. This mouse contains an allele of *Apc* that is floxed at exon 14. In the presence of Cre, exon 14 is removed and the APC protein is truncated. These mice were used to generate genetically homogenous Fabp1-Cre^{+} Pik3ca*$^{+}$ *Apc*$^{fl/+}$ mice. Similar to the Fabp1-Cre^{+} Pik3ca*$^{+}$ *Apc*$^{Min/+}$ mice, they also developed advanced small intestine and colon cancers (Figure 2-10). No appreciable significant differences were identified between the Fabp1-Cre^{+} Pik3ca*$^{+}$ *Apc*$^{Min/+}$ and the Fabp1-Cre^{+} Pik3ca*$^{+}$ *Apc*$^{fl/+}$ mice, including tumor multiplicity and morphology.

Fabp1-Cre^{+} Pik3ca*$^{+}$ Apc $^{Min/+}$ tumors demonstrate downstream activation of the PI3K pathway, MYC expression, and increased CCND1 compared with Apc$^{Min/+}$ controls

The expression of the dominant active PI3K in the Fabp1-Cre^{+} Pik3ca*$^{+}$ *Apc*$^{Min/+}$ tumors results in downstream activation of the PI3K pathway (Figures 2-6C and -11A). RPS6 (ribosomal protein S6) and eukaryotic translation initiation factor 4E binding protein (EIF4EBP1) are phosphorylated in both flat and polypoid Fabp1-Cre^{+} Pik3ca*$^{+}$ *Apc*$^{Min/+}$ tumors. Interestingly, a significant amount of phosphorylated RPS6 and EIF4EBP1 is also seen in

Apc$^{Min/+}$. Only low levels of phosphorylated ERK1/2 are seen in Fabp1-Cre^{+} Pik3ca*$^{+}$ *Apc*$^{Min/+}$ and *Apc*$^{Min/+}$ controls (Figure 2-11A).

The PI3K and WNT signaling pathways are known to converge on GSK3; however, the role of GSK3 in cross-talk between these two pathways remains controversial. In the majority of flat Fabp1-Cre^{+} Pik3ca*$^{+}$ *Apc*$^{Min/+}$ cancers, phosphorylation of GSK3β is increased compared with controls. Interestingly, in the polypoid Fabp1-Cre^{+} Pik3ca*$^{+}$ *Apc*$^{Min/+}$ tumors, GSK3β appears to be phosphorylated less often. Two of these tumors that did not demonstrate phosphorylation of GSK3β did show phosphorylation of GSK3α. Despite the phosphorylation of GSK3β in the flat Fabp1-Cre^{+} Pik3ca*$^{+}$ *Apc*$^{Min/+}$ cancers nuclear localization of CTNNB1 was not observed (Figures 2-7 and 2-9). In addition, no change in total CTNNB1 was observed between the majority of Fabp1-Cre^{+} Pik3ca*$^{+}$ *Apc*$^{Min/+}$ and *Apc*$^{Min/+}$ controls (Figure 2-11B).

The WNT and PI3K pathways also converge on important transcription factors including MYC and CCND1. At necropsy, tumors were excised and prepared for histological analysis. Nuclear MYC was identified in all Fabp1-Cre^{+} Pik3ca*$^{+}$ *Apc*$^{+/+}$ and Fabp1-Cre^{+} Pik3ca*$^{+}$ *Apc*$^{Min/+}$ at similar levels to that seen for the *Apc*$^{Min/+}$ controls (Figure 2-11C). Nuclear CCND1 was observed in the majority of malignant cells in Fabp1-Cre^{+} Pik3ca*$^{+}$ *Apc*$^{+/+}$ and Fabp1-Cre^{+} Pik3ca*$^{+}$ *Apc*$^{Min/+}$, which is increased compared with the *Apc*$^{Min/+}$ controls.

Discussion

Human colorectal cancers are a heterogeneous group, with each cancer individualized by its mutation profile. The presence of certain mutations may change with the biological context, such as the possible interaction between *PIK3CA* mutations and bowel inflammation. This is important clinically as patients with this mutation are more likely to benefit from adjuvant

aspirin therapy[36]. In addition, certain mutations are often associated with each other. Of colon tumors with *PIK3CA* mutations, 86% of these cancers also possess mutant *APC*[15]. In addition, *PIK3CA* mutations have also been associated with *KRAS* and *BRAF* mutations, CpG island methylator phenotype and MSI[37-39].

Concerted efforts to develop improved and more personalized treatment options for all types of cancer continue. Recent advances include improved targeting of directed therapies against the mutational activation of signaling pathways in cancer. This has led to the development of classes of exciting anti-neoplastic agents, such as EGFR, BRAF, MEK, EML4-ALK, MET, MTOR and PI3K inhibitors. To properly develop and utilize these new therapies, a better understanding of how the mutation profile of each cancer affects the tumor biology is required. It is important to recognize the roles of these mutant proteins and how their function is altered by the presence of mutations in other oncogenes or tumor suppressors. Here, we report the first *in vivo* description of the interaction between *APC* and *PIK3CA* mutations in mammalian intestinal tumors.

Previously, we have demonstrated that a dominant active PI3K is able to initiate the development of flat mucinous invasive adenocarcinomas in the proximal colon via a non-canonical mechanism of tumorigenesis (Chapter 2.1). In addition to these lesions, we now demonstrate that the presence of a dominant active PI3K in the setting of allelic loss of *APC* results in increased tumor multiplicity, size, and a more aggressive and less differentiated phenotype. We have demonstrated that this is related to increased activation of AKT and phosphorylation of downstream targets including RPS6 and EIF4EBP1.

Interestingly, in the flat proximal colon mucinous invasive adenocarcinomas, these tumors carry germline mutations in one allele of *Apc*. However, in two tumors we observed the

loss of APC activity as a likely later event. In this setting, cells that lost APC after tumor initiation secondary to PI3K had a change in morphology to a less differentiated state. This indicates that, in addition to tumor initiation, the loss of APC can be a late event in tumorigenesis, and could be responsible for clonal outgrowth in some instances, such as was observed here.

The mechanism for the synergy between WNT and PI3K signaling pathways may occur due to a direct interaction between these pathways. Previous studies have aimed to examine this interaction; however, they have been contradictory. GSK3 is well known to have an important role in both WNT and PI3K signaling, and thus has been a target of multiple investigations examining these pathways. GSK3 is a serine-threonine kinase that occurs in two isoforms GSK3α and GSK3β[40]. These kinases are naturally constitutively active and are inhibited by N-terminal phosphorylation of Ser-21 for GSK3α and Ser-9 for GSK3β, which results in the formation of a pseudosubstrate motif[41]. In WNT signaling, GSK3 has an important role in the degradation of CTNNB1. GSK3 is bound by Axis inhibition protein (AXIN1) and phosphorylates CTNNB1[42]. This phosphorylation of CTNNB1 targets it for ubiquitination and degradation by proteosomes. If GSK3 is inhibited by WNT signaling, then this leads to CTNNB1 accumulation and nuclear translocation, though the mechanism of WNT inhibition of GSK3 remains poorly understood. In PI3K signaling, phosphorylated AKT in turn phosphorylates GSK3 on its inhibitory serines[43].

Multiple studies have demonstrated that an interaction between these pathways might exist related to a single pool of GSK3[26-29]. Contrary to these findings, other groups have proposed that cross-talk between these two pathways does not exist[30,31]. Ng *et al.* demonstrated that a pool of GSK3β is stably bound to AXIN1 and represents only about 3–5% of the total

GSK3β[31]. They also observed that the phosphorylation level of the AXIN1-bound GSK3β was independent of PI3K pathway activation by insulin or inhibition by wortmannin.

Some evidence indicates that the context in which phospho-AKT signaling is taking place has an effect on its ability to inhibit GSK3β that is bound to AXIN1 and thus acting in WNT signaling. Fukumoto *et al.*[27] demonstrated that phospho-AKT is bound to the AXIN1:GSK3β complex in the presence of Dishevelled, promoting phosphorylation of GSK3β and accumulation of free CTNNB1. However, if the WNT cascade was not activated by Dishevelled, then phospho-AKT was not found to be bound to the AXIN1:GSK3β complex and free CTNNB1 levels were not elevated. These data indicate that phospho-AKT is not sufficient, but can enhance the activity of WNT signaling. These findings are consistent with those of Ng and colleagues as WNT was not activated in their experiments.

Here, we demonstrate synergy between the loss of the tumor suppressor APC and the presence of a dominant active PI3K. Fabp1-Cre^{+} Pik3ca*$^{+}$ *Apc*$^{Min/+}$ mice demonstrate increased tumor multiplicity, size and aggressiveness compared with the tumors of control littermates. In the flat mucinous adenocarcinomas, an increase in pGSK3β is observed; however, this is without change in the total levels or nuclear localization of CTNNB1. This proves that phospho-AKT is insufficient for activation of the WNT signaling pathway in this context. In the polypoid tumors, variable phosphorylation of GSK3β was seen. Again, no change in total CTNNB1 levels was seen, but significant nuclear localization of CTNNB1 was noted similar to that seen in *Apc*$^{Min/+}$ controls. We cannot exclude the possibility that phospho-AKT signaling is able to enhance CTNNB1 signaling in the presence of an aberrant WNT pathway, such as mutant *Apc*. Significant levels of nuclear MYC were seen in all the tumors assayed and CCND1 was increased in the Fabp1-Cre^{+} Pik3ca*$^{+}$ *Apc*$^{Min/+}$ tumors above the level seen in *Apc*$^{Min/+}$ tumors,

indicating a potential etiology for the synergy between these mutations at the transcriptional level.

In summary, synergy exists between the loss of the tumor suppressor APC and the presence of a dominant active PI3K in this *in vivo* model of colon cancer. Further studies are required to elucidate to what extent cross-talk between these pathways exists and is responsible for this synergy. In addition, pharmacologic studies using this and similar models will be vital to the development of novel combination therapies for the personalized treatment of patients with colorectal and other cancers.

Materials and Methods

Mouse husbandry and genotyping

All animal studies were conducted under protocols approved by the Institutional Animal Care and Use Committee at the University of Wisconsin-Madison, following the guidelines of the American Association for the Assessment and Accreditation of Laboratory Animal Care. Fabp1-Cre^{+} mice (FVB/N-Tg(Fabp1-Cre)1Jig; NCI Mouse Repository; Strain number 01XD8), Pik3ca*$^{+}$ mice (C57BL/6-*Gt(ROSA)26Sor*$^{tm7(Pik3ca*,EGFP)Rsky/}$J; The Jackson Laboratory; Stock Number-012343) and *Apc*$^{Min/+}$ males (C57BL/6J *Apc*^{Min}/J; The Jackson Laboratory; Stock number 002020) were maintained as previously described[18]. *Apc*$^{Min/+}$ males were crossed with Pik3ca*$^{+}$ females to generate Pik3ca*$^{+}$ *Apc*$^{Min/+}$ mice. Male Pik3ca*$^{+}$ *Apc*$^{Min/+}$ mice were then crossed with Fabp1-Cre^{+} mice to generate F1 Fabp1-Cre^{+} Pik3ca*$^{+}$ *Apc*$^{Min/+}$ mice and the associated controls. Pik3ca*$^{+}$ mice were also crossed to *Apc*$^{fl/fl}$ mice (B6.Cg-*Apc*^{tm2Rak}; NCI Mouse Repository; Strain number 01XAA) to generate Pik3ca*$^{+}$ *Apc*$^{fl/+}$ mice. These mice were then crossed with Fabp1-Cre^{+} mice to generate Fabp1-Cre^{+} Pik3ca*$^{+}$ *Apc*$^{fl/+}$ mice. Mice were

genotyped for Fabp1-Cre, Pik3ca*, *Apc*$^{fl/+}$ and Min as described previously [8,17,18,35]. Tumors from *Apc*$^{Min/+}$ and (SWRxB6) F1 *Apc*$^{Min/+}$ mice treated with 4% dextran sodium sulfate were used as controls.

Tumor fixation and counts

Mice were euthanized by CO_2 asphyxiation. At necropsy, the entire intestine was excised. The small intestine was divided into four sections of equal length (numbered 1 through 4 from proximal to distal) and the colon and cecum were kept intact. Each section of the intestine was then split lengthwise, splayed open, and rinsed. Tissues were fixed flat in 10% buffered formalin for 24–48 h, then stored in 70% ethanol. Tumors in each section of the intestine were counted under a dissecting microscope by a single observer who was blinded to the genotypes.

Histology and immunohistochemistry

Fixed tumors were isolated, embedded in paraffin, and cut into 5 μm sections. Every tenth section was stained with hematoxylin and eosin for histological review. IHC was carried out as described previously (Chapter 2.1). The primary antibodies included rabbit anti-phospho-AKT (Ser473, 1:100, Cell Signaling Technology, Beverly, MA, USA), mouse anti-CTNNB1 (1:200, BD Biosciences—Clone 14, San Diego, CA, USA), rabbit anti-PCNA (Ki-67) (1:1000, Cell Signaling Technology), and CCND1 (1:25, Cell Signaling Technology). The IHC protocol was modified for the anti-MYC antibody N-262 (1:50, Santa Cruz Biotechnology, Dallas, TX, USA) as follows. Upon rehydration, slides were incubated in 0.05% sodium borohydride (Sigma-Aldrich, St Louis, MO, USA) for 10 min followed by incubation in 0.5% Triton X-100 (Sigma-Aldrich). Slides were blocked for 20 min at room temperature with a fresh blocking

solution (2.5 ml 1 M Tris-HCl pH 8.0, 2 ml 5 M NaCl, 2 ml 10% NP-40, 5 g non-fat dry milk, distilled deionized water to 100 ml).

Western blot analysis

Tissue was processed and gels run as previously described (Chapter 2.1). The gels were probed with primary antibodies against p110α, phospho-AKT (Ser473), RPS6 (Ser235/236), phosphor-EIF4EBP1 (Thr37/46), pMAPK (Thr202/Tyr 204), pGSK3α, pGSK3β or Total GSK3 (Cell Signaling Technology) in bovine serum albumin (Sigma-Aldrich) at a 1:1000 ratio for 16 h. Anti-CTNNB1 (BD Biosciences—Clone 14) was probed at a ratio of 1:5000. Anti-GAPDH antibody (Cell Signaling Technology) was utilized as a loading control at a ratio of 1:5000.

MSI analysis

Tumor DNAs from Fabp1-Cre^{+} Pik3ca*$^{+}$ *Apc*$^{+/+}$ and Fabp1-Cre^{+} Pik3ca*$^{+}$ *Apc*$^{Min/+}$ mice were tested for MSI using a multiplex of six mononucleotide repeat loci designed specifically for MSI testing of C57BL/6 mice, including: mBat-56 (GTGTGTATGCTGATTTTATATCCT, GCAAAAATATCATTCGGTATG), mBat-57 (TGAAATCCTTGATGTTCCTCTACTAGGT, GGTCATCCTGTTGTTTCTAAATGATTGT), mBat-58 (CCCCTAAAACTTTCCTTGCTATT, TTCTGAGTTCCAGGGCAGTCTG), mBat-59 (GGTCTTGCCCTGAGGCAAGTAAT, AACCATCCGTAACAAGATCTGACGT), mBat-64 (CAGCCCACACTCCTGAAAACAG, CACTTAGCCAGTTGCGTCACCT) and mBat-66 (TGGGGTGTCTAAAGACAGCTAAG, GCCCACTTCATGCGTAACAG). For MSI analysis, >2 ng of DNA was amplified with 1 × C57BL/6 multiplex fluorescent primer mix, 1 × Gold ST*R Buffer (Promega, Madison, WI, USA) and 0.2 U GoTaqHot Start Polymerase (Promega) in a GeneAmp PCR System 9700

Thermocycler (Applied Biosystems, Foster City, CA, USA). The amplification conditions used were as follows: 95 °C (2 min); 10 cycles of 94 °C (30 s), 58 °C (30 s, 29% ramp), 65 °C (1 min, 23% ramp); 20 cycles of 90 °C (30 s), 58 °C (30 s, 29% ramp), 65 °C (1 min, 23% ramp); and a final extension of 60 °C (30 min). PCR products were denatured in deionized formamide with Internal Lane Standard 600 (Promega) for allele sizing and analyzed on a 3130*xl* Genetic Analyzer using GeneMapper 4.0 Software (Applied Biosystems). For MSI analysis, the microsatellite allelic patterns of tumor and matching normal samples were compared and classified as microsatellite stable if no loci were unstable, MSI-Low if one locus was unstable, and MSI-High if two or more loci were unstable[44].

Disclosure of Potential Conflicts of Interest

Dr. Jamey Weichert is the founder of Cellectar, Inc. (Madison, WI), which holds the licensing rights to the CLR1404 technology, and therefore has a financial interest in this agent. No potential conflicts of interests were disclosed by the other authors.

Acknowledgments

This project was supported by the Conquer Cancer Foundation of the American Society of Clinical Oncology through A Young Investigator Award (D.A.D.); the National Cancer Institute of the U.S. National Institutes of Health through T32 CA009614 (D.A.D.), P50 CA095103 (Gastrointestinal Specialized Program of Research Excellence Grant, Vanderbilt Ingram Cancer Center), R01 CA123438 (R.B.H), P30 CA014520 (Core Grant, University of Wisconsin Carbone Cancer Center); and start-up funds (R.B.H.) from the UW Division of

Gastroenterology and Hepatology, the UW Department of Medicine, and the UW School of Medicine and Public Health.

2.3. Colon tumors with the simultaneous induction of driver mutations in *Apc*, *Kras*, and *Pik3ca* still progress through the adenoma-to-carcinoma sequence.

Jamie N. Hadac, **Alyssa A. Leystra**, Terrah J. Paul Olson, Molly E. Maher, Susan N. Payne, Alexander E. Yueh, Alexander R. Schwartz, Dawn M. Albrecht, Linda Clipson, Cheri A. Pasch, Kristina A. Matkowskyj, Richard B. Halberg, and Dustin A. Deming.

Abstract

Human colorectal cancers often possess multiple mutations, including three to six driver mutations per tumor. The timing of when these mutations occur during tumor development and progression continues to be debated. More advanced lesions carry a greater number of driver mutations, indicating that colon tumors might progress from adenomas to carcinomas through the stepwise accumulation of mutations following tumor initiation. However, mutations that have been implicated in tumor progression have been identified in normal-appearing epithelial cells of the colon, leaving the possibility that these mutations might be present before the initiation of tumorigenesis. We utilized mouse models of colon cancer to investigate whether tumorigenesis still occurs through the adenoma-to-carcinoma sequence when multiple mutations are present at the time of tumor initiation. To create a model in which tumors could concomitantly possess mutations in *Apc*, *Kras*, and *Pik3ca*, we developed a novel minimally invasive technique to administer an adenovirus expressing Cre recombinase to a focal region of the colon. Here, we demonstrate that the presence of these additional driver mutations at the time of tumor initiation results in increased tumor multiplicity and an increased rate of progression to invasive adenocarcinomas. These cancers can even metastasize to retroperitoneal lymph nodes or the

liver. However, despite having as many as three concomitant driver mutations at the time of initiation, these tumors still proceed through the adenoma-to-carcinoma sequence.

In addition to reformatting, the following changes were made for the sake of consistency:

- Figures and references were renumbered
- Minor words were changed to improve readability and clarity
- "*mT/mG*^{1}" mice were renamed "mT/mG^{+}" mice
- "*Kras*$^{G12D/+}$" mice were renamed "*Kras*$^{LSL\text{-}G12D/+}$" mice
- "*Pik3ca*^{p110*}" mice were renamed "Pik3ca*$^{+}$" mice
- "*FC*" mice were renamed "Fabp1-Cre" mice

All animal models described in this paper are briefly defined in Appendix 1.

Authors' Contributions

J.N. Hadac, A.A. Leystra, R.B. Halberg, and D.A. Deming were involved in all aspects of the research and preparation of the manuscript. T.J. Paul Olson assisted with Adeno-Cre protocol design and testing. M.E. Maher, A. Yueh, A.R. Schwartz, D.M. Albrecht, and S. Payne provided technical support. K. Matkowskyj assisted with interpretation of histopathology. L. Clipson assisted with figure and manuscript preparation. All authors discussed results and edited the manuscript.

Introduction

Colorectal cancer is the second-leading cause of cancer-related mortality in the United States [45]. An improved understanding of the processes by which tumorigenesis occurs will allow for the rational development of chemopreventive and therapeutic agents. The canonical adenoma-to-carcinoma sequence has been proposed to describe the processes by which mutations in driver genes accumulate over time causing the progression of adenomas to invasive adenocarcinomas in the colon[2,46].

An important early step in tumorigenesis is the acquisition of alterations in the *Adenomatous Polyposis Coli* (*APC*) tumor suppressor gene. Loss of this gatekeeper gene is thought to be the initiating event in the majority of sporadic human colorectal cancers with approximately 80% to 90% of human colon cancers harboring somatic mutations in *APC*[23,47,48]. In the canonical sequence, tumor initiation caused by loss of APC is followed by mutations in other genes including *KRAS*, *TP53*, *PIK3CA*, and *BRAF*[25]. Some studies have questioned whether the accumulation of mutations over time is necessary for colon cancer development[49-52]. For example, *KRAS* mutations have been detected in non-neoplastic tissue of the colon[49,53]. This observation indicates that somatic mutations occurring before tumor initiation might subsequently influence tumor development and progression[54]. In addition, it could be a potential explanation for interval cancers that form between routine screening colonoscopies.

Because of the prevalence of APC loss in human colorectal cancer, mice carrying mutations in *Apc*, the murine homolog, have been generated to more fully understand intestinal tumorigenesis and to investigate pharmacologic strategies for chemoprevention[55-57]. Here, we utilized genetically engineered mouse models of colon cancer to examine the adenoma-to-carcinoma sequence in the setting of the concurrent induction of common driver mutations. We

developed a minimally invasive procedure for inoculating an adenovirus expressing the Cre recombinase (Adeno-Cre) to induce multiple mutations at a desired location in the colon. This method allows for tumors to be initiated with a predetermined mutation profile at a specific time and location desired by the investigator.

Results

Colon tumors can be initiated using a noninvasive inoculation of the Adeno-Cre virus

KRAS and *PIK3CA* mutations have been identified as occurring concomitantly with the loss of APC in human adenomas and carcinomas[21,39]. Multiple investigations have examined murine models with combinations of loss of APC and activating mutations in either *Kras* or *Pik3ca*[4,58] (Chapter 2.1). These studies had limitations. C57BL/6 (B6) mice carrying the *Min* allele of *Apc* ($Apc^{Min/+}$) have a ubiquitous spatial and temporal expression of a mutant germline allele resulting in alterations of homeostasis along the entire intestinal tract[57]. The life expectancy of these mice is limited owing to their high tumor burden, especially of the small intestine, resulting in anemia or intestinal obstruction. B6 $Apc^{Min/+}$ mice do not develop advanced colon cancers as a consequence of this shortened lifespan. Finally, triggering multiple mutations in the colon concurrently by expressing Cre recombinase from the FABP-1 promoter is lethal (Appendix 4-1). To determine whether additional concomitant mutations would alter the progression of colon tumors through the adenoma-to-carcinoma sequence alternative methodologies were required. A model allowing for spatial control of tumor initiation that can be used to express a number of mutations was needed to further explore their effects on tumorigenesis.

Although there are multiple methods of expressing Cre in the mouse, including organ-specific promoter-based systems, the delivery of an adenovirus carrying Cre recombinase allows for the greatest spatio-temporal control of initiation of colon tumors[59]. To sequester the virus in the colon, an invasive laparotomy procedure has been described[35]. Surgical clips were directly placed both proximally and distally around the colon after exposure of the peritoneal cavity. Adeno-Cre was then injected into the area between the clips. This surgical Adeno-Cre instillation technique allows for the development of colon tumors without the comorbidities related to *Apc* mutations occurring outside of the area of interest. However, this surgical intervention is no trivial task; preparation, surgery, and recovery may all contribute detrimental effects to the overall health of the animal. Unintended consequences from surgical wounds may alter various cellular mechanisms, including inflammatory and wound-healing responses, involved in tumorigenesis[60].

To overcome limitations of the surgical approach, we developed a device to nonsurgically inoculate Adeno-Cre into the colon in homozygous $Apc^{fl/fl}$ mice[61] (Figure 2-12A). Upon expression of Cre recombinase in these mice, exon 14 of *Apc* is excised, resulting in the expression of a truncated, non-functional APC protein. Cre expression controls the location and time at which tumors form, in turn alleviating many of the limitations associated with models carrying germline *Apc* mutations. This nonsurgical approach induced tumorigenesis in a physiologically relevant setting, while minimizing the systemic effects of a surgical procedure.

Biocompatible materials have been used to enhance the delivery of viruses in a variety of research settings[62]. One such biomaterial, GelFoam (Pharmacia and Upjohn), is a collagen-based sponge. It has been used to deliver viruses in gene therapy research owing to its ability to localize and protect virus[63]. GelFoam saturated in adenovirus solution has been implanted in

mice and rats to facilitate gene expression for the study of wound healing and to elicit immune responses in tumors[64,65]. These studies have demonstrated that GelFoam can be used to improve the sustained delivery of adenovirus *in vivo*. Therefore, we found it an attractive alternative to surgery for use in localizing the virus in specific areas of the mouse.

A slotted tube housing GelFoam soaked with Adeno-Cre was placed 1.5 to 3.5 cm into the colon of each prepared $Apc^{fl/fl}$ mouse. After the procedure, tumor formation and growth were monitored by endoscopy. Tumors were visible as early as 3 weeks post-treatment and these tumors were monitored over 14 weeks post-treatment. Fifty-eight percent (18/31) of treated $Apc^{fl/fl}$ mice developed tumors. Tumors originated at the desired location, both in radial orientation and depth in the colon (Figure 2-12B). No tumors developed in mice infected with adenovirus carrying an empty vector.

Differential growth patterns occur in tumors after the simultaneous loss of both normal APC alleles

Small animal endoscopy was performed every other week over a 14-week period to follow tumor growth in homozygous $Apc^{fl/fl}$ mice treated with Adeno-Cre. Tumors visible one month after adenoviral treatment were relatively small, occluding less than 30% of the lumen. However, in the following weeks, tumors exhibited many different patterns of growth (Figure 2-12C). Some tumors grew rapidly to eventually occlude the entire lumen, while others grew more incrementally, or even remained stable in size over this time. One small tumor ultimately regressed. These dynamic growth patterns, observed even in the earliest adenomas, were similar to tumor growth patterns in other murine colon tumor models with loss of APC[66].

After 14 weeks of monitoring, necropsy was performed. None of the mice became moribund before this time point. Histologic evaluation was completed on six tumors which

revealed that 83% were adenomas, and 17% were invasive adenocarcinomas with invasion into the muscularis mucosa (Figure 2-12D). No evidence of regional nodal disease or metastatic disease was observed.

Epithelial tumors arise secondary to inoculation of the colon with Adeno-Cre

When the Adeno-Cre virus is instilled into the colon, it might infect cells other than the epithelial cells lining the intestine. To make certain that only epithelial cells were being infected with the Adeno-Cre virus, mT/mG^{+} *Apc*$^{fl/fl}$ *Kras*$^{LSL\text{-}G12D/+}$ Pik3ca*$^{+}$ mice were treated with Adeno-Cre. mT/mG is a reporter from which red (tdTomato) fluorescent protein is ubiquitously expressed preceding Cre recombinase expression and GFP is expressed following Cre recombinase expression. Green fluorescence was detected only within the colonic epithelium confirming that the intended cell type was being infected with the Adeno-Cre (Figure 2-13). Nuclear localization of CTNNB1 (β-catenin) and activation of the anticipated downstream signaling cascades were observed within the transformed epithelial cells indicating that recombination following Cre expression was occurring as anticipated (Figure 2-13).

Adeno-Cre tumor initiation rate depends upon the mutation profile

Our minimally invasive technique allows for temporal and spatial control of the initiation of colon tumors with multiple simultaneous mutations. Mice with *Apc*$^{fl/fl}$, *Kras*$^{LSL\text{-}G12D/+}$, and/or Pik3ca*$^{+}$ were generated and treated with Adeno-Cre (Figure 2-14A). After 3 to 4 weeks, tumors were identified on endoscopy. When additional driver mutations were present in addition to the loss of APC, an increase in the rate of tumor development was observed. Tumors developed in 79% of *Apc*$^{fl/fl}$ mice carrying *Kras*$^{LSL\text{-}G12D}$ and/or Pik3ca* compared with 58% of *Apc*$^{fl/fl}$ mice

without these additional driver mutations (Figure 2-14A, *P* (one-sided) = 0.031, Barnard exact test). All mice were treated according to the same Adeno-Cre protocol and on the same homogeneous genetic background. In the 14 samples that were successfully tested, recombination was confirmed in nearly all cases (12/14, Appendix 4-2). Exceptions were found within two of three samples from a single $Apc^{fl/fl}$ $Kras^{LSL\text{-}G12D/+}$ Pik3ca*$^{+}$ mouse: only two of the three Cre-dependent alleles appeared to recombine in two tumors, but all three Cre-dependent alleles recombined in the third tumor.

In the setting of multiple mutations, Adeno-Cre induction resulted in adenoma formation

Mice with $Apc^{fl/fl}$ plus $Kras^{LSL\text{-}G12D/+}$ and/or Pik3ca*$^{+}$ were generated and treated with Adeno-Cre to determine how the simultaneous induction of these mutations would alter tumor biology. Tumors were identified 3 to 8 weeks after viral treatment (Figure 2-14B). Histologic sectioning of tumors revealed that all tumors from these mice carrying mutations in two to three genes at this early time point were small adenomas. An example of a small adenoma from an $Apc^{fl/fl}$ Pik3ca*$^{+}$ mouse is presented in Figure 2-14B. The expected nuclear localization of CTNNB1 and activation of the PI3K cascade with abundant phosphorylation of RPS6 were observed (Figure 2-14B).

The addition of Kras and Pik3ca* mutations does not significantly alter the rate of proliferation in colon tumors compared with loss of APC alone

To estimate the rate at which the tumors with different mutation profiles were growing, $Apc^{fl/fl}$ Pik3ca*$^{+}$ mice and $Apc^{fl/fl}$ $Kras^{LSL\text{-}G12D/+}$ Pik3ca*$^{+}$ mice were monitored with serial endoscopy every 2 weeks following treatment with Adeno-Cre (Figure 2-15A). Lumen occlusion by the colon tumor was used as a marker of cellular proliferation within tumors. Occlusion of 75% of the colonic lumen was observed in 65% of tumors in $Apc^{fl/fl}$ Pik3ca*$^{+}$, and $Apc^{fl/fl}$ $Kras^{LSL\text{-}G12D/+}$ Pik3ca*$^{+}$ mice. For the tumors that eventually occluded at least 75% of the lumen, the mean time required to reach 75% occlusion was 15 weeks. No statistically significant difference in the mean time to 75% lumen occlusion was observed between tumors with APC loss and the addition of one or two oncogenes (Figure 2-15B). Interestingly, in one instance, a tumor from an $Apc^{fl/fl}$ Pik3ca*$^{+}$ mouse regressed (Appendix 4-2). Histologic analysis of this regressed area revealed a predominant lymphocytic infiltrate, indicating a potential immune-mediated mechanism for the regulation of some colon tumors.

To confirm that mean time to lumen occlusion is a useful marker for cellular proliferation within tumors, histologic sectioning of tumors from $Apc^{fl/fl}$, $Apc^{fl/fl}$ Pik3ca*$^{+}$, and $Apc^{fl/fl}Kras^{LSL\text{-}G12D/+}$ Pik3ca*$^{+}$ mice was performed and these sections were stained for Ki-67, a standard marker of cell proliferation (Figure 2-15C). The Ki-67 proliferative index (Ki-67 PI) was measured as the percentage of nuclei staining positive for Ki-67 per tumor. The mean Ki-67 PI of $Apc^{fl/fl}$ tumors was 11.1% (range 0.8–24.8), $Apc^{fl/fl}$ Pik3ca*$^{+}$ tumors was 18.5% (range 7.3–25.8), and $Apc^{fl/fl}$ $Kras^{LSL\text{-}G12D/+}$ Pik3ca*$^{+}$ was 15.7% (range 11.3–20.8). A trend for increased Ki-67 PI was observed in the presence of additional mutations, but this was not statistically significant (P = 0.22).

Tumors with simultaneous loss of Apc and oncogenic mutations in Kras and Pik3ca progress from adenomas to adenocarcinomas to metastatic disease

Additional *Apc*$^{fl/fl}$ Pik3ca*$^{+}$ and *Apc*$^{fl/fl}$ *Kras*$^{LSL\text{-}G12D/+}$ Pik3ca*$^{+}$ mice were monitored with serial endoscopies (Figure 2-15). After 14 weeks, subsets of these mice underwent necropsy. At this time-point, approximately 50% of tumors from each these genetic profiles were invasive adenocarcinomas. The remaining tumors were adenomas with many of them exhibiting high-grade dysplasia.

The remaining *Apc*$^{fl/fl}$ Pik3ca*$^{+}$ and *Apc*$^{fl/fl}$ *Kras*$^{LSL\text{-}G12D/+}$ Pik3ca*$^{+}$ mice were aged until moribund. No difference in survival was observed between the two groups with a median survival of approximately 200 days (Figure 2-16A). The tumors progressed from small polypoid lesions to invasive adenocarcinomas that filled the majority of the colonic lumen (Figure 2-16B). These tumors even progressed to "apple-core" lesions often seen in advanced colon cancers in humans[67] (Figure 2-5B, far right). When these mice were moribund, only 20% of their tumors were preinvasive lesions, all of which were associated with high-grade dysplasia. The remaining 80% of tumors in these mice were invasive adenocarcinomas, many of which had a significant proportion of the tumor extending beyond the muscularis propria to involve the serosa (Figure 2-16C). Metastatic disease was identified in two of these mice, including metastases to a retroperitoneal para-aortic lymph node (Figure 2-17A) and metastatic cancer within the liver (Figure 2-17B). These are common locations for human colorectal cancer to metastasize. No lung metastases were identified.

Discussion

The progression from an adenoma to an invasive carcinoma is a histologic determination defined by spread of tumor into the submucosa. Invasion into the submucosa has been associated with the presence of additional driver mutations beyond the loss of APC, but does not necessitate molecular progression beyond mutations that have been observed in adenomas. An important consideration, often ignored, about colon cancer tumorigenesis is the time necessary for the acquired mutations to alter the phenotype of the tumor. This is important when investigating the potential timing of acquired mutations.

Activation of the WNT signaling cascade following the loss of APC or mutations in *CTNNB1* results in tumorigenesis in the majority of human colorectal cancers[12,68]. Although activation of the WNT pathway is important for tumor initiation, it is not sufficient for progression to an invasive cancer[69]. In fact, the vast majority of polyps that form due to loss of APC will not become invasive cancers and some will actually regress[70]. Additional genetic alterations including *KRAS*, *BRAF*, *PIK3CA*, and *TP53* mutations are important for adenomas to develop high-grade dysplasia and progress to invasive adenocarcinomas[71]. The timing of when these additional genetic changes occur has been debated[72], though these additional genetic changes likely occur very early in tumorigenesis.

Because of the proliferative nature of the intestine, mutations are known to accumulate over time in the normal epithelium[54]. In colon cancers, an average of approximately 90 mutations are seen per tumor[73]. This number changes significantly depending upon the age at which the patient develops cancer. Most of these mutations are considered to be passenger mutations and are not thought to engender a selective growth advantage[74]. It has been estimated that half, if not more, of these mutations occur before tumor initiation[54]. To investigate whether driver mutations

can occur before tumor initiation, investigations into the presence of *KRAS* mutations in the normal epithelium have been performed. *KRAS* mutations have been identified in colon cancers, adenomas, tumor-associated epithelial tissue, and completely normal appearing mucosa[75]. This indicates that cells with mutations that are important for tumor progression, such as *KRAS*, might be present before tumor initiation.

If driver mutations are present within intestinal epithelial cells before or at least at the time of tumor initiation, tumor biology may be dramatically affected. Here, we show that the presence of *KRAS* and *PIK3CA* mutations at the time of initiation owing to loss of APC results in increased tumor multiplicity and an increased rate of progression to invasive adenocarcinomas. The tumors in the models described here even metastasize to retroperitoneal lymph nodes and the liver at relatively short intervals, indicating the potential for an increased probability of early metastatic spread. These results could explain interval cancers that develop in patients that are routinely screened following current recommendations. Of note, the results from these experiments might not be directly translated for all mutation profiles, and it is possible that certain mutations might be able to circumvent the adenoma-to-carcinoma sequence and need to be studied further.

Interestingly, we demonstrated that despite having both *Kras* and *Pik3ca* mutations at the time of tumor initiation from loss of APC, these cancers still develop through the adenoma-to-carcinoma sequence. Following inoculation of the colon with Adeno-Cre, a visible tumor can be identified in just a few weeks. These tumors are premalignant adenomas. The formation of the early polyp is most likely related to WNT signaling[76]. The loss of APC leads to the nuclear accumulation of CTNNB1, which results in cellular proliferation and polyp formation. Without additional genetic events, the polyps tend to stabilize in size and do not progress to cancers and

may actually regress[76]. With time, the vast majority of the tumors possessing mutations in *KRAS*, *PIK3CA*, or both will develop into invasive adenocarcinomas. The selective advantage conferred upon a cell carrying an additional driver mutation has been estimated to increase the probability of proliferation by 0.4% *in silico*[77]. Because driver mutations are being identified in tumors containing less than 10^9cells (~1 cm in diameter), clones carrying these mutations are likely developing very early. This possibility might explain why a statistically significant change in the proliferation rate could not be detected in the described experiments when additional driver mutations were added. Other factors including angiogenesis and stromal cell signaling might also limit the proliferation rate *in vivo*. Interestingly, because driver mutations are identified in tumors containing less than 10^9 cells (~1 cm in diameter), clones carrying these mutations are likely developing very early[78]. For these clones to outcompete others in the same tumor to a detectable extent, these additional driver mutations are likely occurring when the tumor consists of 10^4 cells or less. The small probability of proliferation causes dramatic changes as the number of cells in these tumors enlarges. These driver mutations *in vivo* augment tumor progression by more than just increasing cell proliferation, but also by suppressing apoptosis, stimulating angiogenesis, recruiting stroma, and evading immune surveillance, among others[79].

The presence of *Kras* and *Pik3ca* mutations at the time of tumor initiation in the setting of loss of Apc does not eliminate the formation of the premalignant intermediary. This is important because there is still the possibility to prevent invasion of these tumors if the polyps can be resected at colonoscopy. In addition, the malignant potential of these lesions might not be predicted purely on tumor growth rate and morphology as it appears based on the experiments presented here that loss of APC might be the key mediator of early tumor growth. The increased rate of tumor progression to invasive disease in the setting of concomitant driver mutations

indicates that it is likely beneficial to understand the biology of the polyps that are removed from patients. Prognostic stratification of premalignant lesions might be beneficial for determining the likelihood of these tumors harboring foci of invasive disease and potentially the risk of future lesions developing. Further investigation is needed, but it might be necessary to screen patients more frequently if they develop adenomas with high-risk molecular features.

The combinatorial accumulation of driver mutations, opposed to the timing of potential sequential mutations, has the greatest impact on tumor development and progression[77]. The timing of when these mutations occur is very important, however, as this will impact the amount of time necessary for these lesions to become invasive cancers. In many instances, the canonical mechanism of tumorigenesis with mutations slowly accumulating over time does likely occur. This study and others demonstrate, though, that there are likely some instances when the canonical pathway is not followed. This could explain the development of interval cancers between colonoscopies. We have characterized an effective mouse model for further investigations into the mechanisms of tumorigenesis that can ultimately be applied to the better understanding of the molecular progression of colon tumors. These studies will allow for improved risk stratification to dictate screening intervals and the development of better chemopreventive strategies.

Materials and Methods

Mouse husbandry

All animal studies were conducted under protocols approved by the Institutional Animal Care and Use Committee at the University of Wisconsin-Madison (Madison, WI), following the guidelines of the American Association for the Assessment and Accreditation of Laboratory

Animal Care. Fabp1-Cre^{+} mice (FVB/N-Tg(Fabp1-Cre)1Jig/Nci; NCI Mouse Repository, strain number 01XD8), *Kras*$^{LSL\text{-}G12D/+}$ mice (C57BL/6N.Cg-*Kras*^{tm4Tyj}/CjDswJ; The Jackson Laboratory, stock number 019104), Pik3ca*$^{+}$ mice (C57BL/6-*Gt(ROSA)26Sor*$^{tm7(Pik3cap110*,EGFP)Rsky/}$J; The Jackson Laboratory, stock number 012343), *Apc*$^{fl/fl}$ mice (C57BL/6.Cg-*Apc*^{tm2Rak}/Nci; NCI Mouse Repository, strain number 01XAA), and mT/mG^{+} mice (B6.129(Cg)-Gt(ROSA)26Sor$^{tm4(ACTB\text{-}tdTomato,\text{-}EGFP)Luo}$/J; The Jackson Laboratory, stock number 007676) were maintained and genotyped as previously described[8,59,61,80,81]. Pik3ca*$^{+}$ and *Kras*$^{LSL\text{-}G12D/+}$ mice were also crossed to *Apc*$^{fl/fl}$ mice to generate *Apc*$^{fl/fl}$ *Kras*$^{LSL\text{-}G12D/+}$, *Apc*$^{fl/fl}$ Pik3ca*$^{+}$, and *Apc*$^{fl/fl}$ *Kras*$^{LSL\text{-}G12D/+}$ Pik3ca*$^{+}$ mice on a homogeneous B6 genetic background for Adeno-Cre delivery. In addition, mT/mG^{+} mice were crossed to generate B6 mT/mG^{+} *Apc*$^{fl/fl}$ *Kras*$^{LSL\text{-}G12D/+}$ Pik3ca*$^{+}$ mice. All Pik3ca*$^{+}$ mice were hemizygous for this allele.

Nonsurgical exposure of the colon to Adeno-Cre

Polyethylene tubing (I.D. 1.4 mm, O.D. 1.90 mm; Becton Dickinson, Sparks, MD) was cut to sizes appropriate for mice (7–12 cm). A 1-cm window was notched into the tubing and the end of the tubing was closed with edges being rounded to avoid perforation of the bowel (Figure 2-13A). Marks corresponding to 1 cm intervals were made on the tubing. A longitudinal stripe was also applied corresponding to the orientation of the window. Similarly sized polyethylene tubing was cut to size without a slot to be used as a sheath for a 2.2-mm caliber soft bristle brush (DenTek Oral Care).

Mice were anesthetized using 2% isoflurane. The colon was flushed with PBS. A narrow ribbon of GelFoam (Pharmacia and Upjohn) was inserted into the window cut into the polyethylene tube. Of note, 200 μL of 0.05% trypsin (Hyclone) was injected into the tubing and inserted into the mouse colon at the desired depth and radial orientation. After 10 minutes, the

slotted tube was removed and the sheath with the small soft bristle brush was introduced at the same intraluminal location. The brush was then used to abrade the epithelium for up to 3 minutes. After PBS irrigation, a slotted tubing containing GelFoam was then filled with 200 μL PBS containing 10^9 PFU of Adeno-Cre (Ad5CMVCre and Ad5CMVEmpty, University of Iowa Gene Transfer Vector Core, IA). After 30 minutes of incubation, the tubing was removed. Owing to the anatomical limitations of the mouse, only the most distal half of the colon (~4 cm) could be inoculated in this way. Mice recovered quickly after the procedure and did not exhibit overt signs of pain or distress following the procedure, as they quickly became active. Note that nonsteroidal anti-inflammatory drugs were not used for post-procedure analgesia as these agents have been shown to suppress intestinal tumorigenesis in both humans and laboratory mice.

Murine colonoscopy/PET imaging

Mice were anesthetized using 2% isoflurane and the colons were flushed with PBS. The Coloview System was used to monitor tumor formation and growth in the distal half of the colon as previously described[82] (Karl Storz). ImageJ analysis was utilized to measure the percent lumen occlusion as described previously[35].

Animals were fasted for at least 6 hours before injection of ^{18}F-FDG (160 μCi; IBA Molecular). After injection, the animals were kept under anesthesia for 60 minutes and then prepared for microPET colonography as described previously[83].

Histology and IHC

Mice were euthanized and the colons were excised and opened longitudinally. Tumor tissue was fixed in 10% buffered formalin. Fixed tumors were embedded in paraffin and cut into

5 μm sections. Every tenth section was stained with hematoxylin and eosin (H&E) for histologic review. IHC was carried out as described previously[66] with the exception that tissues were blocked with Background Sniper (Biocare Medical) for 10 minutes. The primary antibodies included rabbit anti-phospho-AKT (Ser473, 1:100, Cell Signaling Technology #4060), rabbit anti-phospho-S6 Ribosomal Protein (Ser235/236, 1:50, Cell Signaling Technology #4858), rabbit anti-CTNNB1 (1:100–1:200, Cell Signaling Technology #8480), rabbit anti-Ki67 (1:400, Cell Signaling Technology #12202), and rabbit anti-phospho-ERK1/2 (1:400, Cell Signaling Technology #4370). The Ki-67 proliferation index was measured as the percent of nuclei staining positive for Ki-67 per tumor using ImmunoRatio, an ImageJ plugin (http://jvsmicroscope.uta.fi/sites/default/files/software/immunoratio-plugin/index.html).

Recombination Testing

To validate that all alleles were recombined within tumors, neoplastic tissue was scraped from FFPE sections with a sterile size 10 surgical blade with normal epithelium left behind. DNA was isolated from the scraped tissue using the Maxwell 16 FFPE Tissue LEV DNA Purification Kit (Promega). Samples with a sufficient amount of DNA were analyzed for Cre-mediated recombination between *loxP* sites.

Recombination of the *loxP* sites within the Apc^{fl} allele and upstream of the $KRAS^{LSL\text{-}G12D}$allele was confirmed using previously described PCR primers and protocols (http://jacks-lab.mit.edu/protocols/genotyping/kras_cond)[61]. Recombination of the *loxP* sites upstream of the Pik3ca*$^{+}$ allele was confirmed using the forward primer 5′-CGCGGTTGAGGACAAACTCT-3′ and the reverse primer 5′-ACCATAATTCCACCACCACCA-3′. Cycling conditions were one cycle of 94°C for 3 minutes, followed by 35 cycles of 94°C for 20 seconds, 61°C for 60 seconds,

and 72°C for 60 seconds, with one final extension cycle at 72°C for 2 minutes. Recombined DNA resulted in amplification of a 561-bp product.

Disclosure of Potential Conflicts of Interest

No potential conflicts of interest were disclosed.

Acknowledgements

This work was partially funded by Funk Out Cancer, a memorial event dedicated to Kate Gates Falaschi. This work was also supported by the Conquer Cancer Foundation of the American Society of Clinical Oncology through A Young Investigator Award (to D.A. Deming); T32 CA09017 (to T.J. Paul Olson), T32 CA009135 (to J.N. Hadac. and A.A. Leystra), R21 CA170876 (to R.B. Halberg) and R01 CA123438 (to R.B. Halberg) from the NIH; 2012 AACR Career Development Award for Colorectal Cancer Research, Grant Number 12-20-01-HALB (to R.B. Halberg); start-up funds (to R.B. Halberg) from the UW Division of Gastroenterology and Hepatology, the UW Department of Medicine, and the UW School of Medicine and Public Health; and start-up funds (to D.A. Deming) from the UW Carbone Cancer Center, UW Department of Medicine, UW School of Medicine and Public Health, and the UW Graduate School through the Wisconsin Alumni Research Foundation; P30 CA014520 (Core Grant, University of Wisconsin Carbone Cancer Center); UW Carbone Cancer Center Gastrointestinal Disease Oriented Working Group (to R.B. Halberg and D.A. Deming); and Funk Out Cancer (to D.A. Deming).

Figures

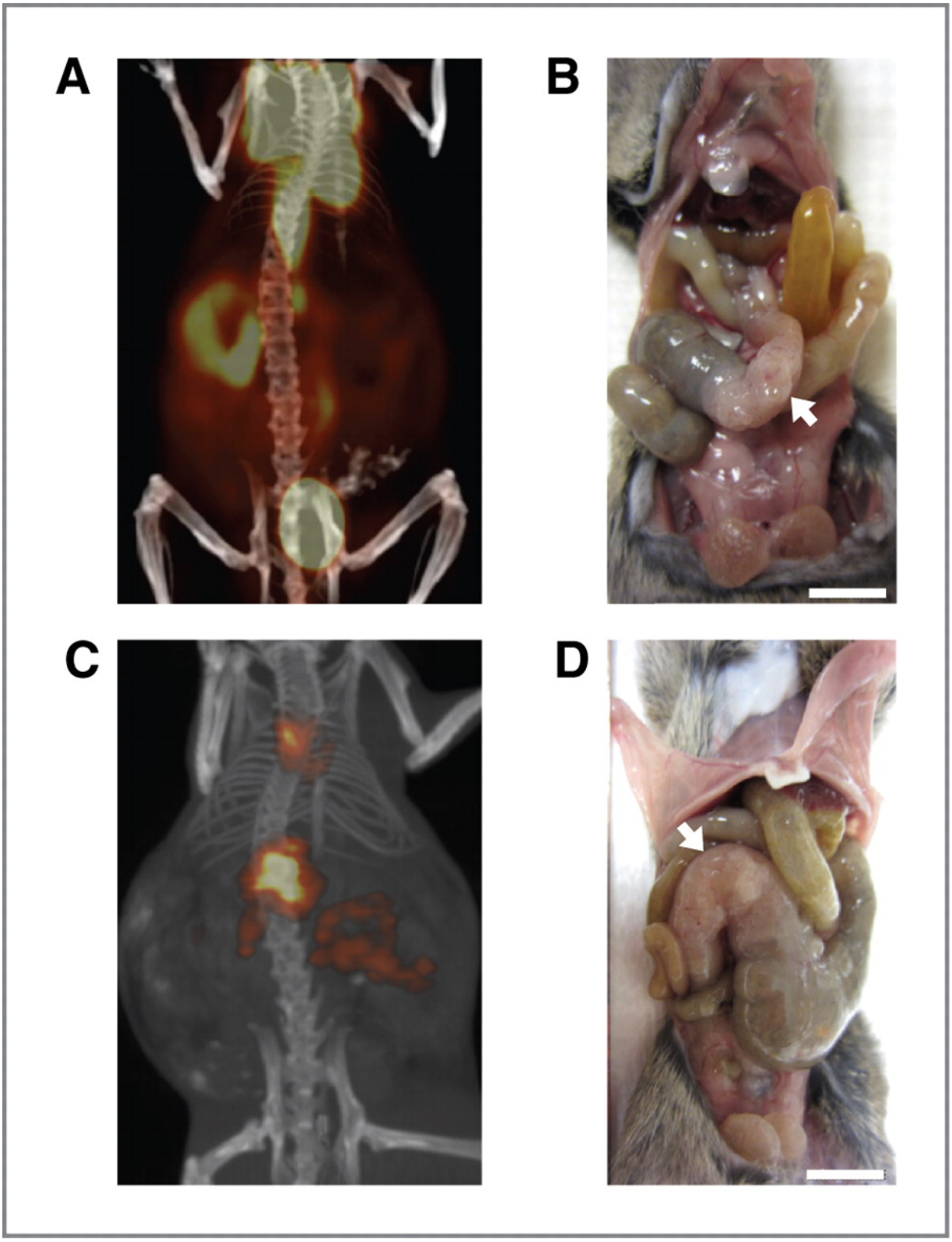

Figure 2-1. Fabp1-Cre^{+} Pik3ca*$^{+}$ mice develop intestinal obstruction due to large proximal colon tumors. The tumors exhibit a high avidity for FDG (A) and CLR1404 (C). The mouse was injected with the imaging agent and scanned, and the data were reconstructed with standard algorithms. Following scan acquisition, each mouse was sacrificed and the abdominal wall was dissected, revealing tumors in the proximal colon (B and D, arrows). Scale bars, 1 cm.

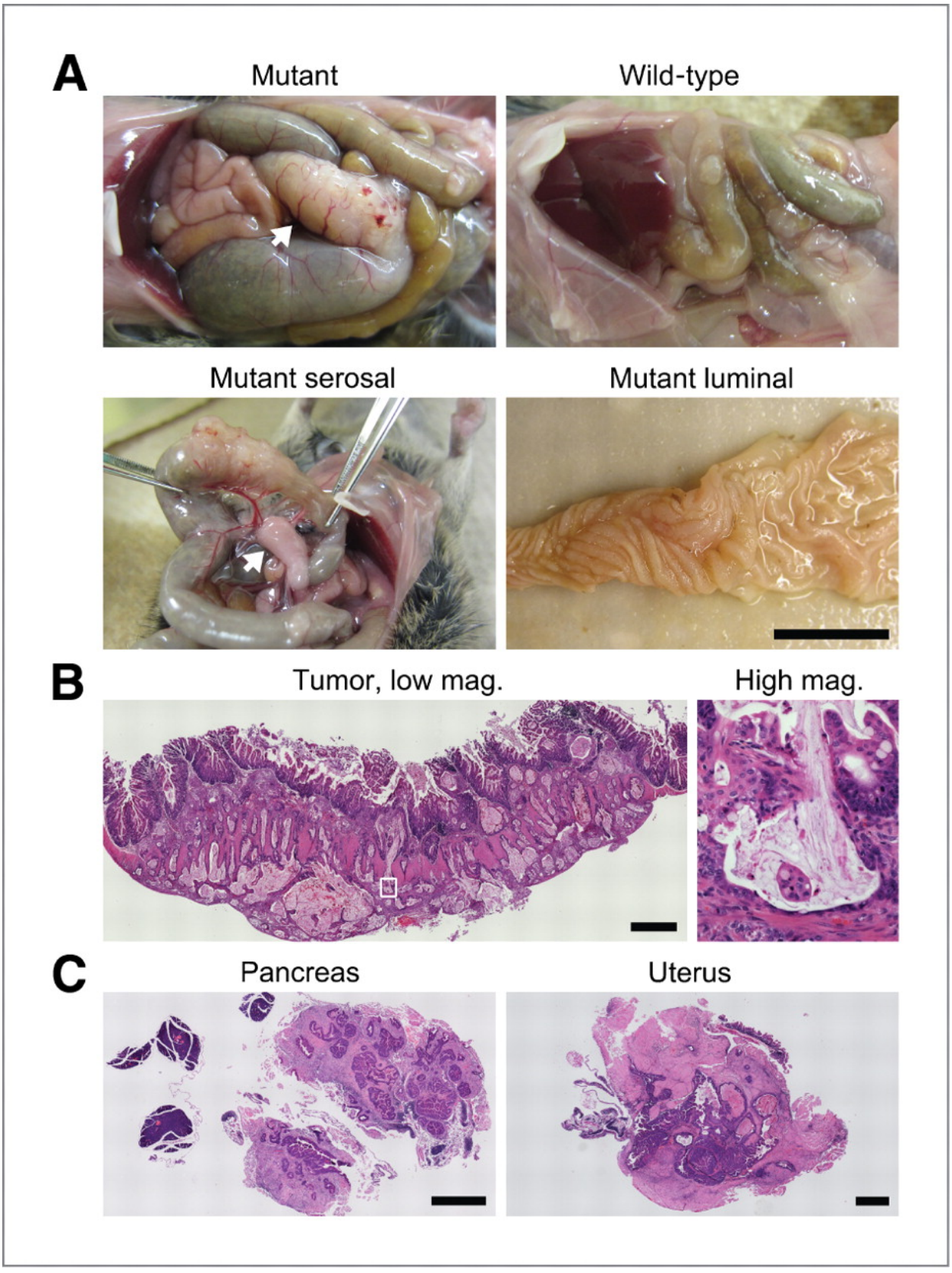
A
Mutant
Wild-type
Mutant serosal
Mutant luminal
B
Tumor, low mag.
High mag.
C
Pancreas
Uterus

Figure 2-2. The large tumors in the proximal colon are invasive mucinous adenocarcinomas. (A) Fabp1-Cre^{+} Pik3ca*$^{+}$ mouse and its wild-type littermate were sacrificed at 56 days of age and dissected (top left and right, respectively). In the mutant, severe dilation of the small bowel and cecum was due to obstruction by a massive tumor (top left, arrow). The tumor was associated with large penetrating blood vessels and thickened mesentery (bottom left, arrow). The intestine was removed, split lengthwise, and splayed out. The epithelium was hyperplastic, but no obvious polypoid intermediary was observed (bottom right). (B) The tumor was removed, embedded in paraffin, and cut. Sections were stained with H&E. Islands of malignant glands in mucin lakes were evident at higher magnification (right). (C) One cecal tumor seemed to directly extend to surrounding organs including the pancreas and in the uterus. Scale bars, 1 cm (A) and 1 mm (B and C).

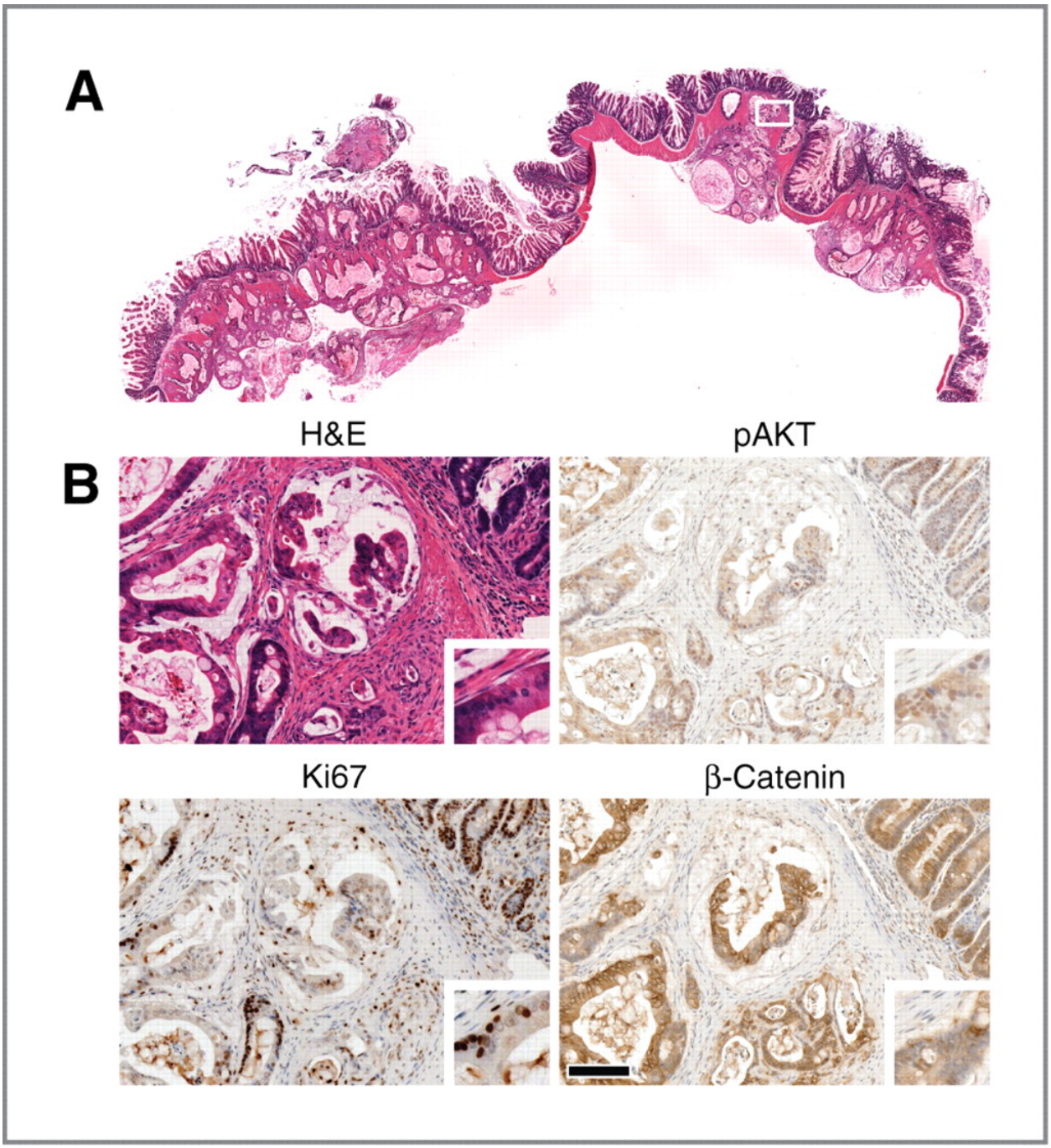
A
H&E
pAKT
B
Ki67
β-Catenin

Figure 2-3. Pik3ca* induces cellular proliferation. (A) A section of a tumor from a 61-day-old Fabp1-Cre^{+} Pik3ca*$^{+}$ mouse was stained with H&E. The tumor invaded through the musculature into the adipose tissue of the colonic mesenteries. (B) The boxed region in A is shown at higher magnification below. The activation of AKT, a downstream target of PI3K, is revealed by immunohistochemistry using antibodies specific for pAKT (top right). The majority of nuclei are positive (brown). This change was coupled with an increase in cellular proliferation as measured by immunohistochemistry using antibodies against Ki67 (bottom left). The invasive adenocarcinomas that develop in this model do not appear to rely on aberrant WNT signalling, as β-catenin is membrane-bound rather than nuclear, as shown by immunohistochemistry (bottom right). This localization of β-catenin was observed in 10 of 10 tumors. Insets were taken from the left edge of each panel and magnified 2-fold (B). Scale bar, 100 μm.

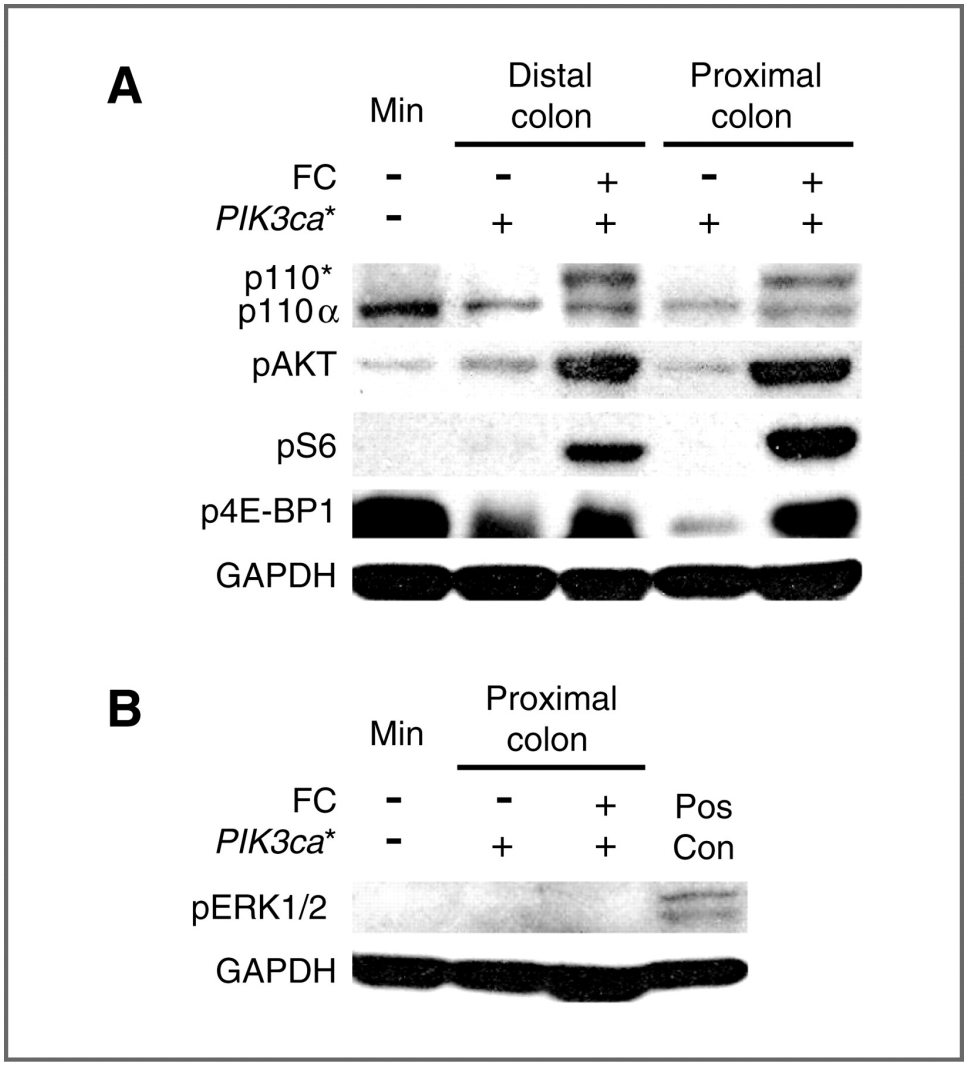
A
Min
Distal colon
Proximal colon
FC - - + - +
PIK3ca* - + + + +
p110* p110α
pAKT
pS6
p4E-BP1
GAPDH
B
Min
Proximal colon
FC - - + Pos
PIK3ca* - + + Con
pERK1/2
GAPDH

Figure 2-4. Activation of the PI3K/AKT/mTOR pathway occurs in the colonic mucosa and tumors of Fabp1-Cre^{+} Pik3ca*$^{+}$ mice without increasing pERK1/2. (A) Protein extracts were prepared from scrapings of the mucosa that were taken from either the proximal or distal colon of experimental and control mice. Note that the scrapings from the proximal colon of Fabp1-Cre^{+} (FC) Pik3ca*$^{+}$ mice contained tumor tissue. Protein extracts were also prepared from a colon tumor that was taken from an *Apc*$^{Min/+}$ (Min) mouse for comparison. p110* is identifiable by Western blotting in the proximal and distal colon of Fabp1-Cre^{+} Pik3ca*$^{+}$ mice (A). The level of p110α is similar in all tissues tested. Upregulation of the PI3K/AKT/mTOR pathway is noted by increased phosphorylation in AKT, S6, and 4E-BP1. (B) Phosphorylation of ERK1/2 was undetectable in protein extracts from proximal colon tumors of 4 Fabp1-Cre^{+} Pik3ca*$^{+}$ mice, a representative is shown. DLD-1, a human colorectal cancer cell line that expresses mutant KRAS, was used as a positive control (Pos Con); GAPDH was used as a loading control.

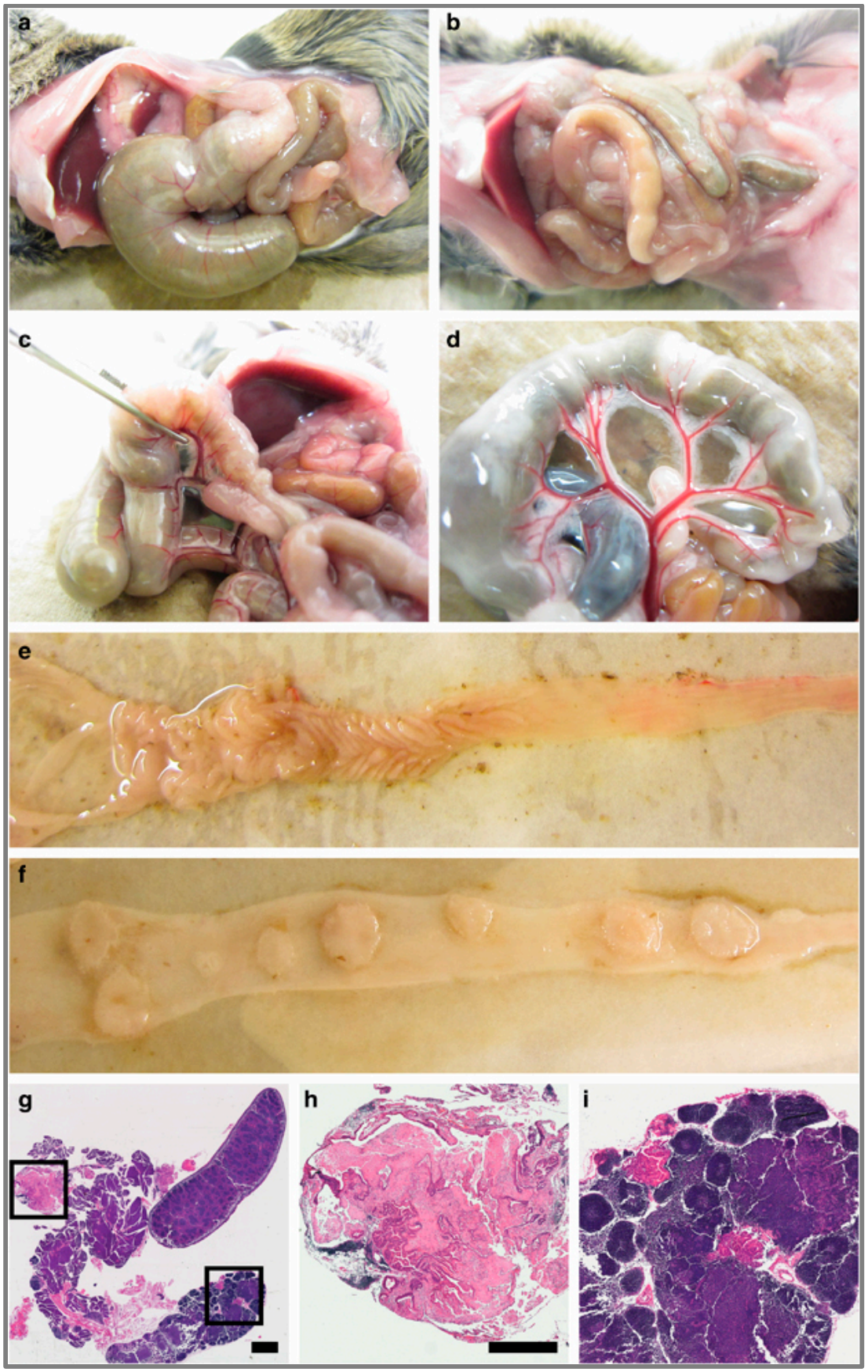
a
b
c
d
e
f
g
h
i

Figure 2-5. Fabp1-Cre^{+} Pik3ca*$^{+}$ *Apc$^{Min/+}$* mice become moribund by 52 days of age on average due to obstructive enteropathy or anemia. (A-B) At necropsy, large proximal colon cancers result in distention of the cecum and small intestine (A) compared with control (B). (C-D) These tumors are associated with enlarged mesenteric adenopathy. In addition, an impressive vascular supply is noted supplying tumors in the colon (C) and distal small intestine (D). (E) The colon was removed and split lengthwise demonstrating a large flat proximal colon cancer and other smaller tumors in the colon. (F) The distal small intestine was also resected and split lengthwise revealing multiple large tumors. The mesentery was also examined closely following removal of the colon and small intestine. Hyperplasia of the lymphatic tissue was seen in all mice (C, G). In some mice, tumor deposits were seen in the mesenteric adipose tissue (G, H) or within the lymphatic tissue (G, I). Size bars: (G)=2 mm; (H, I)=1 mm. (H, I) Enlargements of the boxes in (G).

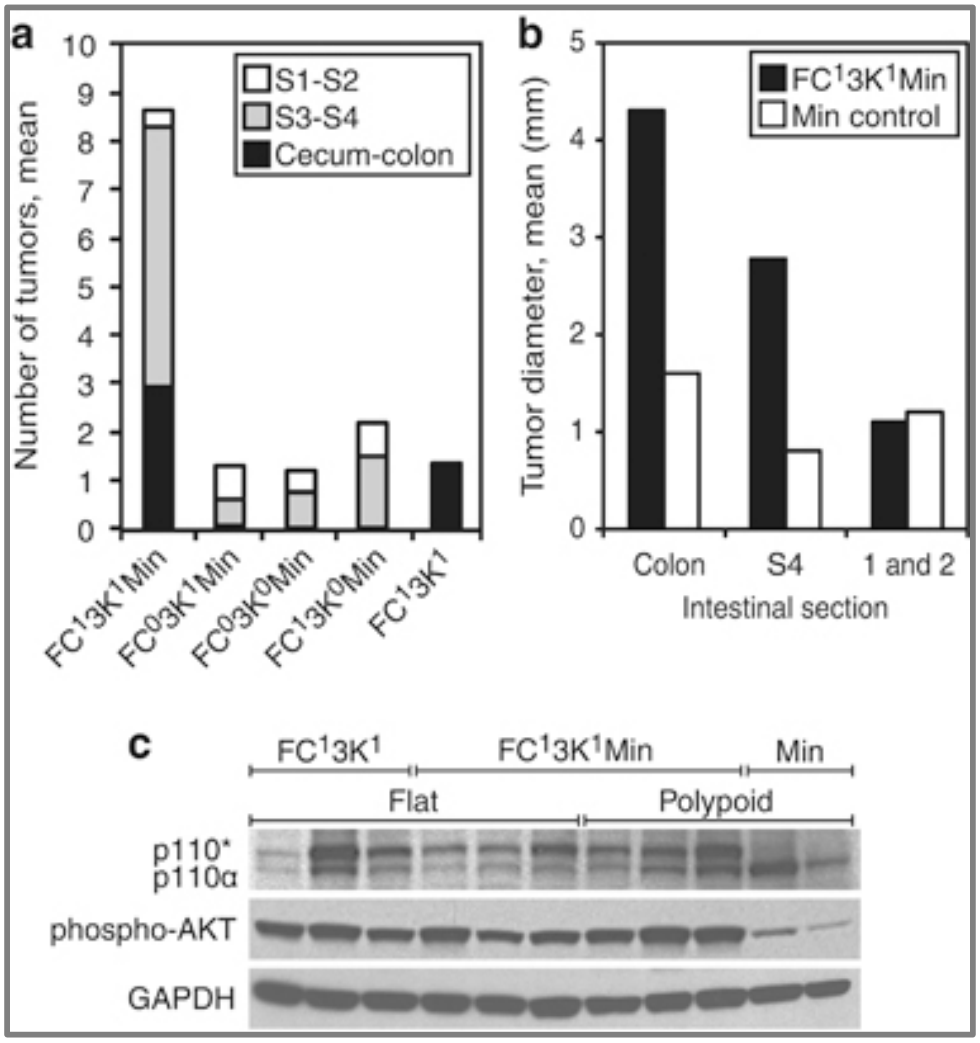
a
Number of tumors, mean
S1-S2
S3-S4
Cecum-colon
FC13K1Min
FC03K1Min
FC03K0Min
FC13K0Min
FC13K1
b
Tumor diameter, mean (mm)
FC13K1Min
Min control
Colon
S4
1 and 2
Intestinal section
c
FC13K1
FC13K1Min
Min
Flat
Polypoid
p110*
p110α
phospho-AKT
GAPDH

Figure 2-6. Activation of the PI3K pathway in the intestine of *Apc*$^{Min/+}$ mice results in increased tumor number and size. (A) In the Fabp1-Cre^{+} Pik3ca*$^{+}$ *Apc*$^{Min/+}$ (labeled "FC^{1}3K^{1}Min"), the median number of tumors seen was 8.7 compared with the control littermates (Fabp1-Cre^{0} Pik3ca*$^{+}$ *Apc*$^{Min/+}$ labeled "FC^{0}3K^{1}Min"; Fabp1-Cre^{+} Pik3ca*^{0} *Apc*$^{Min/+}$ labeled "FC^{1}3K^{0}Min"; Fabp1-Cre^{0} Pik3ca*^{0} *Apc*$^{Min/+}$ labeled "FC^{0}3K^{0}Min" or "Min"; and Fabp1-Cre^{+} Pik3ca*$^{+}$ *Apc*$^{+/+}$ labeled "FC^{1}3K^{1}") which averaged 2.2 or less. This effect was seen prominently in the colon, where the Fabp1-Cre^{+} Pik3ca*$^{+}$ *Apc*$^{Min/+}$ mice have a mean of 2.9 tumors per mouse and only 1 colon tumor was seen in 32 *Apc*$^{Min/+}$ control littermates (A). In the proximal small intestine, no difference was noted in tumor number which is consistent with the activated form of PI3K not being expressed in this area in the Fabp1-Cre^{+} Pik3ca*$^{+}$ *Apc*$^{Min/+}$ mice. (B) An increase in tumor size was also noted in Fabp1-Cre^{+} Pik3ca*$^{+}$ *Apc*$^{Min/+}$ (colon: mean 4.3 mm, median 3, range 2–10 mm; S4: mean 2.8 mm, median 2.3 mm, range 0.7–7 mm) compared with *Apc*$^{Min/+}$ (colon: 1.6 mm, only one colon tumor was observed in 32 mice; S4: mean 0.8 mm, median 0.5 mm, range 0.4–2 mm, P=0.004). No change in tumor size was noted in the proximal 2 segments of the small intestine, which is consistent with the lack of expression of the activated form of PI3K in this area. (C) The increase in tumor number and size is related to the expression of the activated form of PI3K, p110*, in the Fabp1-Cre^{+} Pik3ca*$^{+}$ *Apc*$^{Min/+}$ mice, as this can be detected in these tumors and is associated with increased phosphorylation of AKT as compared with *Apc*$^{Min/+}$ control tumors.

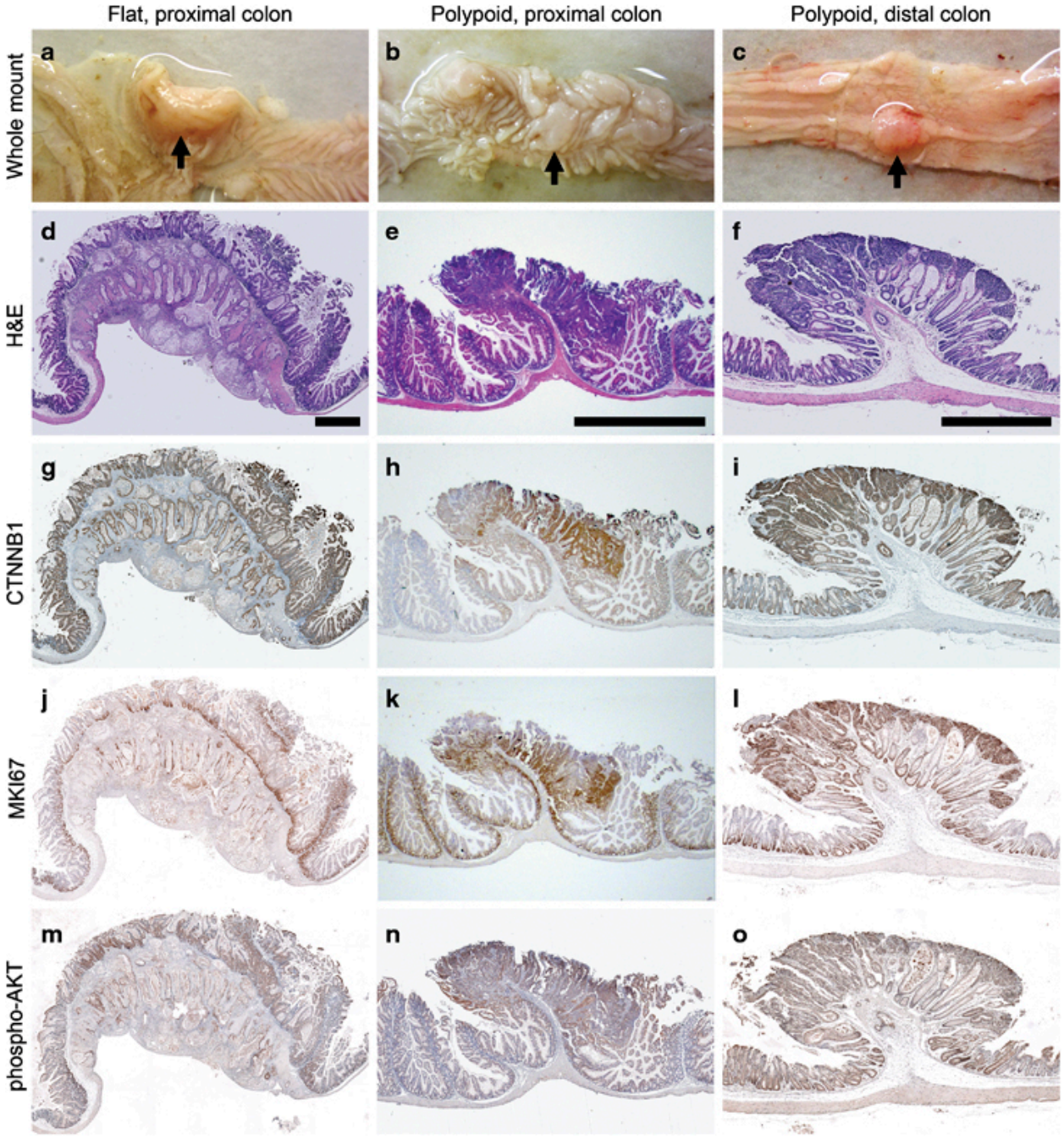
Flat, proximal colon
Polypoid, proximal colon
Polypoid, distal colon
Whole mount
H&E
CTNNB1
MKI67
phospho-AKT
a
b
c
d
e
f
g
h
i
j
k
l
m
n
o

Figure 2-7. Fabp1-Cre^{+} Pik3ca*$^{+}$ *Apc$^{Min/+}$* mice develop multiple tumors with distinct morphologies. Large flat moderately differentiated mucinous adenocarcinomas develop in the proximal colon (A, D). This cancer penetrates through the serosal surface consistent with a T4 lesion. Polypoid intramucosal carcinomas arising in the setting of villous/serrated hyperplasia are seen also in the proximal colon (B, E). In the mid and distal colon, tumors range from small adenomas to large adenomas with high-grade dysplasia to adenocarcinomas. A large adenoma with solid growth pattern and a focal area of adenocarcinoma in the submucosa is pictured in (C, F). The flat mucinous lesions do not possess nuclear CTNNB1 (G), while the polypoid tumors demonstrate nuclear CTNNB1 IHC staining (H, I). The MKI67 and phospho-AKT IHC staining of all of these tumors indicates that these tumors are highly proliferative and have activated PI3K/AKT signaling (J–O). Scale bars: (D)=1 mm; (E)=500 μm; (F)=1 mm. All experiments were completed at least in triplicate.

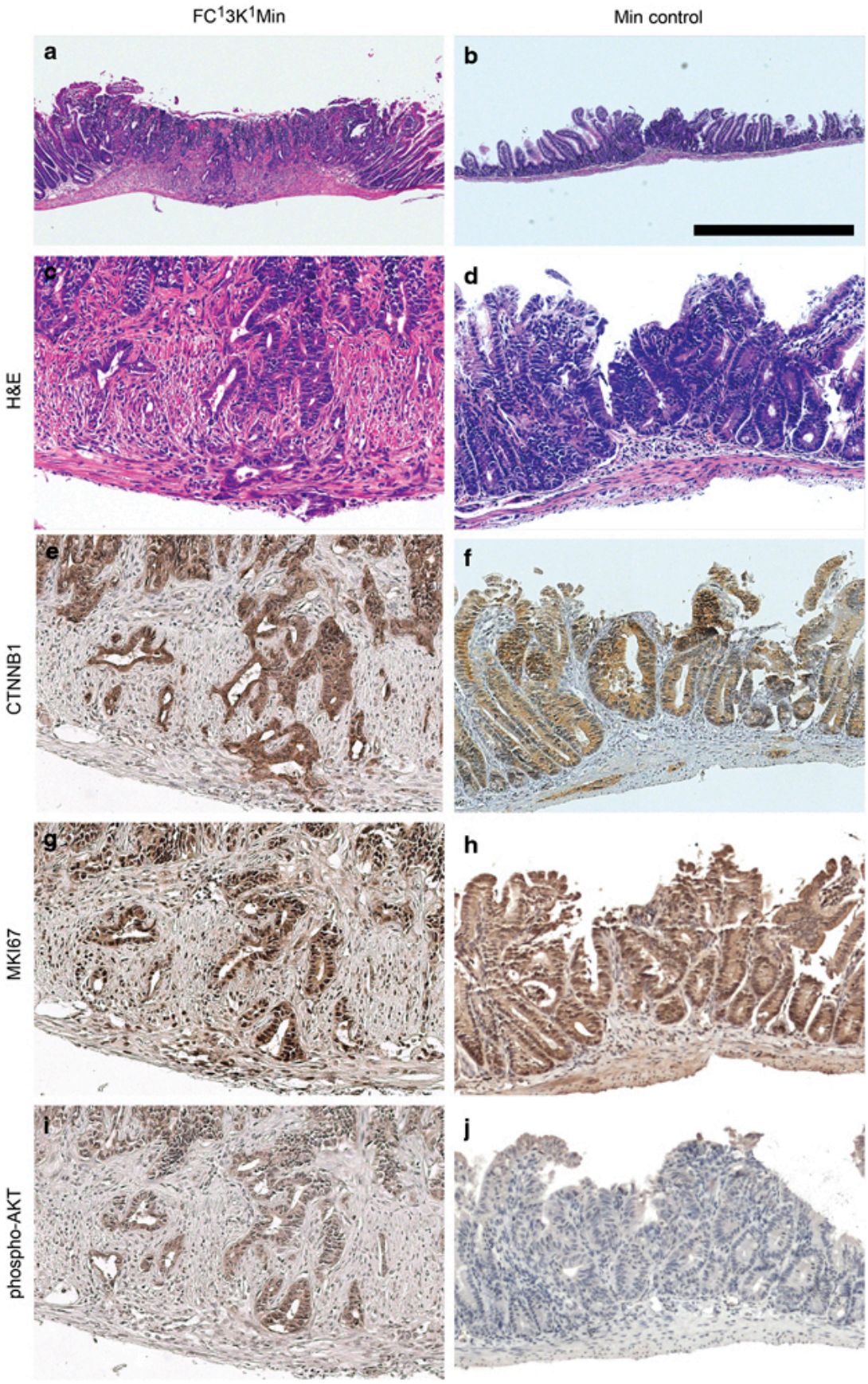
FC13K1Min
Min control
a
b
c
d
e
f
g
h
i
j
H&E
CTNNB1
MKI67
phospho-AKT

Figure 2-8. Advanced small bowel tumors are seen in Fabp1-Cre^{+} Pik3ca*$^{+}$ *Apc$^{Min/+}$* mice. Large ulcerated adenocarcinomas are present in segments 3 and 4 of the small intestine (A, C). Some of these tumors even penetrate through the serosal surface. This is compared with the small adenomas that form less frequently in the *Apc$^{Min/+}$* (Min) controls (B, D). CTNNB1 expression is nuclear in both Fabp1-Cre^{+} Pik3ca*$^{+}$ *Apc$^{Min/+}$* (FC^{1}3K^{1}Min) tumors and controls (E, F). An increase in MKI67 and phospho-AKT IHC staining is noted in the Fabp1-Cre^{+} Pik3ca*$^{+}$ *Apc$^{Min/+}$* tumors compared with control (G–J). Scale bars: (A, B)=1 mm; (C–J) are 4 × enlargements.

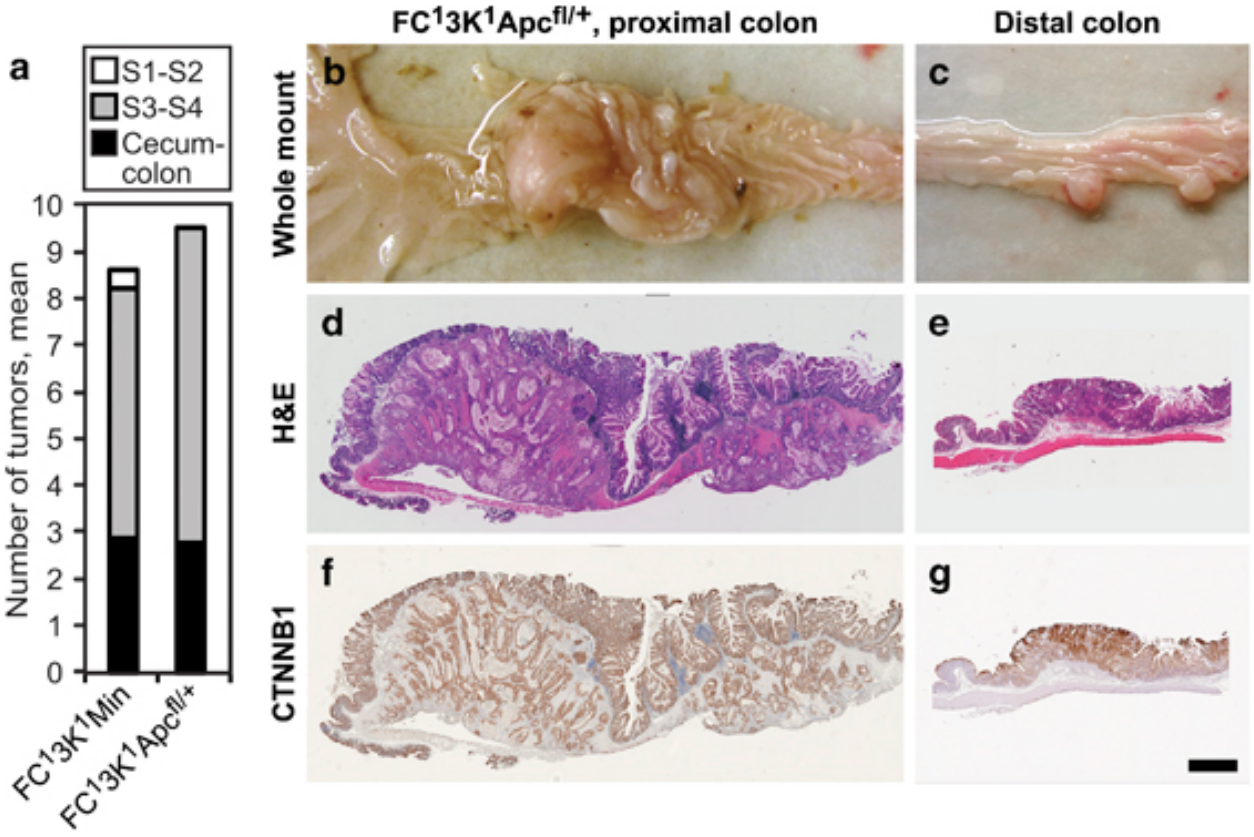
a
S1-S2
S3-S4
Cecum-colon
Number of tumors, mean
0
1
2
3
4
5
6
7
8
9
10
FC13K1Min
FC13K1Apcfl/+
FC13K1Apcfl/+, proximal colon
Distal colon
Whole mount
H&E
CTNNB1
b
c
d
e
f
g

Figure 2-9. In *Apc*$^{Min/+}$ mice, one functional allele of *Apc* is lost in all cells, including the epithelial and stromal cells. To examine if a similar phenotype exists when APC is lost only in the epithelial cells, mice possessing an allele of *Apc* with exon 14 floxed (*Apc*$^{fl/+}$) were utilized. In the Fabp1-Cre^{+} Pik3ca*$^{+}$ *Apc*$^{fl/+}$ mice (FC^{1}3K^{1}Apc$^{fl/+}$), one allele of *Apc* was lost only in the epithelial cells of the distal small intestine and colon. No difference in tumor number was noted in Fabp1-Cre^{+} Pik3ca*$^{+}$ *Apc*$^{fl/+}$ and Fabp1-Cre^{+} Pik3ca*$^{+}$ *Apc*$^{Min/+}$ (FC^{1}3K^{1}Min) mice in the distal small intestine and colon (A). In addition, no difference in tumor morphology or CTNNB1 localization was noted (B–G). Scale bar (D–G)=1 mm.

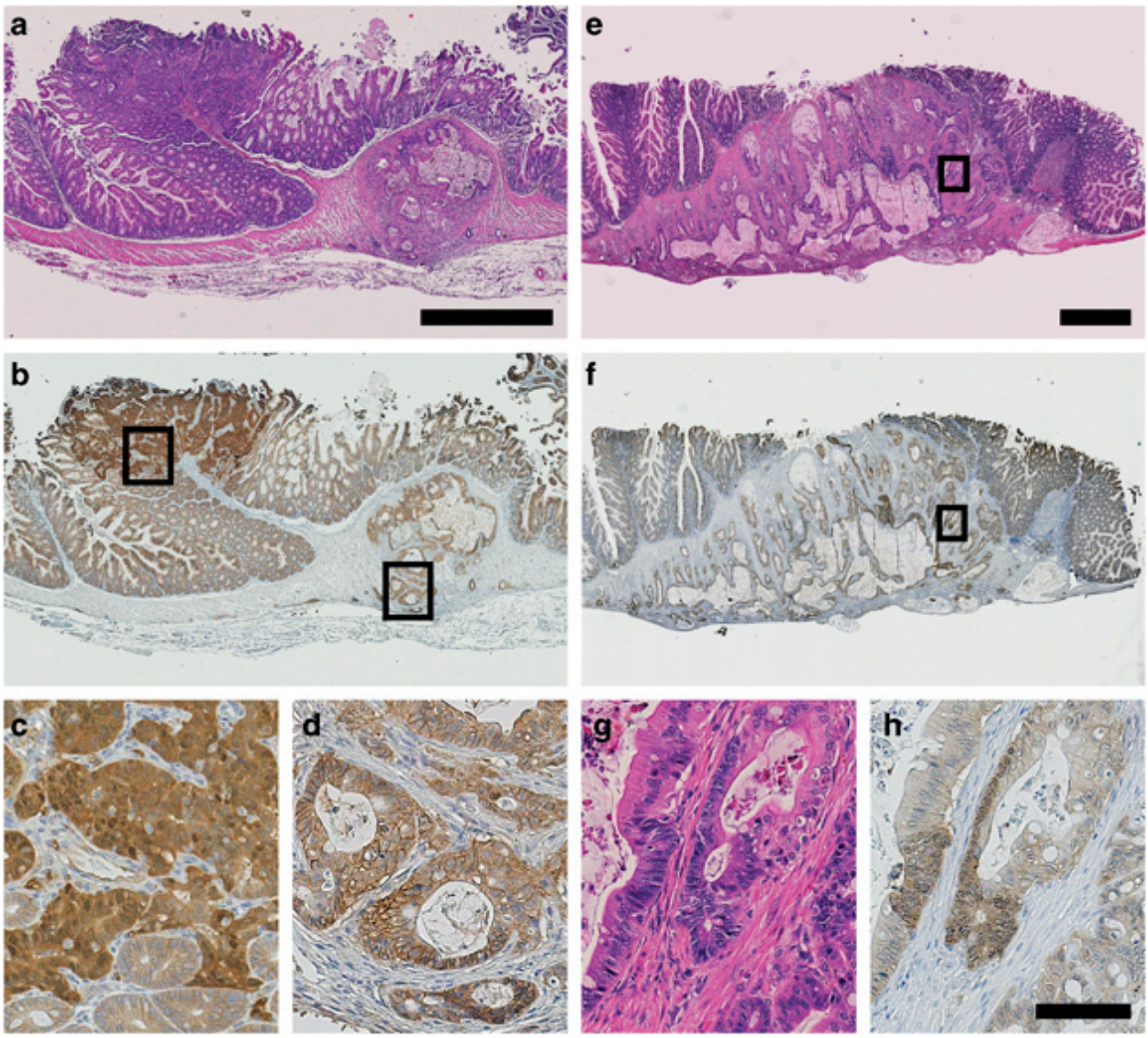
a
e
b
f
c
d
g
h

Figure 2-10. The tumors of the Fabp1-Cre^{+} Pik3ca*$^{+}$ *Apc*$^{Min/+}$ mice develop by both canonical and non-canonical pathways. Exophytic polypoid adenomas with high-grade dysplasia (A, left) and mucinous adenocarcinomas (A, right) develop in the proximal colon of Fabp1-Cre^{+} Pik3ca*$^{+}$ *Apc*$^{Min/+}$ mice. The exophytic polypoid lesions possess a high amount of nuclear CTNNB1 (tumor on the left in B, enlarged in C), while the flat mucinous adenocarcinomas do not possess significant levels of nuclear CTNNB1 (tumor on the right in B, enlarged in D). This indicates that the polypoid lesions are arising secondary to aberrant WNT signaling, while the flat mucinous lesions form via a non-canonical mechanism. Rarely, the large flat mucinous adenocarcinomas have islands of cells with nuclear CTNNB1 (E, H&E; F, CTNNB1). The cells with nuclear CTNNB1 also have a different morphology (G, H, enlargements of E and F, respectively), with a higher nucleus-to-cytoplasm ratio, nuclear enlargement and hyperchromasia, and a more basophilic cytoplasm. Scale bars: (A, B)=1 mm; (E, F)=1 mm; (C, D, G, H)=100 μm.

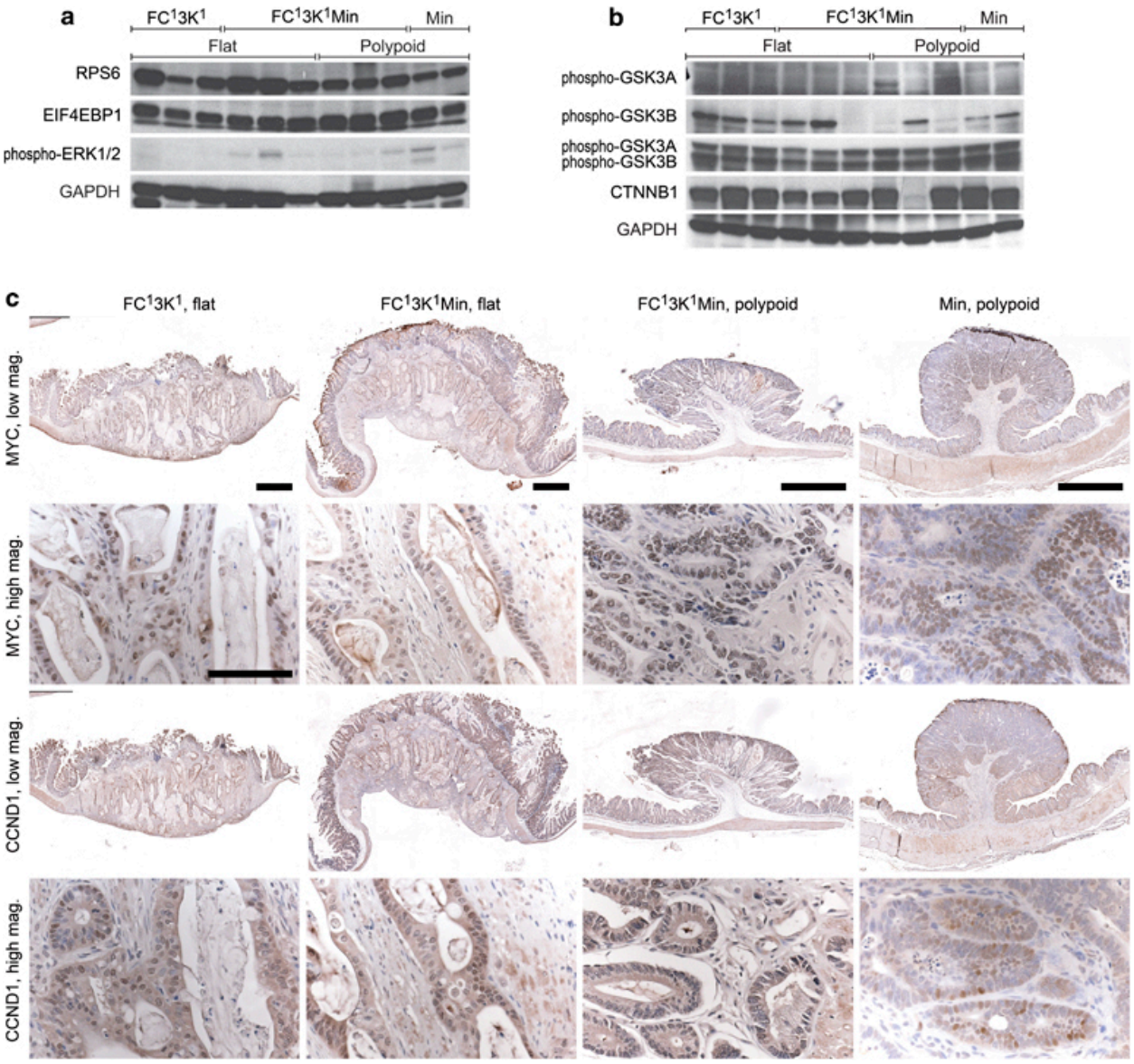
a
FC¹3K¹
FC¹3K¹Min
Min
Flat
Polypoid
RPS6
EIF4EBP1
phospho-ERK1/2
GAPDH
b
FC¹3K¹
FC¹3K¹Min
Min
Flat
Polypoid
phospho-GSK3A
phospho-GSK3B
phospho-GSK3A
phospho-GSK3B
CTNNB1
GAPDH
c
FC¹3K¹, flat
FC¹3K¹Min, flat
FC¹3K¹Min, polypoid
Min, polypoid
MYC, low mag.
MYC, high mag.
CCND1, low mag.
CCND1, high mag.

Figure 2-11. Several key mediators of PI3K and WNT signaling are altered in Fabp1-Cre^{+} Pik3ca*$^{+}$ *Apc$^{Min/+}$* mice. (A, B) Western blots. Phosphorylation of RPS6 and EIF4EBP1 is observed in the Fabp1-Cre^{+} Pik3ca*$^{+}$ *Apc$^{+/+}$* (*FC^{l}3K^{l}*) tumors (A). Only low amounts of phospho-ERK1/2 are seen in these tumors (A). Increased pGSK3β is detected in the majority of flat Fabp1-Cre^{+} Pik3ca*$^{+}$ *Apc$^{Min/+}$* (FC^{1}3K^{1}Apc$^{Min/+}$) cancers with variable phosphorylation noted in the polypoid lesions (B). No change in the levels of total GSK3α or GSK3β was observed. In addition, in the majority of tumors no change in the levels of CTNNB1 was seen (B). (C) Similar levels of MYC were seen in all tumors. Increased nuclear CCND1 levels were observed in the Fabp1-Cre^{+} Pik3ca*$^{+}$ *Apc$^{+/+}$* (*FC^{l}3K^{l}Apc$^{+/+}$*) and Fabp1-Cre^{+} Pik3ca*$^{+}$ *Apc$^{Min/+}$* tumors compared with *Apc$^{Min/+}$* (Min) tumors (C). Scale bars low mag 1 mm and high mag 100 μm. All experiments were completed at least in triplicate.

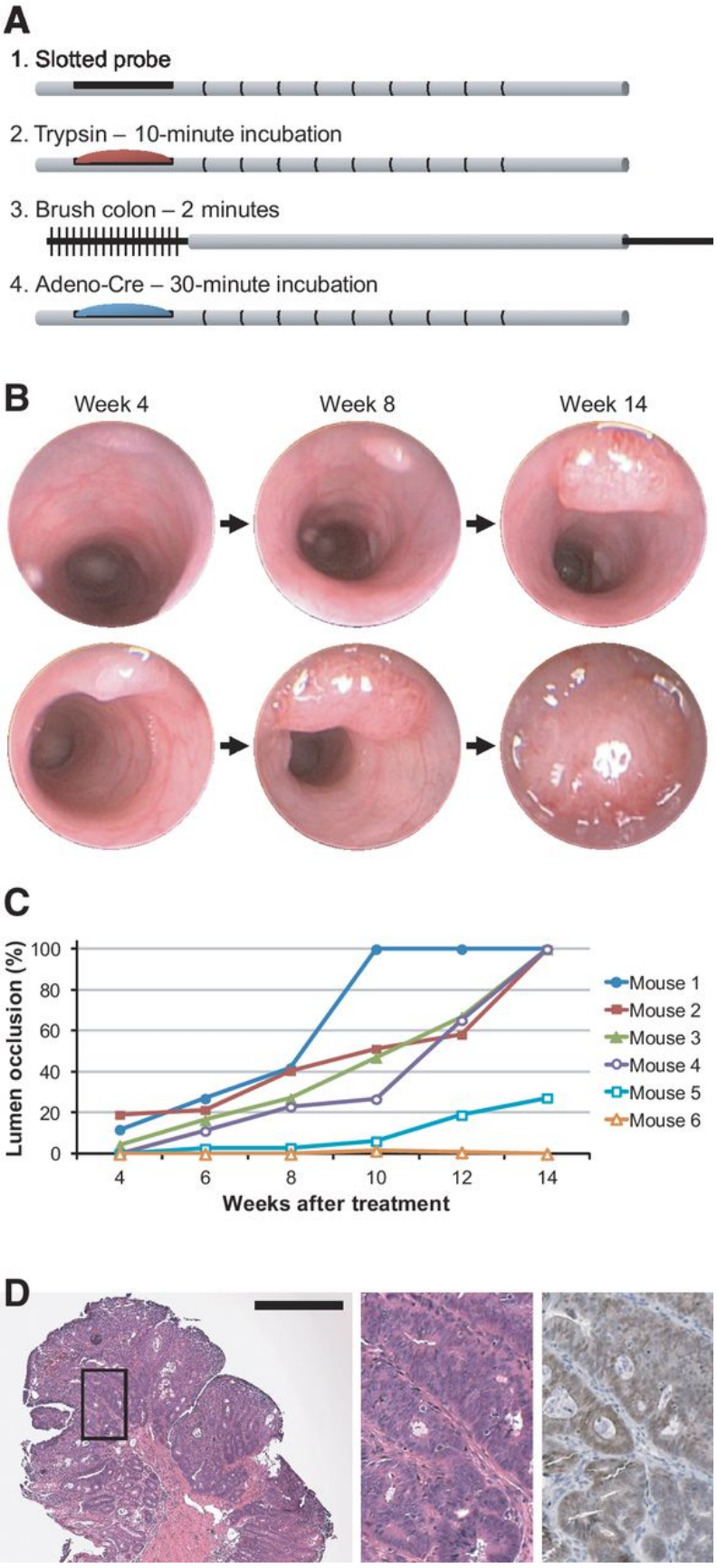
A
1. Slotted probe
2. Trypsin – 10-minute incubation
3. Brush colon – 2 minutes
4. Adeno-Cre – 30-minute incubation
B
Week 4
Week 8
Week 14
C
Lumen occlusion (%)
100
80
60
40
20
0
4
6
8
10
12
14
Weeks after treatment
Mouse 1
Mouse 2
Mouse 3
Mouse 4
Mouse 5
Mouse 6
D

Figure 2-12. A minimally invasive technique for inoculation of the colon with Adeno-Cre initiates tumorigenesis in *Apc*$^{fl/fl}$ mice. We have developed a novel technique that can be utilized to sequester Adeno-Cre within the colon without laparotomy, as was required with prior methodologies. (A) In this technique, a slotted tube housing GelFoam allows for the treatment of the colon with trypsin. Abrasion of the colon is then performed before incubation with Adeno-Cre–soaked GelFoam at the desired location. (B) Colon tumors are visualized by endoscopy within 3 to 7 weeks following treatment with Adeno-Cre and can be monitored over time with serial endoscopy. (C) Interestingly, these tumors have varying growth patterns over 14 weeks of observation, despite being induced in the same manner. (D) Histologic evaluation demonstrated that the majority (83%) of these lesions were adenomas with nuclear CTNNB1 consistent with activation of the WNT pathway. The area indicated by the rectangle is shown enlarged at the right; at the far right the same area in an adjacent slide stained for CTNNB1 is shown. Size bar = 1 mm.

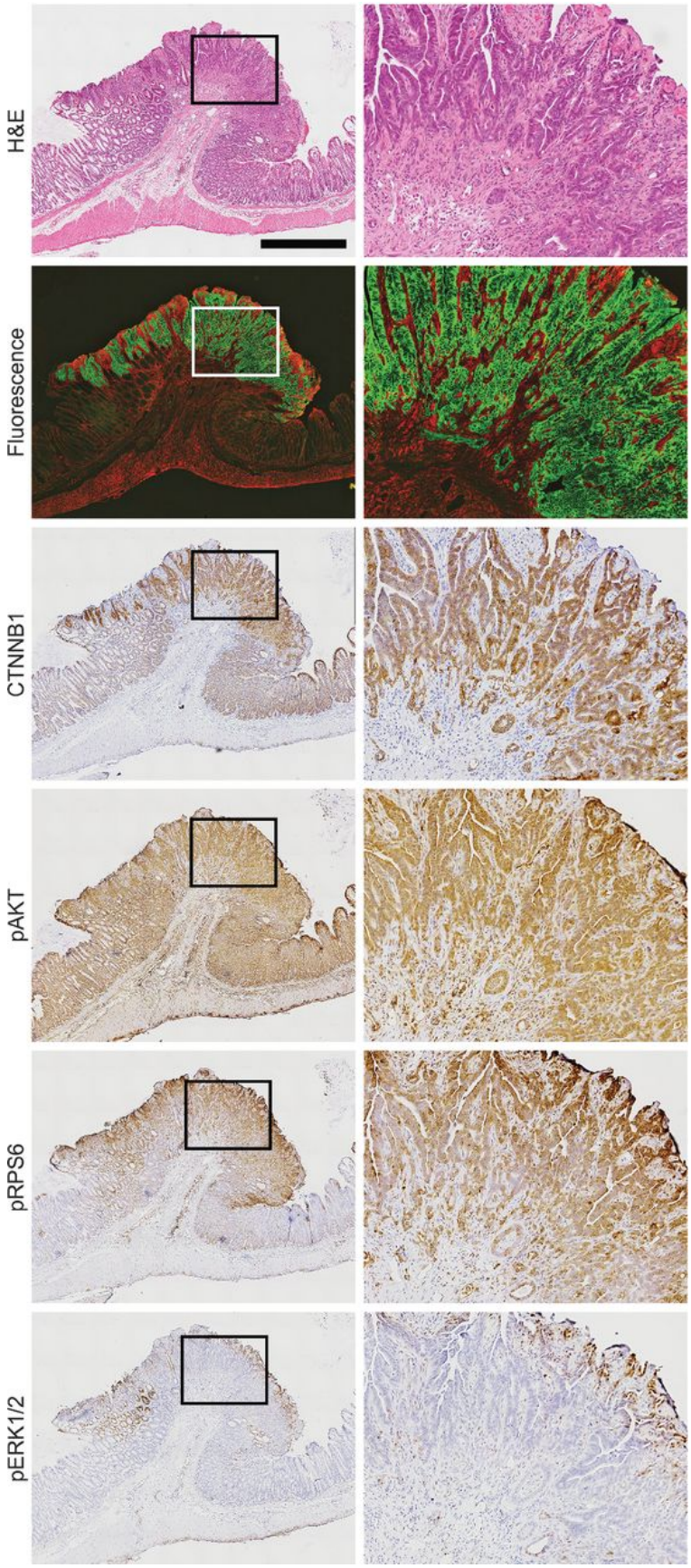
H&E
Fluorescence
CTNNB1
pAKT
pRPS6
pERK1/2

Figure 2-13. Multiple mutations were simultaneously expressed within the epithelium of the colon following a novel minimally invasive Adeno-Cre technique resulting in the development of colon tumors. To be certain that our mutations were being activated only in the epithelial cells of the colon with this technique, mT/mG^{+} *Apc*$^{fl/fl}$ Pik3ca*$^{+}$ mice were examined. Upon Cre recombination, a gene encoding a red fluorescent marker in these mice is excised and a green fluorescent protein is expressed. A representative histologic section is displayed demonstrating that Cre-mediated recombination has only occurred in the epithelial cells of these lesions. IHC confirmed CTNNB1 (β-catenin) localization to the nucleus and activation of the PI3K signaling cascade with intense staining for phosphorylated AKT (pAKT) and phosphorylated RPS6 (pRPS6), as expected. Activation of ERK1/2 was not observed in these tumors. The area indicated by each rectangle is shown enlarged at the right. Size bar = 1 mm.

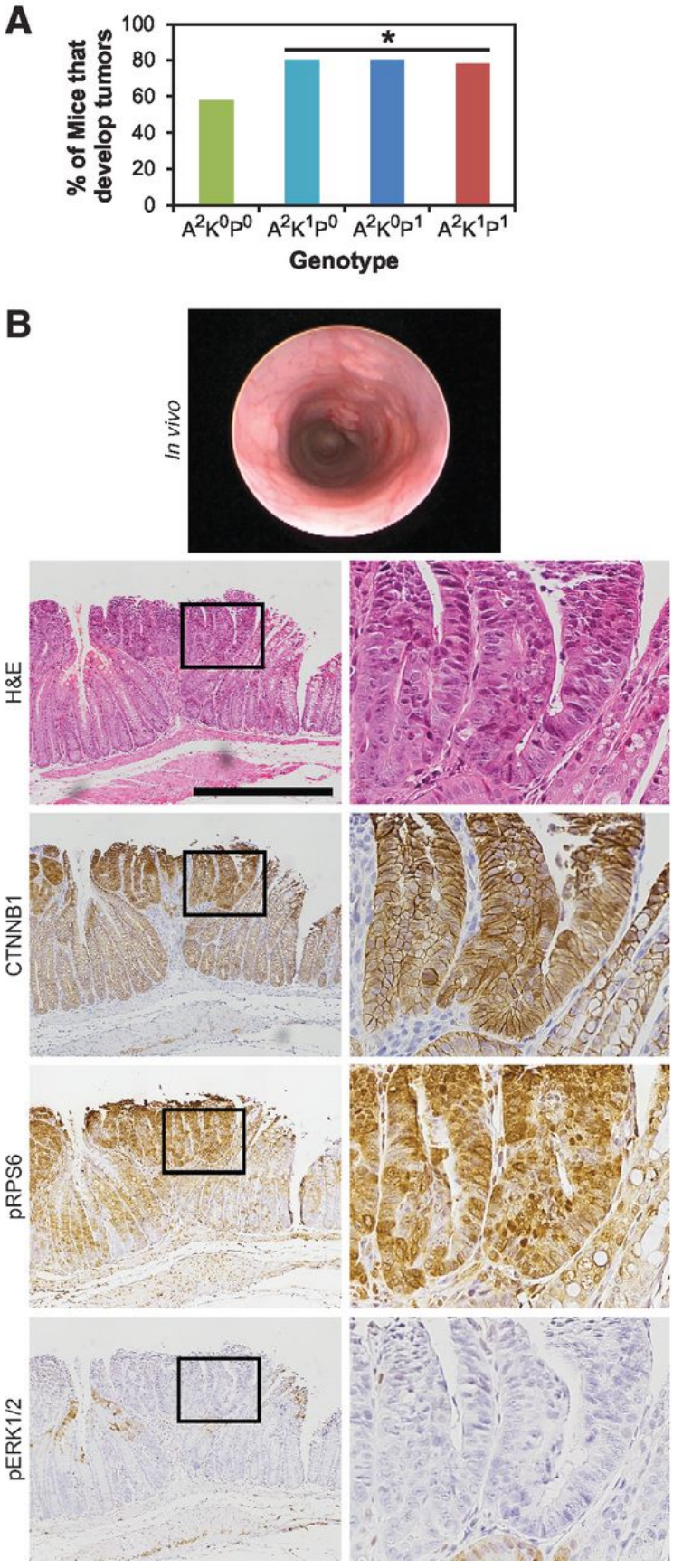
A
% of Mice that develop tumors
100
80
60
40
20
0
*
A2K0P0
A2K1P0
A2K0P1
A2K1P1
Genotype
B
In vivo
H&E
CTNNB1
pRPS6
pERK1/2

Figure 2-14. *Apc*$^{fl/fl}$ *Kras*$^{LSL\text{-}G12D/+}$ ($A^2K^1P^0$), *Apc*$^{fl/fl}$ Pik3ca*$^+$ ($A^2K^0P^1$), and *Apc*$^{fl/fl}$ *Kras*$^{LSL\text{-}G12D/+}$ Pik3ca*$^+$ ($A^2K^1P^1$) mice were treated with Adeno-Cre at 40 to 50 days of age. (A) Incidence of tumors increases with the addition of *Kras*$^{LSL\text{-}G12D/+}$ and/or Pik3ca*$^+$ to the mutation profile [due to the relatively small sample sizes and the similar tumor incidence rates among *Apc*$^{fl/fl}$ *Kras*$^{LSL\text{-}G12D/+}$, *Apc*$^{fl/fl}$ Pik3ca*$^+$, and *Apc*$^{fl/fl}$ *Kras*$^{LSL\text{-}G12D/+}$ Pik3ca*$^+$ mice, the tumor incidence data from these strains were pooled (31/39) for comparison with *Apc*$^{fl/fl}$ ($A^2K^0P^0$) (18/31); *P* (one-sided) = 0.031, Barnard exact test]. (B) Tumors were identified by endoscopy in the colon as early as 3 to 4 weeks after viral inoculation. Histologic sectioning was performed on tumors shortly after identification on endoscopy revealing that these lesions were small adenomas without evidence of invasion into the muscularis mucosa. An adenoma from an *Apc*$^{fl/fl}$ Pik3ca*$^+$ mouse is shown here. Nuclear localization of CTNNB1 and phosphorylation of RPS6 were observed without phosphorylation of ERK1/2 indicating that recombination was occurring as expected. The area indicated by each rectangle is shown enlarged at the right. Size bar = 500 μm.

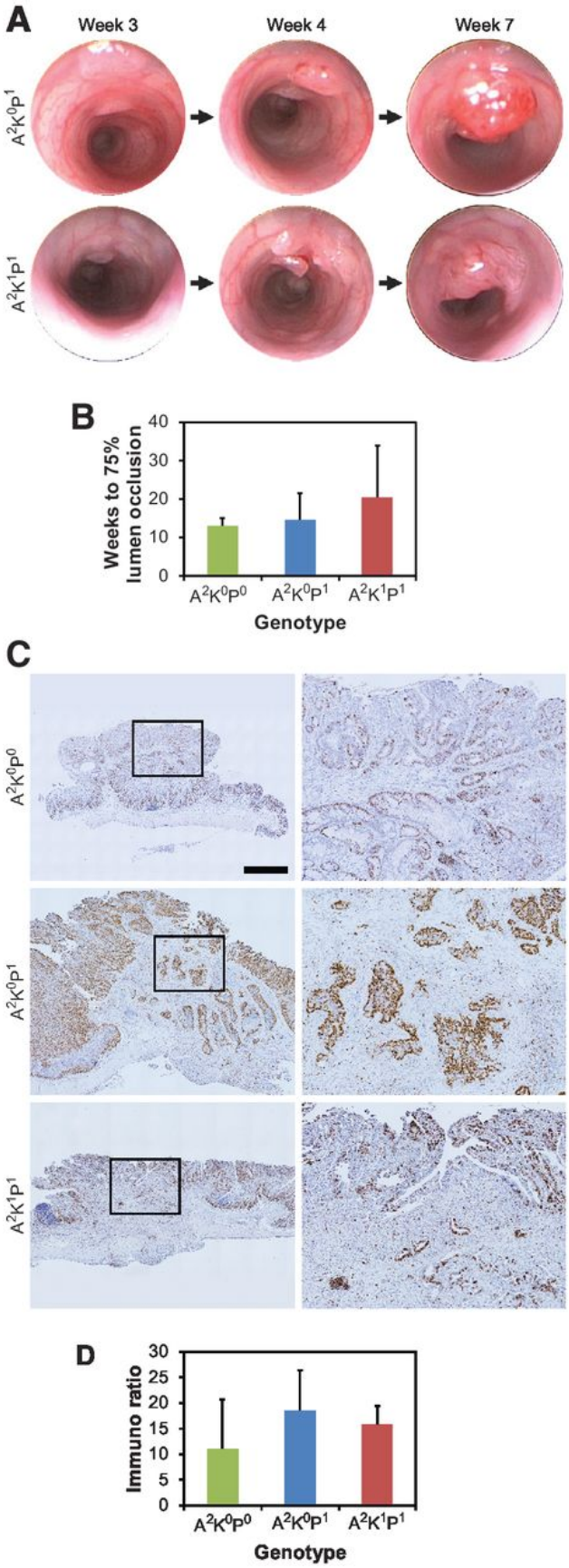
A
Week 3
Week 4
Week 7
A2K0P1
A2K1P1
B
Weeks to 75% lumen occlusion
40
30
20
10
0
A2K0P0
A2K0P1
A2K1P1
Genotype
C
A2K0P0
A2K0P1
A2K1P1
D
Immuno ratio
30
25
20
15
10
5
0
A2K0P0
A2K0P1
A2K1P1
Genotype

Figure 2-15. The addition of *Kras* and *Pik3ca* mutations to the loss of APC has a modest effect on tumor proliferation. (A) $Apc^{fl/fl}$ ($A^2K^0P^0$), $Apc^{fl/fl}$ Pik3ca*$^+$ ($A^2K^0P^1$), and $Apc^{fl/fl}$ $Kras^{LSL\text{-}G12D/+}$ Pik3ca*$^+$ ($A^2K^1P^1$) mice were treated with Adeno-Cre and followed with serial endoscopy. (B) Change in percent lumen occlusion was used as a marker of tumor proliferation. The time required for tumors to occlude 75% of the lumen was determined. No difference was seen among groups. (C) To confirm these results these tumors were sectioned and stained for Ki-67. The Ki-67 proliferation index was calculated for each tumor. (D) No statistically significant increase in Ki-67 staining was observed when additional mutations occurred concomitantly with loss of APC ($P = 0.35$, Kruskal–Wallis test). The area indicated by each rectangle is shown enlarged at the right. Size bar = 1 mm.

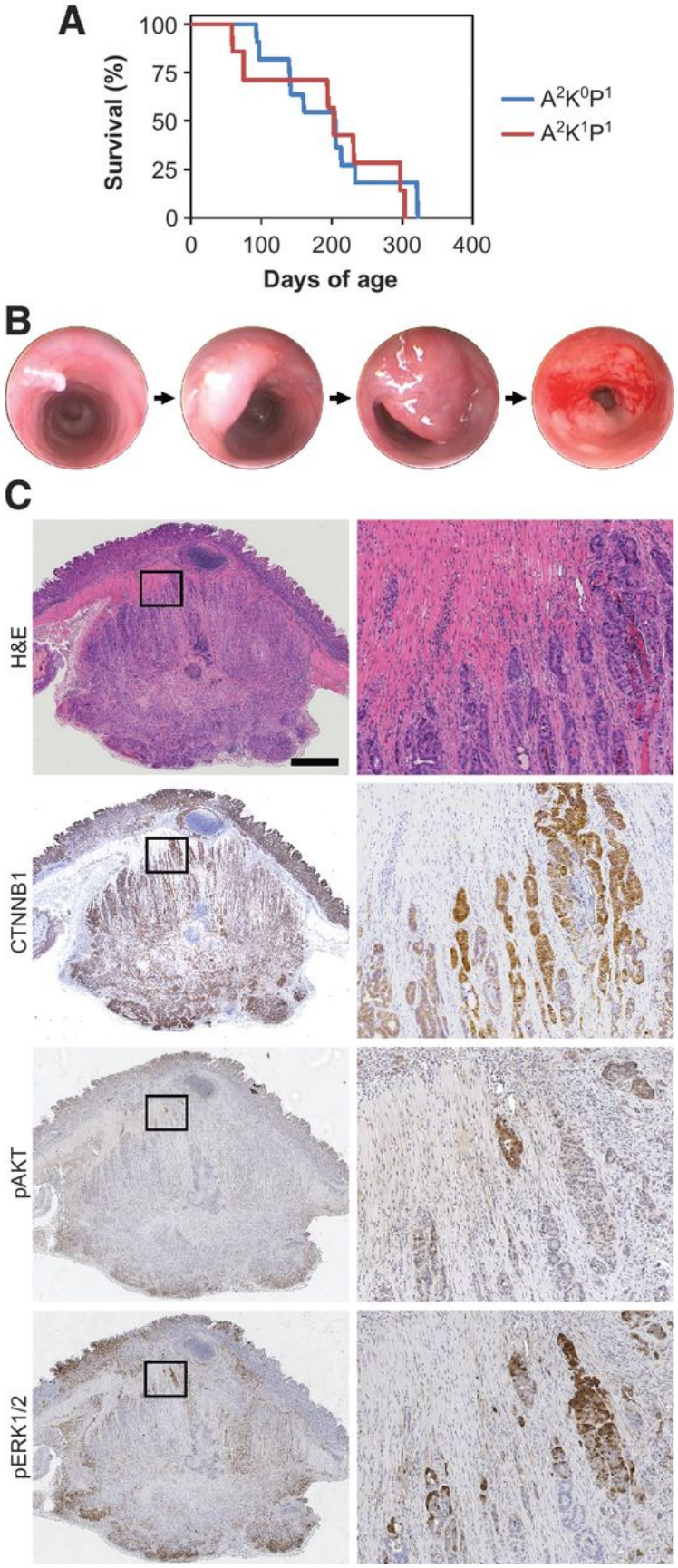
A
Survival (%)
100
75
50
25
0
0
100
200
300
400
Days of age
A2K0P1
A2K1P1
B
C
H&E
CTNNB1
pAKT
pERK1/2

Figure 2-16. Tumors with multiple driver mutations present at the time of initiation progressed through the adenoma to carcinoma sequence. *Apc*$^{fl/fl}$ Pik3ca*$^{+}$ ($A^2K^0P^1$) and *Apc*$^{fl/fl}$ *Kras*$^{LSL\text{-}G12D/+}$ Pik3ca*$^{+}$ ($A^2K^1P^1$) mice were treated with Adeno-Cre, as described, at 40 to 50 days of age and aged until moribund. (A) No difference in survival between these two groups was noted. (B) The resulting tumors were followed with serial endoscopy; they developed initially as polypoid lesions within the colon and progressed to occlude the majority of the lumen. These tumors could be followed as long as 12 months after viral inoculation and developed into "apple-core" lesions, as seen in the far right photo, similar to advanced colorectal tumors in humans. These mice became moribund due to anemia or intestinal obstruction. At necropsy, large colon tumors approached 1 cm in diameter. (C) Upon histologic analysis, these lesions were invasive adenocarcinomas penetrating through muscularis propria and into the serosa in many instances. H&E staining of a large invasive cancer from an *Apc*$^{fl/fl}$ *Kras*$^{LSL\text{-}G12D/+}$ Pik3ca*$^{+}$ ($A^2K^1P^1$) mouse is shown. Nuclear localization of CTNNB1 and activation of AKT and ERK1/2 signaling were observed. The area indicated by each rectangle shown enlarged at the right. Scale bar = 1 mm.

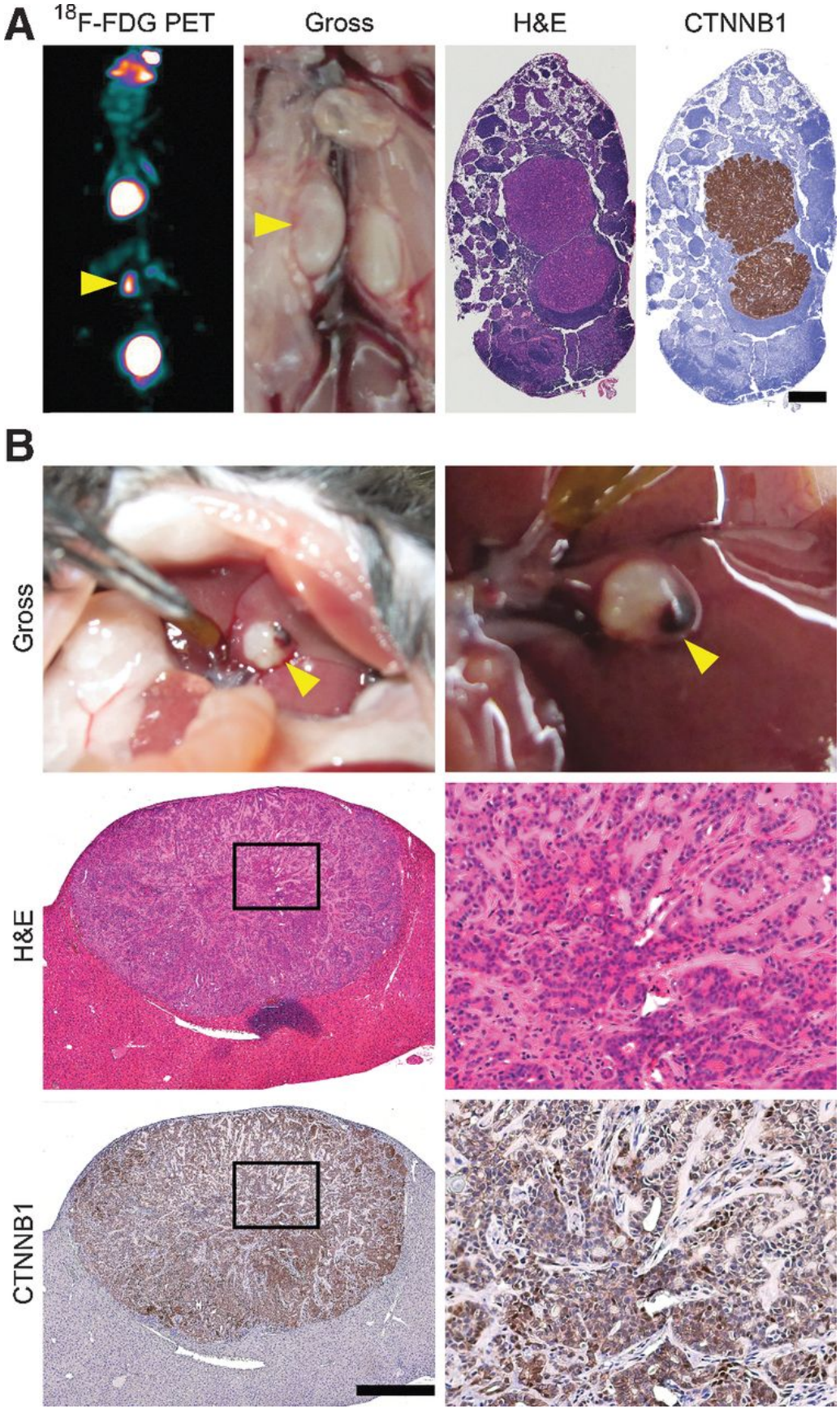
A
18F-FDG PET
Gross
H&E
CTNNB1
B
Gross
H&E
CTNNB1

Figure 2-17. Metastatic colon adenocarcinoma was identified within Adeno-Cre treated mice. An *Apc*$^{fl/fl}$ *Kras*$^{LSL\text{-}G12D/+}$ Pik3ca*$^{+}$ mouse became moribund after treatment with Adeno-Cre. (A) ^{18}F-FDG PET imaging demonstrated an avid para-arotic lymph node in addition to increased avidity of the primary tumor. Enlarged adenopathy was identified at necropsy. On histologic sectioning, well-differentiated adenocarcinoma consistent with the colon primary tumor was observed. Staining for CTNNB1 demonstrated nuclear localization consistent with loss of APC. (B) In addition, metastatic adenocarcinoma in the liver was identified in a moribund Adeno-Cre–treated *Apc*$^{fl/fl}$ Pik3ca*$^{+}$ mouse. A hepatic mass was observed grossly. H&E staining of histologic sections demonstrated a well-differentiated adenocarcinoma arising within the liver. Staining demonstrated nuclear localization of CTNNB1 consistent with the primary colon tumor. The area indicated by each rectangle in photos of stained sections is shown enlarged at the right. Size bars, 500 μm.

References

1. Sottoriva, A. *et al.* A Big Bang model of human colorectal tumor growth. *Nat Genet* **47,** 209–216 (2015).
2. Fearon, E. R. & Vogelstein, B. A genetic model for colorectal tumorigenesis. *Cell* **61,** 759–767 (1990).
3. Kosmidou, V. *et al.* Tumor Heterogeneity Revealed by *KRAS*, *BRAF*, and *PIK3CA* Pyrosequencing: *KRAS* and *PIK3CA* Intratumor Mutation Profile Differences and Their Therapeutic Implications. *Human Mutat* **35,** 329–340 (2014).
4. Haigis, K. M. *et al.* Differential effects of oncogenic K-Ras and N-Ras on proliferation, differentiation and tumor progression in the colon. *Nat Genet* **40,** 600–608 (2008).
5. Vivanco, I. & Sawyers, C. L. The phosphatidylinositol 3-Kinase–AKT pathway in human cancer. *Nat. Rev. Cancer.* **2,** 489–501 (2002).
6. Samuels, Y. High Frequency of Mutations of the *PIK3CA* Gene in Human Cancers. *Science* **304,** 554–554 (2004).
7. Zhao, L. & Vogt, P. K. Hot-spot mutations in p110α of phosphatidylinositol 3-kinase (PI3K): Differential interactions with the regulatory subunit p85 and with RAS. *Cell Cycle* **9,** 596–600 (2014).
8. Srinivasan, L. *et al.* PI3 Kinase Signals BCR-Dependent Mature B Cell Survival. *Cell* **139,** 573–586 (2009).
9. Klippel, A. *et al.* Membrane localization of phosphatidylinositol 3-kinase is sufficient to activate multiple signal-transducing kinase pathways. *Mol Cell Biol* **16,** 4117–4127 (1996).
10. Pinchuk, A. N. *et al.* Synthesis and Structure−Activity Relationship Effects on the Tumor

Avidity of Radioiodinated Phospholipid Ether Analogues. *J Med Chem* **49,** 2155–2165 (2006).

11. Chu, P. G. & Weiss, L. M. Keratin expression in human tissues and neoplasms. *Histopathology* **40,** 403–439 (2002).
12. Powell, S. M. *et al.* APC mutations occur early during colorectal tumorigenesis. *Nature* **359,** 235–237 (1992).
13. Nozoe, T., Anai, H., Nasu, S. & Sugimachi, K. Clinicopathological characteristics of mucinous carcinoma of the colon and rectum. *J Surg Oncol* **75,** 103–107 (2000).
14. Genome, W. T. Wellcome Trust Sanger Institute Cancer Genome Project. at <http://www.sanger.ac.uk/genetics/CGP>
15. Nosho, K. *et al. PIK3CA* Mutation in Colorectal Cancer: Relationship with Genetic and Epigenetic Alterations. *Neoplasia* **10,** 534–541 (2008).
16. Claper, M. L., Cooper, H. S. & Chang, W.-C. L. Dextran sulfate sodium-induced colitis-associated neoplasia: a promising model for the development of chemopreventive interventions. *Acta Pharmacologica Sinica* **28,** 1450–1459 (2007).
17. Saam, J. R. & Gordon, J. I. Inducible gene knockouts in the small intestinal and colonic epithelium. *J Biol Chem* **274,** 38071–38082 (1999).
18. Su, L. K. *et al.* Multiple intestinal neoplasia caused by a mutation in the murine homolog of the APC gene. *Science* **256,** 668–670 (1992).
19. Durkee, B. Y. *et al.* Reproducibility of Tumor Volume Measurement at MicroCT Colonography in Living Mice. *Acad Radiol* **15,** 334–341 (2008).
20. Tarver, T. Cancer Facts & Figures 2012. American Cancer Society (ACS). *J Consum Health Internet* **16,** 366–367 (2012).

21. Muzny, D. M. *et al.* Comprehensive molecular characterization of human colon and rectal cancer. *Nature* **487,** 330–337 (2012).

22. Kinzler, K. W. & Vogelstein, B. in *The Genetic Basis of Human Cancer* (eds. Vogelstein, B. & Kinzler, K. W.) 583–612 (2002).

23. Goss, K. H. & Groden, J. in *Encyclopedia of Cancer* 143–151 (Elsevier, 2002). doi:10.1016/B0-12-227555-1/00015-0

24. Clevers, H. & Nusse, R. Wnt/β-Catenin Signaling and Disease. *Cell* **149,** 1192–1205 (2012).

25. Markowitz, S. D. & Bertagnolli, M. M. Molecular Basis of Colorectal Cancer. *N Engl J Med* **361,** 2449–2460 (2009).

26. Desbois-Mouthon, C. *et al.* Insulin and IGF-1 stimulate the β-catenin pathway through two signalling cascades involving GSK-3β inhibition and Ras activation. *Oncogene* **20,** 252–259 (2001).

27. Fukumoto, S. *et al.* Akt Participation in the Wnt Signaling Pathway through Dishevelled. *J Biol Chem* **276,** 17479–17483 (2001).

28. Naito, A. T. Phosphatidylinositol 3-Kinase-Akt Pathway Plays a Critical Role in Early Cardiomyogenesis by Regulating Canonical Wnt Signaling. *Circ Res* **97,** 144–151 (2005).

29. Fang, D. *et al.* Phosphorylation of beta-Catenin by AKT Promotes beta-Catenin Transcriptional Activity. *J Biol Chem* **282,** 11221–11229 (2007).

30. Ding, V. W., Chen, R. H. & McCormick, F. Differential Regulation of Glycogen Synthase Kinase 3 by Insulin and Wnt Signaling. *J Biol Chem* **275,** 32475–32481 (2000).

31. Ng, S. S. *et al.* Phosphatidylinositol 3-Kinase Signaling Does Not Activate the Wnt Cascade. *J Biol Chem* **284,** 35308–35313 (2009).

32. Guetz, Des, G. *et al.* Does microsatellite instability predict the efficacy of adjuvant chemotherapy in colorectal cancer? A systematic review with meta-analysis. *European Journal of Cancer* **45,** 1890–1896 (2009).

33. Bacher, J. W., Abdel Megid, W. M., Kent-First, M. G. & Halberg, R. B. Use of mononucleotide repeat markers for detection of microsatellite instability in mouse tumors. *Mol Carcinog* **44,** 285–292 (2005).

34. Tanwar, P. S., Zhang, L., Roberts, D. J. & Teixeira, J. M. Stromal Deletion of the APC Tumor Suppressor in Mice Triggers Development of Endometrial Cancer. *Cancer Res.* **71,** 1584–1596 (2011).

35. Hung, K. E. *et al.* Development of a mouse model for sporadic and metastatic colon tumors and its use in assessing drug treatment. *Proc Natl Acad Sci U S A.* **107,** 1565–1570 (2010).

36. Liao, X. *et al.* Aspirin Use, Tumor PIK3CAMutation, and Colorectal-Cancer Survival. *N Engl J Med* **367,** 1596–1606 (2012).

37. Armaghany, T., Wilson, J. D., Chu, Q. & Mills, G. Genetic Alterations in Colorectal Cancer. *Gastrointest Cancer Res* 19–27 (2012).

38. Whitehall, V. L. J. *et al.* Oncogenic *PIK3CA* mutations in colorectal cancers and polyps. *Int J Cancer* **131,** 813–820 (2011).

39. Velho, S. *et al. BRAF*, *KRAS* and *PIK3CA* mutations in colorectal serrated polyps and cancer: Primary or secondary genetic events in colorectal carcinogenesis? *BMC Cancer* **8,** 255 (2008).

40. Doble, B. W. GSK-3: tricks of the trade for a multi-tasking kinase. *J Cell Sci* **116,** 1175–1186 (2003).

41. Frame, S., Cohen, P. & Biondi, R. M. A Common Phosphate Binding Site Explains the Unique Substrate Specificity of GSK3 and Its Inactivation by Phosphorylation. *Mol Cell* **7,** 1321–1327 (2001).

42. Hinoi, T. *et al.* Complex Formation of Adenomatous Polyposis Coli Gene Product and Axin Facilitates Glycogen Synthase Kinase-3-dependent Phosphorylation of β-Catenin and Down-regulates β-Catenin. *J Biol Chem* **275,** 34399–34406 (2000).

43. Cross, D. A. E., Alessi, D. R., Cohen, P., Andjelkovich, M. & Hemmings, B. A. Inhibition of glycogen synthase kinase-3 by insulin mediated by protein kinase B. *Nature* **378,** 785–789 (1995).

44. Boland, C. R. *et al.* A National Cancer Institute Workshop on Microsatellite Instability for cancer detection and familial predisposition: development of international criteria for the determination of microsatellite instability in colorectal cancer. in **58,** 5248–5257 (1998).

45. American Cancer Society. Cancer Facts & Figures 2014. *American Cancer Society* (2014).

46. Nowell, P. The clonal evolution of tumor cell populations. *Science* **194,** 23–28 (1976).

47. Kinzler, K. W. & Vogelstein, B. Gatekeepers and caretakers. *Nature* **386,** 761–763 (1997).

48. Segditsas, S. & Tomlinson, I. Colorectal cancer and genetic alterations in the Wnt pathway. *Oncogene* **25,** 7531–7537 (2006).

49. Parsons, B. L. *et al.* ACB-PCR Quantification of K- RAS Codon 12 GAT and GTT Mutant Fraction in Colon Tumor and Non-Tumor Tissue. *Cancer Invest* **28,** 364–375 (2010).

50. Smith, G. *et al.* Mutations in APC, Kirsten-ras, and p53--alternative genetic pathways to colorectal cancer. *Proc Natl Acad Sci U S A* **99,** 9433–9438 (2002).

51. Sweetser, S., Smyrk, T. C. & Sinicrope, F. A. Serrated Colon Polyps as Precursors to Colorectal Cancer. *Clin Gastroenterol and Hepatol* **11,** 760–767 (2013).

52. Tang, R. Colorectal cancer without high microsatellite instability and chromosomal instability--an alternative genetic pathway to human colorectal cancer. *Carcinogenesis* **25,** 841–846 (2003).

53. Imperiale, T. F., Ransohoff, D. F., Itzkowitz, S. H., Turnbull, B. A. & Ross, M. E. Fecal DNA versus Fecal Occult Blood for Colorectal-Cancer Screening in an Average-Risk Population. *N Engl J Med* **351,** 2704–2714 (2004).

54. Tomasetti, C., Vogelstein, B. & Parmigiani, G. Half or more of the somatic mutations in cancers of self-renewing tissues originate prior to tumor initiation. *Proc Natl Acad Sci U S A* **110,** 1999–2004 (2013).

55. Halberg, R. B. *et al.* Long-lived Min Mice Develop Advanced Intestinal Cancers through a Genetically Conservative Pathway. *Cancer Res* **69,** 5768–5775 (2009).

56. Halberg, R. B. *et al.* Tumorigenesis in the multiple intestinal neoplasia mouse: Redundancy of negative regulators and specificity of modifiers. *Proc Natl Acad Sci U S A* **97,** 3461–3466 (2000).

57. Moser, A., Pitot, H. & Dove, W. A dominant mutation that predisposes to multiple intestinal neoplasia in the mouse. *Science* **247,** 322–324 (1990).

58. Janssen, K. P. *et al.* APC and Oncogenic KRAS Are Synergistic in Enhancing Wnt Signaling in Intestinal Tumor Formation and Progression. *Gastroenterology* **131,** 1096–1109 (2006).

59. Jackson, E. L. Analysis of lung tumor initiation and progression using conditional expression of oncogenic K-ras. *Genes & Development* **15,** 3243–3248 (2001).

60. Abramovitch, R., Marikovsky, M., Meir, G. & Neeman, M. Stimulation of tumour growth by wound-derived growth factors. *Br J Cancer* **79,** 1392–1398 (1999).

61. Kuraguchi, M. *et al.* Adenomatous Polyposis Coli (APC) Is Required for Normal Development of Skin and Thymus. *PLoS Genet* **2,** e146 (2006).

62. Schek, R. Delivery and Protection of Adenoviruses Using Biocompatible Hydrogels for Localized Gene Therapy. *Mol Therapy* **9,** 130–138 (2004).

63. Hu, W.-W., Wang, Z., Hollister, S. J. & Krebsbach, P. H. Localized viral vector delivery to enhance in situ regenerative gene therapy. *Gene Ther* **14,** 891–901 (2007).

64. Dai, Q., Manfield, L., Wang, Y. & Murrell, G. A. C. Adenovirus-mediated gene transfer to healing tendon—enhanced efficiency using a gelatin sponge. *J Orthop Res* **21,** 604–609 (2006).

65. Siemens, D. R. *et al.* Cutting Edge: Restoration of the Ability to Generate CTL in Mice Immune to Adenovirus by Delivery of Virus in a Collagen-Based Matrix. *J Immunol* **166,** 731–735 (2001).

66. Paul Olson, T. J. *et al.* Dynamic tumor growth patterns in a novel murine model of colorectal cancer. *Cancer Prev Res (Phila)* **7,** 105–113 (2014).

67. Rubin, E. M. & Raptopoulos, V. D. The Virtual Apple Core of a Colonic Carcinoma. *N Engl J Med* **352,** 2733–2733 (2005).

68. Samowitz, W. S. *et al.* APC Mutations and Other Genetic and Epigenetic Changes in Colon Cancer. *Mol Cancer Res* **5,** 165–170 (2007).

69. Harada, N. Intestinal polyposis in mice with a dominant stable mutation of the beta - catenin gene. *The EMBO Journal* **18,** 5931–5942 (1999).

70. Loeve, F. *et al.* National Polyp Study data: Evidence for regression of adenomas. *Int J*

Cancer **111,** 633–639 (2004).

71. MD, D. P. J. P. *et al.* Assessment of volumetric growth rates of small colorectal polyps with CT colonography: a longitudinal study of natural history. *Lancet Oncology* **14,** 711–720 (2013).

72. Pritchard, C. C. & Grady, W. M. Colorectal cancer molecular biology moves into clinical practice. *Gut* **60,** 116–129 (2010).

73. Jones, S. *et al.* Comparative lesion sequencing provides insights into tumor evolution. *Proc Natl Acad Sci U S A* **105,** 4283–4288 (2008).

74. Wood, L. D. *et al.* The genomic landscapes of human breast and colorectal cancers. *Science* **318,** 1108–1113 (2007).

75. Yamada, S., Yashiro, M., Maeda, K., Nishiguchi, Y. & Hirakawa, K. A novel high-specificity approach for colorectal neoplasia: Detection of K-ras2 oncogene mutation in normal mucosa. *Int J Cancer* **113,** 1015–1021 (2004).

76. Smith, K. J. *et al.* The APC gene product in normal and tumor cells. *Proc Natl Acad Sci U S A* **90,** 2846–2850 (1993).

77. Bozic, I. *et al.* Accumulation of driver and passenger mutations during tumor progression. *Proc Natl Acad Sci U S A* **107,** 18545–18550 (2010).

78. Vogelstein, B. *et al.* Cancer Genome Landscapes. *Science* **339,** 1546–1558 (2013).

79. Hanahan, D. & Weinberg, R. A. The Hallmarks of Cancer. *Cell* **100,** 57–70 (2000).

80. Muzumdar, M. D., Tasic, B., Miyamichi, K., Li, L. & Luo, L. A global double-fluorescent Cre reporter mouse. *Carcinogenesis* **45,** 593–605 (2007).

81. Wong, M. H., Saam, J. R., Stappenbeck, T. S., Rexer, C. H. & Gordon, J. I. Genetic mosaic analysis based on Cre recombinase and navigated laser capture microdissection.

Proc Natl Acad Sci U S A **97,** 12601–12606 (2000).

82. Becker, C. In vivo imaging of colitis and colon cancer development in mice using high resolution chromoendoscopy. *Gut* **54,** 950–954 (2005).

83. Pickhardt, P. J. *et al.* Microcomputed tomography colonography for polyp detection in an in vivo mouse tumor model. *Proc Natl Acad Sci U S A* **102,** 3419–3422 (2005).

CHAPTER 3

Genetically distinct tumor-founding cells can contribute to tumor initiation, growth, and progression.

Preface

Tumor heterogeneity contributes to chemotherapy resistance and is predictive of a poor clinical prognosis[1-7]. Numerous studies report spatial and temporal heterogeneity between cellular genomes and transcriptomes. However, it remains unclear when tumor heterogeneity arises, what role it plays in early tumor development and evolution, and precisely how it contributes to a poor clinical prognosis.

Multi-ancestral tumors are heterogeneous at the time of tumor initiation due to the presence of multiple transformed tumor-founding cells. The first part of this chapter establishes that multiple ancestral clones can be maintained for a long period of time as a tumor forms and progresses to cancer. The second part of this chapter utilizes the strong tumor driver described in Chapter 2 to show that multi-ancestral tumors form even in the presence of a clinically relevant tumor driver, and that these multiple ancestral clones are not only maintained as the tumor progresses to cancer but might in fact cooperate to accelerate invasion.

3.1 Advanced intestinal cancers often maintain a multi-ancestral architecture.

Christopher D. Zahm, Joseph M. Szulczewski, **Alyssa A. Leystra**, Terrah J. Paul Olson, Linda Clipson, Dawn M. Albrecht, Malisa Middlebrooks, Andrew T. Thliveris, Kristina A. Matkowskyj, Mary Kay Washington, Michael A. Newton, Kevin W. Eliceiri, Richard B. Halberg.

Abstract

A widely accepted paradigm in the field of cancer biology is that solid tumors are uni-ancestral being derived from a single tumor-founding cell and its descendants. However, data have been steadily accruing that indicate early tumors in mice and humans can have a multi-ancestral origin in which a tumor-founding cell facilitates the transformation of neighboring cells. We developed a new mouse model that permits the determination of clonal architecture of intestinal tumors *in vivo* and *ex vivo*, have validated this model, and then used it to assess the clonal architecture of adenomas, intramucosal carcinomas, and invasive adenocarcinomas of the intestine. The percentage of multi-ancestral tumors did not significantly change as tumors progressed from adenomas with low-grade dysplasia [40/65 (62%)], to adenomas with high-grade dysplasia [21/37 (57%)], to intramucosal carcinomas [10/23 (43%]), to invasive adenocarcinomas [13/19 (68%)], indicating that the clone arising from the recruiting tumor-founding cell continues to coexist with clones arising from recruited ancestral clones. Moreover, neoplastic cells from distinct clones within a multi-ancestral adenocarcinoma have even been observed to simultaneously invade into the underlying musculature [2/15 (13%)]. Thus, intratumoral heterogeneity arising early in tumor formation persists throughout tumorigenesis.

Adapted from PLoS One; 11(2):e0150170. ©2016 Zahm et al.

In addition to reformatting, the following changes were made for the sake of consistency:

- Figures and references were renumbered
- Minor words were changed to improve readability and clarity

All animal models described in this paper are briefly defined in Appendix 1.

Authors' Contributions

C.D. Zahm and R.B.H were involved in all aspects of the research and preparation of the manuscript. J.M. Szulczewski assisted with three-dimensional imaging and analysis of tumors. A.A. Leystra assisted with animal husbandry, fluorescence endoscopy, necropsy, imaging of whole-mounted intestines, IHC, IF, sequencing of Apc, and interpretation of results. T.J. Paul Olson, D.M. Albrecht, and M. Middlebrooks provided technical support. K. A. Matkoskyj and M.K. Washington interpretation of histopathology. A.T. Thliveris and K.W. Eliceiri contributed critical reagents and analysis tools. L. Clipson assisted with figure and manuscript preparation. M.A. Newton performed patch-size analyses and provided statistical support. All authors discussed results and edited the manuscript.

Introduction

The heterogeneity of tumors has been recognized for decades. Neoplastic cells within a single tumor vary in several distinguishable properties including differentiation state, proliferation rate, metastatic potential, and therapeutic response. Historically, two models to

explain intratumoral heterogeneity were proposed. The clonal evolution model asserts that different subclones arise from a single tumor-founding cell as a consequence of molecular changes followed by selection for dissimilar microenvironments within a tumor[8]. In contrast, the cancer stem cell model contends that a small population of stem cells originating from a single tumor-founding cell is responsible for tumor maintenance but the progeny can differentiate in several diverse ways[8]. In both models, two key assumptions are that tumors are uni-ancestral, derived from a single tumor-founding cell, and that a subclone will eventually accumulate mutations that drive metastasis to other organs.

Data have been steadily accruing for a third model of intratumoral heterogeneity: solid tumors can have a multi-ancestral architecture[9]. We have demonstrated that hereditary and carcinogen-induced intestinal tumors in the laboratory mouse can be derived from multiple tumor-founding cells[10,11]. Our findings are consistent with those of another laboratory demonstrating that hereditary and sporadic colorectal tumors in humans can be multi-ancestral in architecture[12,13]. Thus, contrary to a widely accepted paradigm in the field of cancer biology, solid tumors can have a multi-ancestral origin and consequently be heterogeneous even as they just begin to form.

The initial studies with animal models primarily relied on aggregation chimeras. Such mice were generated by fusing together early embryos. Typically, one embryo carried the LacZ lineage marker that expresses β-galactosidase so that cells from this embryo stain blue in the presence of 5-bromo-4-chloro-3-indolyl-β-D-galactopyranoside, whereas cells from the other embryo remain white. Tumors that are heterotypic, composed of blue and white neoplastic cells, have a multi-ancestral origin. The use of aggregation chimeras has provided novel insights into the early stages of tumorigenesis. Unfortunately, this powerful experimental tool has some

significant limitations. The generation of aggregation chimeras is time consuming and expensive, so the number of animals analyzed is often low. The clonal architecture of any tumor can be determined only following a lengthy staining procedure that includes two fixation steps and an overnight incubation at 37°C. The staining is often incomplete since the substrate must diffuse into the tumor; consequently not all tumors can be scored. Moreover, the harsh conditions prohibit any subsequent molecular analysis.

In this study, we developed a new mouse model that allows the clonal architecture of intestinal tumors to be determined *in vivo* and *ex vivo*, validated this model, and then used it to determine the clonal architecture of intestinal cancers. The results support the concept that adenomas have a multi-ancestral origin and that this early diversity persists as tumors transition from a benign to malignant state.

Results

To study the clonal architecture of intestinal tumors, we generated mice carrying three genetic elements. The first two were transgenes that are necessary to establish a pattern of mosaicism in the intestine. One transgene consists of the rat fatty acid binding protein 1 promoter fused to the gene encoding Cre recombinase and the other has the mT/mG reporter. In cells that failed to express Cre, red fluorescent protein (tdTomato) was exclusively produced from the reporter even during intestinal tumorigenesis; in cells expressing Cre beginning at day E13.5 (prior to the completion of intestinal morphogenesis and before $Apc^{Min/+}$ tumor formation), green fluorescent protein (EGFP) was exclusively produced as the gene encoding the tdTomato was deleted following recombination. Thus, these two elements created a variegated pattern of cells expressing red or green fluorescent proteins in the distal small intestine, cecum and colon

(Appendix 5-1). This pattern was stable at all time-points assessed (Appendix 5-2). The third element was a single copy of the *Min* allele of the *Adenomatous polyposis coli* (*Apc*) gene[14]. This mutation predisposed the mice to the spontaneous development of tumors throughout the small intestine and colon. Since the reporter status is determined prior to tumors forming and Cre expression is stable during tumorigenesis, tumors consisting of a mixture of red and green neoplastic cells have a multi-ancestral architecture.

To characterize intestinal tumorigenesis in this model, a cohort of 20 mice was generated and euthanized at 150 days of age. The incidence of intestinal tumors was 100% with an average multiplicity of 11 ± 5. A low tumor burden was expected owing to the homogeneous F1 genetic background and was highly desirable as it limited the possibility of two independently initiated tumors coalescing as a consequence of spatial proximity[15]. All tumors from this group of mice that were analyzed were adenomas with low-grade dysplasia.

Many of the adenomas in these mice had a multi-ancestral architecture. The composition of colon tumors was evident *in vivo* by fluorescence endoscopy and *ex vivo* using fluorescent microscopy (Figure 3-1A and B). Of the 63 tumors in the distal small intestine and colon, 32 (51%) were confirmed to be composed of red and green neoplastic cells by histology (Figures 3-1C through 1F and Table 3-1). Features of transformation from normal mucosa to neoplasia/dysplasia were loss of crypt architecture, depletion of surface mucin, and increased mitosis as well as associated nuclear changes including crowding, stratification, elongation and hyperchromasia. In addition, the dysplastic red and green cells had an elevated level of CTNNB1 (β-catenin) and often this protein was localized to the nucleus confirming that cells in both lineages were neoplastic (Figure 3-1C through 1F). Finally, red and green neoplastic clones often carried unique mutations in *Apc* (Table 3-2 and Appendix 5-3), further indicating that these

clones are derived from different tumor-founding cells. Thus, this innovative mouse model is quite suitable for studying the clonal architecture of intestinal tumors. Moreover, an important advantage of this model is that the visualization of different lineages does not impede molecular analyses including immunohistochemistry and DNA sequencing.

The percentage of multi-ancestral tumors in mosaics was similar to the percentage observed in earlier studies with aggregation chimeras (Appendix 5-4; 40–52% in mosaics versus 22–47% in aggregation chimeras). This finding most likely reflects the fact that the patchwork of red and green cells in the distal small intestine and colon of our mosaic mice was comparable to the patchwork of blue and white cells observed in aggregation chimeras in previous studies (Appendix 5-4). All 165 tumors in the proximal small intestine were homotypic red (Table 3-1), as the rat fatty acid binding protein 1 promoter is hardly expressed in this region of the intestinal tract (Appendix 5-1). This observation indicates that the expression of fluorescent proteins from the reporter is stable during tumorigenesis. Because tumorigenesis does not lead to activation of Cre or mutations in the reporter, heterotypic tumors can accurately be determined to have a multi-ancestral structure. This approach can generally be applied to study the clonal architecture of tumors in other tissues, requiring only the use of a different transgene expressing Cre recombinase.

The multi-ancestral architecture of tumors was further confirmed via imaging. A total of five multi-ancestral adenomas were isolated, suspended in 2,2'-thiodiethanol (TDE) as the mounting medium to reduce scattering from lipids, and imaged with a multiphoton microscope. For each adenoma, the collected images were stitched together to generate a three-dimensional reconstruction. These data indicate that some tumors might be more complex than simply biclonal; the number of discrete colored regions ranged from two to four (Appendix 5-7). In one

predominantly red adenoma, three separate green areas could be seen, indicating that this tumor could be derived from four tumor-founding cells whether each clone arose from a unique initiating event (Figure 3-2). However, the preparation for imaging prevented us from being able to perform the sequencing studies that would allow us to determine if the separate green patches had different mutation profiles, which would provide further evidence of their origins.

The multi-ancestral architecture persists as tumors progress from benign to malignant states. A second cohort of mice was generated and allowed to age until moribund. The average age at death was 494 ± 93 days. The incidence of intestinal tumors was 100% with an average multiplicity of 15 ± 5, which was slightly higher than that observed in mice euthanized at 150 days of age ($p = 0.04$; Wilcoxon rank sum, two-sided). In the moribund mice, 16% of the tumors in the distal small intestine and colon were intramucosal carcinomas and 13% were invasive adenocarcinomas (Table 3-3). Similar to that observed in humans, intramucosal carcinomas exhibit neoplastic cell invasion into either the lamina propria or muscularis mucosa and can be associated with a desmoplastic response (Figure 3-3). Note that a previous study demonstrated that long-lived Min mice develop advanced disease even though the tumors exhibited little genetic instability[16]. For a lesion to be considered an invasive adenocarcinoma there had to be invasion of neoplastic cells beyond the muscularis mucosa at least into the submucosa. The neoplastic cells were often columnar in appearance with prominent nucleoli, had a cribriform architecture with back-to-back glands without intervening stroma, granular eosinophilic karyorrhectic debris present within the lumen of the gland, increased mitotic activity and associated with a desmoplastic response. A multi-ancestral architecture was observed in 62% of adenomas with low-grade dysplasia, 57% of adenomas with high-grade dysplasia, 43% of intramucosal carcinomas, and 68% of invasive adenocarcinomas (Table 3-3).

Malignant cells invading the submucosa and muscularis propria can even be derived from different tumor-founding cells. A total of 15 invasive adenocarcinomas from 10 mice were analyzed. Simultaneous invasion of red and green neoplastic cells was observed in 13%. This observation indicates that interactions among clones may persist even as tumors begin to invade from the submucosa into the muscularis propria.

Discussion

We generated a novel mouse model of colorectal cancer, performed validation studies to compare our findings with earlier experimental models, and then utilized the model to study the clonal architecture of malignant cancers in the intestine. The findings not only indicate that cancers are composed of cells derived from multiple tumor-founding cells but that cells from distinct origins can simultaneously invade into the colonic wall musculature. This discovery is contrary to the notion that all solid tumors are uni-ancestral and that a single subclone eventually acquires a selective advantage through epigenetic alterations or mutations and consequently metastasizes from the primary tumor to distant sites.

Our model was validated using several different approaches. The Fabp1-Cre transgene was selected because it is stably expressed in the distal small intestine, cecum, and colon during embryogenesis[17,18] and before tumorigenesis occurs in the $Apc^{Min/+}$ mouse. Consistent with this assertion, the crypts within the normal intestine were either wholly red in the absence of Cre expression or wholly green in the presence of Cre expression. Moreover, the pattern of mosaicism is similar in mice euthanized at 150 days of age and those killed when moribund, indicating that the pattern established early during embryogenesis is stable in adult mice (Appendix 5-2, -5, and 8). If Cre was spontaneously activated in different cells, the intestine

would progressively turn more green as mice age because green cells cannot be converted back into red. In both groups of mice, the proximal half of the intestinal tract was almost entirely red, whereas the distal half was a mixture of red and green with the colon being composed of 37.6% green cells in mice euthanized at 150 days and 38.1% green cells in mice euthanized when moribund ($p = 0.46$, t-test). All 165 tumors that formed in the proximal half of the small intestine and 24 of 63 tumors in the colon and distal half of the small intestine were homotypic red (Table 3-1). This observation indicates that Fabp1-Cre transgene is not aberrantly activated as a consequence of neoplastic transformation. Other tumors in the distal half of the intestinal tract were homotypic green or heterotypic. The percentage of heterotypic, or overtly multi-ancestral, tumors was similar to that observed in previous studies in which aggregation chimeras were employed (Appendix 5-4). The pattern of red and green neoplastic clones within a single tumor varies dramatically with red and green being highly intermingled in some tumors (Figure 3-1B). Such complex mixtures would be difficult to explain by the indeterminate expression of the Fabp1-Cre transgene within a single clone. Finally, within a heterotypic tumor, dysplastic crypts are wholly red or wholly green and distinct clones often carried a different *Apc* mutation (Table 3-2 and Appendix 5-3). Taken together, the data demonstrate that our new model is a powerful new tool for studying the clonal origin of intestinal tumors.

Early intestinal adenomas in mice and humans can have a multi-ancestral origin[9]. Many of the initial studies were performed utilizing aggregation chimeras in which two early embryos were fused together to generate a single animal. One embryo typically carried the LacZ lineage marker, whereas the other did not, so that cells from the two distinct lineages were distinguishable[19]. A significant number of intestinal adenomas were composed of cells from both lineages indicating those tumors were at least biclonal. Our new model enabled us to more

closely examine the number of clones contributing to a single tumor because the tumors can be reconstructed through *ex vivo* imaging using a multiphoton microscope. The number of separate areas, which are likely to be discrete clones, contributing to a single tumor ranged from two to four (Figure 3-2 and Appendix 5-7). This observation is consistent with two other studies that recently demonstrated that cells from three distinct lineages could contribute to a single intestinal tumor in the laboratory mouse[20,21].

Intratumoral heterogeneity appears to arise at the earliest stage of tumorigenesis. We recently reported that multi-ancestral tumors form as a consequence of recruitment in which a tumor-founding cell facilitates the transformation of of other cells (Appendix 7). Interactions among clones have been shown to occur at distances that encompass both first- and second-order neighboring crypts, about 18 crypts on average[10]. Fischer and colleagues recently demonstrated that a field of at least three Apc-deficient crypts is an important intermediate between loss of APC activity and adenoma formation[20]. This observation indicates that additional tumor-founding cells are not mere passengers in the tumor, but might actually facilitate tumorigenesis.

Recruited tumor-founding cells might already carry mutations in driver genes. Parsons and colleagues detected *KRAS* mutations in normal epithelial cells in the human colon[22]. These mutant cells might be more easily recruited to form a multi-ancestral tumor. Early intratumoral heterogeneity is consistent with the "Big Bang" model of tumorigenesis. Sottoriva and colleagues profiled 349 individual crypts from 15 colorectal tumors[23]. Based on their analysis, they proposed that tumors grow predominantly as a single expansion producing numerous intermixed subclones that are not subject to stringent selection with both clonal and subclonal alterations arising early. This work was further extended by Kang and colleagues who extensively analyzed a 6 cm colon tumor by measuring point mutations, chromosome copy

numbers, and DNA passenger methylation[24]. They concluded that multiple related clones arise within the first few divisions. Thus, the recruitment of additional tumor-founding cells with distinct mutation profiles to form a multi-ancestral tumor could further increase intratumoral heterogeneity. Additional studies are needed to further understand the number of ancestral clones present in a single tumor and the relationship among different clones.

Once a multi-ancestral tumor is established, our data indicate that multiple distinct clones persist as tumors progress. This finding complements that of one of the first studies to assess the clonal architecture of human colorectal cancers. In 1967, Beutler and colleagues analyzed a colorectal cancer and numerous liver metastases from an African American woman who was diagnosed in her twenties[25]. They found that the primary tumor and several metastases were derived from multiple ancestral clones. Thus, the clonal architecture might be a valuable predictor of response to therapeutic intervention, as heterogeneous tumors are more likely to be intrinsically resistant or acquire resistance.

Cells from distinct tumor-founding cells within a single tumor simultaneously invaded into the submucosa and muscularis propria. In our model, the cells have equal tumorigenic potential, although more homotypic red tumors were observed in the distal small intestine and colon than homotypic green tumors. Changes in tumor microenvironment that favor invasion could lead to cells from both lineages being present regardless of the invasive potential of any particular clone. However, if one clone gained a selective advantage over the other via mutation in any one of several key genes including *Kras*, *Pik3ca*, and *Tp53*, the dynamic might change such that only that clone invades. These possibilities could explain why not all metastases from the patient in the Beutler study were shown to be multi-ancestral. New mouse models coupled with state-of-the-art fluorescence will enable us to more fully understand how clonal architecture

can impact tumor growth, progression, and response to therapeutic intervention. We can generate mice with tumors that are composed of clones with different mutation profiles and monitor each clone over time to assess natural history or response to therapy. Such a study was not feasible with aggregation chimeras because the generation of mice with the proper genotype was challenging at best, e.g. the odds of fusing together embryos with desired alterations in two genes ranges from 1:16 to 1:256 depending on the breeding scheme and desired genotype.

Our new experimental system is a powerful tool to further our understanding of tumor origin, but it has limitations. First, the Fabp1-Cre transgene is activated early during embryogenesis and remains active throughout the life of the animal, so theoretically the expression pattern could change and cause a previously uni-ancestral tumor to become heterogeneous. However, we demonstrate that the pattern of expression does not change over time and that it is unaffected by tumorigenesis. Second, $Apc^{Min/+}$ mice have a shortened lifespan so tumors rarely metastasize to distant sites; therefore the clonal architecture of metastatic lesions cannot be determined. Third, in $Apc^{Min/+}$ mice, all cells in the entire organism carry one mutant allele of *Apc*. Such cells have altered properties including changes in proliferation, apoptosis, and migration[26]. We considered inducible systems including the Lgr5-CreERT2 transgene, which was developed and characterized by the laboratory of Dr. Hans Clevers[21]. However, with this system Cre is almost exclusively expressed in the small intestine and would leave us unable to assess the origins of colon tumors. The majority of human intestinal tumors form in the colon. Second, Lgr5-positive cells are thought to be at least a subpopulation of stem cells in the small intestine but it is unknown whether these cells are the only stem cells and the only cell type from which tumors arise. Third, inducing Cre expression in the intestine prior to the initiation of tumorigenesis in $Apc^{Min/+}$ mice would be challenging as pregnant females or

neonates would have to be treated with tamoxifen. In our experience, all (10/10) pregnant *Apc*$^{Min/+}$ females treated with tamoxifen lost their litters.

A widely accepted paradigm in the field of cancer biology has been that solid tumors are uni-ancestral and they transition from a benign to malignant states as subclones acquire epigenetic changes and mutations that drive progression. We demonstrated that early intestinal adenomas can be multi-ancestral arising from interactions among multiple ancestral clones. Our approach can be easily adapted to study the clonal architecture of tumors in other tissues, requiring only the tissue-specific, mosaic expression of Cre recombinase and a method to induce tumors. In addition, advances in sequencing are making the clonal analysis of human tumors quite feasible. Thus, a deeper understanding of clonal architecture is likely to impact cancer prevention, diagnosis, and treatment.

Materials and Methods

Mouse strains and generation of mosaic mice

Animal studies were conducted under protocols approved by the Institutional Animal Care and Use Committee at the University of Wisconsin in compliance with policies set by the Office of Laboratory Animal Welfare at the National Institutes of Health. C57BL/6J (B6), FVB/NJ (FVB), B6.ApcMin/J mice that were heterozygous for the *Min* allele of the *Adenomatous polyposis coli* gene (*Apc*$^{Min/+}$), and B6.129(Cg)-*Gt(ROSA)26Sor*$^{tm4(ACTB-tdTomato,-EGFP)Luo}$/J mice that were hemizygous for the mT/mG reporter were obtained from The Jackson Laboratory. FVB/N-Tg(Fabp1-Cre)1Jig mice hemizygous for the Fabp1-Cre transgene in which the promoter from the rat fatty acid binding protein is fused to the gene encoding Cre recombinase, resulting in mosaic expression of Cre prior to the completion of intestinal

morphogenesis, were obtained from the National Cancer Institute Mouse Repository at Frederick. Stocks of these strains were maintained by sibling crosses and backcrossing with B6 or FVB mice that were imported every fifth generation. Offspring were genotyped using DNA isolated from toe clips for PCR as described by the suppliers of animals.

A mouse carrying the *Min* allele of *Apc* was identified in the laboratory of Dr. William F. Dove at the University of Wisconsin following mutagenesis with ethylnitrosourea[14,27]. The founder and its progeny presented with pale feet owing to blood loss from tumors in the intestine[27]. Tumor multiplicity, growth, and progression in $Apc^{Min/+}$ mice are dependent on genetic background. B6 $Apc^{Min/+}$ mice develop on average 100 intestinal tumors and typically die by 150 days of age[27]. Tumors are initiated following the loss of APC activity in intestinal epithelial cells soon after birth and they are almost always benign adenomas[28-32]. By contrast, (SWRxB6) F1 $Apc^{Min/+}$ hybrids develop few tumors and typically live a year or more[16]. The tumors in these mice are often invasive cancers that occasionally metastasize to regional lymph nodes, presumably owing to the increased lifespan[16].

Experimental mice were generated by first crossing B6 mT/mG females to B6 $Apc^{Min/+}$ males to generate B6 $Apc^{Min/+}$; mT/mG^{+} mice that were then crossed to FVB Fabp1-Cre mice to generate (FVBxB6)F1 $Apc^{Min/+}$; $Fabp1\text{-}Cre^{+}$; mT/mG^{+} hybrids. Experimental F1 hybrids were allowed to age to 150 days or until moribund to assess the clonal architecture of tumors at different stages.

Fluorescence endoscopy

Fluorescence endoscopy was performed using a modified Karl Storz Coloview system as described previously[33,34]. Briefly, mice were anesthetized with isoflurane and given an enema of

warm PBS to clear any fecal material. The endoscope was inserted approximately four centimeters and then slowly withdrawn using an Optotronics diode-pumped solid-state laser set to 437nm at a power of 100mW as the light source. Video was collected during the entire procedure and still images were captured of each tumor. Mice were allowed to wake up after the procedure.

Videos and still images were processed with the Fiji package of ImageJ to visualize normal and dysplastic crypts expressing green fluorescent protein.

Imaging of whole-mounted intestines

The intestinal tracts were removed intact at necropsy, opened longitudinally, rinsed with PBS, fixed in 4% paraformaldehyde for 4 hours and stored at 4°C in 70% ethanol. The small intestine, cecum, and colon were mounted in 0.4% agarose in PBS and imaged to capture red fluorescence (mT; tdTomato) and green fluorescence (mG; EGFP) using either a Zeiss microscope at 12.5x and or Nikon microscope at 20x magnification (see Appendix 5-10 for additional details).

Whole-mount images used for statistical analysis were obtained on the Zeiss microscope and processed using the Fiji image-processing package of ImageJ[35]. A macro was used to ensure consistency among images. Briefly, the macro searched a directory for Zeiss image files (ZVI) and converted them to Open Microscopy Environment's (OME) tagged image file format (TIFF) using the LOCI Bio-Formats Importer/Exporter to preserve meta data[36]. It then completed the following set of functions with settings based on which protein was imaged (tdTomato or EGFP): subtracted background, enhanced local contrast (CLAHE), set autothreshold, and converted to binary. Once in binary, the areas of the image containing no tissue were filled with

yellow. The result was a binary image in which white represents tissue expressing tdTomato and black represents tissue expressing EGFP (Appendix 5-6).

Patch size analysis

To assess the relationship between mosaicism and clonal architecture, red and green patches of intestinal epithelium in experimental mice were analyzed using distance maps as previously described for aggregation chimeras [10,11]. Briefly, flat binary images of each intestinal segment were converted to distance map images, which indicate for each position the Euclidean distance to the nearest opposite color, using the EBImage software package[37]. The average minimum distance to the opposite color measures the mosaic patch size, which was compared to patch sizes from aggregation chimeras (Appendix 5-4).

3D reconstruction of tumors

Some adenomas from mice euthanized at 150 days of age were excised and optically cleared using 2,2-thiodiethanol (TDE) as previously described[38]. Cleared adenomas were mounted *en bloc* in 97% TDE and multiphoton excitation imaging was performed on a Prairie Technologies Ultima IV Imaging system at LOCI.

Image stacks from the Ultima IV were stitched together using the default settings in the Grid/Collection Stitching plug-in for ImageJ that is distributed as part of the Fiji project[39]. Background subtraction was performed on both channels using the ImageJ subtract background function with a rolling ball radius of 40 pixels. When showing EGFP only, a threshold was used to eliminate tissue autofluorescence. The threshold was applied equally to all areas of all images that were used in the reconstruction. Images were then opened using the ImageJ 3D viewer plug-

in (Display as: Volume, Color: None; Threshold: 0, Resampling factor: 1) to generate high quality 3D renderings of the OME dataset.

Immunuohistochemistry

All excised tumors were either embedded in FSC 22 (Surgipath) and flash frozen or placed in formalin, processed and embedded in paraffin. Blocks were serially sectioned and arrayed as two 5μm sections per slide. Every tenth slide was stained with hematoxylin and eosin. For more complete analysis, slides of interest were stained by immunohistochemistry for CTNNB1 (1:200 Purified Mouse Anti-β-catenin Antibody, BD Transduction Laboratories) using the HistoMouse Max Kit (Invitrogen) or by immunofluorescence for green fluorescent protein (EGFP) or red fluorescent protein (tdTomato) (primary– 1:1000 Living Colors EGFP Monoclonal Antibody, Clontech, and secondary– 1:1000 goat anti-mouse Alexa Fluor 488, Invitrogen; and/or primary– 1:200 anti-tdTomato, Rockland and secondary– 1:1000 goat anti-rabbit Alexa Fluor 568, Invitrogen) and 4',6-diamidino-2-phenylindole (DAPI) by applying ProLong Gold with DAPI mounting media (Molecular Probes). Note that staining for EGFP and tdTomato was necessary because fixation quenches the fluorescent signal.

Immunofluorescence

Histological sections stained by immunofluorescence were imaged as described in the whole-mount imaging section; the only change was the use of 4x, 5x, 10x or 20x objective lenses. Post-processing of imaging was not necessary. Histological sections stained by immunohistochemistry or hematoxylin and eosin (H&E) were imaged in the same manner with a halogen light source and no color filters.

Pathology

The pathology of each lesion was assessed by two board-certified pathologists (KAM and MKW) by examining H&E stained slides. Tumors were classified as either adenoma with low-grade dysplasia, adenoma with high-grade dysplasia, intramucosal carcinoma, or invasive adenocarcinoma. The histologic criteria used for the classification of lesions are defined as follows: similar to that observed in human tubular adenomas, lesions with low-grade dysplasia exhibited hyperchromatic, elongated nuclei with stratification of nuclei half-way toward the luminal aspect with scatted mitosis. In high-grade dysplasia, the hyperchromatic nuclei are larger, rounded and often contain a prominent nucleolus, exhibit nuclear stratification to the luminal surface, demonstrate complex architecture with back-to-back or cribriform glands, and contain abundant mitotic figures (sometimes atypical) with areas of cell necrosis. In tumors exhibiting intramucosal carcinoma, the nuclear and cytologic features are identical to that seen with high-grade dysplasia, however these lesions also demonstrate neoplastic cell invasion beyond the basement membrane into the lamina propria or muscularis mucosa and can be associated with a desmoplastic reaction. For lesions to be classified as invasive adenocarcinomas, the neoplastic cells must invade beyond the muscularis mucosa into at least the submucosa. The histology of invasive tumors can vary such that tumors can be composed of neoplastic cells with well-formed glands or sheets of cells without gland formation, however in all instances there is an associated desmoplastic response.

***Sequencing of* Apc**

Paraffin sections were prepared for laser capture microdissection (LCM) of regions of interest by staining for EGFP using the HistoMouse Max Kit (Invitrogen) (primary– 1:1000

Living Colors EGFP Monoclonal Antibody, Clontech). Adjacent sections were then cut onto membrane slides and stained with methylene blue. Regions of interest were removed via LCM with the assistance of the Translational Research Initiatives in Pathology (TRIP) Lab, University of Wisconsin–Madison. Alternately, if the patches were large, tissue was scraped by hand from unstained slides containing formalin-fixed, paraffin-embedded sections. Genomic DNA was extracted from the isolated tissue using the Maxwell 16 automated purification system with Maxwell 16 FFPE Plus LEV DNA Purification Kit following the instructions of the manufacturer (Promega, Madison, WI). PCR primers were designed to amplify two regions of exon 15 (codons 747–953 and 1285–1513; Appendix IV-9) of the mouse *Apc* gene, since most mutations occur in these two regions[14,40]. PCR was conducted for 35 cycles. Each cycle consisted of 30 seconds at 94°C, 30 seconds at 55°C, and 1 minute at 72°C. All amplification procedures included DNA-free controls consisting of the amplification cocktail and nuclease-free water (Promega) in place of template DNA. PCR primers were then used for sequencing. Mutation discovery and analysis was conducted using the mSeq 6.0.1 (Norman Drinkwater, McArdle Laboratory for Cancer Research, Department of Oncology, School of Medicine and Public Health, University of Wisconsin–Madison) and Mutation Surveyor (Softgenetics) programs.

Disclosure of Potential Conflicts of Interest

The authors have declared that no competing interests exist.

Acknowledgments

The authors thank Ruth Sullivan for reviewing microscopic slides as well as reading the manuscript and providing several helpful comments. In addition the authors thank Ella Ward and

Jane Weeks in Experimental Pathology at the University of Wisconsin Carbone Cancer Center for technical assistance and all members of the Laboratory Animal Research staff for their conscientious care of animals involved in this and other studies.

This study was supported by the National Cancer Institute (http://www.cancer.gov/) of the National Institutes of Health (R01 CA123438 to RBH; P30 CA014520 to University of Wisconsin Carbone Cancer Center; P30 DK058404, Preclinical Models of Digestive Diseases Core, Vanderbilt Digestive Diseases Research Center; P50 CA095013, Translational Pathology and Imaging Core, Vanderbilt GI SPORE; K08 CA84146 to ATT; T32 CA009135 to CDZ and AAL; and T32 CA090217 to TJPO) and start-up funds from the University of Wisconsin-Madison Division of Gastroenterol and Hepatology, Department of Medicine, and School of Medicine and Public Health to RBH.

3.2 Early heterogeneity owing to a multi-ancestral origin contributes to cancer progression in a model of advanced colorectal cancer.

Alyssa A. Leystra, Amanda M. Wisinger, Brook Luers, Junbo Son, Christopher D. Zahm, Kristina A. Matkowskyj, Dustin A. Deming, Chelsie K. Sievers, Alex Schwartz Dawn M. Albrecht, Linda Clipson, and Michael A. Newton, Richard B. Halberg

Abstract

Colon tumors are frequently derived from multiple tumor-founding cells. While subclonal cooperation provides a growth advantage in some tumors, distinct ancestral clones might cooperate or alternatively compete during tumorigenesis, growth, and progression. Here we show that multiple ancestral clones cooperate to promote tumor cell invasion. Mice carrying the *Min* allele of *Apc* and expressing an activated form of PI3K in a subset of intestinal epithelial cells develop adenomas and adenocarcinomas in the intestine. Cell lineage tracing reveals that many of these tumors are derived from at least two tumor-founding cells, some of which express the activated PI3K. Importantly, a multi-ancestral tumor architecture is associated with tumor progression. Taken together, these data indicate that genetically distinct tumor-founding cells can contribute to colon tumor growth and progression, and likely provide a cooperative growth advantage.

Authors' Contributions

A.A. Leystra and R.B. Halberg were involved in all aspects of the research and preparation of the manuscript. B. Luers, J. Son, and M.A. Newton provided statistical support. C.D. Zahm, C.K.

Sievers, and D.A. Deming, A.M. Wisinger, A. Schwartz, and D.M. Albrecht provided technical support. L. Clipson and K.A. Matkoskyj analyzed experiments. All authors discussed results and edited the manuscript.

Introduction

Intratumoral heterogeneity has been linked to tumor progression, chemotherapy resistance, tumor recurrence, and poor clinical prognosis[2-7]. The degree of variation is estimated using several markers including cell differentiation state, gene expression, genetic mutations, and copy number variation. This heterogeneity is thought to arise either during a "Big Bang" event in which a single malignant cell and its immediate progeny rapidly accumulate mutations or else between a series of clonal sweeps in which a neoplastic cell acquires a mutation that provides a significant fitness advantage allowing its progeny to outcompete other clones within the tumor[23,41] (Figure 1-1). While mathematical modeling supports the Big Bang hypothesis *in silico*, no studies have prospectively tested whether heterogeneity which arises early in the tumor ancestry contributes to tumor progression *in vivo*.

Colon tumors are frequently derived from multiple distinct tumor-founding cells[9-13,15,19,25]. These multi-ancestral tumors likely arise as a consequence of transforming intercellular communication between an initiated tumor-founding cell and corrupted neighboring cells (Appendix 7). The resulting tumors are inherently heterogeneous due to the presence of multiple genetically and phenotypically distinct cells at the earliest point in the ancestry of a tumor.

While multi-ancestral adenomas and adenocarcinomas have been identified in both sporadic and familial disease cases, previous studies do not address the fate of ancestral clones which carry mutations in tumor driver genes such as *TP53*, *KRAS*, or *PIK3CA*, which are

commonly mutated in colon cancers[42-44]. Expression of a tumor driver gene within a single ancestral clone might result in a clonal sweep, resulting in loss of other contributing tumor clones (Figure 1-1). Therefore, while the tumors studied previously were frequently derived from multiple tumor-founding cells, these results may have little clinical impact considering that most colon cancers acquire at least one of these driver mutations in a subset of tumor cells as a tumor progresses from a benign to malignant state

Recently, activated PI3K signaling has been shown to drive rapid tumor initiation, growth, and progression within the mammalian colon, indicating that PI3K is a tumor driver within the colon[45] (Chapter 2). In the present study, we used a transgenic mouse model which conditionally expresses oncogenic PI3K to determine whether activation of a tumor driver within a subset of tumor-founding cells was sufficient to drive an early clonal sweep or whether tumors would maintain early diversity through tumor growth and progression. The results underscore the importance of early genetic diversity arising from multiple tumor-founding cells.

Results

Transgenic animals facilitate labeling cells prior to tumor initiation

To trace individual clones through tumor initiation, growth, and progression, we utilized transgenic animals that stably express reporter genes to differentially label clones. In Fabp1-Cre$^+$ mT/mG$^+$ double transgenic mice, Cre recombinase is expressed in approximately 50% of the colonic epithelium during embryogenesis; cells are then labeled by a reporter which expresses either a derivative of a red fluorescent protein (tdTomato) prior to Cre recombination or an enhanced green fluorescent protein (EGFP) following Cre recombination (Figure 3-4A). In this way, clones are labeled prior to tumor initiation.

To determine whether activation of a tumor driver within a subset of tumor clones would result in an early clonal sweep event, the Pik3ca* transgene was used. This transgene results in expression of constitutively activated PI3K from the Rosa26 promoter within cells which express Cre recombinase[46] (Chapter 2). When combined with the animal model described above, this results in genetically distinct cell lineages labeled prior to tumor formation (Figure 3-4A).

Normal intestinal tissues from experimental animals (Fabp1-Cre^{+} mT/mG^{+} Pik3ca*$^{+}$ *Apc*$^{Min/+}$ mice) were a stable mixture of tdTomato- and EGFP-expressing cell lineages. The proximal small intestine was monochromatic with only tdTomato expressing cells being observed, whereas the distal small intestine (S4) and colon (CO) were a patchwork of tdTomato- and EGFP-expressing cells (Figure 3-4B and C). The pattern of variegation in the normal tissue was assessed using a variegation score which represented the proportion of tissue where differentially labeled crypts were adjacent, allowing for detection of heterotypic tumors. This variegation score was similar between adult animals regardless of age (Figure 3-4D).

Constitutive activation of PI3K results in a tumor-autonomous increase in tumor formation and size

Constitutive activation of PI3K resulted in increased tumor burden and size compared to *Apc*$^{Min/+}$ littermate controls as previously reported (two-sided Wilcoxon Rank Sum test of average tumor multiplicity per mouse compared to *Apc*$^{Min/+}$ controls: $p=0.006$; and average tumor size: $p<0.001$; Figure 3-5, Appendices 6-1 and -2, and Chapter 2.2). These differences were only observed within intestinal regions where PI3K was constitutively activated (two-sided Wilcoxon Rank Sum tests of average multiplicity: S4 $p=0.005$; CO $p=0.005$; and size: S4 $p=0.001$).

Importantly, expression of the mT/mG reporter transgene did not change tumor multiplicity or size (Appendices 6-3 and -4).

To determine whether the Pik3ca-dependent increase in tumor size was a tumor-autonomous or a systemic effect, the size of tumors within experimental mice were compared. The tumor architecture was predicted from fluorescent images of the surface of whole tumors (Figure 3-6). Some tumors were composed entirely of tdTomato expressing cells (homotypic red) where constitutive activation of PI3K was not expected or else contained EGFP-expressing epithelial cells (green) where constitutive activation of PI3K was expected. The number and size of homotypic red tumors overall and within each intestinal segment was similar to the total number and size of tumors in $Apc^{Min/+}$ control mice (Figure 3-5). Meanwhile, tumors which contained green cells were significantly larger than homotypic red tumors and tumors from $Apc^{Min/+}$ control mice. Thus, the increase in tumor multiplicity and size in experimental animals can be accounted for by tumors which contain green cells. Together, these data indicate that the PI3K-dependent increase in tumor size was primarily a tumor-autonomous effect.

Multi-ancestral tumors formed despite expression of the Pik3ca* transgene

While some tumors from experimental animals appeared to be homotypic, being composed entirely of cells from either tdTomato- or EGFP-expressing lineages, others appeared to be heterotypic, being composed of a mixture of cells from both tdTomato- and EGFP-expressing cell lineages (Figure 3-6, Table 3-4). As cells are labeled with tdTomato or EGFP prior to tumor initiation, heterotypic tumors that contain cells from both cell lineages must be derived from multiple tumor-founding cells. Interestingly, heterotypic tumors from experimental mice were significantly larger than either homotypic red or homotypic green tumors from those

mice ($p<0.001$ and 0.008 respectively; Figure 3-6, Table 3-5), indicating that the heterogeneous tumor structure provides a growth advantage even compared to homotypic tumors with similar mutations. Interestingly, the size of tumors which contain green cells varied significantly depending on the background strain of the mice, indicating that the genetic background might modify the impact of PI3K activation (Appendix 6-9).

Multi-ancestral tumor architecture was associated with progression to malignancy

To confirm the presence of multiple neoplastic clones within tumors, a subset of tumors were fixed in 4% paraformaldehyde, embedded in paraffin, sectioned, and stained with hematoxylin and eosin or for tdTomato and EGFP (Figure 3-7). Only a few sections of each tumor were examined after histological sectioning, resulting in a potential bias toward falsely classifying heterotypic tumors as homotypic. Overall, 12% (8/68) of sectioned tumors were classified as homotypic red, being composed entirely of tdTomato expressing neoplastic cells, and 44% (30/68) were were classified as homotypic green, being composed entirely of EGFP-expressing neoplastic epithelial cells intermingled with tdTomato-expressing stromal cells (Figure 3-7). The remaining 44% (30/68) of tumors were heterotypic being composed of a mixture of tdTomato- and EGFP-expressing neoplastic epithelial cells, indicating that multiple clones still contributed to a single tumor even when at least one clone expressed the Pik3ca* transgene prior to tumor initiation. In fact, the presence of multiple ancestral clones was strongly associated with the likelihood that a tumor had progressed to an adenocarcinoma; only 3% (1/38) of adenomas were heterotypic compared to 97% (29/30) of adenocarcinomas (two-sided Fisher's Exact test, $p<0.01$; Figure 3-7).

Multiple clones within multi-ancestral tumors exhibited invasive behavior

Given that the multi-ancestral tumor architecture was associated with invasion, we sought to determine whether the clones were cooperating to their mutual advantage. tdTomato-labeled cells were invasive in 25% (2/8) of homotypic red tumors, which lacked a neoplastic EGFP-labeled component, and in 61% (18/30) of heterotypic tumors in which the tdTomato-labeled cells had a neoplastic EGFP-labeled partner (two-sided Fisher's Exact Test, p=0.1). Conversely, EGFP-labeled cells were invasive in 66% (18/30) of homotypic green tumors compared to 97% (29/30) of heterotypic tumors (two-sided Fisher's Exact Test, p=0.001). Additionally, both clones invaded farther in invasive multi-ancestral tumors than in their homotypic counterparts (Figure 3-7). Thus, multi-ancestral architecture influences invasion regardless of the distinct mutation profiles of individual ancestral clones.

Discussion

This study is the first to investigate multi-ancestral intestinal cancers with a known oncogenic driver. Despite constitutive activation of PI3K prior to tumor initiation, multiple clones contribute to cancer progression. Multi-ancestral tumors are larger and more invasive than other tumors. Furthermore, co-evolved clones within multi-ancestral tumors are more invasive than within homotypic tumors.

Interclonal cooperation can drive tumor maintenance, growth, and progression. Multiple cooperating tumor clones can be essential for tumor propagation[47]. Additionally, non-dominant clones can promote the survival and metastatic potential of dominant clones[48]. Similarly, multiple co-evolved ancestral clones might cooperate to promote survival, growth, and invasion.

PI3K activation has often been considered a late event in tumor evolution. Activating

mutations in *PIK3CA* are seldom detected in adenomas and are instead restricted to cancers. However, tumors carrying activated PI3K signaling still undergo the traditional adenoma-to-adenocarcinoma transition, albeit likely at an increased rate (Chapter 2.3). Additionally, these mutations are often detected within only a subset of tumor cells[42]. Some *in silico* models predict that if a mutation confers a sufficient competitive advantage to a cell, that the cell can rapidly outcompete other nearby clones and thus expand to detectable levels within large tumors[41]. If PI3K drives clonal sweeps, however, our endogenous tumor model in which PI3K mutations can be present when the tumor initiates should not result in any heterogeneous tumors. Contrary to this possibility, tumors were frequently heterotypic. Our data would therefore indicate that the frequent presence of PI3K within a subset of tumor cells might not be a consequence of late arrival but rather an important aspect of tumor biology. In contrast, other important colorectal cancer drivers which are often found in a majority of tumor cells (including TP53 and KRAS) might result in different competitive dynamics and might therefore impact the progression of multi-ancestral tumors differently. A limitation of our study is that recombination of different floxed alleles varies dependent on a number of parameters but especially distance between *loxP* sites.

Unfortunately, Cre recombination is not equally efficient for all transgenes in all cells[49,50]. However, tumors labeled with tdTomato were similar in frequency and size to tumors from control animals which lacked Pik3ca* expression, and tumors labeled with EGFP were significantly larger and more invasive than those which lacked EGFP expression. Additionally, the patchwork of red and green cells remains stable across age groups, and cells were never observed to change color in *in vitro* experiments, indicating that once a clone is labeled with EGFP or tdTomato that label is not likely to change. Therefore, regardless of the genetic status of

the individual clones, heterotypic tumors were likely truly multi-ancestral.

In the age of genomics and sequencing, a major focus of cancer research is upon identifying the genetic aberrations within clones. This focus emphasizes genetic heterogeneity as a potential mechanism for tumor adaptability and survivability; in the presence of insults such as immune system activation, hypoxic conditions, or chemotherapy, a genetically heterogeneous tumor has numerous opportunities to contain a pre-existing resistant clone. In this view of tumor heterogeneity, each clone exists independent of all other clones. Another component of tumor heterogeneity, however, is cooperation between clones[51]. Just as intercellular interactions are critical to angiogenesis and immune escape, interclonal interactions likely contribute to tumor malignancy[48]. Identifying and understanding the biological mechanism and repercussions of these interclonal interactions might therefore lead to the discovery of effective novel prevention and treatment strategies.

Methods

Mice

Animal studies were conducted under protocols approved by the Institutional Animal Care and Use Committee at the University of Wisconsin in compliance with policies set by the Office of Laboratory Animal Welfare at the National Institutes of Health. All animals were housed in a pathogen-free facility and fed a standard chow diet containing 4% fat. Genotyping was performed by PCR as described by the suppliers of animals.

FVB/N- and C57BL/6J-*Tg*$^{(Fabp1\text{-}Cre)1}$*Jig* mice homozygous for the Fabp1-Cre transgene were crossed with B6.129(Cg)-*Gt(ROSA)26Sor*$^{tm4(ACTB\text{-}tdTomato,\text{-}EGFP)Luo}$*/J* mice homozygous for the mT/mG transgene to generate (FVBxB6)F1 Fabp1-Cre mT/mG mice and a B6.Fabp1-Cre

mT/mG line, respectively. The B6.Fabp1-Cre mT/mG line was maintained by sibling crosses for no more than ten generations prior to backcrossing to C57BL/6J mice obtained from The Jackson Laboratory.

C57BL/6-*Gt(ROSA)26Sor*$^{tm7(Pik3ca*,EGFP)Rsky}$/J mice that were homozygous for the Pik3ca* transgene were crossed with B6.Apc^{Min} mice which were heterozygous for the *Min* allele of the *Adenomatous polyposis coli* gene to generate a B6.Pik3ca*Apc^{Min} line. These mice were maintained by sibling crosses for no more than ten generations prior to backcrossing to C57BL/6J mice obtained from The Jackson Laboratory or newly imported C57BL/6-*Gt(ROSA)26Sor*$^{tm7(Pik3ca*,EGFP)Rsky}$/J mice.

(FVBxB6)F1 Fabp1-Cre mT/mG and B6.Fabp1-Cre mT/mG were crossed with B6.Pik3ca*Apc^{Min} to generate (FVBxB6)xB6 N2 and B6.Fabp1-Cre mT/mG Pik3ca*Apc^{Min} mice respectively. Resulting progeny which were hemizygous for all transgenes and heterozygous for the Apc^{Min} allele were experimental animals while littermate controls lacked one or more of the transgenes or were wild type at the *Apc* locus.

Whole Tissue Imaging

Intestinal tracts were removed at necropsy, opened longitudinally, rinsed with PBS, fixed in 4% paraformaldehyde for two days at 4°C and then stored in 70% ethanol at 4°C. The small intestine, cecum, and colon were mounted in 0.4% agarose and imaged with a Nikon Eclipse TI-S microscope or Zeiss AxioPlan II (Appendix 5-10). As the goal of fluorescent imaging was to detect fluorescence but not to quantify its intensity, exposure times were set for each individual tissue such that regions with fluorescence were clearly visible, while regions which lacked

fluorescence were minimally detected. These exposure times varied based on the thickness of the tissue and the length of time the tissue had been stored prior to imaging.

Whole Tissue Patchwork Analysis

Whole tissue fluorescent images taken on a Nikon Eclipse TI-S microscope were exported from ND2 files to single channel TIFF files prior to analysis. All images regardless of which microscope with which they were acquired were processed using a macro for the Fiji image-processing package of ImageJ to ensure consistency. Briefly, the macro searched a directory for Zeiss image files (ZVI) and converted them to TIFF files using the LOCI Bio-Formats Importer. It then identified all TIFF files, set an autothreshold, converted to binary, and measured the area and perimeter of patches of pixels which represented green fluorescence and the area and perimeter of patches of pixels which represented red fluorescence. Areas of the image containing no tissue were filled with gray. The result was a binary image in which white represented tissue expressing tdTomato and black represented tissue expressing EGFP. For quality control, binary images were compared to color overlays; when necessary, the images were manually manipulated to more accurately reflect the patchwork of the tissue.

A variegation score was assigned to each binary image (Appendix 6-10). The length of the perimeter of the patches of green pixels was assumed to be proportional to the number of crypts which were adjacent to at least one crypt of a different color. However, some of the perimeter would be positioned on the edge of the tissue instead of adjacent to crypts of a different color. To correct for this, it was assumed that the proportion of the total perimeter of the tissue which was composed of green pixels would be approximately equal to the proportion of the total area of the tissue which was composed of green pixels. Therefore, the perimeter of

green pixels was corrected by subtracting out the appropriate proportion of the total tissue perimeter. The corrected perimeter was then normalized to the square root of the total area of the tissue to determine the final variegation score.

$$\text{Variegation Score} = \frac{perimeter(green) - (proportion(green) * perimeter(tissue))}{\sqrt{area(tissue)}}$$

Immunofluorescence

Tumors which were easily visible without the use of a dissecting microscope (usually >2mm in diameter) were excised, embedded in paraffin, and cut into 5µm sections. Every twentieth section was stained with hematoxylin and eosin (H&E).

Slides of interest were stained by immunofluorescence for tdTomato and EGFP using the following conditions: permeabilization in 0.5% Tween20 solution in PBS; antigen presentation in 0.5% $NaBH_4$ solution in PBS for 10 minutes; blocking in 5% dehydrated milk in PBS for at least one hour; incubated in anti-tdTomato (1:200 anti-RFP Rabbit pAB Rockland; RL600-401-379, VWR Scientific, Radnor PA) and anti-EGFP (1:1000 Living Colors anti-EGFP Mouse mAB; 632569, Clontech Laboratories, Fitchburg WI) primary antibodies overnight; incubated in anti-rabbit (1:1000 Alexa Fluor 568 anti-rabbit IgG (H+L) Goat mAB; A11011, Invitrogen, Carlsbad CA) and anti-mouse (1:1000 Alexa Fluor 488 anti-mouse IgG2a Goat mAB; A21131, Invitrogen) secondary antibodies overnight; and nuclei were stained with 4',6-diamidino-2-phenylindole (DAPI) by applying ProLong Gold with DAPI mounting media (P36931, Invitrogen).

Images of H&E and immunohistochemical stained slides were acquired on a Nikon Eclipse TI-S microscope using a halogen light source, no color filters, and either a 4x or 10x objective lens.

Images of immunofluorescent stained slides were acquired on either a Zeiss AxioPlan II or Nikon Eclipse TI-S microscope as previously described with either a 10x or 20x objective lens (Appendix 5-10). As the goal of fluorescent imaging was to detect fluorescence but not to quantify its intensity, exposure times were set for each individual tissue sections such that regions with fluorescence were clearly visible, while regions which lacked fluorescence were minimally detected. These exposure times varied based on length of time the stained slides had been stored prior to imaging.

Acknowledgments

We thank Ella Ward in Experimental Pathology at the UW Carbone Cancer Center for technical assistance, Joshua Barnes for critical review of Fiji macros, and Quincy Rosemarie for critical review of this manuscript. The project was supported by the Conquer Cancer Foundation of the American Society of Clinical Oncology through A Young Investigator Award (D.A.D.); the National Cancer Institute of the U.S. National Institutes of Health through T32 CA009135 (A.A.L, C.K.S., and C.D.Z.), R01 CA123438 (R.B.H); and start-up funds (R.B.H.) from the UW Division of Gastroenterol and Hepatology, the UW Department of Medicine, and the UW School of Medicine and Public Health.

Figures

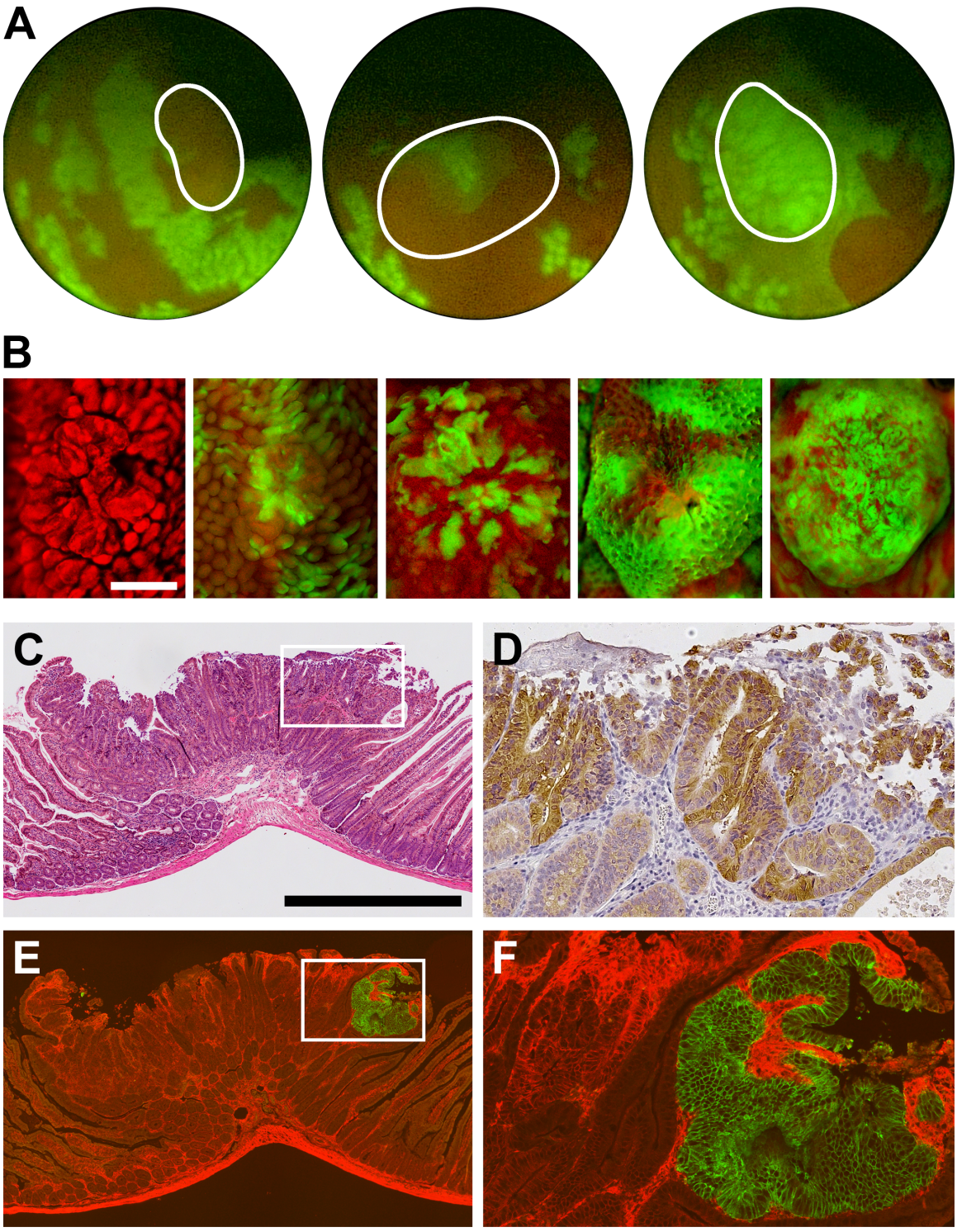

Figure 3-1. Mosaics are a powerful experimental tool for studying tumorigenesis. The clonal architecture of colon tumors is visible *in vivo* using fluorescence endoscopy. The intestinal epithelium is a single layer of cells that is replaced every three to five days. New cells are produced from stem cells lying near the base of the each crypt. In our model, crypts are homotypic red or homotypic green with the latter being particularly evident during fluorescence endoscopy, as each crypt appears as a discrete green circle (A). Tumors can be composed of only red crypts (left panel), a mixture of red and green crypts (middle panel), or only green crypts (right panel). The tumors are outlined in white. The high variability in clonal architecture is also evident in whole mounts (B). Tumors were homotypic red (left panel), heterotypic (middle three panels), or homotypic green (right panel). The mixture of red and green crypts varies among multi-ancestral tumors, with some being primarily composed of either red crypts or green crypts, whereas others are roughly an equal number of both types. Histology is necessary to determine architecture, as tumors can appear heterotypic with neoplastic crypts of one color intermingled with normal crypts of the other color. The clonal architecture of tumors is scored from histologic sections. Neoplastic cells were visualized following H&E staining (C) with high levels of CTNNB1 (β-catenin) expression in the cytoplasm and nucleus (D, brown stain). As shown in a nearby section from the same tumor stained by immunofluorescence, neoplastic cells within a single tumor often arose from both the red and green cell lineages (E-F). Panel B photos are shown at the same magnification; size bar = 1mm. Panels C and E are shown at the same magnification; size bar = 500μm. Panel D shows a 4x enlargement in an adjacent section of the outlined area in Panel C. Panel F shows a 4x enlargement of the area outlined in Panel E.

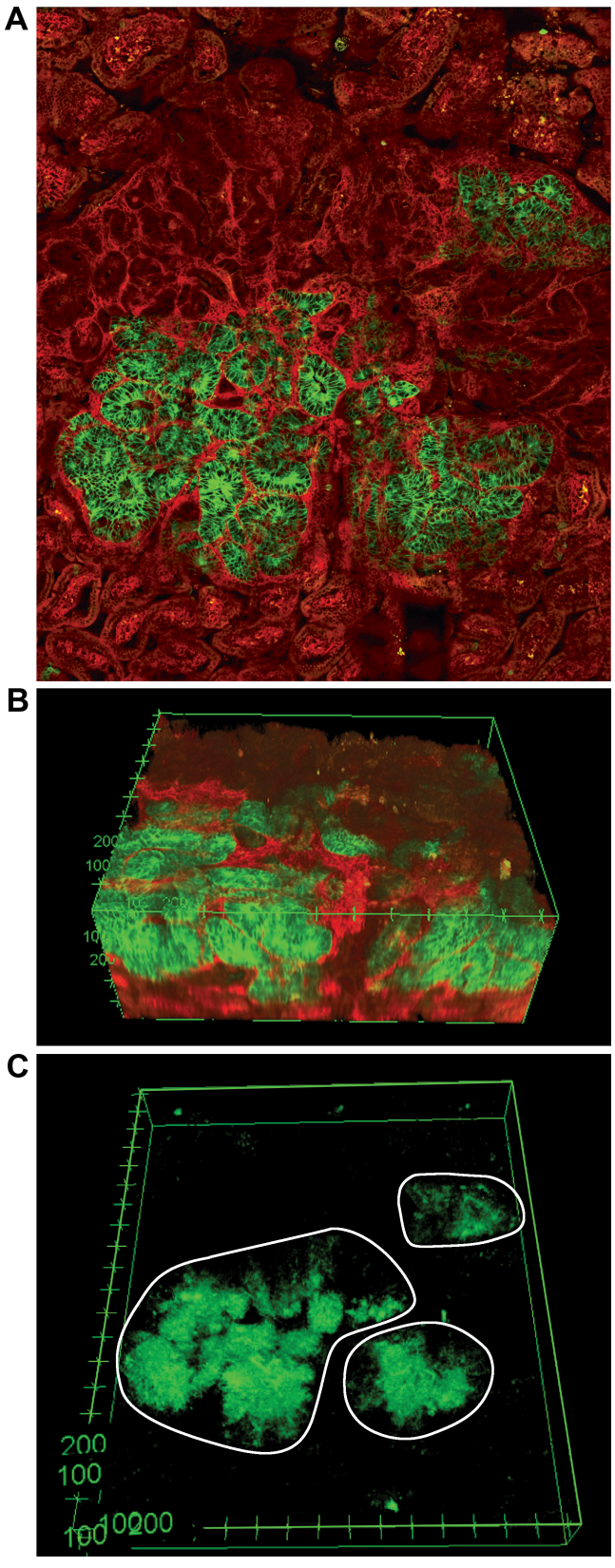
A
B
C
200
100
200
100
200
100
200

Figure 3-2. Multi-ancestral tumors appear to be derived from up to four tumor-founding cells. The expression of fluorescent proteins facilitates the use of multiphoton excitation imaging to reconstruct the tumor in three dimensions Reconstructions permit the exploration of structure beneath the surface of the tumors (A, surface; B, side view) without distortions and artifacts that occur when imaging multiple histological sections. Four distinct colored areas were evident in one tumor. Three discrete green areas were evident when the red was subtracted (C). These areas of green were separated by at least 100 microns, which is equivalent to the diameter of 1 to 2 crypts.

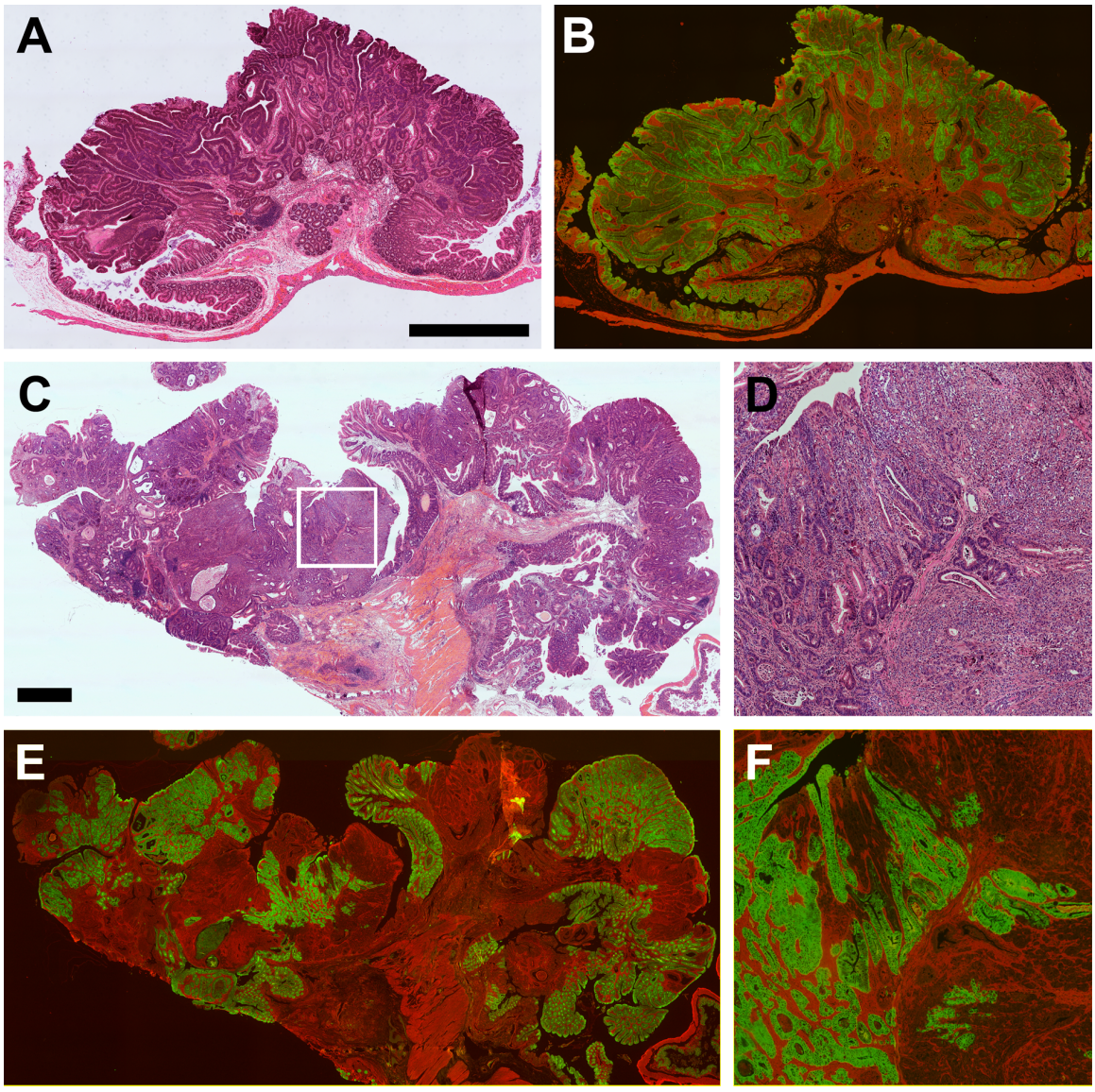
A
B
C
D
E
F

Figure 3-3. In mice that were allowed to age until moribund, some tumors were adenomas with high-grade dysplasia (A and B), whereas others were intramucosal carcinomas (C-F). The neoplastic cells identified on H&E stained sections (A, C and D) were a mixture of both red and green cells (B, E and F). Panels A and B are shown at the same magnification; size bar = 1mm. Panels C and E are same magnification; size bar = 1mm. Panels D and F are 4x enlargements of the area outlined in C.

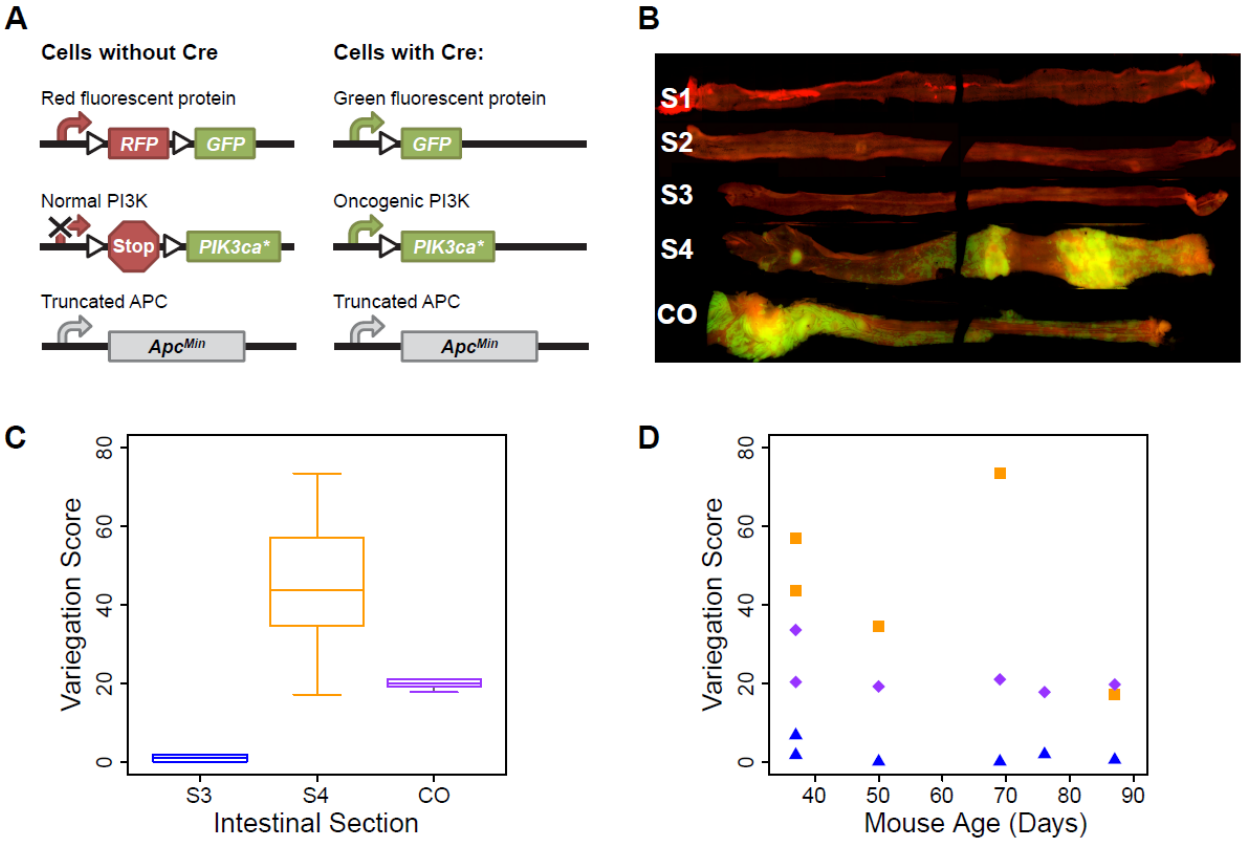
A
Cells without Cre
Cells with Cre:
Red fluorescent protein
RFP
GFP
Green fluorescent protein
GFP
Normal PI3K
Stop
PIK3ca*
Oncogenic PI3K
PIK3ca*
Truncated APC
ApcMin
Truncated APC
ApcMin
B
S1
S2
S3
S4
CO
C
Variegation Score
0
20
40
60
80
S3
S4
CO
Intestinal Section
D
Variegation Score
0
20
40
60
80
40
50
60
70
80
90
Mouse Age (Days)

Figure 3-4. The distal intestines of Fabp1-Cre^{+} mT/mG^{+} Pik3ca*$^{+}$ *Apc*$^{Min/+}$ mice were a variegated pattern of fluorescently-labeled cells. (A) Cre recombinase was expressed in about half of the epithelial cells of the distal small intestine and colon. Cells without Cre recombinase expressed tdTomato. In cells expressing Cre recombinase, however, recombination at *loxP* sites (triangles) within two transgenes led to expression of EGFP in place of tdTomato and expression of a constitutively activated PI3K oncoprotein. All cells lacked one functional allele of *Apc* (*Apc*$^{Min/+}$). (B) The distal small intestine and colon were therefore a mosaic of tdTomato-expressing (red) cells with low relative risk and EGFP-expressing (green) cells with high relative risk of malignant transformation. S1-S4, proximal to distal quarters of small intestine; CO, colon. (C) The distal quarter of the small intestine (S4) displayed the greatest degree of variegation. (D) The degree of variegation within the tissue sections did not change significantly over time. Blue triangles, segment 3 of small intestine; orange squares, segment 4 of small intestine; purple diamonds, colon.

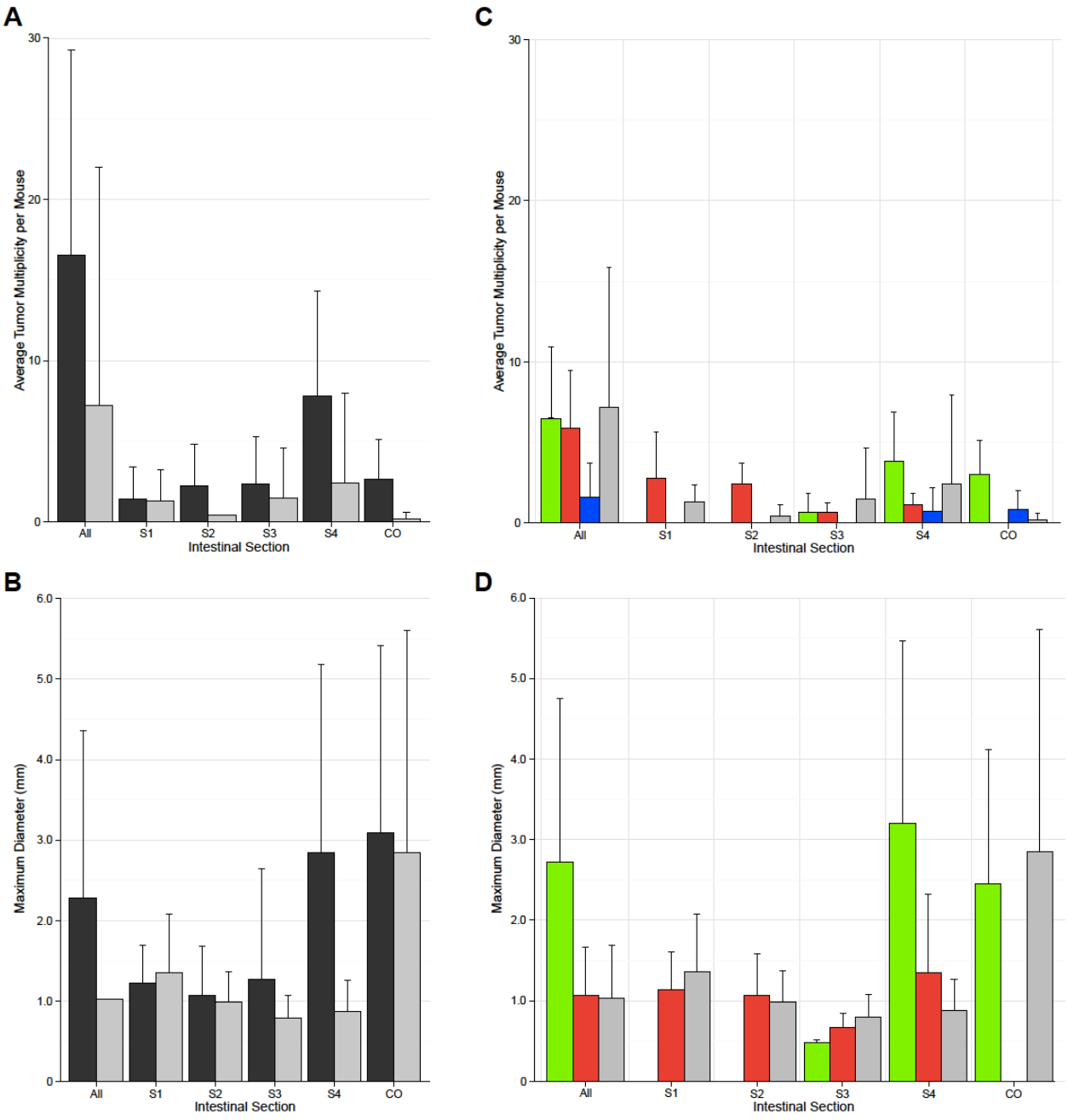
A
Average Tumor Multiplicity per Mouse
30
20
10
0
All
S1
S2
S3
S4
CO
Intestinal Section
C
Average Tumor Multiplicity per Mouse
30
20
10
0
All
S1
S2
S3
S4
CO
Intestinal Section
B
Maximum Diameter (mm)
6.0
5.0
4.0
3.0
2.0
1.0
0
All
S1
S2
S3
S4
CO
Intestinal Section
D
Maximum Diameter (mm)
6.0
5.0
4.0
3.0
2.0
1.0
0
All
S1
S2
S3
S4
CO
Intestinal Section

Figure 3-5. Constitutive activation of PI3K resulted in a tumor-autonomous increase in multiplicity and size. (A) Tumor multiplicity was higher in intestinal regions of Fabp1-Cre^{+} mT/mG^{+} Pik3ca*$^{+}$ *Apc*$^{Min/+}$ mice where PI3K was constitutively activated than in *Apc*$^{Min/+}$ controls (two-Sided Wilcoxon Rank Sum tests: Overall p<0.006; S1 p=0.8; S2 p=0.03; S3 p=0.2; S4 p=0.005; CO p=0.005). (B) Tumor size was similarly higher in regions where PI3K was constitutively activated compared to controls (two-Sided Wilcoxon Rank Sum tests: Overall p<0.001; S1 p=0.8; S2 p=0.9; S3 p=0.6; S4 p<0.001; CO p=0.8). (C) The number of tumors from Fabp1-Cre^{+} mT/mG^{+} Pik3ca*$^{+}$ *Apc*$^{Min/+}$ mice which were entirely composed of tdTomato-expressing cells (red) were similar to the total number of tumors from *Apc*$^{Min/+}$ controls (gray; two-sided Wilcoxon Rank Sum tests: Overall p=0.2; S1 p=0.2; S2 p=0.004; S3 p=0.9; S4 p=0.4; CO p=0.3). Thus, the increase in tumor multiplicity within these animals can be explained by tumors in which PI3K is constitutively activated (green). Some tumors within these mice could not be classified (blue). (D) Tumor size was also similar between Fabp1-Cre^{+} mT/mG^{+} Pik3ca*$^{+}$ *Apc*$^{Min/+}$ tumors which were entirely composed of tdTomato-expressing cells (red) and *Apc*$^{Min/+}$ control tumors (gray; two-sided Wilcoxon Rank Sum tests: Overall p=0.8; S1 p=0.5; S2 p=0.9; S3 p=0.4; S4 p=0.5). Thus, the increase in tumor size within these animals can be explained by tumors in which PI3K is constitutively activated (green; two-sided Wilcoxon Rank Sum tests compared to *Apc*$^{Min/+}$ control tumors: Overall p<0.001; S3 p=0.1; S4 p<0.001; CO p=0.8).

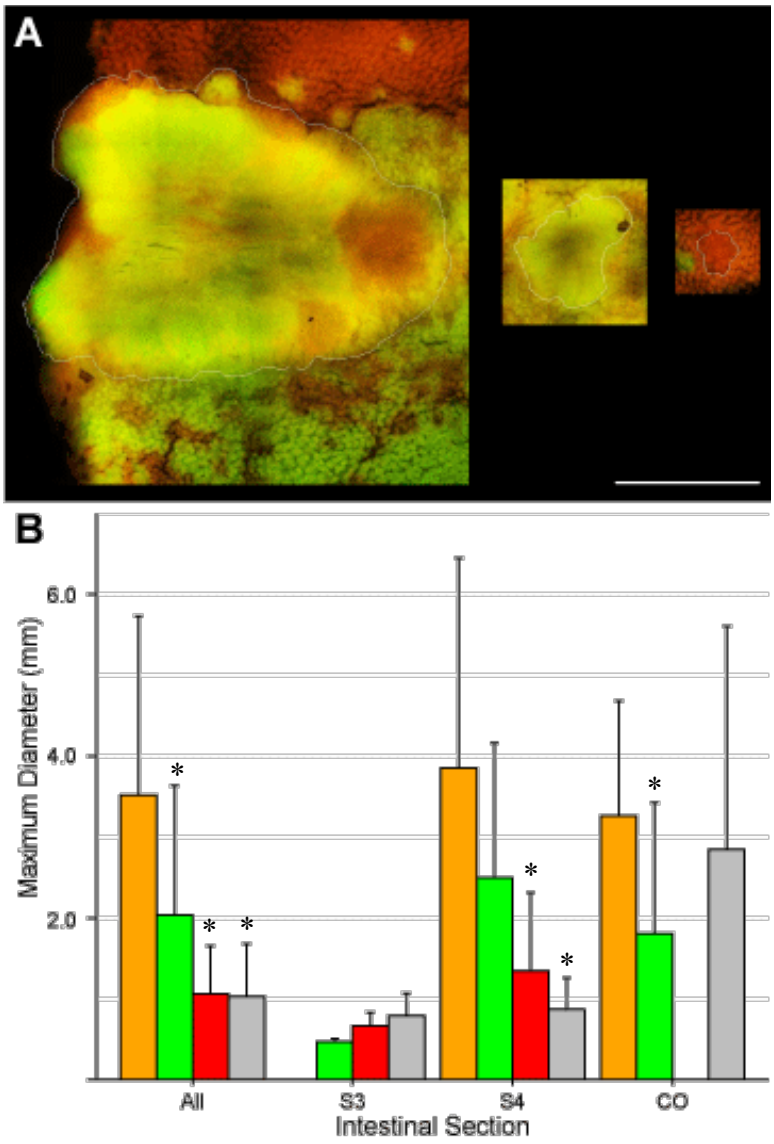
A
B
Maximum Diameter (mm)
6.0
4.0
2.0
All
S3
S4
CO
Intestinal Section

Figure 3.6. Multiple ancestral clones persist in large tumors. (A) Since cells were labeled prior to tumor initiation, tumor-founding cells could be followed through tumorigenesis. One or more tdTomato-expressing tumor-founding cells intermingling with one or more EGFP-expressing tumor-founding cells would propagate a heterotypic tumor with multi-ancestral origins; one or more EGFP-expressing tumor-founding cells would propagate a homotypic green tumor with uni- or multi-ancestral origins; and one or more tdTomato-expressing tumor-founding cells would propagate a homotypic red tumor with uni- or multi-ancestral origins. scale bar = 2.0 mm. (B) Heterotypic multi-ancestral tumors were larger than their homotypic counterparts. *two-sided Wilcoxon Rank Sum Test compared to heterotypic tumors; $p \leq 0.05$.

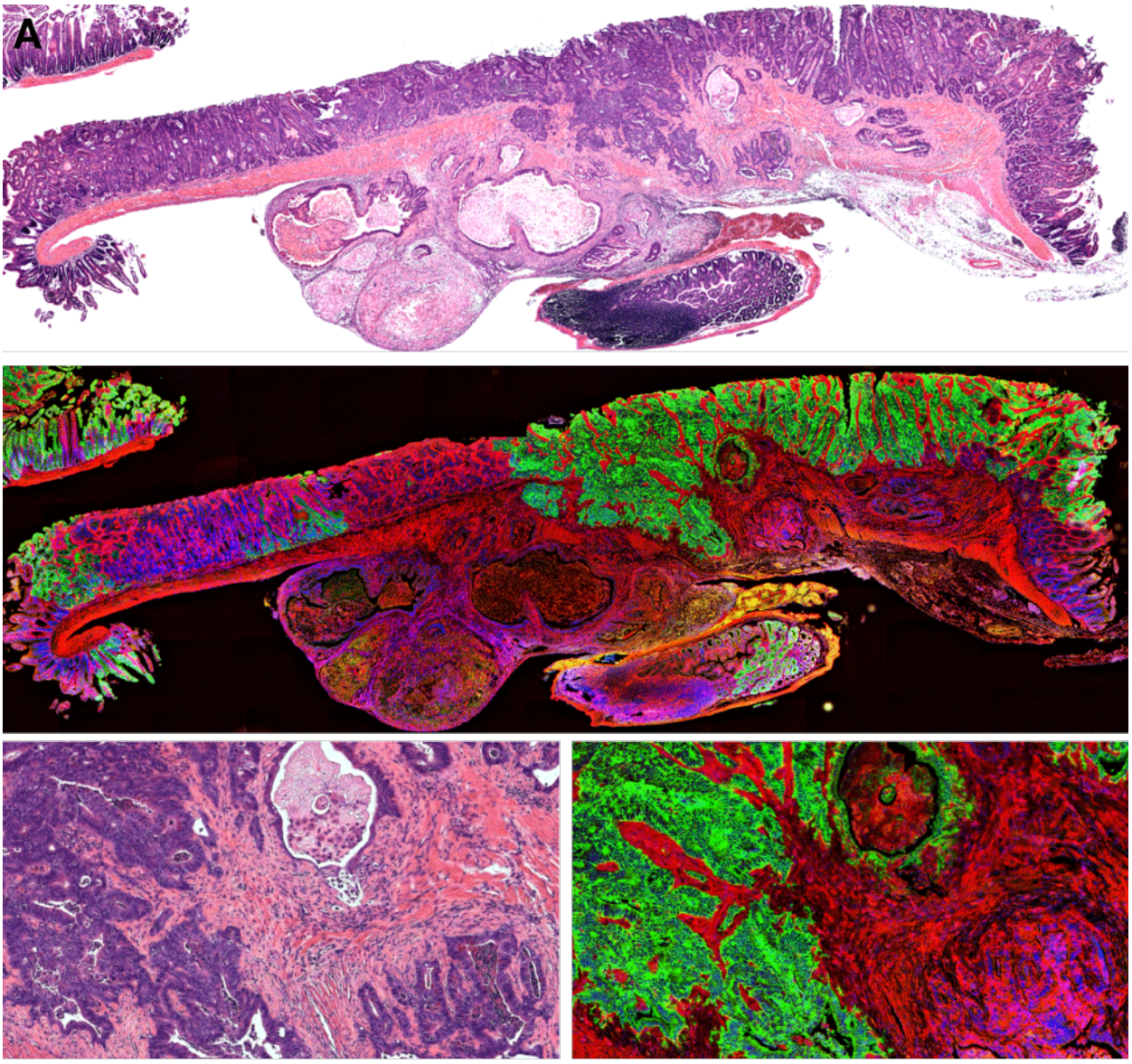
A

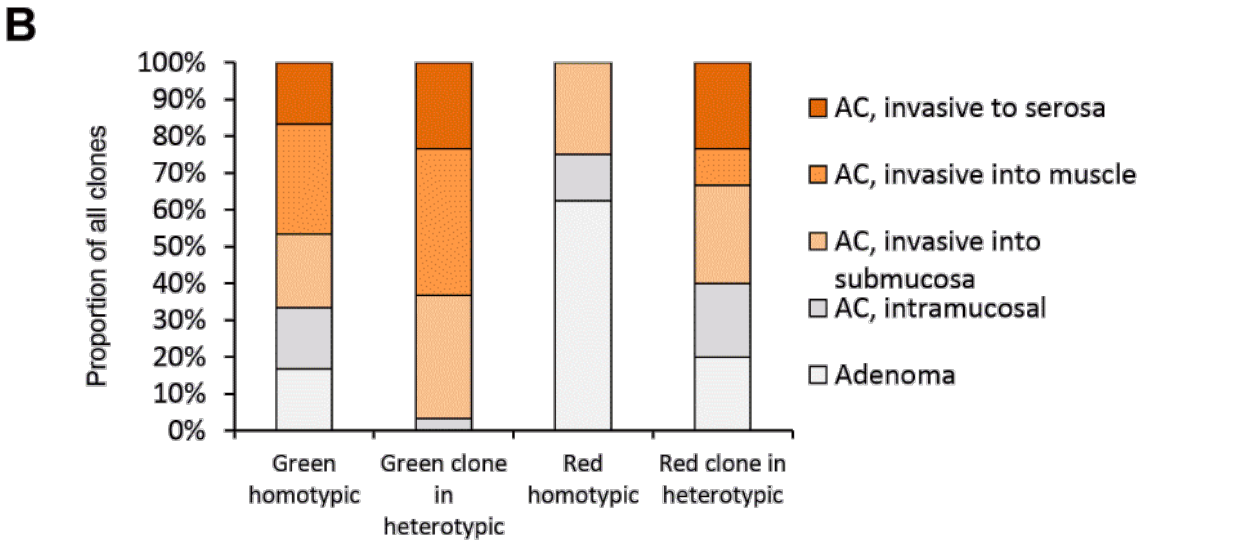
B
100%
90%
80%
70%
60%
50%
40%
30%
20%
10%
0%
Proportion of all clones
Green homotypic
Green clone in heterotypic
Red homotypic
Red clone in heterotypic
AC, invasive to serosa
AC, invasive into muscle
AC, invasive into submucosa
AC, intramucosal
Adenoma

Figure 3-7. Multiple clones within multi-ancestral tumors were frequently invasive. (A) Hematoxylin and eosin (H&E) of tissue sections revealed the many tumors were invasive. Multiple clones could be identified within multi-ancestral tumors by staining for tdTomato (red and EGFP (green). Close examination of neoplastic red and green cells frequently revealed invasion of both clones into the muscle layer. (B) Clones were scored for degrees of invasion. Some clones were not invasive through the lamina propria (shades of gray) and some were (shades of orange). Both clones within heterotypic tumors were more frequently invasive and tended to invade farther than similarly colored clones in homotypic tumors.

Tables

Table 3-1. Clonal architecture of intestinal tumors from 20 mosaic mice euthanized at 150 days of age.

			Phenotype, N (%)		
Intestinal region	**Pathological category**	**N**	**Heterotypic**	**Homotypic red**	**Homotypic green**
Proximal SI	ND	165	0	165 (100%)	0
Distal SI & colon	Adenoma with LGD	63	32 (51%)	24 (38%)	7 (11%)

ND, not determined; SI, small intestine; LGD, low-grade dysplasia.

doi:10.1371/journal.pone.0150170.t001

Table 3-2. Apc mutations in multi-ancestral tumors.

Tumor ID	Clone color	Nucleotide	Codon[a]	Base change	Amino acid change	Zygosity
6105 S4-A	Red	4109	1370	G > A	S > N	Heterozygous
	Green	2734	912	T > C	C > R	Heterozygous
6105 S4-C[b]	Red	2549	850	T > A	L > X	Heterozygous
	Green	2549	850	T > A	L > X	Homozygous
3866 CO-A	Red	2471	824	T > A	L > X	Heterozygous
	Green	2349	783	C > T	No change	Homozygous
	Green	2691	897	C > T	No change	Heterozygous
3704 CO-A	Red[c]	-	-	-	-	-
	Green	2506	836	A > G	R > G	Homozygous

[a]Mutations in Apc codons 747–953 and 1285–1513 were identified as described in Methods. The heterozygous Min mutation was detected in all tumor samples except 6105 S4-C green, in which the mutation was homozygous.

[b]Tumor 6105 S4-A was mostly red with only one small green clone as shown S4 Fig.

[c]The red tissue in tumor 3704 CO-A lacked the mutation at nucleotide 2506 found in the green tissue.

doi:10.1371/journal.pone.0150170.t002

Table 3-3. Clonal architecture of intestinal tumors from the distal small intestine and colon of 31 mosaic mice euthanized when moribund.

		Phenotype, N (% of pathological category)		
Pathological category	**N (% of total)**	**Heterotypic**	**Homotypic red**	**Homotypic green**
Adenoma with LGD	65 (45%)	40 (62%)	23 (35%)	2 (3%)
Adenoma with HGD	37 (26%)	21 (57%)	15 (41%)	1 (3%)
Intramucosal carcinoma	23 (16%)	10 (43%)	13 (57%)	0
Invasive adenocarcinoma	19 (13%)	13 (68%)	6 (32%)	0
Total, N (%)	144 (100%)	84 (58%)	57 (40%)	3 (2%)

LGD, low-grade dysplasia; HGD, high-grade dysplasia.

doi:10.1371/journal.pone.0150170.t003

Table 3-4. Average size of tumors from Fabp1-Cre^{+} mT/mG^{+} Pik3ca*$^{+}$ *Apc$^{Min/+}$* mice.

Tumor color	N of tumors	Tumor size (maximum diameter in mm), mean +/- standard deviation						
		All	S1	S2	S3	S4	CE	CO
Heterotypic	24	3.5 +/- 2.2	ND	ND	ND	3.9 +/- 2.7	2.2 +/- 2.2	3.3 +/- 1.4
Homotypic Green	28	2.0 +/- 1.6*	ND	ND	0.5 +/- 0.04	2.5 +/- 1.7	1.9 +/- 1.4	1.8 +/- 1.6*
Homotypic Red	43	1.1 +/- 0.6*	1.1 +/- 0.5	1.1 +/- 0.5	0.7 +/- 0.2	1.4 +/- 1.0*	ND	ND

S1-S4, proximal to distal quarters of the small intestine; CE, cecum; CO, colon

ND, not determined due to lack of tumors in this region

*Wilcoxon Rank Sum test compared to first row; p-value ≤ 0.050

References

1. Murugaesu, N., Chew, S. K. & Swanton, C. Adapting Clinical Paradigms to the Challenges of Cancer Clonal Evolution. *Am J Path* **182,** 1962–1971 (2013).
2. Suguro, M. *et al.* Clonal heterogeneity of lymphoid malignancies correlates with poor prognosis. *Cancer Sci* **105,** 897–904 (2014).
3. Medeiros, B. C., Othus, M., Fang, M., Appelbaum, F. R. & Erba, H. P. Cytogenetic heterogeneity negatively impacts outcomes in patients with acute myeloid leukemia. *Haematologica* **100,** 331–335 (2015).
4. Mengelbier, L. H. *et al.* Intratumoral genome diversity parallels progression and predicts outcome in pediatric cancer. *Nature Commun* **6,** 6125 (2015).
5. Mroz, E. A. *et al.* Intra-tumor genetic heterogeneity and mortality in head and neck cancer: analysis of data from the Cancer Genome Atlas. *PLoS Med* **12,** e1001786 (2015).
6. Landau, D. A. *et al.* Evolution and Impact of Subclonal Mutations in Chronic Lymphocytic Leukemia. *Cell* **152,** 714–726 (2013).
7. Anaka, M. *et al.* Intratumoral genetic heterogeneity in metastatic melanoma is accompanied by variation in malignant behaviors.*BMC Med Genomics* **6,** 40 (2013).
8. Pietras, A. Cancer stem cells in tumor heterogeneity. *Adv Cancer Res* **112,** 255–281 (2011).
9. Parsons, B. L. Many different tumor types have polyclonal tumor origin: Evidence and implications. *Mutat Res Rev Mutat Res* **659,** 232–247 (2008).
10. Thliveris, A. T. *et al.* Polyclonality of familial murine adenomas: Analyses of mouse chimeras with low tumor multiplicity suggest short-range interactions. *Proc Natl Acad Sci U S A* **102,** 6960–6965 (2005).

11. Thliveris, A. T. *et al.* Clonal Structure of Carcinogen-Induced Intestinal Tumors in Mice. *Cancer Prev Res* **4,** 916–923 (2011).

12. Novelli, M. R. *et al.* Polyclonal Origin of Colonic Adenomas in an XO/XY Patient with FAP. *Science* **272,** 1187–1190 (1996).

13. Thirlwell, C. *et al.* Clonality Assessment and Clonal Ordering of Individual Neoplastic Crypts Shows Polyclonality of Colorectal Adenomas. *Gastroenterol* **138,** 1441–1454.e7 (2010).

14. Su, L. K. *et al.* Multiple intestinal neoplasia caused by a mutation in the murine homolog of the *APC* gene. *Science* **256,** 668–670 (1992).

15. Newton, M. A., Clipson, L., Thliveris, A. T. & Halberg, R. B. A Statistical Test of the Hypothesis that Polyclonal Intestinal Tumors Arise by Random Collision of Initiated Clones. *Biometrics* **62,** 721–727 (2006).

16. Halberg, R. B. *et al.* Long-lived Min Mice Develop Advanced Intestinal Cancers through a Genetically Conservative Pathway. *Cancer Res* **69,** 5768–5775 (2009).

17. Saam, J. R. & Gordon, J. I. Inducible gene knockouts in the small intestinal and colonic epithelium. *J Biol Chem* **274,** 38071–38082 (1999).

18. Wong, M. H., Saam, J. R., Stappenbeck, T. S., Rexer, C. H. & Gordon, J. I. Genetic mosaic analysis based on Cre recombinase and navigated laser capture microdissection. *Proc Natl Acad Sci U S A* **97,** 12601–12606 (2000).

19. Merritt, A. J., Gould, K. A. & Dove, W. F. Polyclonal structure of intestinal adenomas in $Apc^{Min/+}$ mice with concomitant loss of Apc^{+} from all tumor lineages. *Proc Natl Acad Sci U S A* **94,** 13927 (1997).

20. Fischer, J. M., Schepers, A. G., Clevers, H., Shibata, D. & Liskay, R. M. Occult

progression by Apc-deficient intestinal crypts as a target for chemoprevention. *Carcinogenesis* **35,** 237–246 (2014).

21. Schepers, A. G. *et al.* Lineage Tracing Reveals Lgr5^{+} Stem Cell Activity in Mouse Intestinal Adenomas. *Science* **337,** 730–735 (2012).
22. Parsons, B. L. *et al.* ACB-PCR Quantification of *K- RAS* Codon 12 GAT and GTT Mutant Fraction in Colon Tumor and Non-Tumor Tissue. *Cancer Invest* **28,** 364–375 (2010).
23. Sottoriva, A. *et al.* A Big Bang model of human colorectal tumor growth. *Nat Genet* **47,** 209–216 (2015).
24. Kang, H. *et al.* Many private mutations originate from the first few divisions of a human colorectal adenoma. *J Pathol* **237,** 355–362 (2015).
25. Beutler, E., Collins, Z. & Irwin, L. E. Value of genetic variants of glucose-6-phosphate dehydrogenase in tracing the origin of malignant tumors. *N Engl J Med* **276,** 389–391 (1967).
26. Sansom, O. J. *et al.* Loss of Apc in vivo immediately perturbs Wnt signaling, differentiation, and migration. *Genes & Development* **18,** 1385–1390 (2004).
27. Moser, A., Pitot, H. & Dove, W. A dominant mutation that predisposes to multiple intestinal neoplasia in the mouse. *Science* **247,** 322–324 (1990).
28. Halberg, R. B. *et al.* Tumorigenesis in the multiple intestinal neoplasia mouse: Redundancy of negative regulators and specificity of modifiers. *Proc Natl Acad Sci U S A* **97,** 3461–3466 (2000).
29. Luongo, C., Moser, A. R., Gledhill, S. & Dove, W. F. Loss of Apc+ in Intestinal Adenomas from Min Mice. *Cancer Res* **54,** 5947–5952 (1994).
30. Luongo, C. & Dove, W. F. Somatic genetic events linked to the apc locus in intestinal

adenomas of the min mouse. *Genes, Chromosomes and Cancer* **17,** 194–198 (1996).

31. Haigis, K. M. *et al.* Tumor regionality in the mouse intestine reflects the mechanism of loss of Apc function. *Proc Natl Acad Sci U S A* **101,** 9769–9773 (2004).
32. Amos-Landgraf, J. M. *et al.* Monoallelic silencing and haploinsufficiency in early murine intestinal neoplasms. *Proc Natl Acad Sci U S A* **109,** 2060–2065 (2012).
33. Elahi, S. F., Miller, S. J., Joshi, B. & Wang, T. D. Targeted imaging of colorectal dysplasia in living mice with fluorescence microendoscopy. *Biomed Opt Express, BOE* **2,** 981–986 (2011).
34. Olson, T. J. P. & Halberg, R. B. Experimental Small Animal Colonoscopy. *Colonoscopy* (2011). doi:10.5772/21573
35. Schindelin, J. *et al.* Fiji: an open-source platform for biological-image analysis. *Nature Methods* **9,** 676–682 (2012).
36. Linkert, M. *et al.* Metadata matters: access to image data in the real world. *J Cell Biol* **189,** 777–782 (2010).
37. Skylar, O., Pau, G., M, S. & W, H. EBImage: Image processing toolbox for R. R package version 3.8.0. (2012). at <http://www.bioconductor.org/packages//2.7/bioc/html/EBImage.html>
38. Quyn, A. J., Swift, S., Nathke, I. & Appleton, P. L. Preparation of wholemount mouse intestine for high-resolution three-dimensional imaging using two-photon microscopy. *Journal of Microscopy* **234,** 196–204 (2009).
39. Preibisch, S., Saalfeld, S. & Tomancak, P. Globally optimal stitching of tiled 3D microscopic image acquisitions. *Bioinformatics* **25,** 1463–1465 (2009).
40. Nagase, H. & Nakamura, Y. Mutations of the *APC* adenomatous polyposis coli gene.

Human Mutat **2,** 425–434 (1993).

41. Waclaw, B. *et al.* A spatial model predicts that dispersal and cell turnover limit intratumour heterogeneity. *Nature* **525,** 261–264 (2015).

42. Kosmidou, V. *et al.* Tumor Heterogeneity Revealed by *KRAS*, *BRAF*, and *PIK3CA* Pyrosequencing: *KRAS* and *PIK3CA* Intratumor Mutation Profile Differences and Their Therapeutic Implications. *Human Mutat* **35,** 329–340 (2014).

43. Samuels, Y. High Frequency of Mutations of the *PIK3CA* Gene in Human Cancers. *Science* **304,** 554–554 (2004).

44. Vogelstein, B. *et al.* Genetic Alterations during Colorectal-Tumor Development. *N Engl J Med* **319,** 525–532 (2010).

45. Hare, L. M. *et al.* Physiological expression of the PI3K-activating mutation *Pik3ca*^{H1047R} combines with Apc loss to promote development of invasive intestinal adenocarcinomas in mice. *Biochemical Journal* **458,** 251–258 (2014).

46. Srinivasan, L. *et al.* PI3 Kinase Signals BCR-Dependent Mature B Cell Survival. *Cell* **139,** 573–586 (2009).

47. Cleary, A. S., Leonard, T. L., Gestl, S. A. & Gunther, E. J. Tumour cell heterogeneity maintained by cooperating subclones in Wnt-driven mammary cancers. *Nature* **508,** 113–117 (2014).

48. Marusyk, A. *et al.* Non-cell-autonomous driving of tumour growth supports sub-clonal heterogeneity. *Nature* **514,** 54–58 (2014).

49. Vooijs, M., Jonkers, J. & Berns, A. A highly efficient ligand-regulated Cre recombinase mouse line shows that LoxP recombination is position dependent. *EMBO reports* **2,** 292–297 (2001).

50. Anastassiadis, K., Glaser, S., Kranz, A., Bernhardt, K. & Stewart, A. F. A Practical Summary of Site-Specific Recombination, Conditional Mutagenesis, and Tamoxifen Induction of CreERT2. *Guide to Techniques in Mouse Development, Part B: Mouse Molecular Genetics, 2nd Edition* **477,** 109–123 (2010).

51. Tabassum, D. P. & Polyak, K. Tumorigenesis: it takes a village. *Nat Rev Cancer* **15,** 473–483 (2015).

CHAPTER 4

Looking forward: improved methods and models for studying intratumoral heterogeneity and multi-ancestral cancers.

Introduction

High intratumoral heterogeneity contributes to a poor clinical prognosis. Multiple ancestral clones can significantly enhance early genetic diversity within a cancer. If multiple ancestral clones are maintained throughout tumor evolution, the resulting heterogeneity might impact the growth, progression, and chemotherapy resistance of the tumor and consequently the prognosis of the patient. The work presented within this thesis establishes the significance of multiple tumor-founding cells in tumor initiation, growth, and progression.

Early activation of PI3K signaling drives tumor progression

PI3K drives rapid transformation of epithelial cells to malignancy within the proximal colon (Chapter 2.1). This effect was observed using a mouse model in which a PI3K construct expresses a constitutively active form of the kinase owing to the direct linkage of the catalytic subunit to the regulatory subunit. Results were reproduced using a mouse model which expresses a clinically relevant mutation in *Pik3ca* (H1047R), though penetrance decreased and latency of observable tumors increased (Appendix 8). However, these findings contrast with another published study which found no tumors in the intestines of mice following expression of the H1047R mutation in 1-5% of intestinal cells[1]. A few key factors might account for the difference. First, animals housed at different institutions have unique microbiomes which can drastically impact the penetrance of a neoplastic phenotype[2]. In our model, tumor initiation was localized to the proximal colon. In the model used by Hare and colleagues, the PI3K signaling may not have occurred in the cells which were most susceptible to transformation. Additionally, PI3K activation might need to occur larger fields of cells to facilitate tumor initiation. Even in our model, we observed very few tumors, indicating PI3K alone rarely drives tumor initiation

compared to the number of cells in which the transgene is expressed. Regardless, this mechanism of rapid transformation to malignancy might account for a small portion of interval cancers which arise between screening colonoscopies in patients. Administration of a PI3K-targeted inhibitor might provide a significant benefit in these patients (Appendices 8 and 9).

Activation of PI3K in cells which also carry at least one mutation in *Apc* results in increased tumor multiplicity and size (Chapter 2.2). Unlike tumors which formed in the absence of aberrations in the WNT pathway, these tumors exhibit nuclear β-catenin and a polypoid morphology similar to tumors initiated via loss of *Apc.* Therefore, PI3K activation prior to transformation likely facilitates WNT-mediated transformation and increases tumor growth rate and risk of progression to an adenocarcinoma. These results were later reproduced by another group using the Pik3ca(H1047R) gene mutation[1]. Altogether, these studies indicate that activation of the PI3K pathway is a driver of rapid tumor initiation, growth, and progression.

PI3K is often found in a subset of cancer cells and has thus been interpreted as a late event in tumorigenesis[3-5].However, tumors in which PI3K is constitutively active still progress through the adenoma-to-carcinoma sequence, albeit at an increased rate (Chapter 2.3). While this finding indicates that PI3K mutations can be identified within adenomas, the reduced time a tumor remains an adenoma likely accounts for the lack of adenomas identified with these mutations. Since PI3K is a driver of tumor growth and progression, one might expect cells expressing an activated form of PI3K to outcompete other clones, and therefore be found in most or all tumor cells of an advanced cancer if the mutation was present early in tumor evolution. However, in the multi-ancestral tumor setting, PI3K could be present in one of the tumor-founding cells prior to tumor initiation and still be found in only a subset of the overall tumor,

especially if PI3K signaling contributes to the recruitment or maintenance of additional tumor-founding cells and their progeny (Figure 1-1C and D).

Growth and progression of multi-ancestral tumors

The ancestral structure of tumors might change over time. Unless the multi-ancestral tumor architecture is necessary for tumor initiation, additional tumor-founding cells might be recruited sometime after a tumor mass already formed. Conversely, one ancestral clone might compete with other clones within a tumor, ultimately resulting in the purification of the tumor to a uni-ancestral structure.

Multiple ancestral clones are maintained during tumor progression (Chapter 3.1). The proportion of multi-ancestral tumors detected did not change over time between 150 day old mice and moribund mice (average age 494 +/- 93 days old), indicating that the multi-ancestral tumor structure likely arises early within the adenoma-to-carcinoma sequence. Multiple ancestral clones are maintained as the tumor progresses even after a long period of time in which ancestral clones could have been lost through poor competitive fitness.

the presence of multiple co-evolved clones is associated with tumor invasion and is consistent with the notion that increased heterogeneity is predictive of outcome (Chapter 3.2). PI3K might even be contributing to ongoing recruitment of additional tumor-founding cells or to the maintenance of multiple tumor clones. Unfortunately, due to differences in the Cre-recombination efficiency between the reporter and the Pik3ca* transgene, it is difficult to determine whether PI3K signaling was constitutively active within a subset or all ancestral clones within multi-ancestral tumors[6,7]. Even if the transgene was expressed in all ancestral clones, however, the multi-ancestral tumor architecture was still more frequently invasive than

homotypic tumors in which the transgene was expressed in all cells. Since this model was short-lived, it is unclear whether one clone might have outcompeted other clones. Even if the tumors would have eventually purified, however, the multi-ancestral tumor structure contributed to growth and invasion prior to purification. Determining the mechanism by which tumor-founding cells and their resulting progeny interact to promote tumor initiation, growth, and invasion might lead to the development of novel tumor prevention and therapeutic strategies. Unfortunately, it has been challenging to study how multiple ancestral clones contribute to human tumors due to the lack of reliable methods to detect multi-ancestral tumors in the clinic[8].

Detection of multi-ancestral tumors

Large sequencing studies frequently report mutations which are present within a vast majority of cells within any given tumor based on mutant allele frequencies identified within each sample. This approach can lead to the erroneous conclusion that all neoplastic cells within the tumor originated from a single tumor-founding cell. Allele frequencies are only rough estimates of the true pervasiveness of a mutation, and must be corrected for copy number variation, tumor cellularity, and differences in primer specificity and amplification efficiency. Even after correcting for all of these factors, a wide range of corrected frequencies (often >70% for tumor suppressors and >30% for oncogenes) are defined as supposedly clonal or "public" mutations. However, these studies often overlook a number of alternative explanations for these public mutations. Considering the wide range of corrected allele frequencies which are defined as public, minority clones which lack public mutations can be lost if they are less than 10% of the tumor mass. While single cell sequencing studies can theoretically overcome these challenges, the amount of missing data and artifacts introduced to any given cell in addition to

the expense of examining a sufficient number of cells results in the potential to miss or disregard minority clones which lack a common mutation. In addition, public mutations might arise prior to tumor initiation. Numerous reports have found driver mutations in completely pathologically and morphologically normal tissue[9-13]. If a mutation arises within normal tissue and expands into a patch or "field" of normal tissue, a multi-ancestral tumor could later arise from multiple partners within this tissue. Resulting ancestral clones might share a supposed driver mutation, but still represent distinct ancestry with regard to tumor initiation. Finally, public mutations might be present in the tumor stroma; even in tumors where a vast majority of the tumor area is epithelial and allele frequencies are corrected for the "tumor cellularity" of the mass, the densely packed nuclei within the stroma could still account for mutations. Indeed, key driver mutations in genes such as *APC*, *TP53* and *PTEN* have biologically significant impacts upon a tumor when found in stromal cells[14-16].

Multi-ancestral tumors might therefore be defined into different subsets based on the degree of genetic variance among ancestral clones. Since tumor-founding cells are not defined by their mutations, it is possible a multi-ancestral tumor might form from multiple unique tumor-founding cells which do not share any driver mutations or from multiple diverging tumor-founding cells which arise from within a field of cells which share at least one common mutation. The former case might therefore lead to a more genetically diverse tumor than the latter, but both should still have a greater degree of early genetic heterogeneity than uni-ancestral tumors, and disrupting the interactions among either unique or diverging tumor-founding cells might still reduce the frequency of tumor initiation.

While a field of cells might be defined by a given mutation, subfields can form when additional passenger mutations arise. Therefore, even if multiple tumor-founding cells arise

within a field and share a common mutation, it might still be possible to detect multi-ancestral tumors through comparing mutations between tumor and adjacent normal. If a mutation can be detected within adjacent normal which is present in only a subset of tumor cells, one likely explanation is that some tumor-founding cells contained the mutation, whereas others did not; therefore, the tumor is multi-ancestral. Understanding the mechanism by which multiple tumor-founding cells interact during tumor initiation might help identify other markers which could be used to detect multi-ancestral tumors in the clinic.

Formation of multi-ancestral tumors

Fields of mutant but morphologically normal cells might be a key intermediate during colon tumor initiation[13]. In the intestine, fields form when a mutant cell clonally populates a crypt which undergoes fission to create multiple crypts which all contain the same mutation. Fields of mutant crypts can remain morphologically normal for an unknown length of time[9-11,13]. While single crypts might produce insufficient signal to impact their environment, fields of crypts might together reach a critical threshold of signaling required to facilitate transformation. Thus multiple tumor-founding cells interacting within a field of mutant but morphologically normal crypts might promote tumorigenesis.

Two hypotheses might explain the how multiple tumor-founding cells might interact to promote tumorigenesis: recruitment, in which one or more tumor-founding cells transform other nearby cells and thus recruit them to form a tumor mass; and cooperation, in which multiple tumor-founding cells might become independently transformed in close physical and temporal proximity and then cooperate to facilitate tumor initiation. The frequency of multi-ancestral tumors in mouse models in which differentially labeled cells had high versus low risk of

independent transformation was best explained with the recruitment model. (Appendix 7). Another group also detected recruitment and transformation of normal cells during gliomagenesis[17]. In this setting, recruited cells were able to establish tumors in the absence of the recruiter cells after transplantation into a new host. Unfortunately, the mechanism by which cells transform other nearby cells remains unclear. Determining how this occurs might lead to novel tumor prevention strategies.

Inflammation reduces the frequency of multi-ancestral tumors[18]. If multiple tumor-founding cells promote tumorigenesis, inflammation might be sufficient to promote tumor initiation in a single tumor-founding cell. Alternatively, inflammation might disrupt the communication among potential tumor-founding cells, thus eliminating the opportunity for recruitment or cooperation to occur. Finally, inflammation might promote the expansion of similarly labeled, morphologically-normal cells and thus reduce the power to detect multi-ancestral tumors.

The microbiome can also promote colon tumorigenesis[19,20]. A tumor-promoting microbiome might alter the environment sufficiently to facilitate recruitment and transformation of normal cells; alternatively, the microbiome might reduce the dependency upon multiple tumor-founding cells similar to chronic inflammation. Determining how various microbiome species impact the formation of multi-ancestral tumors might guide understanding of how the microbiome impacts tumor initiation. Appropriate modulation of the microbiome might lead to novel tumor prevention strategies.

Chemotherapy response of multi-ancestral tumors

Intratumoral heterogeneity likely contributes to chemotherapy resistance[5,21-25]. Some tumors contain pre-existing clones that are resistance to therapies within minor subclones[5,21,24]. Similarly, targeted therapies chosen specifically to target oncogene addictions can fail in the clinic because not every tumor cell carries the actionable mutation[5]. Resistance can also be conferred non-cell-autonomously among diverse cell populations[26]. Therefore, preventing heterogeneity from arising or being maintained within a tumor might increase a patient's overall prognosis, and targeting the mechanism by which resistance can be conferred non-cell autonomously might help overcome therapy resistance. Unfortunately, it is currently unknown whether multi-ancestral tumors respond differently to therapy than uni-ancestral tumors. The multi-ancestral architecture might provide a useful prognostic indicator for patients, and interactions among ancestral clones might be targeted to help overcome resistance.

Modeling multi-ancestral tumors

Thus far, research on multi-ancestral tumors has been limited in part by the ability to identify these tumors. Most studies in humans and mice have been limited to two labels, allowing detection of a maximum of two ancestral clones, and patches of similarly labeled cells are often so large as to make detection of multi-ancestral tumors unlikely[8,27].

An ideal animal model would label every cell uniquely prior to tumor initiation. While a limited number of fluorescent reporters exist, genetic barcodes produce a virtually infinite number of possible labels. Using an inducible piggyBac transposase system, a short length of DNA can be randomly inserted within the genome[28]. If cells are labeled shortly before tumor initiation, most tumor-founding cells should have unique insertion sites. Thus, sequencing of a bulk tumor mass will reveal the number of unique insertion sites and provide a more accurate

estimate of the number of contributing ancestors than any model system used to date. This would make it possible to answer a number of important questions, including how prevalent the multi-ancestral structure is within a given cancer type, as well as how many ancestors typically contribute to pre-malignant tumors versus advanced disease. Sectioning, isolating, and sequencing distinct tumor regions would reveal the prevalence and location of individual ancestral clones, and might make it possible to determine the degree of genetic variation within and among ancestral clones. Thus, a much greater understanding of tumor evolution can be gained.

To understand the mechanism by which ancestral clones interact during tumor initiation, growth, progression, and chemotherapy response, controlling the genetics of individual tumor-founding cells would be ideal. The Cre-lox system makes it possible to genetically modify clones. Using one such system, we were able to generate mice in which some but not all intestinal epithelial cells expressed an activated form of PI3K (Chapter 2 and 3.2). Unfortunately, due to differences in recombination efficiency, multiple Cre-dependent genes are not always simultaneously recombined within a single cell[6,29]. To be confident a Cre-dependent gene has not recombined within certain tissues, such as when studying the transformation and recruitment of normal epithelial cells, it is therefore advisable to use aggregation chimeras (Appendix 7). If both embryos used to generate each aggregation chimeras contained different transposon-dependent short sequences and the piggyBac transposon system, it would be possible to estimate the number and proximity of recruiter and recruited clones within a tumor mass.

Due to environmental variability and limited control, it is challenging to determine the molecular mechanism by which clones are interacting in mouse models. Primary culture of normal and tumor cells overcomes some of these challenges. For example, using an air-liquid

interface, normal intestinal cells can be grown with or without associated stromal cells[30]. Using this experimental approach, Lemieux and colleagues were able to show a stepwise series of mutations resulted in transformation of these crypts in culture. Such a system could be used to co-culture clones of interest and observe recruitment and cooperation *in vitro*. RNA-seq and secreted factor analyses can then be used to identify molecules of interest. Individual molecules can be examined for their sufficiency and necessity in altering cellular phenotypes *in vitro.* Phenotypes even be confirmed *in vivo* by transplanting the cells back into their endogeneous environment whenever possible; for example, primary colon cells can be grafted into mouse colons[31].

Using these improved models it will be possible to further investigate the biological relevance of multi-ancestral tumors and the mechanism by which these tumors arise, invade, metastasize, and respond to therapy.

Closing thoughts

Early tumor heterogeneity has the greatest opportunity to impact the evolution of a tumor. While at a very small size, tumors must escape immune surveillance, contact inhibition, and other critical checkpoints to grow into a detectable mass. Cellular diversity increases the number of chances to spontaneously evolve one of these tumor hallmarks, while also increasing the opportunity for meaningful interactions to evolve among tumor cell populations.

While the genotype of a cell may provide clues to how that cell will behave, it is not the whole story. Cells carrying tumor driver mutations can maintain a completely normal morphology[9-11,13]. Meanwhile, tumors can form which lack detectable mutations in known tumor drivers[32]. Genetically similar tumors can have vastly different outcomes. Thus, there is a great

deal more to the behavior of cell and its potential malignancy than genetics alone. A cell's environment is highly likely to impact its behavior and vice versa[15,16,22,26,33]. Just as tumor cells interact with their environment to recruit supportive stroma and drive angiogenesis, so too is it likely those tumor cells interact with each other in a meaningful way[33]. Diverse neighbors increase the kinds of interactions that can take place. Indeed, multiple cooperating tumor subclones can be essential for tumor propagation, and non-dominant subclones can promote the survival and metastatic potential of dominant clones[34,35]. It remains to be determined whether multiple diverse ancestral clones are necessary or sufficient to maintain a tumor, or to drive invasion and metastasis.

Altogether, this work reveals the potential that the multi-ancestral tumor architecture might contribute to tumor growth and progression and thus impact the prognosis of the patient. Our data indicate that multiple tumor-founding cells contribute to tumor initiation, and their progeny persist and can cooperate during tumor progression. Additional research is needed to better understand the prevalence of this tumor structure within the clinic and precisely how this structure is associated with prognosis compared to other measurements of heterogeneity. Ultimately, identifying how multiple ancestral clones communicate to contribute to tumor maintenance, invasion, and metastasis might lead to the development of novel treatment strategies. It is time to look beyond the genetics and into the biologically relevant phenotypes which arise as a consequence of clonal interactions within a tumor.

References

1. Hare, L. M. *et al.* Physiological expression of the PI3K-activating mutation Pik3caH1047R combines with Apc loss to promote development of invasive intestinal adenocarcinomas in mice. *Biochemical Journal* **458,** 251–258 (2014).
2. Stappenbeck, T. S. & Virgin, H. W. Accounting for reciprocal host–microbiome interactions in experimental science. *Nature* **534,** 191–199 (2016).
3. Waclaw, B. *et al.* A spatial model predicts that dispersal and cell turnover limit intratumour heterogeneity. *Nature* **525,** 261–264 (2015).
4. Fearon, E. R. & Vogelstein, B. A genetic model for colorectal tumorigenesis. *Cell* **61,** 759–767 (1990).
5. Kosmidou, V. *et al.* Tumor Heterogeneity Revealed by *KRAS*, *BRAF*, and *PIK3CA* Pyrosequencing: *KRAS* and *PIK3CA* Intratumor Mutation Profile Differences and Their Therapeutic Implications. *Human Mutat* **35,** 329–340 (2014).
6. Vooijs, M., Jonkers, J. & Berns, A. A highly efficient ligand-regulated Cre recombinase mouse line shows that LoxP recombination is position dependent. *EMBO reports* **2,** 292–297 (2001).
7. Anastassiadis, K., Glaser, S., Kranz, A., Bernhardt, K. & Stewart, A. F. A Practical Summary of Site-Specific Recombination, Conditional Mutagenesis, and Tamoxifen Induction of CreERT2. *Guide to Techniques in Mouse Development, Part B: Mouse Molecular Genetics, 2nd Edition* **477,** 109–123 (2010).
8. Novelli, M. *et al.* X-inactivation patch size in human female tissue confounds the assessment of tumor clonality. *Proc Natl Acad Sci U S A***100,** 3311–3314 (2003).
9. Yamada, S., Yashiro, M., Maeda, K., Nishiguchi, Y. & Hirakawa, K. A novel high-

specificity approach for colorectal neoplasia: Detection of *K-ras2* oncogene mutation in normal mucosa. *Int. J. Cancer* **113,** 1015–1021 (2004).

10. Tohi, M., Luo, F. C. & Ronai, Z. Detection of K-ras Mutation in Colonic Effluent Samples From Patients Without Evidence of Colorectal Carcinoma. *JNCI* **86,** 1007–1010 (1994).
11. Zhu, D. *et al.* K-ras gene mutations in normal colorectal tissues from K-ras mutation-positive colorectal cancer patients. *Cancer Res***57,** 2485–2492 (1997).
12. Jonason, A. S. *et al.* Frequent clones of p53-mutated keratinocytes in normal human skin. *Proc Natl Acad Sci U S A***93,** 14025–14029 (1996).
13. Fischer, J. M., Schepers, A. G., Clevers, H., Shibata, D. & Liskay, R. M. Occult progression by Apc-deficient intestinal crypts as a target for chemoprevention. *Carcinogenesis* **35,** 237–246 (2014).
14. Bar, J., Moskovits, N. & Oren, M. Involvement of stromal p53 in tumor-stroma interactions. *Seminars in Cell & Developmental Biology* **21,** 47–54 (2010).
15. Trimboli, A. J. *et al.* Pten in stromal fibroblasts suppresses mammary epithelial tumours. *Nature* **461,** 1084–1091 (2009).
16. Tanwar, P. S., Zhang, L., Roberts, D. J. & Teixeira, J. M. Stromal Deletion of the APC Tumor Suppressor in Mice Triggers Development of Endometrial Cancer. *Cancer Res***71,** 1584–1596 (2011).
17. Fomchenko, E. I. *et al.* Recruited Cells Can Become Transformed and Overtake PDGF-Induced Murine Gliomas In Vivo during Tumor Progression. *PLoS ONE* **6,** e20605 (2011).
18. Leedham, S. J. *et al.* Clonality, Founder Mutations, and Field Cancerization in Human

Ulcerative Colitis–Associated Neoplasia. *Gastroenterol* **136,** 542–550.e6 (2009).

19. Commensal bacteria drive endogenous transformation and tumour stem cell marker expression through a bystander effect. 1–10 (2015). doi:10.1136/gutjnl-2014-307213
20. Zackular, J. P. *et al.* The Gut Microbiome Modulates Colon Tumorigenesis. *mBio* **4,** e00692–13–e00692–13 (2013).
21. Landau, D. A. *et al.* Evolution and Impact of Subclonal Mutations in Chronic Lymphocytic Leukemia. *Cell* **152,** 714–726 (2013).
22. Merlo, L. M. F., Pepper, J. W., Reid, B. J. & Maley, C. C. Cancer as an evolutionary and ecological process. *Nat Rev Cancer* **6,** 924–935 (2006).
23. Greaves, M. & Maley, C. C. Clonal evolution in cancer. *Nature* **481,** 306–313 (2012).
24. Tougeron, D. *et al.* Effect of low-frequency KRAS mutations on the response to anti-EGFR therapy in metastatic colorectal cancer. *Ann Oncol* **24,** 1267–1273 (2013).
25. Gerlinger, M. *et al.* Intratumor Heterogeneity and Branched Evolution Revealed by Multiregion Sequencing. *N Engl J Med* **366,** 883–892 (2012).
26. Straussman, R. *et al.* Tumour micro-environment elicits innate resistance to RAF inhibitors through HGF secretion. *Nature* **487,** 500–504 (2012).
27. Parsons, B. L. Many different tumor types have polyclonal tumor origin: Evidence and implications. *Mutat Res Rev Mutat Res* **659,** 232–247 (2008).
28. Cadiñanos, J. & Bradley, A. Generation of an inducible and optimized piggyBac transposon system. *Nucl Acids Res* **35,** e87–e87 (2007).
29. Wong, M. H., Saam, J. R., Stappenbeck, T. S., Rexer, C. H. & Gordon, J. I. Genetic mosaic analysis based on Cre recombinase and navigated laser capture microdissection. *Proc Natl Acad Sci U S A* **97,** 12601–12606 (2000).

30. Lemieux, E., Cagnol, S., Beaudry, K., Carrier, J. & Rivard, N. Oncogenic KRAS signalling promotes the Wnt/β-catenin pathway through LRP6 in colorectal cancer. **34,** 4914–4927 (2014).

31. Enquist, I. B. *et al.* Lymph node-independent liver metastasis in a model of metastatic colorectal cancer. *Nature Commun* **5,** 3530 (2014).

32. Bozic, I. *et al.* Accumulation of driver and passenger mutations during tumor progression. *Proc Natl Acad Sci U S A* **107,** 18545–18550 (2010).

33. Tabassum, D. P. & Polyak, K. Tumorigenesis: it takes a village. *Nat Rev Cancer* **15,** 473–483 (2015).

34. Cleary, A. S., Leonard, T. L., Gestl, S. A. & Gunther, E. J. Tumour cell heterogeneity maintained by cooperating subclones in Wnt-driven mammary cancers. *Nature* **508,** 113–117 (2014).

35. Marusyk, A. *et al.* Non-cell-autonomous driving of tumour growth supports sub-clonal heterogeneity. *Nature* **514,** 54–58 (2014).

APPENDICES

APPENDIX 1. Transgenes and gene mutations used in animal models throughout the thesis.

Genetic element	Locus	Cre-dependent?	Effect
Adeno-Cre	Viral	No	Adenovirus transiently expresses Cre-recombinase in infected cells
Apc^{1638N}	Endogenous	No	Expresses a truncated APC; slightly predisposes to intestinal tumorigenesis
Apc^{CKO}	Endogenous	Yes	Expresses a truncated APC after Cre recombination; predisposes to intestinal tumorigenesis
Apc^{Min}	Endogenous	No	Expresses a truncated APC; predisposes to intestinal tumorigenesis
Fabp1-Cre	Unknown	No	Expresses Cre-recombinase in some distal intestinal epithelial cells
Kras$^{LSL-G12D}$	Endogenous	Yes	Expresses a constitutively activated KRAS after Cre recombination
mT/mG	Rosa26	Yes	Expresses tdTomato prior to Cre-recombination; Expressed EGFP after Cre-recombination
Pik3ca*	Rosa26	Yes	Expresses a constitutively activated PI3K after Cre-recombination; predisposes to intestinal tumorigenesis and malignant transformation
Pik3ca(H1047R)	Rosa26	Yes	Expresses a constitutively activated PI3K after Cre-recombination; slightly predisposes to intestinal tumorigenesis and malignant transformation

APPENDIX 2. Supplemental Figures for Chapter 2.1: Mice Expressing Activated PI3K Rapidly Develop Advanced Colon Cancer

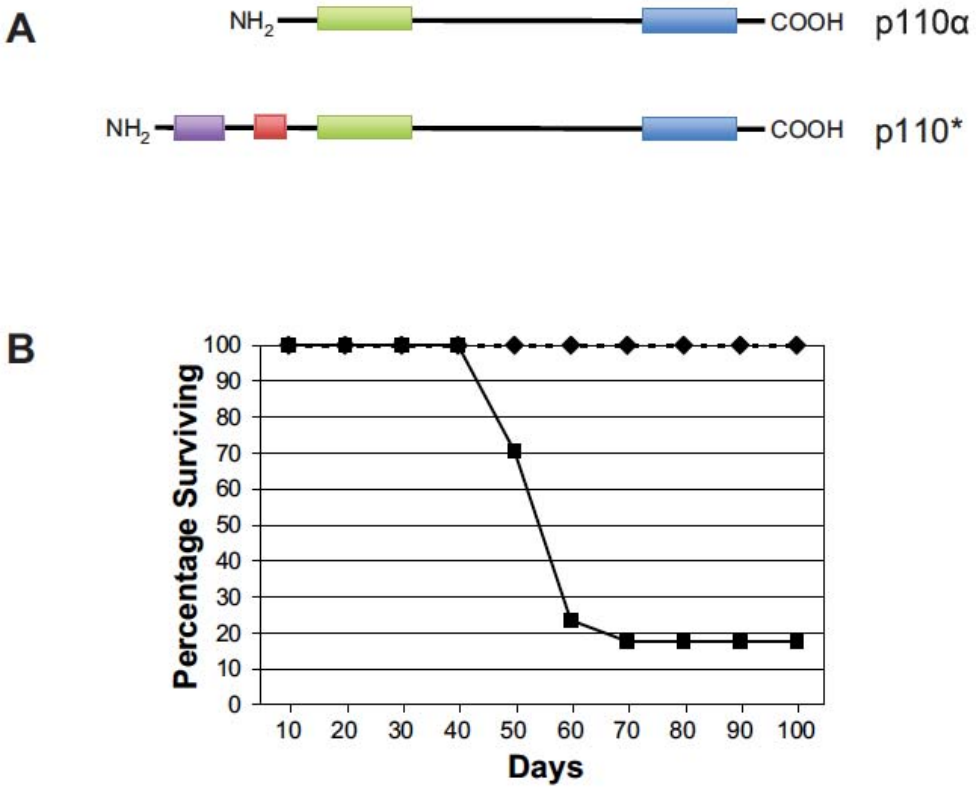

Appendix 2-1.

(A) PIK3ca* encodes a dominant active form of PI3K (p110*). p110α is the native subunit of PI3K that was modified to create p110*, which consists of p110α (green and blue rectangles) bound by a glycine kinker (red rectangle) to the iSH2 domain of the p85 subunit of PI3K (purple rectangle). (B) Fabp1-Cre^{+} PIK3ca*$^{+}$ mice die very young. The Kaplan-Meier survival curve demonstrates PIK3ca*$^{+}$ mice (squares, 3/17) survived up to 100 days of age, whereas all Fabp1-Cre^{0} PIK3ca*$^{+}$ littermates (diamonds, 5/5) were healthy at that time. The three Fabp1-Cre^{+} PIK3ca*$^{+}$ mice that survived to 100 days were sacrificed; one was noted to have severe intestinal obstruction but had not yet become moribund, whereas the other two did not possess grossly visible colon tumors. Note that Fabp1-Cre^{+} PIK3ca*$^{+}$ mice were indistinguishable from Fabp1-Cre^{0} PIK3ca*$^{+}$ littermates with respect to size, weight, and activity level until they became moribund.

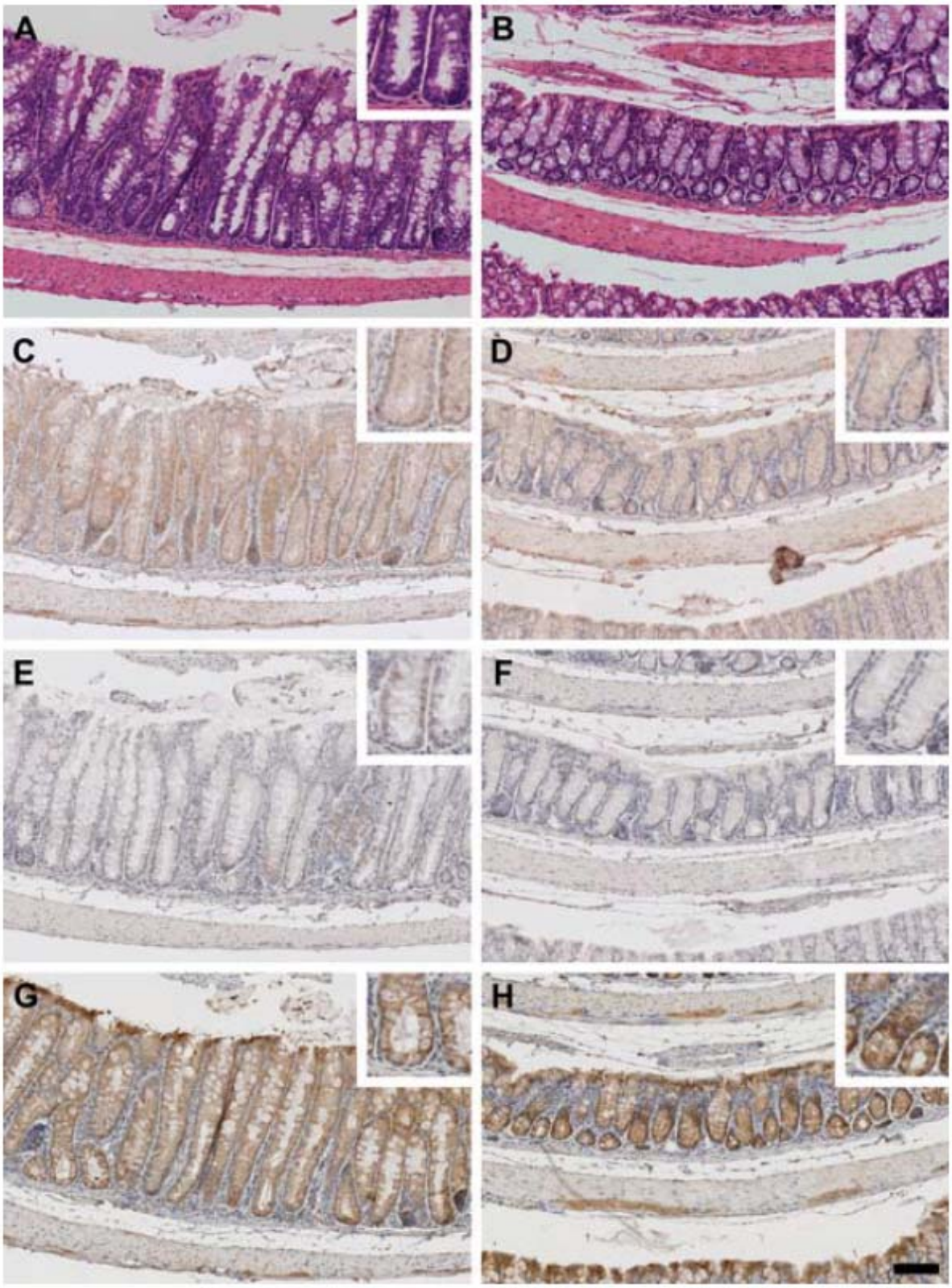
A
B
C
D
E
F
G
H

Appendix 2-2. The colon in Fabp1-Cre^{+} PIK3ca*$^{+}$ mice shows marked hyperproliferation. A mutant (A, C, E, G) and its wild-type littermate (B, D, F, H) were sacrificed at 58 days of age. The colon was removed, splayed open, rolled, embedded in paraffin, and cut. Sections were stained for H&E (A and B). The crypts in mutants were approximately three times longer than those in controls. Immunohistochemistry (IHC) reveals that this change correlates with AKT being more highly phosphorylated (C and D) and having increased cellular proliferation (E and F) by antibodies against pAKT and Ki67, respectively. This hyperproliferation does not appear to rely on aberrant WNT signaling, as β-catenin is not elevated or nuclear as shown by IHC (G and H). Scale bar: 100 μm.

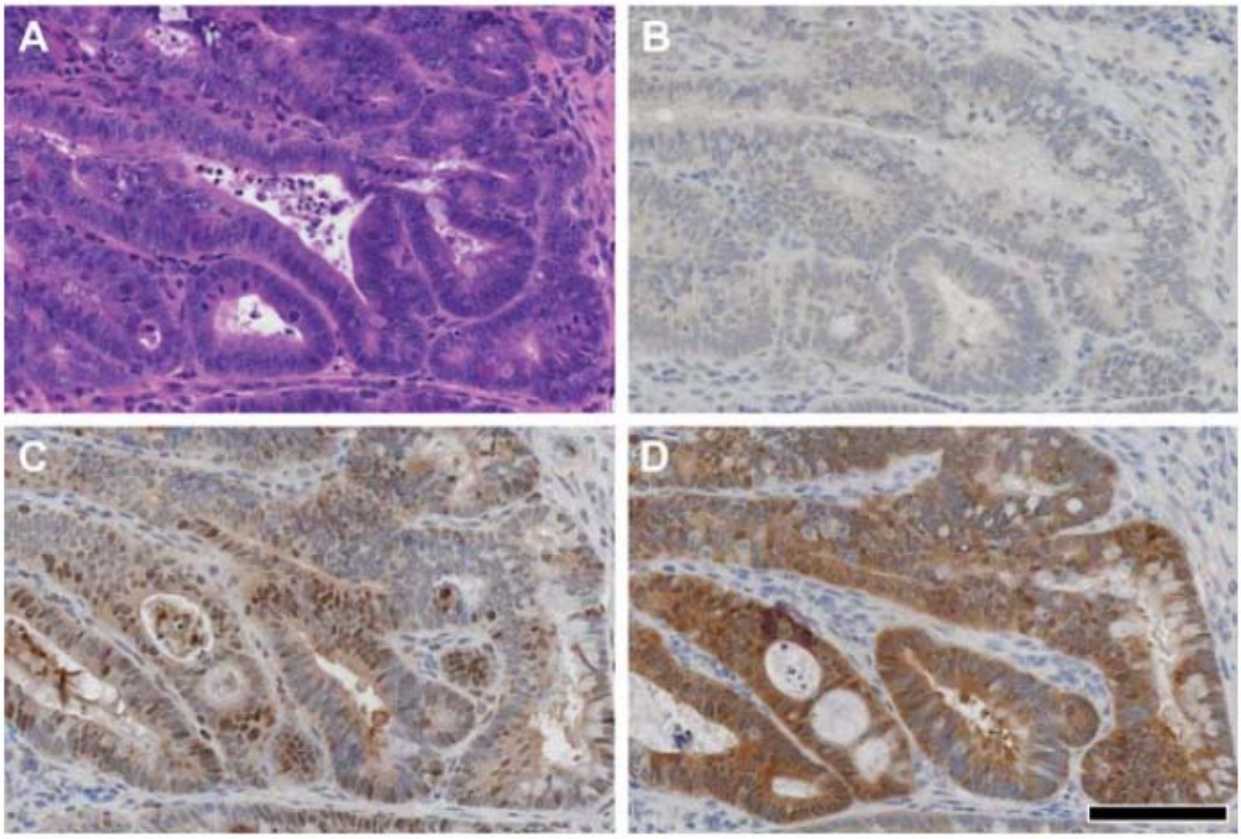
A
B
C
D

Appendix 2-3. PI3K/AKT signaling appears unperturbed in colon adenocarcinomas from F1 *Apc*$^{Min/+}$ mice. Sections of an adenocarcinoma from an F1 *Apc*$^{Min/+}$ mouse were stained with H&E (A). Immunohistochemical (IHC) staining using antibodies against pAKT and Ki67 revealed that the level of pAKT was relatively low (B), whereas the level of cellular proliferation was moderately high (C), respectively. The neoplastic transformation was coupled to the translocation of the β-catenin to the nucleus which indicative of aberrant WNT signaling as shown by IHC (D). Scale bar: 100 μm.

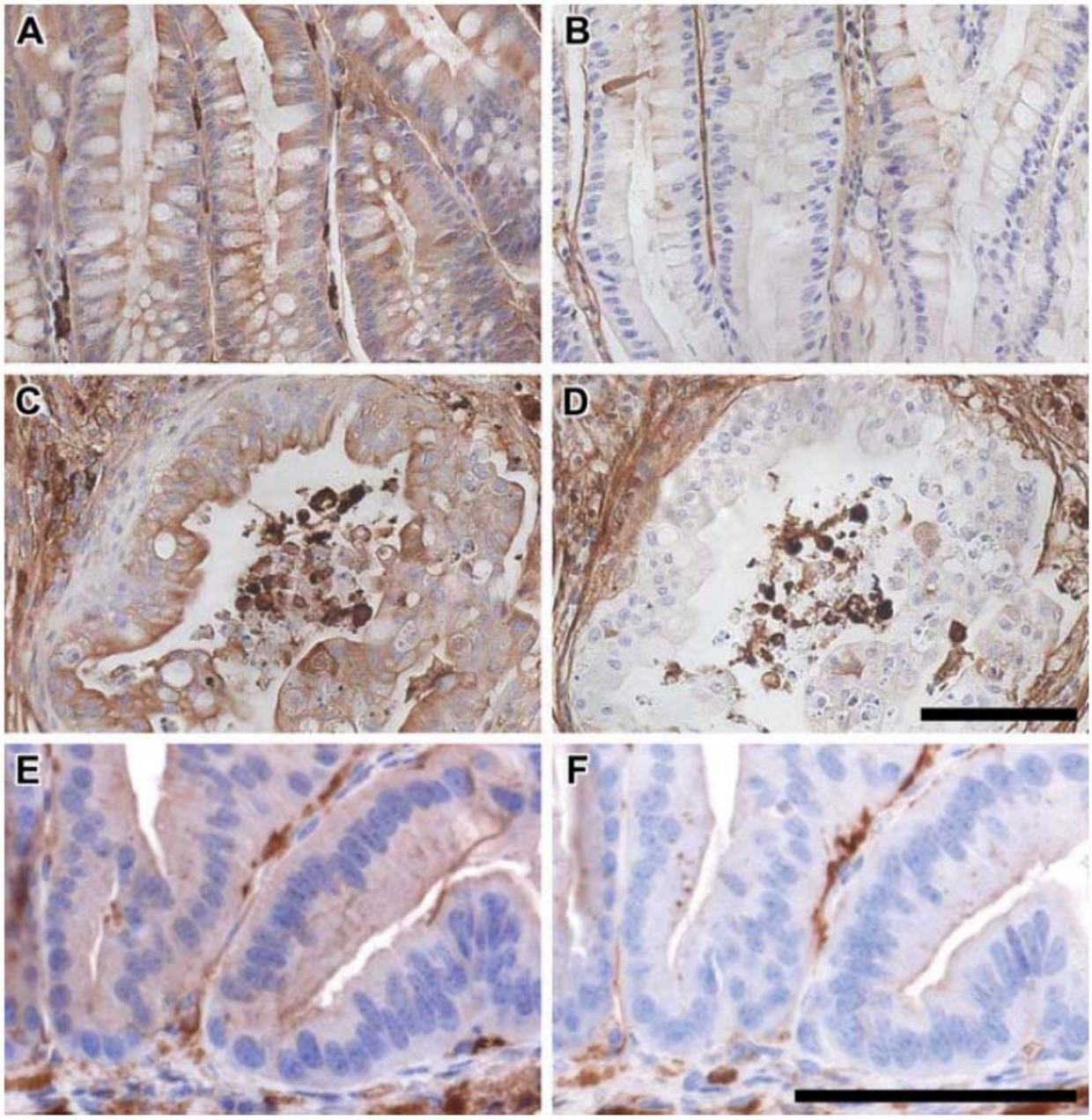
A
B
C
D
E
F

Appendix 2-4. Cytokeratin staining of the colon epithelium and tumor of Fabp1-Cre^{+} PIK3ca*$^{+}$ mice. The colonic epithelium (A and B), a proximal colon tumor (C and D), a tumor extending into the ovary (E and F) of Fabp1-Cre^{+} PIK3ca*$^{+}$ mice were stained for cytokeratin 20 (A, C, E) and cytokeratin 7 (B, D, F). The tumor tissue demonstrates 1+ cytokeratin 20 staining and negative cytokeratin 7 signaling indicating that these tumors are of intestinal origin. Scale bar (A-D): 100 μm. Scale bar (E-F): 100 μm.

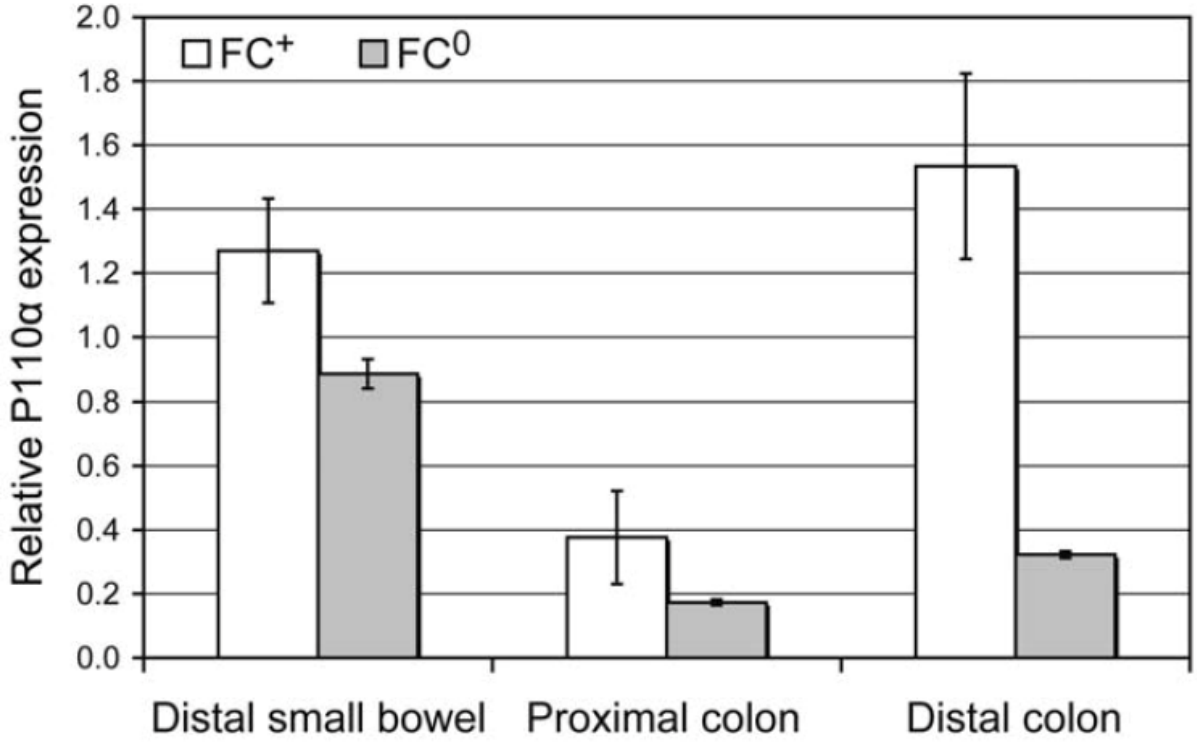
2.0
1.8
1.6
1.4
1.2
1.0
0.8
0.6
0.4
0.2
0.0
FC+
FC0
Relative P110α expression
Distal small bowel
Proximal colon
Distal colon

Appendix 2-5. Expression of p110α is greater in the colon of Fabp1-Cre^{+} PIK3ca*$^{+}$ mice than Fabp1-Cre^{0} PIK3ca*$^{+}$ mice. Quantitative PCR revealed that transcription of p110α was higher in experimental animals (FC^{+}) than controls (FC^{0}). P-values (two-tailed Student's t-test) = 0.02 for distal small bowel, 0.07 for proximal colon and 0.002 for distal colon.

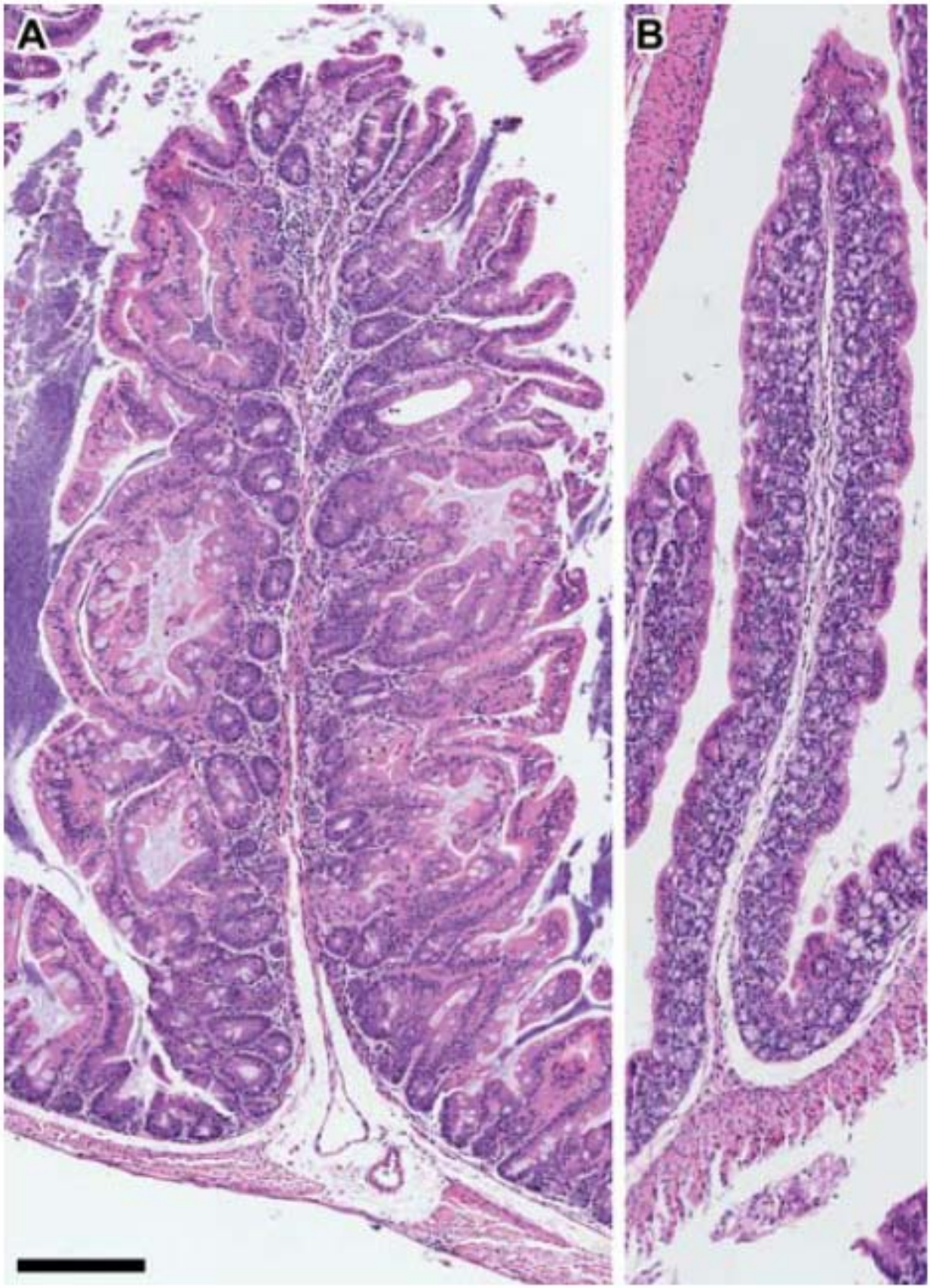
A
B

Appendix 2-6. PIK3ca* induces mucosal hyperplasia throughout the colon. A Fabp1-Cre^{+} PIK3ca*$^{+}$ mouse and its wild-type littermate were sacrificed at 20 days of age. A H&E stained cross-section of a rugal fold from the proximal colon of a Fabp1-Cre^{+} PIK3ca*$^{+}$ mouse exhibited a villiform hyperplasia with numerous dilated crypts filled with mucin (A). These lesions are reminiscent of sessile serrated adenomas in humans, which are also preferentially located in the right colon and are associated with mucinous adenocarcinoma. Such lesions were never observed in the proximal colon of controls (B). Scale bar: 200 μm.

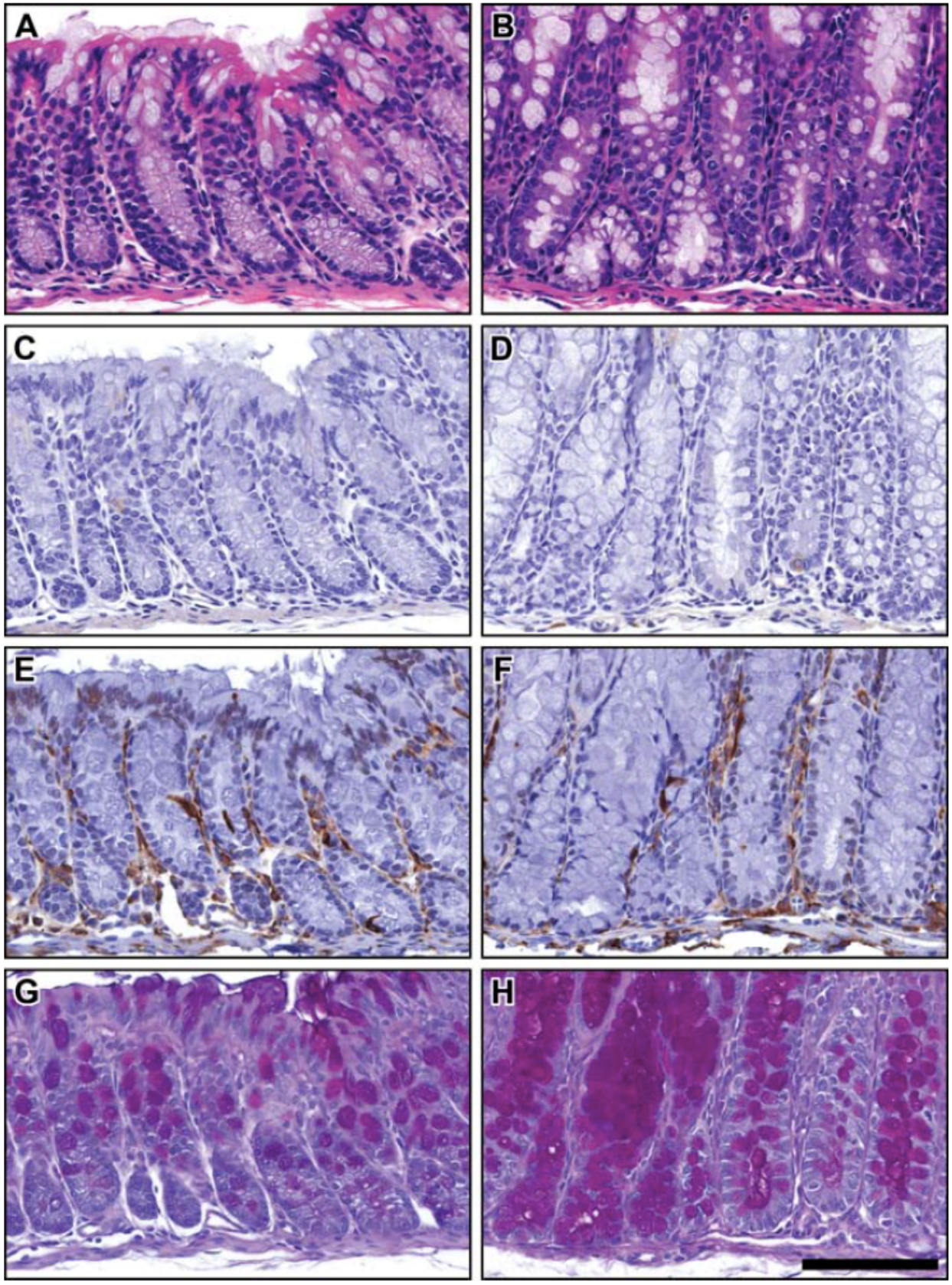
A
B
C
D
E
F
G
H

Appendix 2-7. Intestinal cell fate is maintained in the intestines of Fabp1-Cre^{+} PIK3ca*$^{+}$ mice. Experimental mice (right panel) and controls (left panel) were sacrificed at 30 days of age. The intestinal tract was isolated, rolled, fixed, processed, embedded in paraffin, and sectioned. Sections were stained with H&E (A and B), for lysozyme (C and D), for synatophysin (E and F), and with PAS (G and H) to assess absorptive, Paneth, enteroendocrine, and goblet cells. Scale bar: 100 μm.

APPENDIX 3. Supplemental Table and Figures for Chapter 2.2: *PIK3CA* and *APC* mutations are synergistic in the development of intestinal cancers.

Genotype	N of mice	Age in days, mean (range)	Gender (M:F)	Tumor number, mean (range)			
				Total	Cecum and colon	S3 and S4	S1 and S2
FC^{1}3K^{1}Apc$^{Min/+}$	18	52 (42-82)	7:11	8.7 (1-16)	2.9 (1-7)	5.3 (0-11)	0.4 (0-11)
FC^{0}3K^{1}Apc$^{Min/+}$	17	52 (42-82)	12:5	1.3 (0-8)*	0.1 (0-1)*	0.5 (0-3)*	0.7 (0-6)
FC^{0}3K^{0}Apc$^{Min/+}$	9	58 (44-84)	3:6	1.2 (0-2)*	0 (0)*	0.8 (0-2)*	0.4 (0-4)
FC^{1}3K^{0}Apc$^{Min/+}$	6	61 (44-84)	3:3	2.2 (1-6)*	0 (0)*	1.5 (0-4)*	0.7 (0-2)
FC^{1}3K^{1}Apc$^{+/+}$	11	48 (42-55)	7:4	1.4 (0-3)*	1.4 (0-3)*	0 (0)*	0 (0)
FC^{1}3K^{1}Apc$^{fl/+}$	23	56 (35-76)	10:13	9.5 (4-18)	2.8 (1-8)	6.7 (1-13)	0 (0)

Appendix 3-1. Baseline characteristics of the Fabp1-Cre^{+} Pik3ca*$^{+}$ *Apc$^{Min/+}$*, Fabp1-Cre^{+} Pik3ca*$^{+}$ *Apc$^{fl/+}$*, and control littermates. Fabp1-Cre^{+} Pik3ca*$^{+}$ *Apc$^{Min/+}$* mice became moribund on average by 52 days of age. Necropsy was performed on these mice with age matched control littermates. The Fabp1-Cre^{+} Pik3ca*$^{+}$ *Apc$^{Min/+}$* mice develop a significant increase in the total number of tumors compared to control littermates. This is due to an increase in both distal small intestinal and colon cancers. No significant difference was noted between Fabp1-Cre^{+} Pik3ca*$^{+}$ *Apc$^{Min/+}$* and Fabp1-Cre^{+} Pik3ca*$^{+}$ *Apc$^{fl/+}$* mice in age at moribund and total, distal small intestinal, and colonic tumors. No lesions were seen in Fabp1-Cre^{+} Pik3ca*$^{+}$ *Apc$^{fl/+}$* mice in the proximal small intestine as an allele of *Apc* is not lost in this section of the intestines. * $p<0.01$ compared to Fabp1-Cre^{+} Pik3ca*$^{+}$ *Apc$^{Min/+}$* (Wilcoxon Rank Sum test).

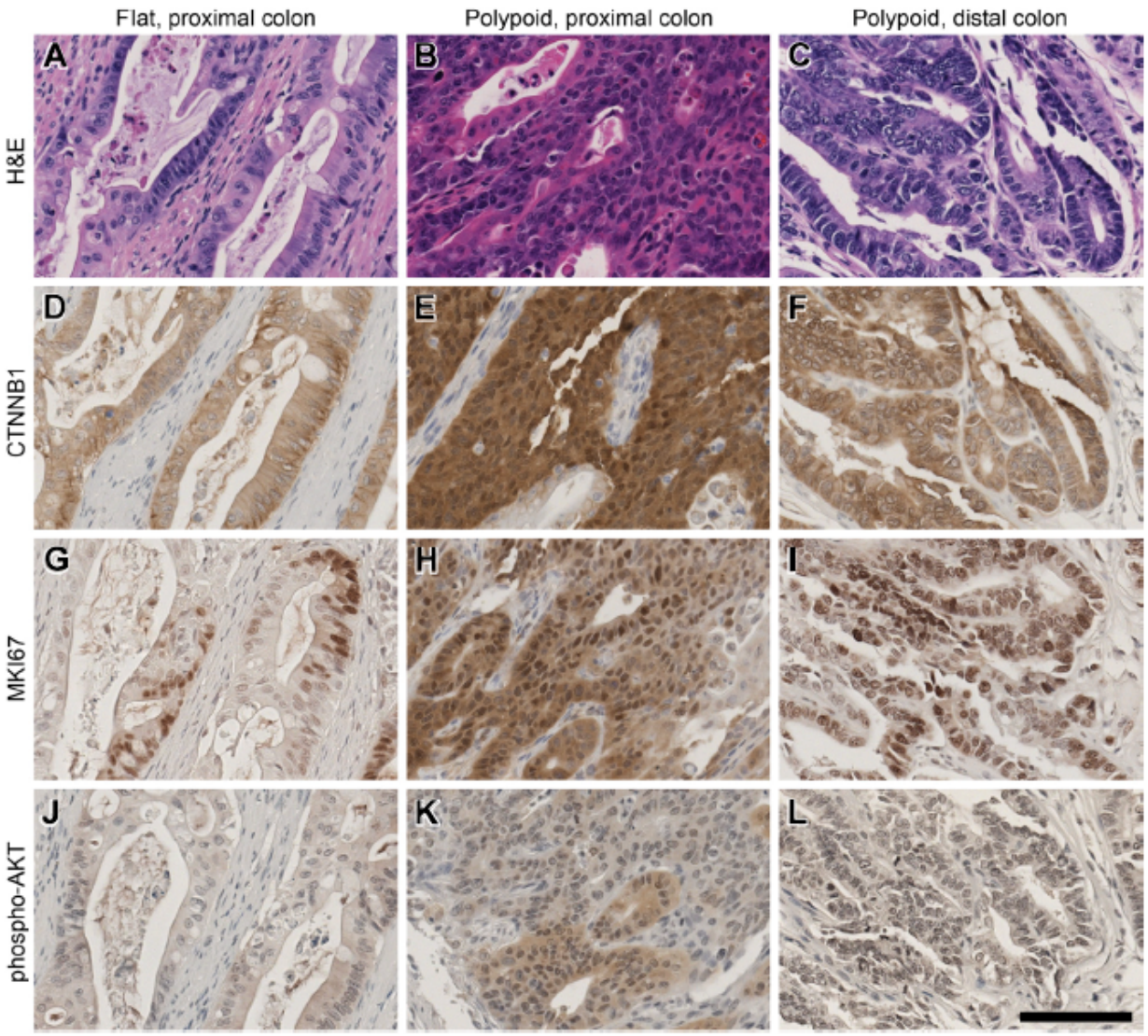
Flat, proximal colon
Polypoid, proximal colon
Polypoid, distal colon
H&E
CTNNB1
MKI67
phospho-AKT
A
B
C
D
E
F
G
H
I
J
K
L

Appendix 3-2. High magnification of histological sections presented in Figure 2-7. Large flat moderately differentiated mucinous adenocarcinomas develop in the proximal colon and polypoid lesions develop in both the proximal and distal colon with distinct morphologies. The flat mucinous lesions do not possess nuclear CTNNB1 (D), while the polypoid tumors do (E and F). The MKI67 and phospho-AKT staining of all of these tumors indicates that these tumors are highly proliferative and have activated PI3K/AKT signaling (G-L). Scale bar 100μm.

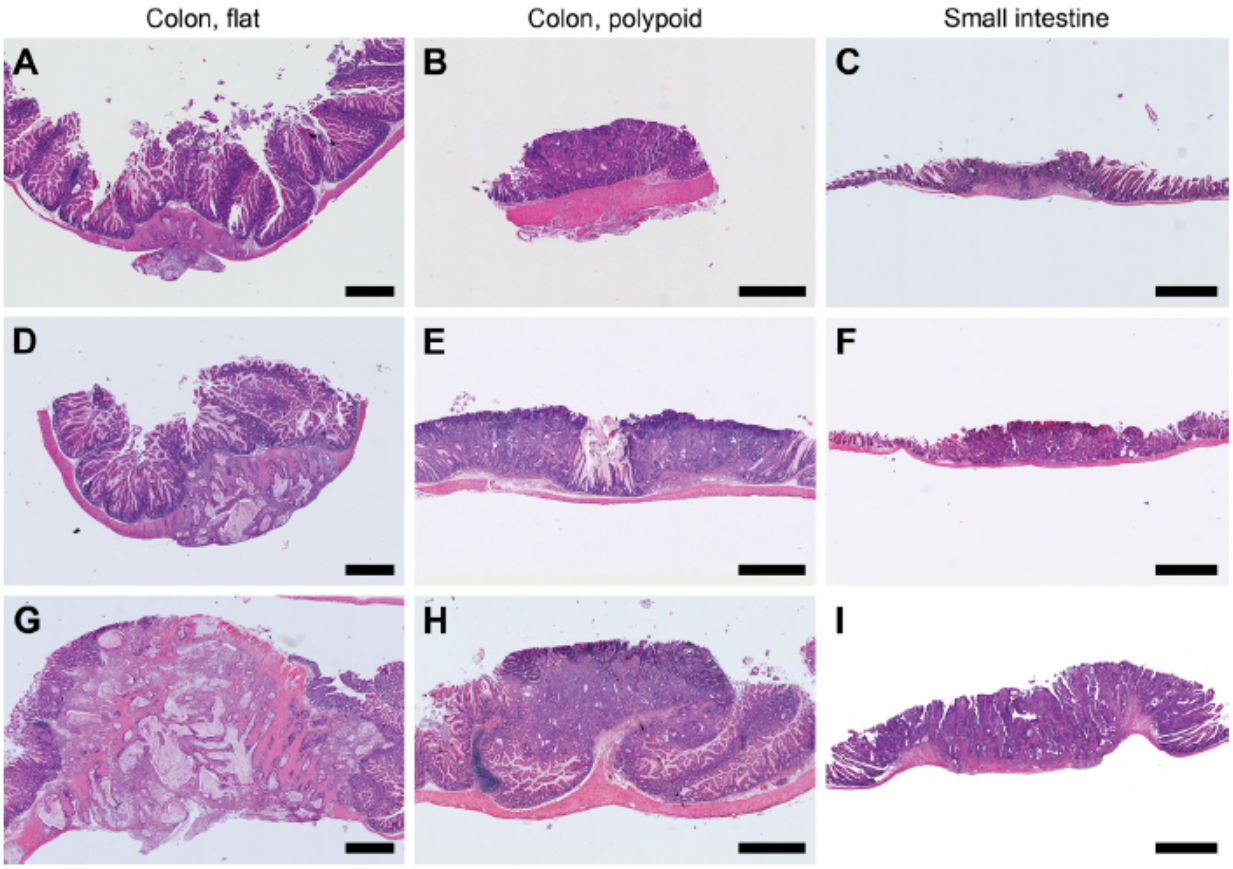
Colon, flat
Colon, polypoid
Small intestine
A
B
C
D
E
F
G
H
I

Appendix 3-3. Additional examples of tumors in Fabp1-Cre^{+} Pik3ca*$^{+}$*Apc*$^{Min/+}$ tumors.

Large flat mucinous adenocarcinomas form in the proximal colon (A, D, and G). Polypoid lesions ranging from small adenomas to adenomas with high grade dysplasia to adenocarcinomas are also found throughout the colon (B, E and H). Invasive cancers are also seen in the small intestine (C, F, and I). Scale bar 1mm.

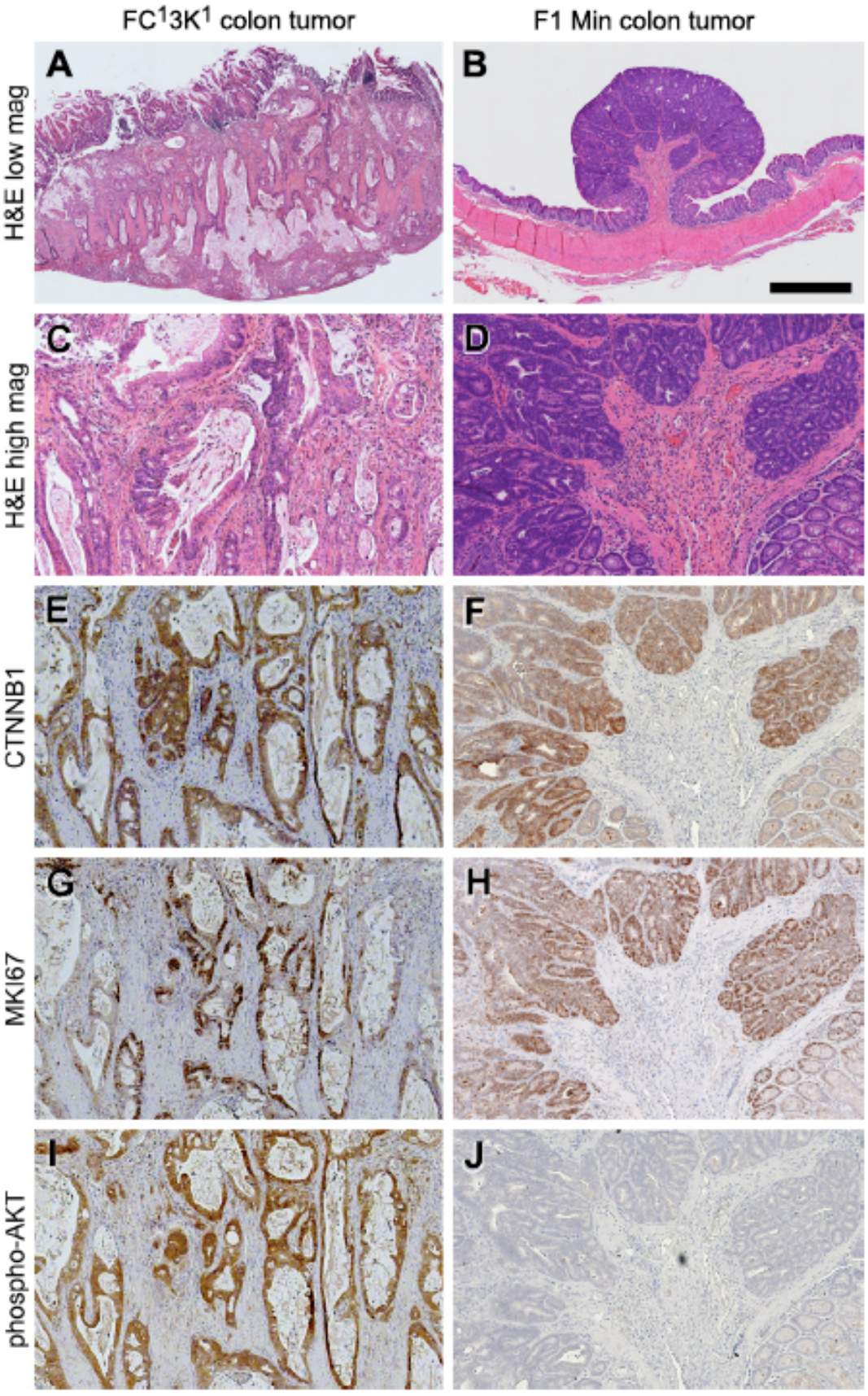
FC13K1 colon tumor
F1 Min colon tumor
H&E low mag
H&E high mag
CTNNB1
MKI67
phospho-AKT
A
B
C
D
E
F
G
H
I
J

Appendix 3-4. Fabp1-Cre^{+} Pik3ca*$^{+}$*Apc*$^{+/+}$ and *Apc*$^{Min/+}$ control colon tumors for comparison to the Fabp1-Cre^{+} Pik3ca*$^{+}$*Apc*$^{Min/+}$ tumors pictured in Figure 2-7. In Fabp1-Cre^{+} Pik3ca*$^{+}$*Apc*$^{+/+}$ mice, large flat mucinous adenocarcinomas develop in the proximal colon and cecum. These cancers penetrate through the serosal layer and have an abundance of mucin lakes (A and C). CTNNB1 is not nuclear in these tumors indicating a non-canonical mechanism of tumorigenesis (E). A high rate of proliferation and increased phosphorylation of AKT are noted (G and I). The presented *Apc*$^{Min/+}$ control mouse was treated with 4% DSS to increase the number and size of colon tumors to compare to the Fabp1-Cre^{+} Pik3ca*$^{+}$*Apc*$^{Min/+}$ colon tumors (B and D). In these tumors CTNNB1 is nuclear (F). Prominent MKI67 staining demonstrates that these tumors are proliferative (H). Minimal phospho-AKT staining is noted (J). Scale bar A-B 1mm. C-J are 4x enlargements.

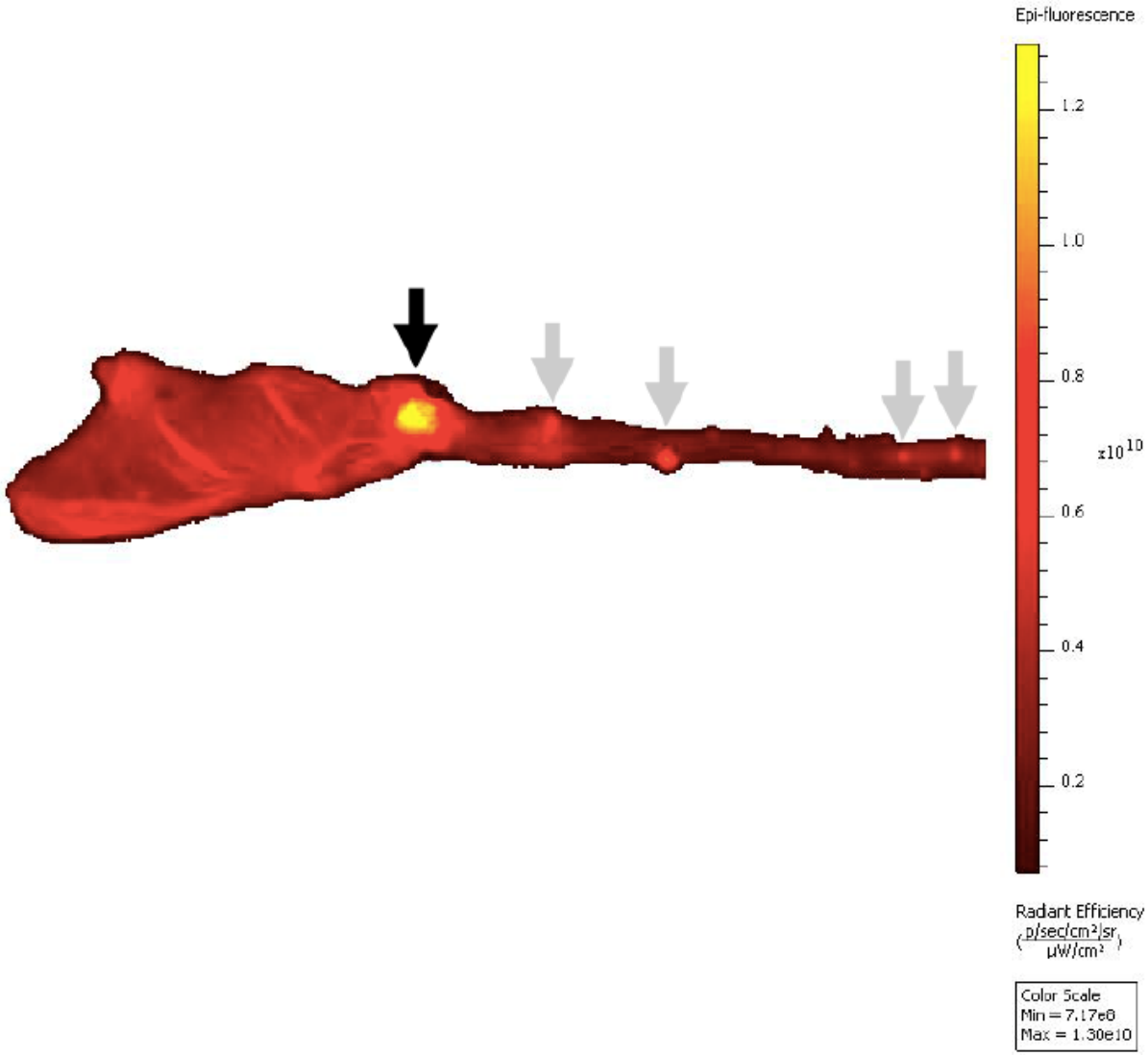
Epi-fluorescence
1.2
1.0
0.8
x10^10
0.6
0.4
0.2
Radiant Efficiency
(p/sec/cm²/sr / µW/cm²)
Color Scale
Min = 7.17e8
Max = 1.30e10

Appendix 3-5. CLR1502 is a novel near-infrared phospholipid ether analog that selectively accumulates in tumors. Fabp1-Cre^{+} Pik3ca*$^{+}$*Apc*$^{Min/+}$ mice were treated with CLR1502 prior to becoming moribund at a dose of 300µg/mouse. After 96 hours, necropsy was performed. The colon was excised and fluorescence was measured using the Spectrum IVIS Caliper Life Science Live Imager. Increased uptake of CLR1502 was observed in the large flat proximal colon cancers (black arrow) and to a lesser extent the smaller polypoid tumors throughout the colon (grey arrows).

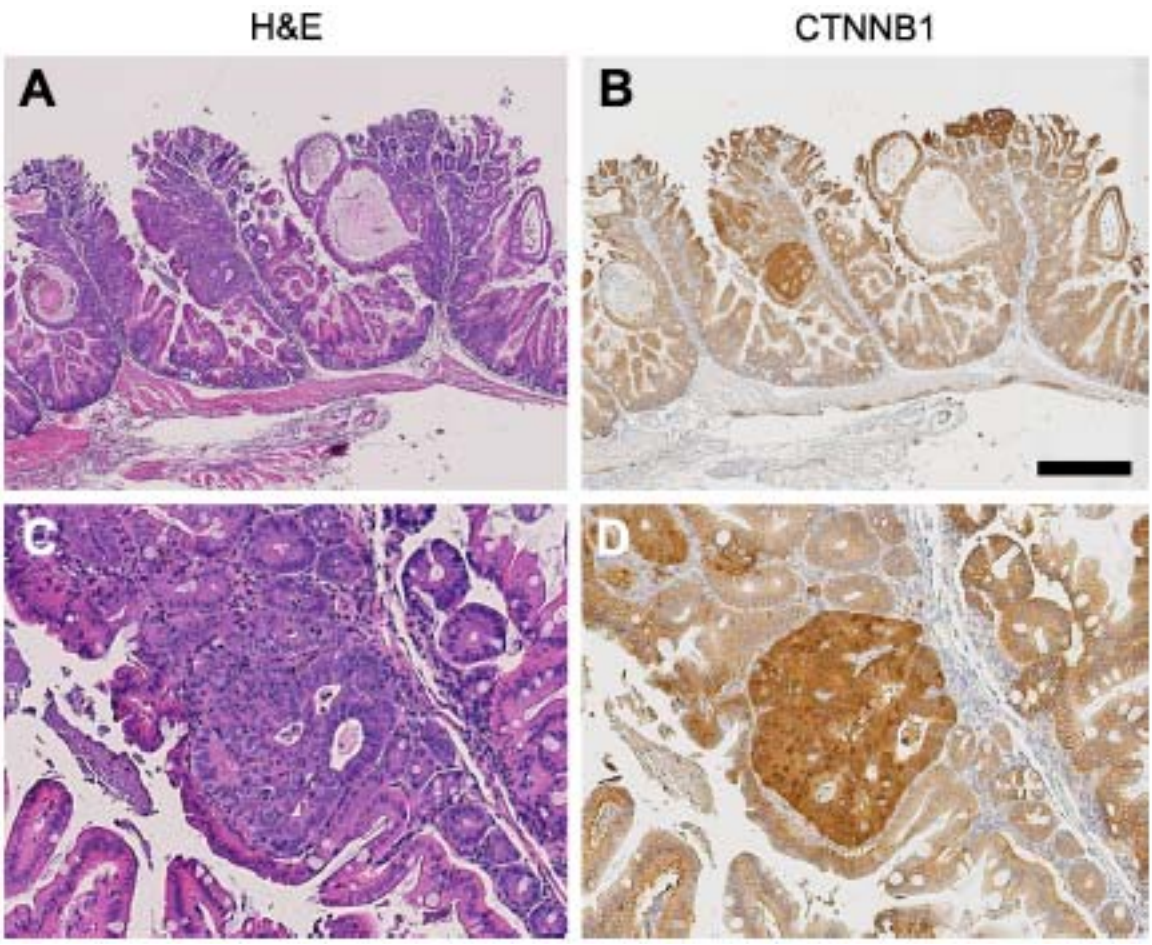
H&E
CTNNB1
A
B
C
D

Appendix 3-6. CTNNB1 staining can identify microscopic adenomas. Following necropsy the colons were excised, splayed out flat, and rolled. The colon then underwent histological sectioning. Upon H&E staining hyperplasia and dysplasia was noted throughout the proximal colon (A and C). After CTNNB1 staining, small foci of nuclear CTNNB1 could be identified within the mucosa, consistent with microscopic adenomas (B and D). Scale bar a-b 500μm. c and d are 4x enlargements.

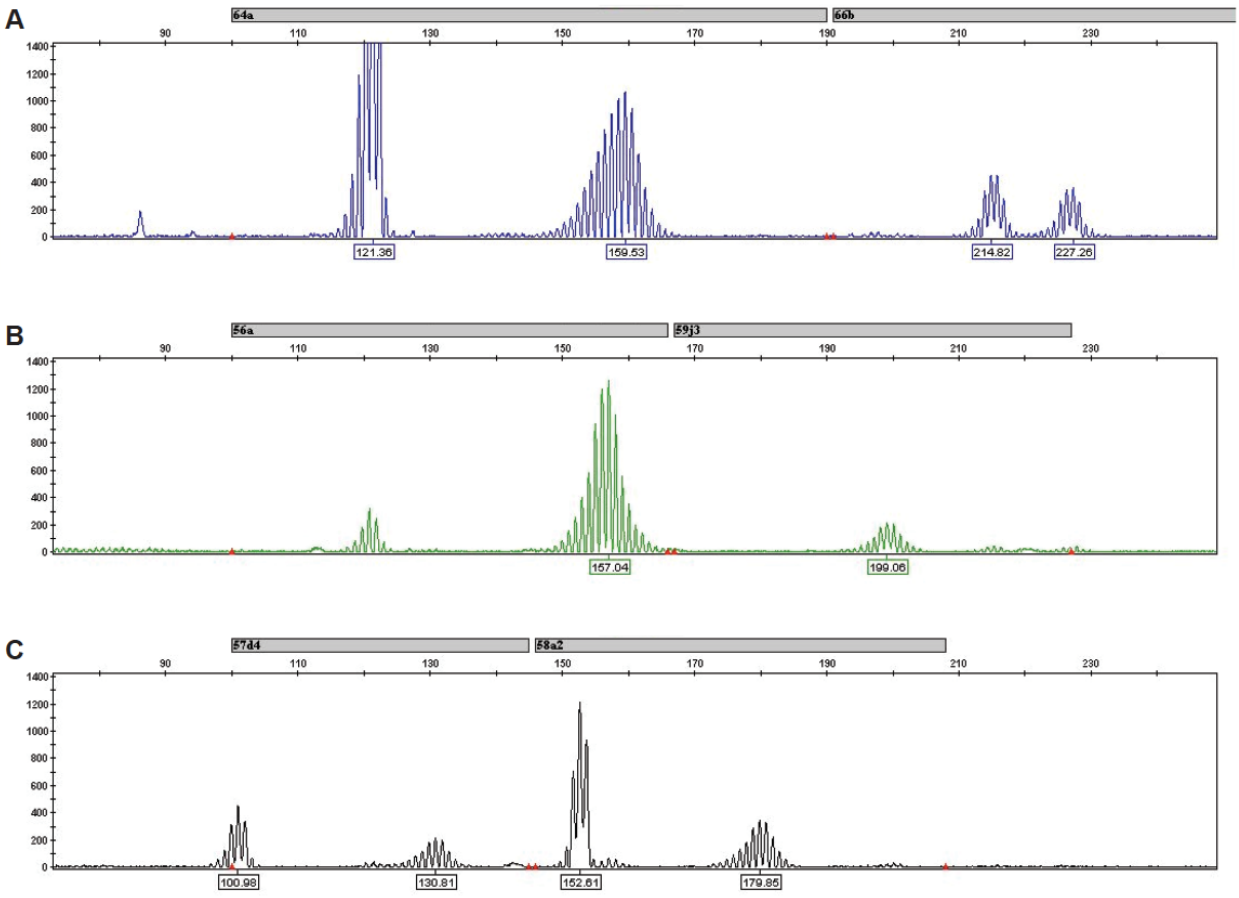
A
64a
66b
90
110
130
150
170
190
210
230
1400
1200
1000
800
600
400
200
0
121.36
159.53
214.82
227.26
B
56a
59j3
157.04
199.06
C
57d4
58a2
100.98
130.81
152.61
179.85

Appendix 3-7. MSI analysis of tumors with activated PI3K. Tumor and normal DNA was amplified using a multiplex of six mononucleotide repeat loci and PCR products were analyzed using a 3130*xl* Genetic Analyzer. The resulting allelic profiles and sizes (base pairs) for mBat-64 and mBat-66 are shown in blue (A), for mBat-56 and mBat-59 in green (B), and for mBat-57 and mBat-58 in black (C). 18 out of 22 tumor samples and their matching normal samples had the same allelic profile shown above and were therefore considered microsatellite stable. 4 out of 22 samples all had the same novel mBat-66 allele (sized at 235 bp compared to 227 bp for wild type allele), and were therefore attributed to a breeding colony polymorphism and not scored as MSI positive.

APPENDIX 4. Supplemental figures for Chapter 2.3: Colon tumors with simultaneous induction of driver mutations in *APC*, *KRAS*, and *PIK3CA* still progress through the adenoma-to-carcinoma sequence.

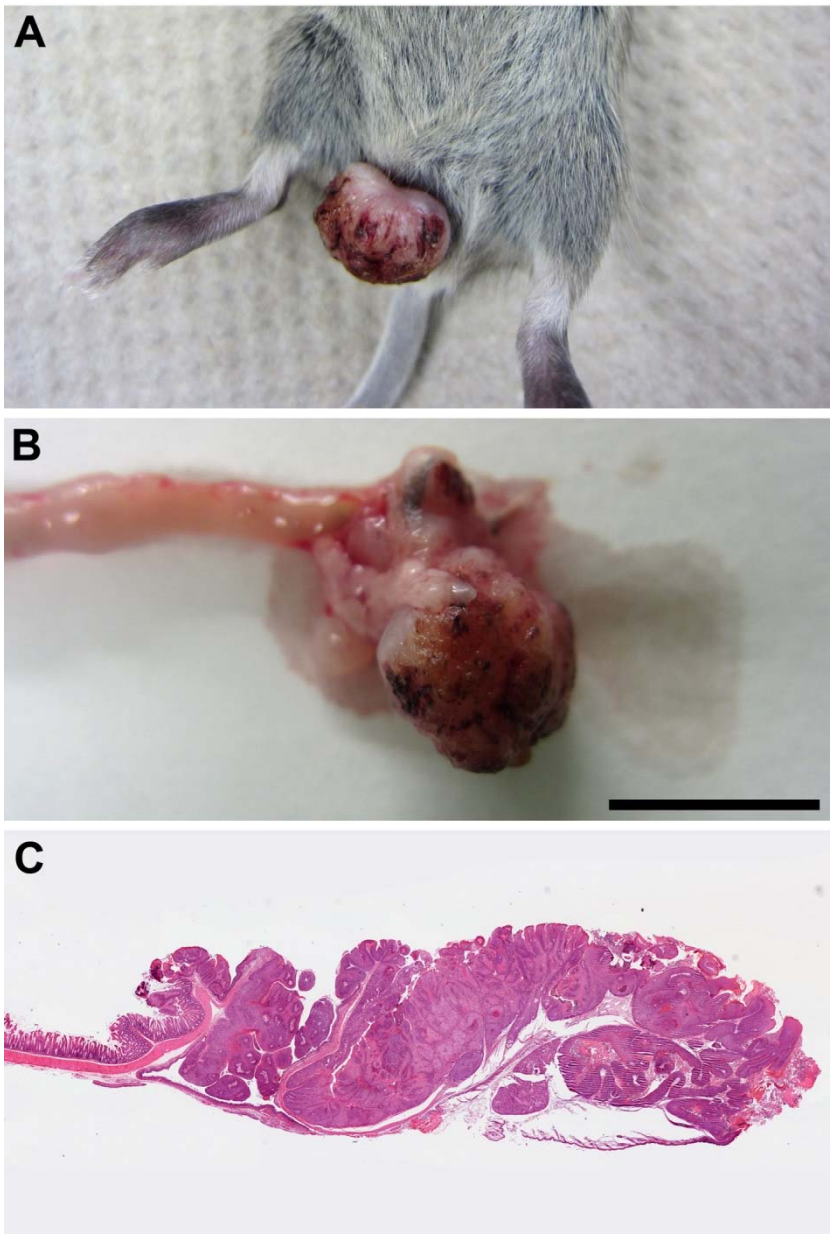

Appendix 4-1. Fabp1-Cre^{+} *Kras*$^{LSL\text{-}G12D/+}$ Pik3ca*$^{+}$ mice developed urogenital masses by 10 days of age and were moribund by a median of 16 days of age. These early deaths are due to the small amount of expression of the Cre recombinase from the Fabp-1 promoter in the urogenital system. No masses were noted within the colon. A, in situ. B, whole mount. C, upon histological staining no lesions were observed in the colonic mucosa, but large masses with squamous cells were observed (C). Scale bar for B = 1cm.

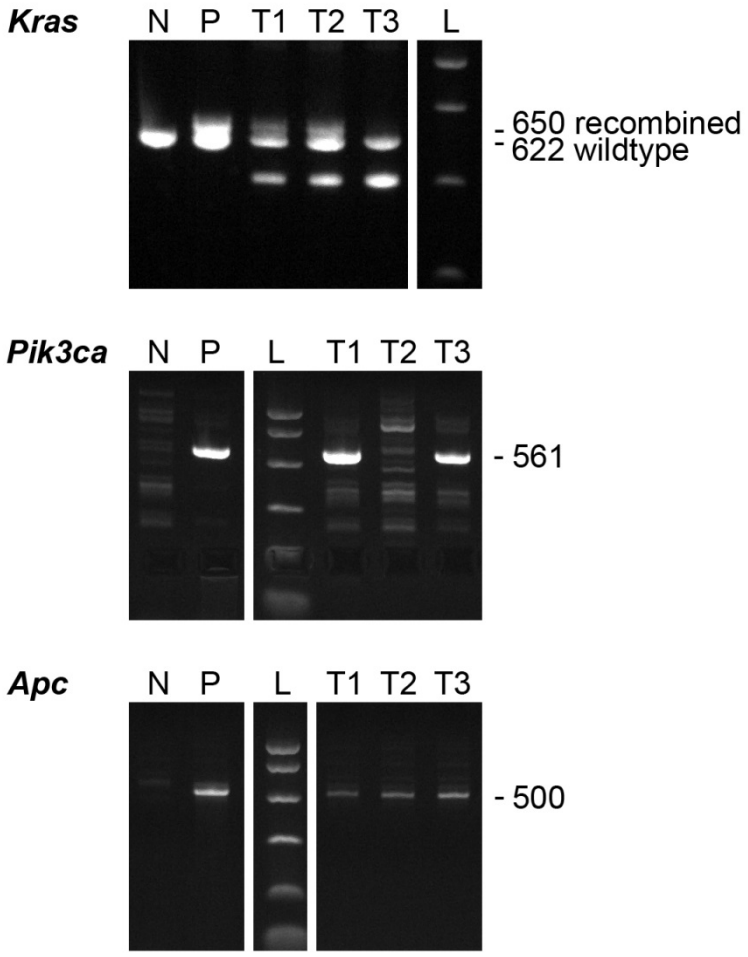
Kras
N P T1 T2 T3 L
650 recombined
622 wildtype
Pik3ca
N P L T1 T2 T3
561
Apc
N P L T1 T2 T3
500

Appendix 4-2. Recombination of floxed alleles was confirmed by PCR. Pictured above is a representative example of a tumor which has recombined all three alleles (T1), a tumor which has recombined the *Apc*^{fl} and *Kras*$^{LSL\text{-}G12D}$ alleles (T2), and a tumor which has recombined the *Apc*^{fl} and Pik3ca* alleles (T3). N, negative control; P, positive control; L, ladder.

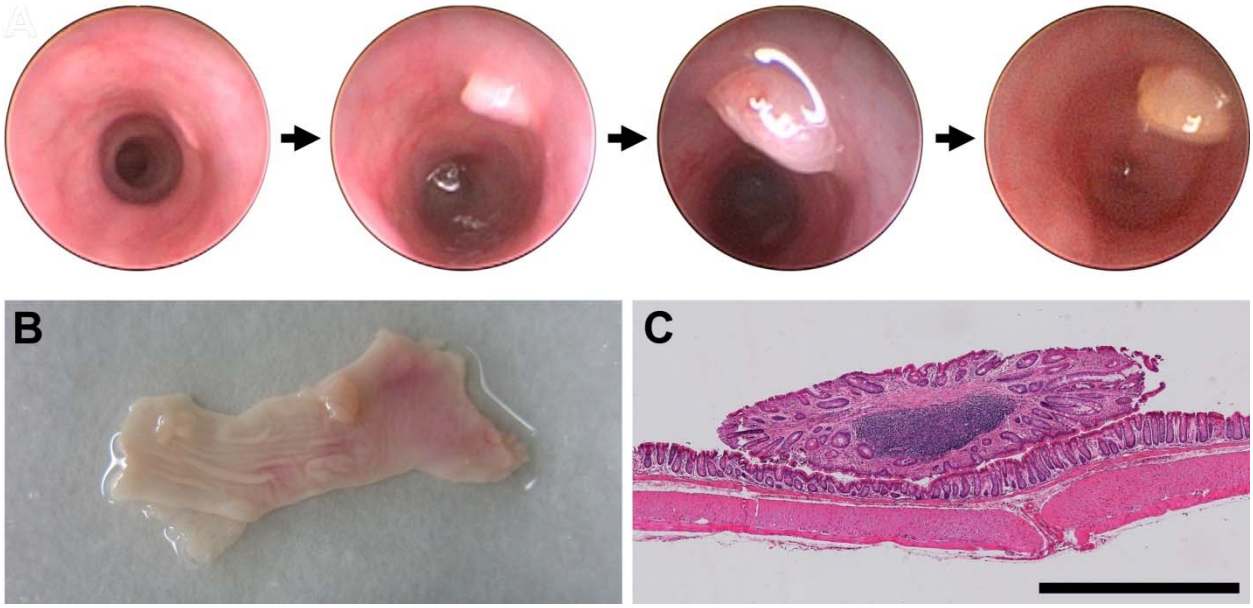
B
C

Appendix 4-3. Multiple *Apc*$^{fl/fl}$ Pik3ca*$^{+}$ mice were inoculated with Adeno-Cre and formed colonic tumors. However, in one instance a tumor was identified at 4 weeks post viral treatment. (A) This lesion grew in size over the next few weeks, but then spontaneously began decreasing in size and developed a more yellow and mucoid appearance. (B) At necropsy a small polypoid lesion was identified. (C) Upon histological sectioning and H&E staining the lesion was found to be infiltrated by lymphocytes without evidence of dysplasia. This potentially indicates that some colon polyps may be regulated by the immune system and could undergo immune-mediated tumor regression.

APPENDIX 5. Supplemental figures, tables, and methods for Chapter 3.1: Advanced intestinal cancers often maintain a multi-ancestral architecture.

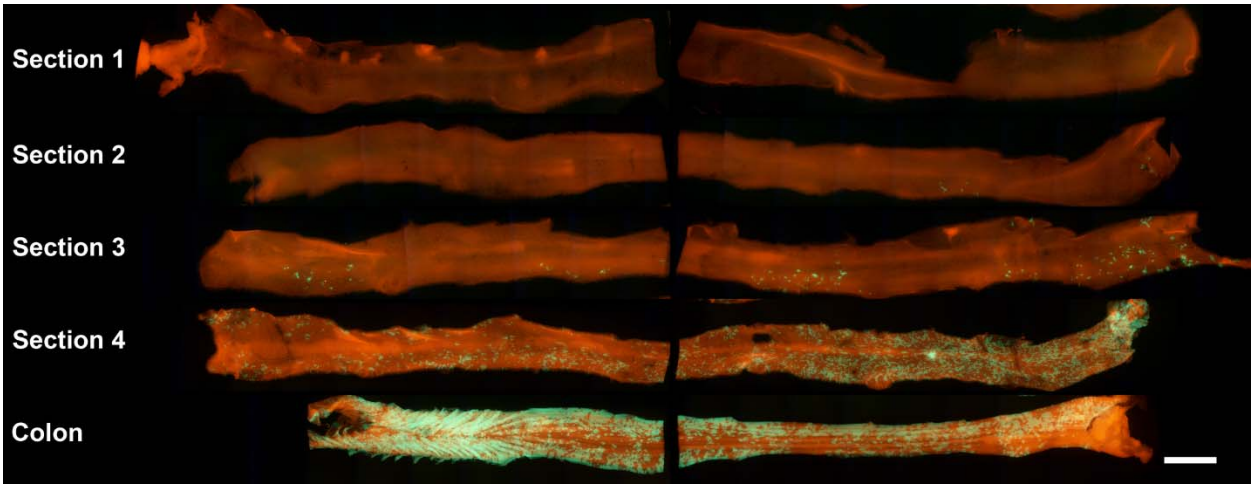

Appendix 5-1. The pattern of mosaicism varies along the length of the intestinal tract. The rat fatty acid binding protein promoter is expressed in very few cells in the duodenum and jejunum (sections 1–3) so these regions of the small intestine are primarily red, whereas it is expressed in many cells in the ileum (section 4) and colon so these regions are a mixture of red and green. The intestinal tract is shown with the duodenum at the top proceeding to the colon at the bottom. Size bar: 5mm.

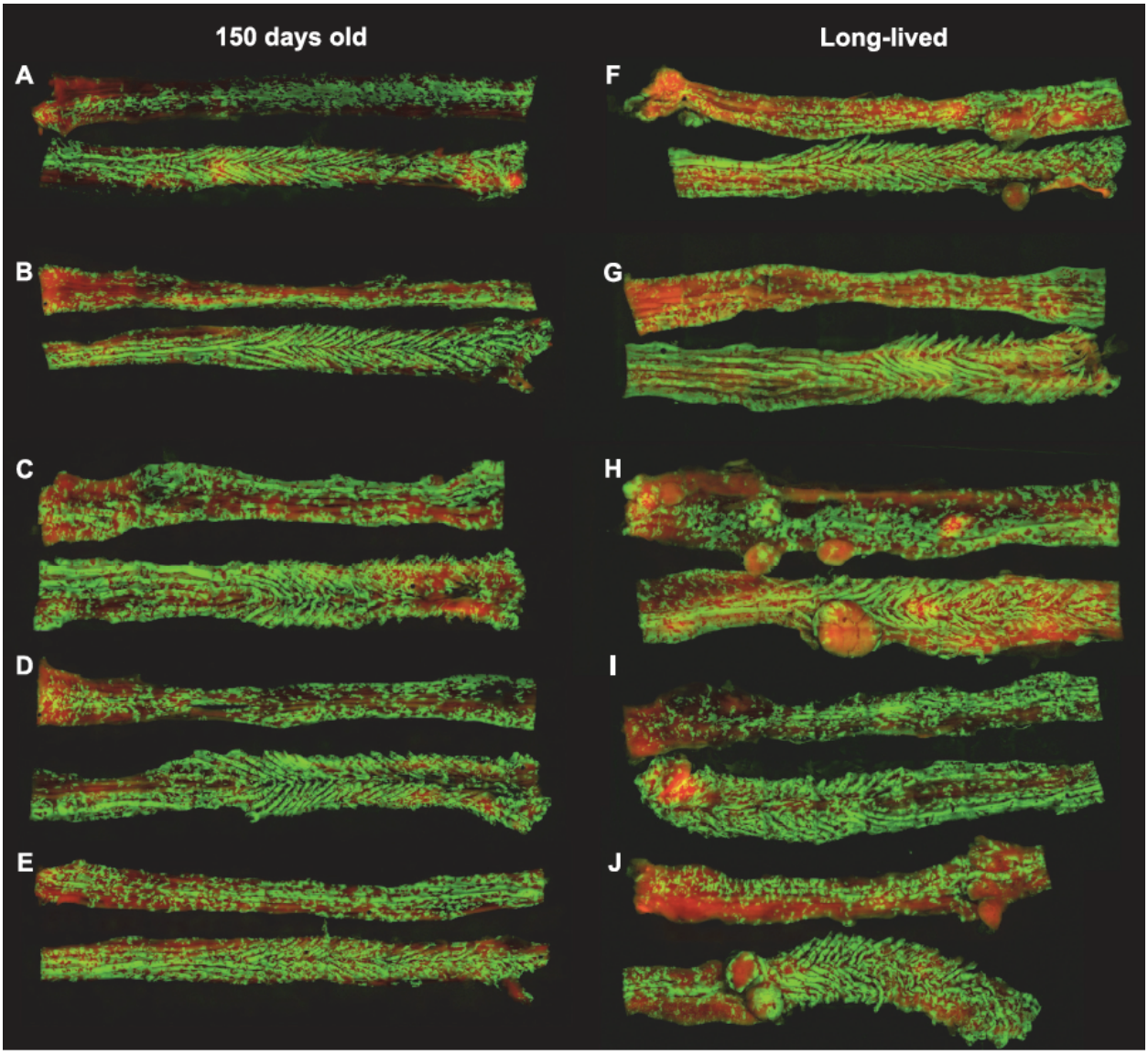
150 days old
Long-lived
A
B
C
D
E
F
G
H
I
J

Appendix 5-2. The pattern of mosaicism is quite similar when comparing mice euthanized at 150 days to those euthanized when moribund. Colons are shown from mosaic mice euthanized at 150 days (A-E) and those euthanized when moribund (F-J). The percentage of green cells ranged from 28.6 to 44.6. Note large tumors are evident in the long-lived mosaic mice.

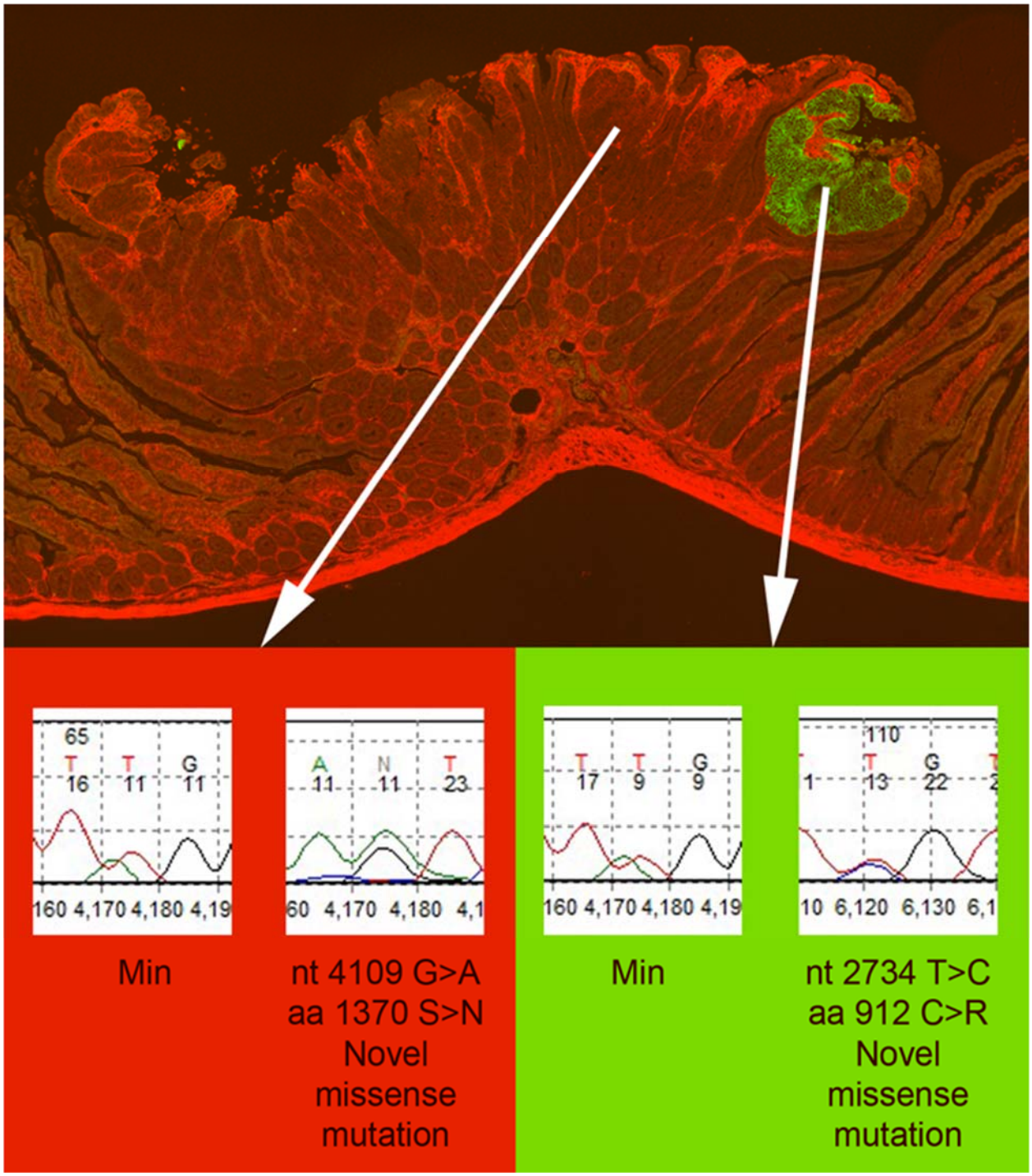
65
T 16
T 11
G 11
160 4,170 4,180 4,19
A 11
N 11
T 23
60 4,170 4,180 4,1
T 17
T 9
G 9
160 4,170 4,180 4,19
110
T 13
G 22
1
10 6,120 6,130 6,1
Min
nt 4109 G>A
aa 1370 S>N
Novel
missense
mutation
Min
nt 2734 T>C
aa 912 C>R
Novel
missense
mutation

Appendix 5-3. Sequencing of *Apc* indicates that different clones within a single tumor are distinct. DNA was prepared from the red and green clones in the biclonal tumor that is shown in Figure 3-1 and a region of *Apc* was sequenced. The red clone carried a missense mutation at codon 4109 resulting in a change serine to asparagine, whereas the green clone carried a missense mutation at codon 912 resulting in a change from cysteine to arginine. Both clones carried the *Min* allele. Note that only a small region of exon 15 of the gene was sequenced.

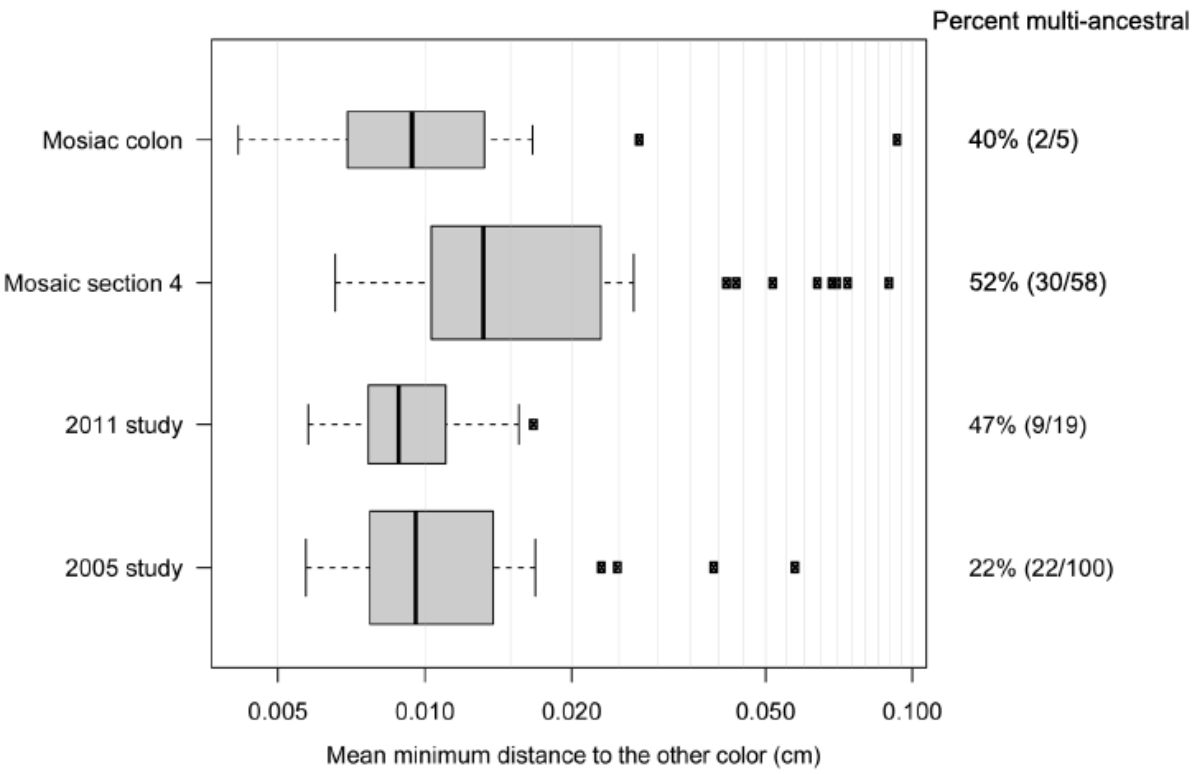
Percent multi-ancestral
Mosiac colon
Mosaic section 4
2011 study
2005 study
40% (2/5)
52% (30/58)
47% (9/19)
22% (22/100)
0.005
0.010
0.020
0.050
0.100
Mean minimum distance to the other color (cm)

Appendix 5-4. The percentage of multi-ancestral tumors is similar in different models.

The ideal experimental system for studying the clonal origin and architecture of intestinal tumors would uniquely label each stem cell/crypt. With our system, patches of Cre-negative (tdTomato) and Cre-positive (EGFP) are relatively small and evenly distributed in the distal half of the small intestine and colon, which is conducive to identifying heterotypic, overtly multi-ancestral tumors if they exist. The distance between cells of different colors was calculated for mosaic mice in this study and aggregation chimeras in previous studies[1,2]. The distance in the distal small intestine and colon from 150-day-old mice in this study was comparable to that observed in aggregation chimeras, indicating that the pattern of mosaicism was similar in the two different experimental platforms. Note that the small intestine was divided into four equal sections with Section 1 correlating to the duodenum, Section 2 plus 3 correlating to the jejunum, and Section 4 correlating to ileum. Since the pattern of mosaicism in the mice in this study varied along the length of the intestinal tract, the distances for section 4 and the colon were plotted separately. Note that the percentage of green cells was 12.0% in section 4 but 37.6% in the colon of mice euthanized at 150 days. By contrast, the pattern of mosaicism in aggregation chimeras from previous studies was quite consistent along the length of the intestinal tract, so the distances for sections 1, 2, 3, 4 and the colon were all plotted together. Power calculations considering the pattern of mosaicism indicate that we could detect multi-ancestral tumors in mosaics or aggregation chimeras if they were only 1 out of every 100 tumors.

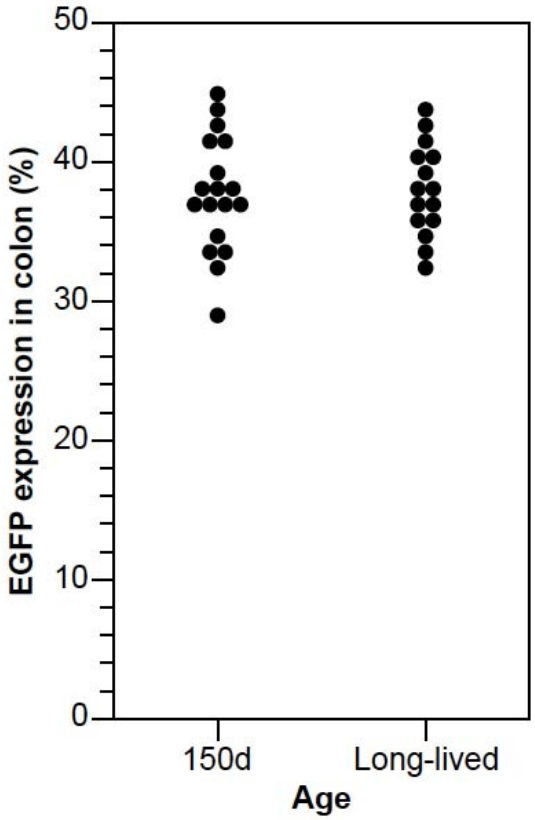
50
40
30
20
10
0
EGFP expression in colon (%)
150d
Long-lived
Age

Appendix 5-5. The pattern of mosaicism in the colon does not change over time. The percentage of cells expressing EGFP was plotted for mice euthanized at 150 days of age (n = 18) and those euthanized when moribund (n = 15). The average was 37.6% for 150-day-old mice and 38.1% for long-lived mice (p = 0.46, t-test).

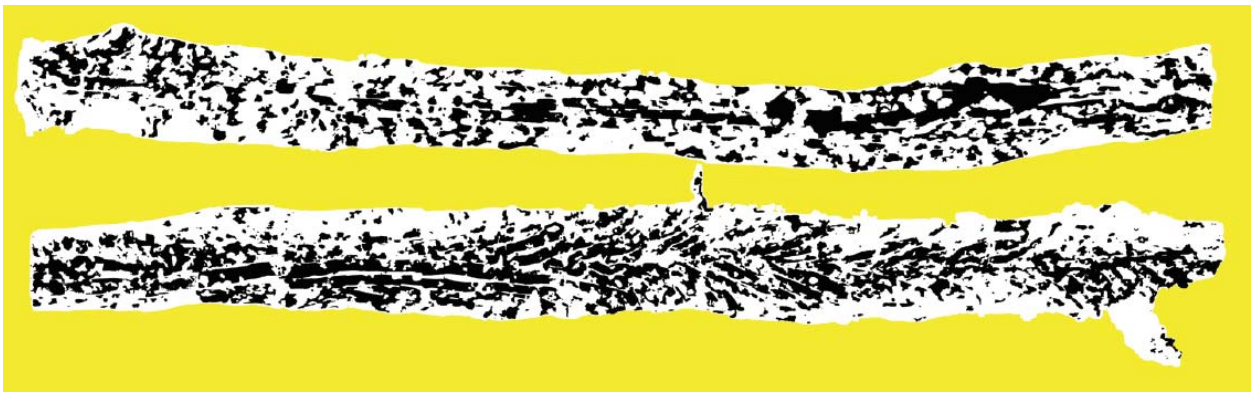

Appendix 5-6. The color images of whole mounts were converted to black and white images so that the pattern of mosaicism could be characterized. An ideal model for studying polyclonality would have very small patch sizes; smaller patches enhance the ability to detect polyclonal tumors because the probability that tumor-founding cells arise from different marked lineages increases. Note that the larger patch size arising as a consequence of X-inactivation heavily biased the analysis of human tumors towards the conclusion that human colorectal tumors are monoclonal[3].

Appendix 5-7. 3D reconstruction of polyclonal adenomas revealed the number of discrete clones.

		N of distinct regions	
Tumor ID	Intestinal region	Red	Green
6105C	Distal small intestine	1	3
3859E	Distal small intestine	1	2
3862C	Distal small intestine	1	2
3862E	Distal small intestine	1	1
4000A	Colon	1	1

Appendix 5-8. The pattern of mosaicism does not change with age. SI, small intestine.

Intestinal section	Percentage of tissue expressing EGFP, mean ± SD		p value (t-test)
	150 day old mice (n = 18)	Long-lived mice (n = 15)	
SI section 1	0.0 ± 0.0	0.0 ± 0.0	0.26
SI section 2	0.0 ± 0.0	0.1 ± 0.1	0.07
SI section 3	0.4 ± 0.6	0.5 ± 0.6	0.68
SI section 4	12.0 ± 2.6	11.5 ± 1.4	0.33
Colon	37.6 ± 4.1	38.1 ± 3.3	0.46

Appendix 5-9. Primers used for Apc sequencing.

	Forward primer		Reverse primer		
Primer Name	Sequence	Melting temperature (°C)	Sequence	Melting temperature (°C)	Product Size (bp)
ApcEx15a-1	CACGTTAGGAAACAGAAAGC	58.3	AAAAGCATAGTCACCATAAA	54.7	147
ApcEx15a-2	CGGAGTAAGCAGAGACACAA	60.7	TCTAAACTTCCCCTTGAGGA	59.3	170
ApcEx15a-3	CATGACTGTTCTTTCACCAT	57.4	TCGTTTTGATGAGGTTCCTG	59.3	175
ApcEx15a-4	GCCTCAGTGCTTACCATCCA	63.2	CTGTCGTCTGCCACACAATG	62.5	181
ApcEx15a-5	TCCCAGGACGACAGAAGTTC	62.5	TGGCATAAGGCATAGAGCAT	60.7	160
ApcEx15b-1	GGTGCAGTTCATTATCATCA	57.3	CTCTAGCATTCTGGGACACT	60.1	177
ApcEx15b-2	AATGATGTAACTCGGTCAGC	59.2	GGGGGACTTTTGGGTGTCTG	63.9	194
ApcEx15b-3	GCCAAGTCTCCCTCCAAAAG	61.9	GCCACTCACCATTCCACTAC	61.6	177
ApcEx15b-4	TTTGAGAGTCGCTCCATTGC	61.9	ACTTTACTTTTTGGCACCTC	57.9	185
ApcEx15b-5	ACCTCCTCCACAGACAGTGC	64.8	GCTGGAGGAACAAGAAAACC	60.4	196

Appendix 5-10. Supplementary Methods.

Equipment and Settings

Whole mount and histological tissue sections were imaged on one of three microscopes:

1. Zeiss AxioPlan II

- Software: AxioVision 4.8.2 with the Mosaix package
- Camera: Zeiss AxioCam MR3
- Fluorescent excitation source: HBO 103 W/2 mercury vapor short-arc lamp (product# 000000-1007-978-000)
- Objective lenses: Plan-Neofluar 1.25x NA 0.04 (item #440300-0000-000-000), Plan-Neofluar 2.5x NA 0.075 (item #440310-0000-000-000), Plan-Neofluar 10x NA 0.30 (item #440330-0000-000-000), Plan-Apochromat 20x NA 0.75 (item #440649-0000-000-000) Filters sets used: Zeiss filter set 1 - EX 365/12nm, EM LP 397nm (item # 488001-9901- 000), Zeiss filter set 10 - EX 470/40nm, EM 540/50nm (item # 488010-9901-000), Zeiss filter set 31 - EX 565/30nm, EM 620/60nm (item# 000000-1031-350)

2. Nikon Eclipse TI-S

- Software: NIS-Elements: Advanced Research with the 6D acquisition module
- Camera: Nikon Digital Sight DS-Ri1 (product #MQA16050)
- Fluorescent excitation source: C-HGFI Intensilight mercury illuminator (product#MBF72655)
- Objective lenses: CFI Plan Achromat UW 2X NA 0.06 WD 7.5MM (product #MRL00022), CFI Plan Fluor 4X NA 0.13 WD 17.2MM, Eco-Glass (product #MRH00041), CFI Plan Fluor 10X NA 0.3 WD 16MM, Eco-Glass (product

#MRH00101), CFI Plan Fluor 20X NA 0.5 WD 2.1MM, Spring-Loaded Eco-Glass (product #MRH00201)

- Filters sets: C-FL UV-2E/C DAPI Filter Block DM-400, EX 360/40, EM 460/50 (product # 96310), C-FL B-2E/C FITC Filter Block DM 505, EX 480/30, EM 535/40 (product # 96311), C-FL G-E/C TRITC Filter Block DM 565, EX 540/25, BA 620/60 (product # 96312)

3. Prairie Technologies Ultima IV

- Software: PrairieView v.4
- Detector: Hamamatsu Multi alkali Photo Multiplier Tubes
- Fluorescent excitation source: Spectra-Physics Insight DeepSee Ultrafast Laser
- Objective lenses: Zeiss Plan-Apochromat 20x NA 1.0
- Filters sets used: Chroma 525/50nm and 620/60nm filters and a T545lp dichroic mirror

Acquisition settings for images used in figures are as follows:

- Figure 3-1B: All images were taken with the Zeiss microscope using the 2.5x objective lens and filter sets 10 and 31 for the EGFP and tdTomato, respectively. The camera was set to 32-bit RGB color with a resolution of 4.98μm/pixel and linear look up tables. Exposure settings were as follows (left to right):

  tdTomato 153 ms; EGFP 522 ms.

  tdTomato 366 ms; EGFP 1046 ms.

  tdTomato 175 ms; EGFP 540 ms.

  tdTomato 160 ms; EGFP 274 ms.

  tdTomato 425 ms; EGFP 800 ms.

- Figure 3-1 C through F: All images were taken with the Nikon microscope using linear look up tables and the following objectives and settings:

  Panel C – Imaged using the 10x objective lens with the camera set to 8-bit RGB color with no filters at a resolution of 0.92µm/pixel.

  Panel D – Imaged using the 20x objective with the camera set to 8-bit RGB color with no filters at a resolution of 0.46µm/pixel.

  Panels E and F – Imaged using the 20x objective lens with the FITC and TRITC filter blocks for EGFP and tdTomato, respectively. The camera was set to 8-bit emulated monochrome with a resolution of 0.46µm/pixel. Exposure times were 600ms for EGFP and 1s for tdTomato. The gain was set to 1x for EGFP and 3.4x for tdTomato.

- Figure 3-2: All panels were created from the same original image set taken on the Prairie Technologies Ultima IV microscope using the 20x objective lens, Spectra-Physics Mai Tai DeepSee set to a wavelength of 1000nm for excitation, and emission was filtered using the T545lp dichroic mirror with Chroma filters 525/50nm and 620/60nm for EGFP and tdTomato, respectively. The images were taken at a resolution of 0.94µm/pixel in the X and Y planes and with a step of 2µm/image in the Z plane.

- Figure 3-3: Images for Panels A and B were taken with the Nikon microscope using the 10x objective lens at a resolution of 0.92µm/pixel. Panels C and E were taken with the Nikon microscope using the 4x objective lens at a resolution of 0.37µm/pixel. Panels D and F were taken with the Nikon microscope using the 20x objective lens at a resolution of 0.46µm/pixel. All panels use linear look up tables.

  Panels A, C, and D – The camera was set to 8-bit RGB color with no filters.

Panels B, E, and F – The camera was set to 8-bit emulated monochrome using the FITC and TRITC filter blocks for EGFP and tdTomato, respectively. Exposure times were 800ms for EGFP and 3s for tdTomato. The gain was set to 1x for EGFP and 3.4x for tdTomato.

- Appendix IV-1 Fig: All sections were imaged with the Nikon microscope using the 2x objective lens with the FITC and TRITC filter blocks for EGFP and tdTomato, respectively. The camera was set to 8-bit RGB color with a 2x2 bin and a resolution of 9.15μm/pixel. Linear look up tables were used. Exposure times and gains were as follows:

  Section 1 (top) – tdTomato 30 ms, 1.4x gain; EGFP 20 ms, 1.4x gain.

  Section 2 – tdTomato 30 ms, 1.4x gain; EGFP 20 ms, 1.4x gain.

  Section 3 – tdTomato 40 ms, 1.4x gain; EGFP 20 ms, 1.4x gain.

  Section 4 – tdTomato 80 ms, 1.4x gain; EGFP 20 ms, 1.4x gain.

  Colon (bottom) – tdTomato 80 ms, 1.4x gain; EGFP 20 ms, 1.4x gain.

- Appendix IV-3: Image used is Figure 3-1 panel E.

References

1. Thliveris, A. T. *et al.* Polyclonality of familial murine adenomas: Analyses of mouse chimeras with low tumor multiplicity suggest short-range interactions. *Proc. Natl. Acad. Sci. U.S.A.* **102,** 6960–6965 (2005).

2. Thliveris, A. T. *et al.* Clonal Structure of Carcinogen-Induced Intestinal Tumors in Mice. *Cancer Prev Res* **4,** 916–923 (2011).

3. Novelli, M. *et al.* X-inactivation patch size in human female tissue confounds the assessment of tumor clonality. *Proc. Natl. Acad. Sci. U.S.A.* **100,** 3311–3314 (2003).

APPENDIX 6. Supplemental figures, tables, and methods for Chapter 3.2: Early heterogeneity owing to a multi-ancestral origin contributes to cancer progression in a model of advanced colorectal cancer.

Appendix 6-1. Tumor multiplicity from Fabp1-Cre^{+} Pik3ca*$^{+}$ *Apc*$^{Min/+}$ mice and littermate controls.

PI3K activation via transgene	*Apc* locus	N of mice	Tumor multiplicity, mean +/- standard deviation						
			Total	S1	S2	S3	S4	CE	CO
Yes	*Min/+*	13	16.5 +/- 12.8	1.4 +/- 2.0	2.3 +/- 2.6	2.9 +/- 3.4	7.8 +/- 6.5	0.8 +/- 0.9	2.7 +/- 2.4
No	*Min/+*	10	7.2 +/- 14.8*	1.3 +/- 1.9	1.8 +/- 4.3	1.5 +/- 3.1	2.4 +/- 5.6*	0 +/- 0*	0.2 +/- 0.4*
Yes	*+/+*	3	0.3 +/- 0.6*	0 +/- 0	0 +/- 0	0 +/- 0*	0 +/- 0*	0 +/- 0	0.3 +/- 0.6
No	*+/+*	8	0 +/- 0*	0 +/- 0*	0 +/- 0*	0 +/- 0*	0 +/- 0*	0 +/- 0*	0 +/- 0*

S1-S4, proximal to distal quarters of the small intestine; CE, cecum; CO, colon

*Wilcoxon Rank Sum test compared to first row; p-value ≤ 0.050

Each row represents a pool of animals with different strains and genotypes. Individual characteristics of each row can be found in the following tables: row 1 – appendices 6-3 and -4; row 2 – appendices 6-5 and -6; row 3 – appendix 6-7; and row 4 – appendix 6-8.

Appendix 6-2. Average size of tumors from Pik3ca*$^{+}$ *Apc*$^{Min/+}$ mice and littermate controls.

PI3K activation via transgene	*Apc* locus	N of tumors	Tumor size (maximum diameter in mm), mean +/- standard deviation						
			All	S1	S2	S3	S4	CE	CO
Yes	*Min/+*	208	2.3 +/- 2.1	1.2 +/- 0.5	1.1 +/- 0.6	1.3 +/- 1.4	2.9 +/- 2.3	2.5 +/- 1.7	3.1 +/- 2.3
No	*Min/+*	73	1.0 +/- 0.7*	1.4 +/- 0.7	1.0 +/- 0.4	0.8 +/- 0.3	0.9 +/- 0.4*	ND	2.9 +/- 2.8

S1-S4, proximal to distal quarters of the small intestine; CE, cecum; CO, colon

ND, not determined due to lack of tumors in this region

*Wilcoxon Rank Sum test compared to first row; p-value ≤ 0.050

Each row represents a pool of animals with different strains and genotypes. Individual characteristics of each row can be found in the following tables: row 1 – appendices 6-3 and -4; row 2 – appendices 6-5 and -6; row 3 – appendix 6-7; and row 4 – appendix 6-8.

Appendix 6-3. Tumor multiplicity from Fabp1-Cre^{+} Pik3ca*$^{+}$ *Apc*$^{Min/+}$ mice.

Strain	Genotype	N of mice	Tumor multiplicity, mean +/- standard deviation						
			Total	S1	S2	S3	S4	CE	CO
All	All	13	16.5 +/- 12.8	1.4 +/- 2.0	2.3 +/- 2.6	2.9 +/- 3.4	7.8 +/- 6.5	0.8 +/- 0.9	2.7 +/- 2.4
B6	All	5	25.4 +/- 15.6	0.6 +/- 0.9	3.4 +/- 3.4	5.6 +/- 3.8	11.8 +/- 7.9	1.0 +/- 1.2	3.0 +/- 2.1
N2	All	8	11.0 +/- 7.0	2.0 +/- 2.4	1.4 +/- 1.6	1.0 +/- 1.0	5.0 +/- 3.7	0.7 +/- 0.8	2.4 +/- 2.8
All	Fabp1-Cre^{+} mT/mG^{+} Pik3ca*$^{+}$ *Apc*$^{Min/+}$	9	15.2 +/- 8.4	1.4 +/- 2.2	2.0 +/- 1.4	2.4 +/- 3.3	5.9 +/- 4.5	0.6 +/- 0.5	2.9 +/- 2.6
B6	Fabp1-Cre^{+} mT/mG^{+} Pik3ca*$^{+}$ *Apc*$^{Min/+}$	4	19.5 +/- 9.7	0.8 +/- 1.0	2.0 +/- 1.4	4.8 +/- 3.9	8.8 +/- 4.6	0.5 +/- 0.6	2.8 +/- 2.4
N2	Fabp1-Cre^{+} mT/mG^{+} Pik3ca*$^{+}$ *Apc*$^{Min/+}$	5	11.8 +/- 6.1	2.0 +/- 2.9	2.0 +/- 1.6	0.6 +/- 0.9	3.6 +/- 3.2	0.6 +/- 0.5	3.0 +/- 3.1
All	Fabp1-Cre^{+} mT/mG^{0} Pik3ca*$^{+}$ *Apc*$^{Min/+}$	4	19.5 +/- 21.14	1.3 +/- 1.5	3.0 +/- 5.2	4.3 +/- 4.0	13.7 +/- 9.1	1.7 +/- 1.5	2.0 +/- 2.0
B6	Fabp1-Cre^{+} mT/mG^{0} Pik3ca*$^{+}$ *Apc*$^{Min/+}$	1	49	0	9	9	24	3	4
N2	Fabp1-Cre^{+} mT/mG^{0} Pik3ca*$^{+}$ *Apc*$^{Min/+}$	3	9.7 +/- 9.5	2.0 +/- 1.4	0 +/- 0	2.0 +/- 0	8.5 +/- 2.1	1.0 +/- 1.4	1.0 +/- 1.4

S1-S4, proximal to distal quarters of the small intestine; CE, cecum; CO, colon

Wilcoxon Rank Sum test comparing pooled genotypes by strain (blue rows): no significant differences ($p \leq 0.050$) were found when comparing total multiplicity nor multiplicity within any sections except S3 ($p=0.045$).

Wilcoxon Rank Sum test comparing B6 and N2 mice within the same genotype: no significant differences ($p \leq 0.050$) were found when comparing total multiplicity nor multiplicity within any sections.

Fisher's Method to combine Wilcoxon Rank Sum tests comparing B6 and N2 mice within the same genotype: no significant differences ($p \leq 0.050$) were found when comparing total multiplicity nor multiplicity within any sections.

Wilcoxon Rank Sum test comparing pooled strains by genotype (yellow rows): no significant differences ($p \leq 0.050$) were found when comparing total multiplicity nor multiplicity within any sections.

Wilcoxon Rank Sum tests comparing Fabp1-Cre^{+} mT/mG^{+} Pik3ca*$^{+}$ *Apc*$^{Min/+}$ and Fabp1-Cre^{+} mT/mG^{0} Pik3ca*$^{+}$ *Apc*$^{Min/+}$ mice within the same strain: no significant differences ($p \leq 0.050$) were found when comparing total multiplicity nor multiplicity within any sections.

Fisher's Method to combine Wilcoxon Rank Sum tests comparing Fabp1-Cre^{+} mT/mG^{+} Pik3ca*$^{+}$ *Apc*$^{Min/+}$ and Fabp1-Cre^{+} mT/mG^{0} Pik3ca*$^{+}$ *Apc*$^{Min/+}$ mice within the same strain: no significant differences ($p \leq 0.050$) were found when comparing total multiplicity nor multiplicity within any sections.

Appendix 6-4. Average size of tumors from Pik3ca*$^{+}$ *Apc*$^{Min/+}$ mice.

Strain	Genotype	N of tumors	Tumor size (maximum diameter in mm), mean +/- standard deviation						
			All	S1	S2	S3	S4	CE	CO
All	All	208	2.3 +/- 2.1	1.2 +/- 0.5	1.1 +/- 0.6	1.3 +/- 1.5	2.9 +/- 2.3	2.5 +/- 1.7	3.1 +/- 2.3
B6	All	122	1.9 +/- 1.5	1.5 +/- 0.3	1.1 +/- 0.6	1.3 +/- 1.5	2.4 +/- 1.7	2.1 +/- 1.3	1.8 +/- 0.9
N2	All	86	2.8 +/- 2.6	1.1 +/- 0.5	1.1 +/- 0.7	1.1 +/- 0.5	3.6 +/- 3.0	3.1 +/- 2.2	4.3 +/- 2.6
All	Fabp1-Cre^{+} mT/mG^{+} Pik3ca*$^{+}$ *Apc*$^{Min/+}$	132	2.1 +/- 1.9	1.2 +/- 0.5	1.0 +/- 0.5	0.7 +/- 0.2	2.7 +/- 2.2	2.1 +/- 1.2	3.0 +/- 2.1
B6	Fabp1-Cre^{+} mT/mG^{+} Pik3ca*$^{+}$ *Apc*$^{Min/+}$	74	1.7 +/- 1.3	1.5 +/- 0.4	1.0 +/- 0.2	0.7 +/- 0.3	2.2 +/- 1.6	1.5 +/- 1.0	1.8 +/- 1.0
N2	Fabp1-Cre^{+} mT/mG^{+} Pik3ca*$^{+}$ *Apc*$^{Min/+}$	58	2.7 +/- 2.3	1.1 +/- 0.5	1.1 +/- 0.7	0.7 +/- 0.1	3.7 +/- 2.8	2.9 +/- 1.2	4.0 +/- 2.2
All	Fabp1-Cre^{+} mT/mG^{0} Pik3ca*$^{+}$ *Apc*$^{Min/+}$	76	2.6 +/- 2.4	1.2 +/- 0.5	1.2 +/- 0.8	2.1 +/- 1.9	3.0 +/- 2.6	3.1 +/- 2.2	3.3 +/- 3.4
B6	Fabp1-Cre^{+} mT/mG^{0} Pik3ca*$^{+}$ *Apc*$^{Min/+}$	48	2.3 +/- 1.8	1.4+/- 0.3	1.2+/- 0.8	2.4+/- 2.2	2.7 +/- 2.0	2.9 +/- 1.3	1.8+/- 0.5
N2	Fabp1-Cre^{+} mT/mG^{0} Pik3ca*$^{+}$ *Apc*$^{Min/+}$	28	3.0 +/- 3.1	1.1 +/- 0.6	ND	1.3 +/- 0.6	3.5 +/- 3.3	3.4 +/- 4.0	6.5 +/- 5.3

S1-S4, proximal to distal quarters of the small intestine; CE, cecum; CO, colon

ND, not determined due to lack of tumors in this region

Wilcoxon Rank Sum test comparing pooled genotypes by strain (blue rows): significant differences ($p \leq 0.050$) were found when comparing overall average tumor size; when combining comparisons within individual segments, significant differences were only found in the colon.

Wilcoxon Rank Sum test comparing B6 and N2 mice within the same genotype: significant differences ($p \leq 0.050$) were found when comparing overall average tumor size from each strain within the Fabp1-Cre^{+} mT/mG^{+} Pik3ca*$^{+}$ *Apc*$^{Min/+}$ genotype but not the Fabp1-Cre^{+} mT/mG^{0} Pik3ca*$^{+}$ *Apc*$^{Min/+}$ genotype; when comparing within individual segments, significant differences were only found in the colon within the Fabp1-Cre^{+} mT/mG^{+} Pik3ca*$^{+}$ *Apc*$^{Min/+}$ genotype.

Fisher's Method to combine Wilcoxon Rank Sum tests comparing B6 and N2 mice within the same genotype: significant differences ($p \leq 0.050$) were found when combining comparisons of overall average tumor size from each genotype within each strain; when combining comparisons within individual segments, significant differences were only found in the colon.

Wilcoxon Rank Sum test comparing pooled strains by genotype (yellow rows): no significant differences ($p \leq 0.050$) were found when comparing overall average tumor size nor average tumor size within any sections except section 3.

Wilcoxon Rank Sum tests comparing Fabp1-Cre^{+} mT/mG^{+} Pik3ca*$^{+}$ *Apc*$^{Min/+}$ and Fabp1-Cre^{+} mT/mG^{0} Pik3ca*$^{+}$ *Apc*$^{Min/+}$ mice within the same strain: significant differences ($p \leq 0.050$) were found when comparing overall average tumor size from each genotype within the B6 strain but not the N2 strain; when comparing within individual segments, significant differences were only found in segment 3 within the B6 strain.

Fisher's Method to combine Wilcoxon Rank Sum tests comparing Fabp1-Cre^{+} mT/mG^{+} Pik3ca*$^{+}$ *Apc*$^{Min/+}$ and Fabp1-Cre^{+} mT/mG^{0} Pik3ca*$^{+}$ *Apc*$^{Min/+}$ mice within the same strain: no significant differences ($p \leq 0.050$) were found when overall average tumor size nor average tumor size within any sections except section 3.

Appendix 6-5. Tumor multiplicity from *Apc*$^{Min/+}$ control mice.

Strain	Genotype	N of mice	Tumor multiplicity, mean +/- standard deviation						
			Total	S1	S2	S3	S4	CE	CO
All	All	10	7.2 +/- 14.8	1.3 +/- 1.9	1.8 +/- 4.3	1.5 +/- 3.1	2.4 +/- 5.6	0 +/- 0	0.2 +/- 0.4
B6	All	1	49	6	14	10	18	0	1
N2	All	9	2.6 +/- 1.9	0.8 +/- 1.1	0.4 +/- 0.7	0.6 +/- 0.9	0.7 +/- 1.0	0 +/- 0	0.1 +/- 0.3
All	Fabp1-Cre^{0} mT/mG^{+} Pik3ca^{*+} *Apc*$^{Min/+}$	2	3.0 +/- 2.8	1.5 +/- 0.7	0.5 +/- 0.7	0 +/- 0	0.5 +/- 0.7	0 +/- 0	0.5 +/- 0.7
B6	Fabp1-Cre^{0} mT/mG^{+} Pik3ca^{*+} *Apc*$^{Min/+}$	0	ND	ND	ND	ND	ND	ND	ND
N2	Fabp1-Cre^{0} mT/mG^{+} Pik3ca^{*+} *Apc*$^{Min/+}$	2	3.0 +/- 2.8	1.5 +/- 0.7	0.5 +/- 0.7	0 +/- 0	0.5 +/- 0.7	0 +/- 0	0.5 +/- 0.7
All	Fabp1-Cre^{0} mT/mG^{0} Pik3ca^{*+} *Apc*$^{Min/+}$	2	1.0 +/- 1.4	0.5 +/- 0.7	0 +/- 0	0 +/- 0	0.5 +/- 0.7	0 +/- 0	0 +/- 0
B6	Fabp1-Cre^{0} mT/mG^{0} Pik3ca^{*+} *Apc*$^{Min/+}$	0	ND	ND	ND	ND	ND	ND	ND
N2	Fabp1-Cre^{0} mT/mG^{0} Pik3ca^{*+} *Apc*$^{Min/+}$	2	1.0 +/- 1.4	0.5 +/- 0.7	0 +/- 0	0 +/- 0	0.5 +/- 0.7	0 +/- 0	0 +/- 0
All	Fabp1-Cre^{0} mT/mG^{0} Pik3ca^{*0} *Apc*$^{Min/+}$	1	4	0	2	2	0	0	0
B6	Fabp1-Cre^{0} mT/mG^{0} Pik3ca^{*0} *Apc*$^{Min/+}$	0	ND	ND	ND	ND	ND	ND	ND
N2	Fabp1-Cre^{0} mT/mG^{0} Pik3ca^{*0} *Apc*$^{Min/+}$	1	4	0	2	2	0	0	0
All	Fabp1-Cre^{0} mT/mG^{+} Pik3ca^{*0} *Apc*$^{Min/+}$	2	2.0 +/- 2.8	0 +/- 0	0 +/- 0	0.5 +/- 0.7	1.5 +/- 2.1	0 +/- 0	0 +/- 0
B6	Fabp1-Cre^{0} mT/mG^{+} Pik3ca^{*0} *Apc*$^{Min/+}$	0	ND	ND	ND	ND	ND	ND	ND
N2	Fabp1-Cre^{0} mT/mG^{+} Pik3ca^{*0} *Apc*$^{Min/+}$	2	2.0	0 +/- 0	0 +/- 0	0.5 +/- 0.7	1.5 +/- 2.1	0 +/- 0	0 +/- 0
All	Fabp1-Cre^{+} mT/mG^{0} Pik3ca^{*0} *Apc*$^{Min/+}$	1	4	3	0	0	1	0	0
B6	Fabp1-Cre^{+} mT/mG^{0} Pik3ca^{*0} *Apc*$^{Min/+}$	0	ND	ND	ND	ND	ND	ND	ND
N2	Fabp1-Cre^{+} mT/mG^{0} Pik3ca^{*0} *Apc*$^{Min/+}$	1	4	3	0	0	1	0	0
All	Fabp1-Cre^{+} mT/mG^{+} Pik3ca^{*0} *Apc*$^{Min/+}$	2	26 +/- 32.5	3.0 +/- 4.2	7.5 +/- 9.2	6.0 +/- 5.7	9.0 +/- 12.7	0 +/- 0	0.5 +/- 0.7
B6	Fabp1-Cre^{+} mT/mG^{+} Pik3ca^{*0} *Apc*$^{Min/+}$	1	49	6	14	10	18	0	1
N2	Fabp1-Cre^{+} mT/mG^{+} Pik3ca^{*0} *Apc*$^{Min/+}$	1	3	0	1	2	0	0	0

S1-S4, proximal to distal quarters of the small intestine; CE, cecum; CO, colon

ND, not determined

Wilcoxon Rank Sum test comparing pooled genotypes by strain (blue rows): no significant differences ($p \leq 0.050$) were found when comparing total multiplicity nor multiplicity within any sections.

Wilcoxon Rank Sum test comparing B6 and N2 mice within the same genotype (only sufficient data for Fabp1-Cre^{+} mT/mG^{+} Pik3ca*^{0} *Apc*$^{Min/+}$): no significant differences ($p \leq 0.050$) were found when comparing total multiplicity nor multiplicity within any sections.

Kruskal-Wallis test comparing pooled strains by genotype (yellow rows): no significant differences ($p \leq 0.050$) were found when comparing total multiplicity nor multiplicity within any sections.

Kruskal-Wallis tests comparing each genotype of N2 mice: no significant differences ($p \leq 0.050$) were found when comparing total multiplicity nor multiplicity within any sections.

Appendix 6-6. Average size of tumors from *Apc*$^{Min/+}$ control mice.

Strain	Genotype	N of tumors	Tumor size (maximum diameter in mm), mean +/- standard deviation					
			All	S1	S2	S3	S4	CO
All	All	73	1.0 +/- 0.7	1.4 +/- 0.7	1.0 +/- 0.4	0.8 +/- 0.3	0.9 +/- 0.4	2.9 +/- 2.8
B6	All	49	1.1 +/- 0.7	1.4 +/- 0.5	1.0 +/- 0.4	0.9 +/- 0.3	0.9 +/- 0.4	4.8
N2	All	24	0.9 +/- 0.6	1.3 +/- 0.9	0.8 +/- 0.2	0.6 +/- 0.1	0.8 +/- 0.5	0.9
All	Fabp1-Cre^{0} mT/mG^{+} Pik3ca^{*+} *Apc*$^{Min/+}$	6	1.2 +/- 0.9	1.6 +/- 1.2	0.7	ND	0.8	0.9
B6	Fabp1-Cre^{0} mT/mG^{+} Pik3ca^{*+} *Apc*$^{Min/+}$	0	ND	ND	ND	ND	ND	ND
N2	Fabp1-Cre^{0} mT/mG^{+} Pik3ca^{*+} *Apc*$^{Min/+}$	6	1.2 +/- 0.9	1.6 +/- 1.2	0.7	ND	0.8	0.9
All	Fabp1-Cre^{0} mT/mG^{0} Pik3ca^{*+} *Apc*$^{Min/+}$	2	1.5 +/- 1.3	2.5	ND	ND	0.6	ND
B6	Fabp1-Cre^{0} mT/mG^{0} Pik3ca^{*+} *Apc*$^{Min/+}$	0	ND	ND	ND	ND	ND	ND
N2	Fabp1-Cre^{0} mT/mG^{0} Pik3ca^{*+} *Apc*$^{Min/+}$	2	1.5 +/- 1.3	2.5	ND	ND	0.6	ND
All	Fabp1-Cre^{0} mT/mG^{0} Pik3ca^{*0} *Apc*$^{Min/+}$	5	0.8 +/- 0.2	ND	1.0 +/- 0.1	0.7 +/- 0.2	ND	ND
B6	Fabp1-Cre^{0} mT/mG^{0} Pik3ca^{*0} *Apc*$^{Min/+}$	0	ND	ND	ND	ND	ND	ND
N2	Fabp1-Cre^{0} mT/mG^{0} Pik3ca^{*0} *Apc*$^{Min/+}$	5	0.8 +/- 0.2	ND	1.0 +/- 0.1	0.7 +/- 0.2	ND	ND
All	Fabp1-Cre^{0} mT/mG^{+} Pik3ca^{*0} *Apc*$^{Min/+}$	4	0.6 +/- 0.1	ND	ND	0.6	0.6 +/- 0.1	ND
B6	Fabp1-Cre^{0} mT/mG^{+} Pik3ca^{*0} *Apc*$^{Min/+}$	0	ND	ND	ND	ND	ND	ND
N2	Fabp1-Cre^{0} mT/mG^{+} Pik3ca^{*0} *Apc*$^{Min/+}$	4	0.6 +/- 0.1	ND	ND	0.6	0.6 +/- 0.1	ND
All	Fabp1-Cre^{+} mT/mG^{0} Pik3ca^{*0} *Apc*$^{Min/+}$	4	1.1 +/- 0.5	0.9 +/- 0.4	ND	ND	1.7	ND
B6	Fabp1-Cre^{+} mT/mG^{0} Pik3ca^{*0} *Apc*$^{Min/+}$	0	ND	ND	ND	ND	ND	ND
N2	Fabp1-Cre^{+} mT/mG^{0} Pik3ca^{*0} *Apc*$^{Min/+}$	4	1.1 +/- 0.5	0.9 +/- 0.4	ND	ND	1.7	ND
All	Fabp1-Cre^{+} mT/mG^{+} Pik3ca^{*0} *Apc*$^{Min/+}$	52	1.0 +/- 0.7	1.4 +/- 0.5	1.0 +/- 0.4	0.8 +/- 0.3	0.9 +/- 0.4	4.8
B6	Fabp1-Cre^{+} mT/mG^{+} Pik3ca^{*0} *Apc*$^{Min/+}$	49	1.4 +/- 0.7	1.4 +/- 0.5	1.0 +/- 0.4	0.9 +/- 0.3	0.9 +/- 0.4	4.8
N2	Fabp1-Cre^{+} mT/mG^{+} Pik3ca^{*0} *Apc*$^{Min/+}$	3	0.6 +/- 0.1	ND	0.7	0.5 +/- 0.0	ND	ND

S1-S4, proximal to distal quarters of the small intestine; CO, colon

ND, not determined due to lack of tumors in this region

Wilcoxon Rank Sum test comparing pooled genotypes by strain (blue rows): no significant differences ($p \leq 0.050$) were found when comparing overall average tumor size nor average tumor size within any sections.

Wilcoxon Rank Sum test comparing B6 and N2 mice within the same genotype (only sufficient data for Fabp1-Cre^{+} mT/mG^{+} Pik3ca*^{0} *Apc*$^{Min/+}$): no significant differences ($p \leq 0.050$) were found when comparing overall average tumor size nor average tumor size within any sections.

Kruskal-Wallis test comparing pooled strains by genotype (yellow rows): no significant differences ($p \leq 0.050$) were found when comparing overall average tumor size nor average tumor size within any sections.

Kruskal-Wallis tests comparing each genotype of N2 mice: no significant differences ($p \leq 0.050$) were found when comparing overall average tumor size nor average tumor size within any sections.

Appendix 6-7. Tumor multiplicity from Pik3ca*$^{+}$ control mice.

Strain	Genotype	N of mice	Tumor multiplicity, mean +/- standard deviation
			Total (all in colon)
All	All	3	0.3 +/- 0.6
B6	All	2	0 +/- 0
N2	All	1	1
All	Fabp1-Cre^{+} mT/mG^{+} Pik3ca*$^{+}$ *Apc*$^{+/+}$	3	0.3 +/- 0.6
B6	Fabp1-Cre^{+} mT/mG^{+} Pik3ca*$^{+}$ *Apc*$^{+/+}$	2	0 +/- 0
N2	Fabp1-Cre^{+} mT/mG^{+} Pik3ca*$^{+}$ *Apc*$^{+/+}$	1	1
All	Fabp1-Cre^{+} mT/mG^{0} Pik3ca*$^{+}$ *Apc*$^{+/+}$	0	ND
B6	Fabp1-Cre^{+} mT/mG^{0} Pik3ca*$^{+}$ *Apc*$^{+/+}$	0	ND
N2	Fabp1-Cre^{+} mT/mG^{0} Pik3ca*$^{+}$ *Apc*$^{+/+}$	0	ND

Wilcoxon Rank Sum test comparing B6 and N2 mice within the same genotype: no significant differences ($p \leq 0.050$) were found when comparing multiplicity.

Appendix 6-8. Strain and genotype of all examined control mice which lacked Pick3ca* expression and Apc mutations.

Strain	Genotype	N of mice
All	All	8
B6	All	4
N2	All	4
All	Fabp1-Cre^{0} mT/mG^{+} Pik3ca^{*+} *Apc*$^{+/+}$	1
B6	Fabp1-Cre^{0} mT/mG^{+} Pik3ca^{*+} *Apc*$^{+/+}$	0
N2	Fabp1-Cre^{0} mT/mG^{+} Pik3ca^{*+} *Apc*$^{+/+}$	1
All	Fabp1-Cre^{0} mT/mG^{0} Pik3ca^{*+} *Apc*$^{+/+}$	1
B6	Fabp1-Cre^{0} mT/mG^{0} Pik3ca^{*+} *Apc*$^{+/+}$	0
N2	Fabp1-Cre^{0} mT/mG^{0} Pik3ca^{*+} *Apc*$^{+/+}$	1
All	Fabp1-Cre^{0} mT/mG^{0} Pik3ca^{*0} *Apc*$^{+/+}$	0
B6	Fabp1-Cre^{0} mT/mG^{0} Pik3ca^{*0} *Apc*$^{+/+}$	0
N2	Fabp1-Cre^{0} mT/mG^{0} Pik3ca^{*0} *Apc*$^{+/+}$	0
All	Fabp1-Cre^{0} mT/mG^{+} Pik3ca^{*0} *Apc*$^{+/+}$	1
B6	Fabp1-Cre^{0} mT/mG^{+} Pik3ca^{*0} *Apc*$^{+/+}$	0
N2	Fabp1-Cre^{0} mT/mG^{+} Pik3ca^{*0} *Apc*$^{+/+}$	1
All	Fabp1-Cre^{+} mT/mG^{0} Pik3ca^{*0} *Apc*$^{+/+}$	1
B6	Fabp1-Cre^{+} mT/mG^{0} Pik3ca^{*0} *Apc*$^{+/+}$	0
N2	Fabp1-Cre^{+} mT/mG^{0} Pik3ca^{*0} *Apc*$^{+/+}$	1
All	Fabp1-Cre^{+} mT/mG^{+} Pik3ca^{*0} *Apc*$^{+/+}$	4
B6	Fabp1-Cre^{+} mT/mG^{+} Pik3ca^{*0} *Apc*$^{+/+}$	4
N2	Fabp1-Cre^{+} mT/mG^{+} Pik3ca^{*0} *Apc*$^{+/+}$	0

ND, not determined

Appendix 6-9. Average size of tumors by color from Pik3ca*$^{+}$ *Apc*$^{Min/+}$ mice.

Strain	Tumor Color	N of tumors	Tumor size (maximum diameter in mm), mean +/- standard deviation						
			All	S1	S2	S3	S4	CE	CO
All	All	95	2.0 +/- 1.8	1.1 +/- 0.5	1.1 +/- 0.5	0.6 +/- 0.2	2.8 +/- 2.2	2.0 +/- 1.5	2.5 +/- 1.7
B6	All	45	1.3 +/- 0.9	1.2	1.0 +/- 0.2	0.6 +/- 0.2	2.0 +/- 1.0	0.6 +/- 0.04	1.2 +/- 0.7
N2	All	50	2.5 +/- 2.1	1.1 +/- 0.5	1.1 +/- 0.7	0.7	3.7 +/- 2.8	2.9 +/- 1.2	3.3 +/- 1.6
All	Heterotypic	24	3.5 +/- 2.2	ND	ND	ND	3.9 +/- 2.7	2.2 +/- 2.2	3.3 +/- 1.4
B6	Heterotypic	8	2.3 +/- 0.8	ND	ND	ND	2.5 +/- 0.6	0.7	2.7
N2	Heterotypic	16	4.1 +/- 2.4	ND	ND	ND	4.9 +/- 3.1	3.8	3.3 +/- 1.5
All	Homotypic Green	28	2.0 +/- 1.6	ND	ND	0.5 +/- 0.03	2.5 +/- 1.7	1.9 +/- 1.4	1.8 +/- 1.6
B6	Homotypic Green	10	1.4 +/- 1.0	ND	ND	0.5 +/- 0.03	1.9 +/- 1.2	0.6	0.9 +/- 0.3
N2	Homotypic Green	19	3.3 +/- 1.8	ND	ND	ND	3.8 +/- 2.0	2.5 +/- 1.3	3.2 +/- 1.9
All	Homotypic Red	43	1.1 +/- 0.6	1.1 +/- 0.5	1.1 +/- 0.5	0.7 +/- 0.2	1.4 +/- 1.0	ND	ND
B6	Homotypic Red	19	0.9 +/- 0.5	1.2	1.0 +/- 0.2	0.7 +/- 0.2	1.3 +/- 1.0	ND	ND
N2	Homotypic Red	24	1.2 +/- 0.7	1.1 +/- 0.5	1.1 +/- 0.7	0.7	1.4 +/- 1.1	ND	ND

S1-S4, proximal to distal quarters of the small intestine; CE, cecum; CO, colon

ND, not determined due to lack of tumors in this region

Wilcoxon Rank Sum test comparing pooled colors by strain (blue rows): significant differences ($p \leq 0.050$) were found when comparing overall average tumor size; when comparing within individual segments, significant differences were only found in the colon.

Wilcoxon Rank Sum test comparing B6 and N2 mice within the same color: significant differences ($p \leq 0.050$) were found when comparing overall average tumor size from each strain within each color except within red tumors; when comparing within individual segments, significant differences were only found in the colon within the green tumors.

Fisher's Method to combine Wilcoxon Rank Sum tests comparing B6 and N2 mice within the same color: significant differences ($p \leq 0.050$) were found when combining comparisons of overall average tumor size from each color within each strain; when combining comparisons within individual segments, significant differences were only found in the colon.

Kruskal-Wallice test comparing pooled strains by color (yellow rows): significant differences ($p \leq 0.050$) were found when comparing overall average tumor size; when comparing within individual segments, significant differences were only found in segment 4 and the colon.

Kruskal-Wallice tests comparing each color within the same strain: significant differences ($p \leq 0.050$) were found when comparing overall average tumor size from each color within each strain; when comparing within individual segments, significant differences were only found in segment 4 within the N2 strain.

Fisher's Method to combine Kruskal-Wallice tests comparing each color within the same strain: significant differences ($p \leq 0.050$) were found when combining comparisons of overall average tumor size from each strain within each color.

$$perimeter\,(green)$$

Green patch perimeter length is directly proportional to the number of green crypts adjacent to crypts of another color.

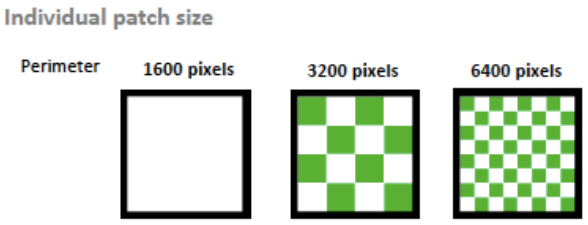

$$\frac{perimeter(green)}{\sqrt{area(tissue)}}$$

Perimeter must be normalized to tissue area or higher resolution images and larger tissues will have falsely higher scores

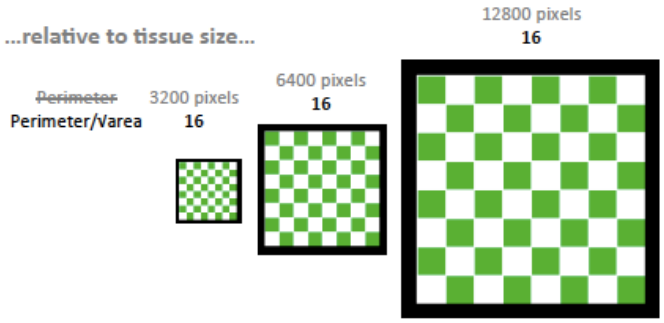

Variegation Score =

$$\frac{perimeter(green)-(proportion(green)*perimeter(tissue))}{\sqrt{area(tissue)}}$$

Green crypts on the tissue perimeter do not have an adjacent crypt of another color and must be subtracted out in order to avoid falsely giving tissues with more green a higher score.

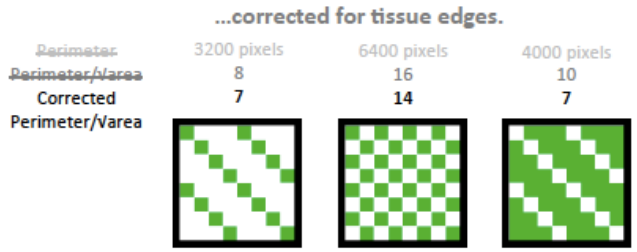

Appendix 6-10. Development of the variegation score. The equation (left) was developed to represent the number of crypts which are adjacent to a crypt of a different color. In this way, a high variegation score would represent a high power to detect multi-ancestral tumors. Images with varying patchwork (right) were used to confirm the equation works as expected.

Appendix 7. Transformation of epithelial cells through recruitment leads to multi-ancestral intestinal tumors.

This manuscript was included in the appendix as evidence for interclonal interactions during tumor initiation and as an example of how multi-ancestral tumors can be modeled.

Andrew T. Thliveris, Brittany Schwefel, Linda Clipson, Lauren Plesh, Christopher D. Zahm, **Alyssa A. Leystra**, Mary Kay Washington, Ruth Sullivan, Dustin A. Deming, Michael A. Newton, and Richard B. Halberg.

Abstract

Intestinal tumors from mice and humans can have a multi-ancestral origin. Statistical analyses indicate that the best explanation for this source of intratumoral heterogeneity is the presence of interactions among multiple progenitors. We sought to better understand the nature of these interactions. An initial progenitor could recruit others by facilitating the transformation of one or more neighboring cells. Alternatively, two progenitors that are independently initiated could simply cooperate to form a single tumor. These possibilities were tested by analyzing tumors from aggregation chimeras that were generated by fusing together embryos with unequal predispositions to tumor development. Strikingly, numerous multi-ancestral tumors were observed even when one genetic component was highly, if not completely, resistant to spontaneous tumorigenesis in the intestine. Moreover, the observed number of multi-ancestral tumors could be explained by the facilitated transformation of a single neighbor within 144 μm of an initial progenitor. These findings strongly support recruitment instead of cooperation. Thus,

it is conceivable that these interactions are necessary for tumors to thrive, so blocking them might be a highly effective method for preventing the formation of tumors in the intestine and other tissues.

Adapted from PNAS; 110(28): 11523–11528. ©2014 Thliveris et al.

In addition to reformatting, the following changes were made for the sake of consistency:

- Figures and references were renumbered
- "Polyclonal" tumors were renamed "multi-ancestral" tumors
- *"Rosa26"* ("*R26*$^{+}$") mice were renamed "ROSA26-LacZ" ("LacZ^{+}") mice

Authors' Contributions

Author contributions: A.T.T. and R.B.H. designed research; A.T.T., L.C., L.P., C.D.Z., A.A.L., D.A.D., and R.B.H. performed research; B.S. and M.A.N. contributed new reagents/analytic tools; A.T.T., B.S., L.C., L.P., C.D.Z., A.A.L., M.K.W., R.S., D.A.D., M.A.N., and R.B.H. analyzed data; and A.T.T., B.S., M.A.N., and R.B.H. wrote the paper.

Introduction

Tumors are often heterogeneous with respect to several distinguishable properties, including differentiation state, proliferation rate, metastatic potential, and therapeutic response. Two models to explain intratumoral heterogeneity have been proposed. The clonal evolution model asserts that different subclones arise from a single progenitor as a consequence of molecular changes followed by selection for dissimilar microenvironments within a tumor[1]. By

contrast, the cancer stem cell model contends that a small population of stem cells originating from a single progenitor is responsible for tumor maintenance but the progeny can differentiate in several diverse ways[1]. A key assumption in both models is that tumors are derived from a single progenitor.

Evidence is steadily accruing that intestinal tumors are often multi-ancestral rather than uni-ancestral[2]. Merritt et al. demonstrated that hereditary tumors in the mouse intestine are often derived from multiple progenitors[3]. In this study, aggregation chimeras were generated by fusing embryos carrying the *Min* allele of the *Adenomatous polyposis coli* gene ($Apc^{Min/+}$) to embryos carrying *Min* and the ROSA26-LacZ lineage marker ($Apc^{Min/+}$ $LacZ^{+}$). Clonal structure was assessed in histologic sections of tumors stained for the lineage marker. A significant number (8%) of early adenomas were heterotypic, being composed of cells from the two different embryos. Using a similar approach, Thliveris et al. demonstrated that carcinogen-induced tumors in mice are also derived from multiple progenitors[4]. In both studies, the intestines consisted of small blue and white patches. This chimeric pattern increases the power to detect the multi-ancestral tumor structure because a heterotypic tumor forming on a border between the two colors is clearly multi-ancestral, whereas a homotypic tumor could be multi-ancestral as the result of being derived from two progenitors with the same LacZ expression status or else uni-ancestral. The findings from the Merritt and Thliveris studies are consistent with those of other investigators demonstrating that hereditary and sporadic colorectal tumors in humans are often multi-ancestral[5,6]. Therefore, multiple progenitors contributing to a single tumor are an additional source of intratumoral heterogeneity.

Although evidence supports the existence of the multi-ancestral tumor structure, this phenomenon could have been merely a consequence of random collision between independently

derived tumors instead of necessary clonal interactions. In the Merritt study, the aggregation chimeras developed far too many tumors to rule out random collision. To distinguish between the possible explanations for the multi-ancestral tumor structure, Thliveris et al. generated aggregation chimeras that developed relatively few intestinal tumors[7]. They found that the percentage of heterotypic tumors was still high (20%), even though the multiplicity of tumors was very low. This observation when combined with statistical analyses ruled out random collision and favored clonal interactions. In the Thliveris study, tumor phenotypes were linked with image data describing the pattern of chimerism to estimate the range of clonal interactions[7]. They found that interactions occurring between progenitors in neighboring crypts (i.e., 40–120 μm apart) were sufficient to account for the percentage of heterotypic tumors that was observed. Thus, the multi-ancestral tumor structure could be explained by multiple progenitors interacting over a very short distance.

The details of clonal interactions during the initial stages of tumorigenesis remain unknown. One possibility is some form of recruitment in which a single progenitor, following the loss of Apc activity, subsequently facilitates the neoplastic transformation of one or more neighboring cells. Alternatively, multiple independently derived progenitors arising in close proximity might effectively cooperate and gain a selective growth advantage over an isolated progenitor. Although prior studies of tumor clonality were unable to distinguish between recruitment and cooperation, the two models predict different frequencies of heterotypic tumors in aggregation chimeras formed from embryos that have unequal susceptibilities to tumorigenesis. On the basis of this realization, we characterized clonal interactions by generating and analyzing two types of aggregation chimeras: C57BL/6 (B6) $Apc^{Min/+}$ ↔ $Apc^{1638N/+}$ $LacZ^{+}$

and B6 $Apc^{Min/+} \leftrightarrow Apc^{+/+}$ $LacZ^{+}$, because B6 $Apc^{Min/+}$ mice spontaneously develop many more intestinal tumors than either B6 $Apc^{1638N/+}$ mice or B6 $Apc^{+/+}$ mice[8].

Results

We reasoned that recruitment and cooperation could be distinguished by generating aggregation chimeras from embryos with unequal tumor susceptibilities (Appendix 7-1). If multi-ancestral tumors form as a consequence of recruitment, the number will depend on how many progenitors lie on the border between patches that are derived from the different embryos and the ability of the susceptible tissue to facilitate the transformation of the more resistant tissue. This number should be relatively high because progenitors arising from cells highly susceptible to neoplastic transformation (white) are common. If multi-ancestral tumors form as a consequence of cooperation, the number will depend on the probability that two or more progenitors are juxtaposed to each other. This number should be relatively low because progenitors arising from cells that are resistant (blue) to neoplastic transformation are rare. Conceptually, these two distinct models explaining the multi-ancestral tumor structure should be distinguishable.

To advance our reasoning, we constructed statistical models that predict the frequency of heterotypic tumors under recruitment and cooperation in chimeras that were formed from embyros with unequal susceptibilities to neoplastic transformation. Calculations leveraged information in the complex chimeric patterns revealed through images of the intestine. These complex chimeric patterns exhibited statistical regularities, for example in terms of proportions of a given color, or typical distances between points of opposite color (Appendix 7-2). A small distance between points of opposite color corresponds to the notion of small patch size; the

precise way in which the chimeric properties predict heterotypic tumors depends on whether we model recruitment or cooperation as the generative mechanism. For recruitment, an $Apc^{Min/+}$ cell at a random position is transformed into its neoplastic counterpart after the loss of Apc activity, and this initial progenitor then facilitates the transformation of neighboring cells. This model is simplified by assuming all neighboring cells can be recruited to form a single tumor derived from several progenitors. In the recruitment calculations, the patch-size information is conveyed by the distribution of the distance from a point to the nearest point of the opposite color. For cooperation, multiple transformed cells arising from independent events in which Apc is inactivated and in close proximity form a single tumor because the interactions provide a selective advantage. Here, the patch-size information is conveyed by properties of locally averaged chimeric images (Appendix 7-2). A key finding is that these models make significantly different predictions about the probability for a tumor to be heterotypic, especially in the case in which chimeras are formed from embyros with unequal tumor susceptibilities (Appendix 7-1B). For example, when one embryo is 100 times more likely to develop a tumor than the other [i.e., the initiation differential (β/α) is 0.01], the heterotypic frequency is roughly 20% under recruitment and less than 1% under cooperation. Recruitment and cooperation are clearly distinguishable by analyzing aggregation chimeras that are generated from embryos with unequal tumor susceptibilities.

We fused B6 $Apc^{Min/+}$ embryos to B6 $Apc^{1638N/+}$ $LacZ^{+}$ embryos because B6 $Apc^{Min/+}$ mice (n = 228) develop on average 95 ± 53 intestinal tumors, whereas B6 $Apc^{1638N/+}$ mice (n = 94) develop on average 0.98 ± 1.17 tumors in our mouse colony. The resulting aggregation chimeras were killed when moribund at ages ranging from 79 to 121 d (Appendices 7-3 and -8). The intestinal tract was removed, divided into five equal segments, splayed open, stained to

identify cells carrying the LacZ lineage marker, and photographed; images were digitized for statistical analysis in which the chimeric pattern was characterized (Appendices 7-3A, -3B, and 8). The fixed samples were scored for intestinal tumors using a dissecting microscope; an average of 118 ± 19 was observed (Appendix 7-8). Many tumors were excised, embedded in paraffin, sectioned, and assessed by two pathologists to determine phenotype (Appendix 7-3D). Seven heterotypic tumors consisting of blue and white neoplastic cells with nuclear β-catenin were observed (Appendix 7-8). To further contrast recruitment with cooperation as distinct models for clonal interactions, we also fused $Apc^{Min/+}$ embryos to $Apc^{+/+}$ LacZ $^{+}$embryos because $Apc^{+/+}$ mice have never been observed to develop intestinal tumors spontaneously. The resulting aggregation chimeras were killed when moribund at ages ranging from 108 to 122 d (Appendices 7-4 and -8). These mice developed on average 18 ± 10 intestinal tumors. Of the 54 tumors excised, 8 were heterotypic and 25 homotypic white (Appendices 7-5 and -8). In both types of aggregation chimeras, multi-ancestral tumors are relatively common in aggregation chimeras that are generated from embryos with unequal tumor susceptibilities.

The probability that a tumor is heterotypic, homotypic blue, or homotypic white depends on the pattern of chimerism surrounding the initiation point and the range of interactions, regardless of the model being tested. These probabilities were calculated for all five segments of the intestinal tract in $Apc^{Min/+} \leftrightarrow Apc^{1638N/+}$ LacZ^{+}and $Apc^{Min/+} \leftrightarrow Apc^{+/+}$ LacZ^{+} aggregation chimeras, considering recruitment in which all neighbors are transformed, partial recruitment in which some neighbors are transformed, and cooperation (Appendix 7-6). The values were compared with the observed rate of heterotypic tumors. Both recruitment models significantly outperformed the cooperation model. This finding supports the notion that multi-ancestral tumors

arise because an initial progenitor following the loss of Apc activity facilitates the transformation of one or more neighboring cells.

The range of interactions for recruitment that are necessary to explain the multi-ancestral tumor architecture was estimated. The maximum log likelihood was calculated at different interaction distances and with different numbers of partners (Appendix 7-7). A distance of 25 μm resulted in the best fit if all neighbors were recruited; the distance increased to 144 μm if only a single neighbor was recruited. Note that the distance between two neighboring crypts is only approximately 50 μm. Thus, recruitment over a very short distance easily accounts for the observed number of multi-ancestral tumors in $Apc^{Min/+} \leftrightarrow Apc^{1638N/+}$ $LacZ^{+}$ and $Apc^{Min/+} \leftrightarrow Apc^{+/+}$ $LacZ^{+}$ aggregation chimeras.

Discussion

Evidence is steadily accruing that indicates that several tumor types can be multi-ancestral as a consequence of being derived from multiple progenitors and not merely the emergence of distinct subclones during tumor evolution. We sought to better understand the interactions among progenitors in the intestine. Aggregation chimeras were generated by fusing together embryos with unequal tumor susceptibilities to create a biological model that allows us to distinguish between recruitment and cooperation. Statistical analyses that combined tumor phenotype with the pattern of chimerism indicated that recruitment is the best explanation for the multi-ancestral tumor architecture. In fact, the formation of a multi-ancestral tumor in this experimental system can be explained by recruitment of only a single neighboring cell within two to three crypts of the initial progenitor.

Tumors were analyzed from two sets of aggregation chimeras. In $Apc^{Min/+} \leftrightarrow Apc^{1638N/+}$ $LacZ^{+}$ aggregation chimeras, the expected number of multi-ancestral tumors was 14 under recruitment and 1 under cooperation. These numbers were calculated by knowing the percentage of the chimera that was derived from each embryo, the multiplicity of intestinal tumors, the phenotype of scorable tumors, and the statistical models for recruitment and cooperation (Appendix 7-1 and 8). The observed number was seven. Similarily, in $Apc^{Min/+} \leftrightarrow Apc^{+/+}$ $LacZ^{+}$ aggregation chimeras, the expected numbers of multi-ancestral tumors was four under recruitment and zero under cooperation because $Apc^{+/+}$ mice never spontaneously develop intestinal tumors. Eight were observed. This finding was unexpected: a previous study found no multi-ancestral tumors in $Apc^{Min/+} \leftrightarrow Apc^{+/+}$ aggregation chimeras[3,9]. Our study differed from the previous study in important ways. One key difference is the way in which aggregation chimeras were constructed. In our study, the $Apc^{+/+}$ embryo always carried the LacZ lineage marker because it is easier to detect blue cells in a predominanlty white mass than it is to detect white cells in a predominantly blue mass. In the previous studies, the embryo carrying the lineage marker varied from chimera to chimera. Another key difference is how the intestines and tumors were analyzed. In our study the entire intestinal tract was removed, stained, and scored, and then all of the tumors were isolated, embedded in paraffin, and sectioned through and through for pathological assessment. In the previous studies only a third of the intestinal tract was removed, and then tumors were sampled from areas in which blue tissue and white tissue were juxtaposed. Finally, in our study, sections from each tumor were examined by two pathologists. Our findings with two sets of aggregation chimeras indicate that an initial progenitor is able to recruit a nearby wild-type partner.

How does an initial progenitor recruit neighboring cells? A number of different mechanisms are possible. The loss of Apc activity in the initial progenitor could trigger the loss of Apc activity in neighboring cells. An $Apc^{Min/+}$ cell could lose the wild-type copy of *Apc* by point mutation or somatic recombination and be transformed into its neoplastic counterpart[10]. This initial progenitor and its immediate descendants might express mitogenic factors that increase the rate of cellular proliferation in neighboring cells. Rapid proliferation might result in spontaneous mutations in *Apc* and consequent loss of activity and neoplastic transformation. Kuraguchi et al. found that intestinal tumors from $Apc^{1638N/+}$ mice lacking DNA mismatch activity often carried two distinct somatic mutations in *Apc*[11]. In addition, Thirlwell et al. found that tumors from patients afflicted with familial adenomatous polyposis often carried two distinct somatic mutations[6]. Thus, recruitment could be mediated through additional genetic events, particularly in the context of hereditary cancers. However, if recruitment involved only *Apc* mutations, the number of multi-ancestral tumors should be higher in $Apc^{Min/+} \leftrightarrow Apc^{1638N/+}$ $LacZ^+$ aggregation chimeras, in which only two hits are required for the development of multi-ancestral tumors, than in $Apc^{Min/+} \leftrightarrow Apc^{+/+}$ $LacZ^+$ aggregation chimeras, in which three are required. However, the number of multi-ancestral tumors was comparable in $Apc^{Min/+} \leftrightarrow Apc^{1638N/+}$ $LacZ^+$ and $Apc^{Min/+} \leftrightarrow Apc^{+/+}$ $LacZ^+$ aggregation chimeras even though in the first set both embryos carry a germ-line *Apc* mutation and in the second set only one embryo carries a germ-line *Apc* mutation. Analyzing the status of *Apc* in multi-ancestral tumors in this study is extremely challenging given the amount of tissue that is available and the condition of the tissue after X-gal staining, which is harsh, involving two fixation steps and an overnight incubation at 37 °C.

Another possible mechanism for recruitment is paracrine oncogenic signaling. The initial $Apc^{Min/+}$ progenitor after the loss of Apc activity and its immediate progeny could produce signaling factors that facilitate transformation of neighboring cells that are responsive to the signal. For example, secreted Wnt molecules could lead to the translocation of β-catenin to the nucleus in neighboring cells that are expressing Frizzled receptors. β-Catenin is clearly localized to the nucleus in neoplastic cells that are derived from the $Apc^{Min/+}$, $Apc^{1638N/+}$, and even the $Apc^{+/+}$ lineages (Appendix 7-5). Thus, recruitment might involve signaling instead of additional genetic events in certain biological contexts. Thirlwell et al. have demonstrated that some sporadic colon cancers were multi-ancestral, consisting of dysplastic crypts that carry mutations in *Apc* and those that do not[6].

Several lines of investigation support the notion that recruitment could be mediated by Wnt molecules. Neoplastic cells in which β-catenin is localized to the nucleus protrude out from the normal crypt structure[12]. This change in position would place an initial progenitor and its immediate progeny in close proximity to neighboring cells such that secreted factors could elicit changes in signaling. Once β-catenin has translocated to the nucleus, it stimulates the expression of numerous genes, including *Wnt3A*[13]. Several Wnt signaling molecules are transforming factors in vitro and in vivo[14-16]. Epithelial cells expressing Wnt1 can transform other epithelial cells. Mammary tumors that are induced by a virus in GR mice are usually multi-ancestral with two or more mutually interdependent cell populations, but only one population expresses activated Wnt1[15]. Similarly, stromal cells expressing Wnt1 can transform epithelial cells. Fibroblasts expressing Wnt1 elicit a morphological transformation of neighboring mammary epithelial cells in coculture experiments when the neighboring cells are responsive to the signal[16]. Recently, other investigators have suggested that Wnt signaling is a marker of colon

cancer stem cells (CSC) and that it is regulated by the microenvironment[17]. Tumor cells that have lost the capacity to form tumors can be reprogrammed to express CSC markers including CD133 and regain tumorigenic capacity when stimulated by myofibroblast-derived factors that activate Wnt signaling[17]. Thus, recruitment might involve interactions among epithelial cells as well as interactions among epithelial and stromal cells that are mediated through molecules that affect Wnt signaling.

This study has limitations. The statistical models described are extreme simplifications of the dynamic mechanisms truly at work. As has been found in so many other domains, the use of such simplified models provides a language to discuss primary factors affecting the system and puts a sharper focus on the information content of the available data[18]. We also recognize that staining to detect the LacZ lineage marker severely impairs the type of molecular analyses that can be performed.

This study extends our understanding of the clonal origin of intestinal tumors. An initial progenitor recruits neighboring cells within a very short distance; molecules mediating this interaction might affect Wnt signaling. The ability of one cell to facilitate the transformation of another cell has been observed with cancer-associated fibroblasts[18]. Understanding recruitment will likely impact prevention strategies. For example, if the initial progenitor that transforms neighboring cells is responsive to some mitogenic factor, drugs that target that factor might prevent tumors from forming or becoming established and growing. A number of known naturally occurring factors down-regulate Wnt signaling including Dickkopf-1[19]. New models are now becoming available to identify the cells involved and the molecules that mediate clonal interactions that give rise to multi-ancestral tumors.

Methods

Mouse strains and generation of aggregation chimeras

All animal studies were conducted under protocols approved by the Institutional Animal Care and Use Committee at the University of Wisconsin-Madison, following the guidelines of the American Association for the Assessment and Accreditation of Laboratory Animal Care. C57BL/6J (B6) mice heterozygous for *Apc*^{Min} were from the laboratory stock of William F. Dove at the University of Wisconsin. B6 and B6 mice heterozygous for the ROSA26-LacZ transgene expressing LacZ were obtained from The Jackson Laboratory. B6 mice heterozygous for *Apc*^{1638N} were obtained from the National Cancer Institute Repository. Stocks of these strains were maintained by continually backcrossing to B6 mice (The Jackson Laboratory) that were imported every fifth generation. Offspring were screened for *Apc*^{Min}, ROSA26-LacZ, and *Apc*^{1638N} using PCR assays of DNA isolated from toe clips[7,20].

Aggregation chimeras were generated by fusing together embryos from two crosses: B6 *Apc*$^{+/+}$ × B6 *Apc*$^{Min/+}$ and B6 *Apc*$^{+/+}$ × B6 *Apc*$^{1638N/+}$ ROSA26-LacZ^{+}. Ear snips were also taken from each animal and stained with 5-bromo-4-chloro-indolyl-β-D-galactopyranoside (X-Gal) (United States Biological) to ascertain chimerism for β-galactosidase activity.

Tumor phenotyping

Wholemounts of the intestines were prepared, stained with X-gal, photographed and digitized. Tumors were isolated, embedded in paraffin, serially sectioned *in toto*, and counterstained with hematoxylin and eosin. The phenotype of each tumor was determined by two pathologists independently of each other. Some slides were stained with β-catenin to confirm

heterotypic tumors were composed of blue and white neoplastic cells. Details were described previously[7].

Statistical analysis

Treating the intestinal epithelium as a finite planar region, we consider positions x on this surface in an aggegation chimera, and we let $c(x)$ be the indicator function that defines the chimeric pattern. Say, $c(x) = 1$ indicates the tissue is blue at x and $c(x) = 0$ indicates the tissue is white, as evidenced by image data (Appendix 7-7). Let $d(x,y)$ denote the distance along the intestinal surface between points x and y, and further let $D(x, \delta)$ denote a disk on the surface centered at x and having radius δ; that is, $D(x, \delta) = \{y : d(x,y) \leq \delta \}$. Allowing different rates of tumor initiation in the contributing lineages, we treat the probability density of initiation events as $f(x) = \alpha + (\beta - \alpha)c(x)$, where the different tumor susceptibilities are α (white tissue) and β (blue tissue). The initiation differential $\rho = \beta/\alpha$ is relevant in comparing the probabilities of the different tumor phenotypes in different models.

Cooperation model

The central concept is that multiple progenitors initiated independently but in close proximity have a selective advantage over an isolated progenitor. A simple mathematical expression of this idea involves two initiation events at random locations X and Y, distributed independently and possibly nonuniformly according to $f(x)$ as above. We consider a tumor forming only if the distance $d(X,Y)$ is less than some value δ. The tumor is homotypic blue if $c(X) = c(Y) = 1$; it is homotypic white if $c(X) = c(Y) = 0$, and otherwise it is heterotypic. In the cooperation model, tumor phenotype probabilities under these assumptions are:

$$\Pr(\text{blue}|\text{cooperate}) = k\beta^2 \int c(x)h(x,\delta)dx$$
$$\Pr(\text{white}|\text{cooperate}) = k\alpha^2 \int [1-c(x)][1-h(x,\delta)]dx$$
$$\Pr(\text{heterotypic}|\text{cooperate}) = k\alpha\beta \int \{c(x)[1-h(x,\delta)] + [1-c(x)]h(x,\delta)\}dx,$$

where k is a normalizing constant, and the function $h(x,\delta)$, shown in Appendix 7-7, is a smoothed version of a chimeric pattern $c(x)$; that is, $h(x,\delta) = (1/(\pi\delta^2)) \int 1[d(x,y) \leq \delta]\, c(y)\, dy$. Probabilities are computed using parameter settings and image characteristics derived from smoothed chimeric pattern images. Additional details are provided in *SI Methods*.

Recruitment model

An elementary recruitment model entails a single initiation event at a random position$X$, followed by neoplastic transformation of all cells in the disk $D(X, \delta)$. The tumor initiated at X is homotypic blue if $c(y) = 1$ for all y in the disk [i.e., all cells within a given distance are blue, homotypic white if all $c(y) = 0$, and otherwise heterotypic]. The rationale is simply that to be homotypic blue, the initiation point X must occur in blue tissue and also be sufficiently far from white tissue to avoid recruitment of that opposite type. In the original version of this model that was proposed by Thliveris et al., the initiation point X is uniformly distributed over the surface, but uniformity is an unnecessary restriction and can be usefully extended to the density $f(x)$ (above) when we consider chimeras formed from two genetic backgrounds that differ in tumor susceptibility[7]. Probabilities of the three tumor phenotypes have integral representations:

$$\Pr(\text{blue}|\text{recruit}) = \beta \int c(x)g(x,\delta)dx$$
$$\Pr(\text{white}|\text{recruit}) = \alpha \int [1-c(x)]g(x,\delta)dx$$
$$\Pr(\text{heterotypic}|\text{recruit}) = 1 - \Pr(\text{blue}|\text{recruit}) - \Pr(\text{white}|\text{recruit}),$$

where integrals are over the planar intestinal surface, and $g(x,\delta)$ indicates that position x is more than δ units from any cell of the opposite lineage; that is, $g(x, \delta) = 1$ if $c(y) = c(x)$ for all y in $D(x, \delta)$, otherwise $g(x, \delta) = 0$. Fixing parameters α, β, and δ, phenotype probabilities are computable in a given intestinal region using characteristics of the chimeric patterns recorded in the image data. Each binary image is converted to a distance-map image, which records at each pixel the distance to the nearest pixel of the opposite color. The empirical distribution of these distances, separated for blue and white source pixels, determines the integrals and thus the phenotype probabilities. We used the R package EBImage to compute these distance maps[21].

The heterotypic rate Pr(heterotypic|recruit) increases with disk radius δ, because larger disks are more likely to include both lineages. Thliveris et al. estimated that a value for δ of 40–120 μm was sufficiently large to explain the observed percentage of heterotypic tumors in seven aggregation chimeras[7]. For various values of the initiation differentials ρ, the probability of each tumor phenotype is shown (Appendix 7-1B and 7). In this elementary recruitment model, the rate of heterotypic tumors is affected very slightly by the initiation differential ρ.

By comparison, a key observation concerns the behavior of Pr(heterotypic|cooperate) for initiation differentials ρ that are far from unity. Under cooperation, it becomes highly improbable to see a heterotypic tumor when the two tissue types exhibit substantially different initiation rates (Appendix 7-1B and 7). The present analyses quantify predictions from recruitment vs. cooperation calculations to support statistical testing generated in the proposed experiments.

Partial recruitment

We considered a variation of the recruitment model in which only a select number of neighboring cells were transformed. Specifically, we allowed a single initiation event at random

position Xfollowing density $f(x)$, as in the recruitment model. Next some number of partners (ν), sampled uniformly at random in the disk $D(X, \delta)$, are recruited to form a tumor whose phenotype is homotypic if $c(X)$ matches that of all of the partners, otherwise it is heterotypic. The phenotype probabilities involve smoothing images rather than taking distance maps, as in the cooperation model, and they take the following specific forms.

$$\Pr(\text{blue}|\text{partial recruit}) = \beta \int c(x)[h(x,\delta)]^{\nu} dx$$
$$\Pr(\text{white}|\text{partial recruit}) = \alpha \int [1 - c(x)][h(x,\delta)]^{\nu} dx$$
$$\Pr(\text{heterotypic}|\text{partial recruit}) = 1 - \Pr(\text{blue}|\ldots) - \Pr(\text{white}|\ldots).$$

It is readily confirmed that these probabilities converge to the full-recruitment probabilities as ν increases.

Likelihood computations

The phenotype of each tumor (homotypic blue, homotypic white, or heterotypic) was treated as the realization of a random variable with trinomial probabilities determined by the specific model on test as well as by image characteristics of the intestinal region harboring the tumor. Intestines were segmented into five regions for this purpose. Initiation rate parameters α and β were fixed at values estimated from the multiplicity of tumors in parental strains; $Apc^{Min/+}$ mice develop on average 100 tumors, whereas $Apc^{1638N/+}$ mice develop on average 1 tumor, and $Apc^{+/+}$ mice develop none. With PHENO_i, the phenotype of tumor i, the log likelihood in a given model MODEL is:

$$\text{log likelihood} = \sum_i \log \Pr(\text{PHENO}_i|\text{MODEL}).$$

Free parameters in each MODEL, including disk diameter and the number of recruited partners, were fixed by maximizing this log likelihood.

Source code

R scripts to perform all computations are available online as supporting information for the published manuscript[22]. Scripts were generated to calculate distance maps, smooth images, compute phenotype probabilities, and calculate likelihoods.

Disclosure of Potential Conflicts of Interest

The authors declare no conflict of interest.

Acknowledgments

We thank Ella Ward and Jane Weeks in Experimental Pathology at the University of Wisconsin (UW) Carbone Cancer Center for technical assistance, members of the Laboratory Animal Research staff for their conscientious care of animals involved in this and other studies, and Drs. William F. Dove, Norman Drinkwater, Mark Reichelderfer, and William Schelman for critical review of the manuscript.

This study was supported by funding from National Cancer Institute Grants R01 CA123438 (to R.B.H.), R01 CA063677 (to W. F. Dove), P30 CA014520 (UW Carbone Cancer Center Core Grant), P50 CA095103 (Gastrointestinal Specialized Program of Research Excellence Grant, Vanderbilt-Ingram Cancer Center), K08 CA84146 (to A.T.T.), T32 CA009614 (to D.A.D.), and T32 CA009135 (to C.D.Z.), and by start-up funds from the UW Division of Gastroenterology and Hepatology, the UW Department of Medicine, and the UW School of Medicine and Public Health (to R.B.H.).

Figures

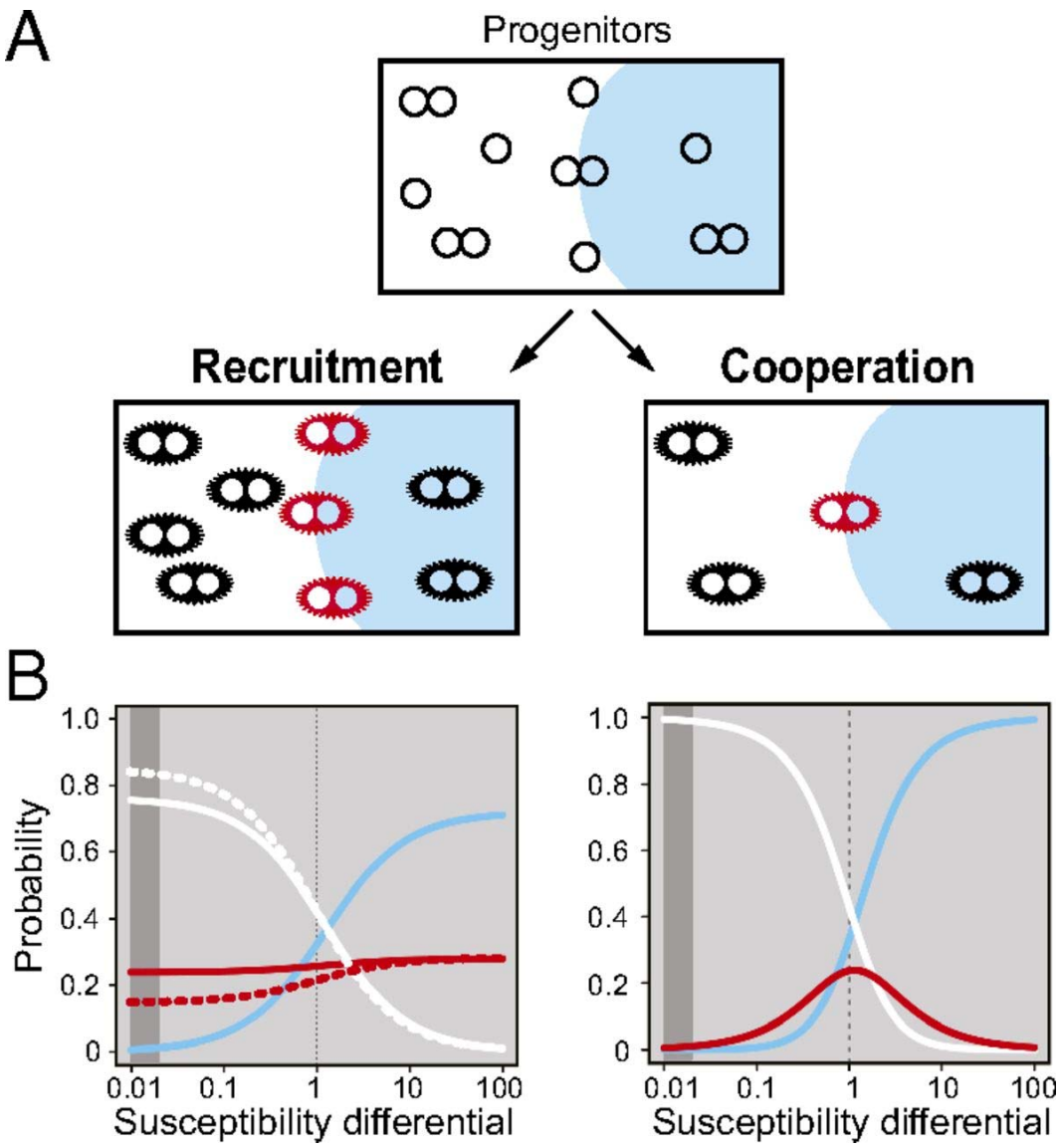
A
Progenitors
Recruitment
Cooperation
B
Probability
1.0
0.8
0.6
0.4
0.2
0
0.01
0.1
1
10
100
Susceptibility differential
1.0
0.8
0.6
0.4
0.2
0
0.01
0.1
1
10
100
Susceptibility differential

Appendix 7-1. Different models could explain interactions leading to the formation of multi-ancestral tumors. Aggregation chimeras were generated by fusing an embryo that is relatively susceptible to the formation of intestinal tumors (white) to an embryo that is relatively resistant (blue). (A) The number of multi-ancestral tumors that are heterotypic with a mixture of white and blue (red star) will be high if the more susceptible white progenitors are able to recruit the more resistant neighboring blue cells (Left), but the number will be low if one of the white progenitor needs to be juxtaposed to a rare blue progenitor (Right). (B) Statistical modeling validated this conceptualization. The percentage of tumors that were predicted to be homotypic white (white lines), homotypic blue (blue lines), or a mixture of white and blue (red lines) was plotted vs. the initiation differential, which is the ratio of tumor susceptibilities, using average image statistics for all measured chimeric patterns and using different tumor formation models (each optimized in its parameters): full recruitment with interactions of 67 μm (Left, solid lines); partial recruitment with interactions over 144 μm (Left, dashed lines); and cooperation with interactions over 5,004 μm (Right). The models make distinguishable predictions when the initiation differential is far from one (e.g., 0.15 or less). The dark gray band ranges from 0.01 to 0.02, which is the probable initiation differential between $Apc^{1638N/+}$ and $Apc^{Min/+}$. In contrast, when the ratio is 1 (i.e., both embryos are equally susceptible to the formation of intestinal tumors as in previous studies[3,4,7]), the two models are indistinguishable.

$c(x) = 1_{\text{blue lineage}}$

$\text{dmin}(x) = \text{distance to nearest opposite color}$

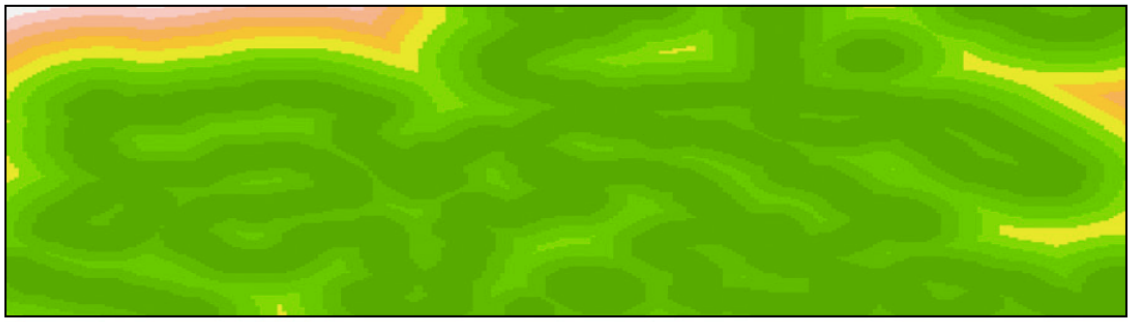

$g(x, \delta) = 1_{\text{dmin}(x)>\delta}$

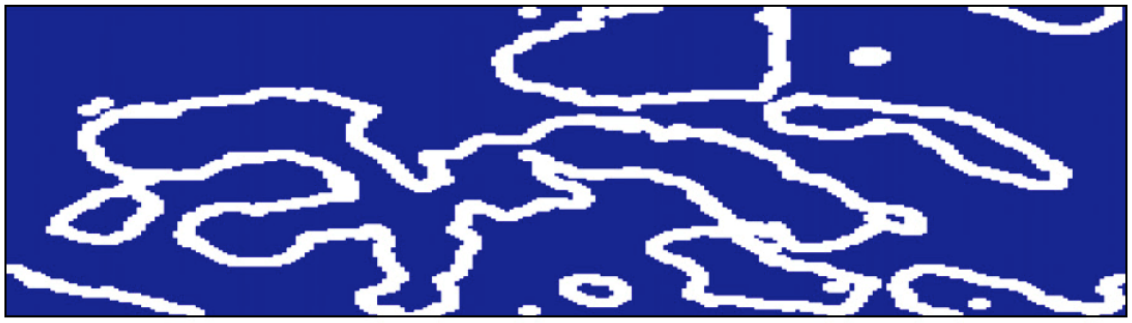

$h(x, \delta) = \text{smoothed image}$

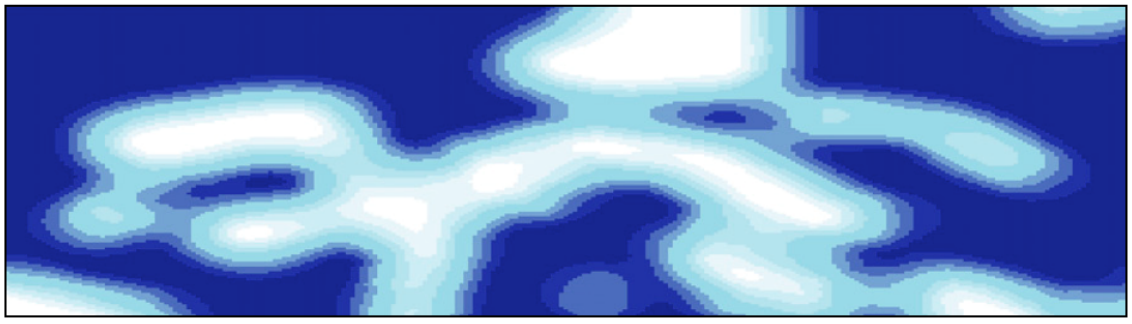

Appendix 7-2. Example chimera intestinal section (Upper) and various computed summaries used for statistical inference.

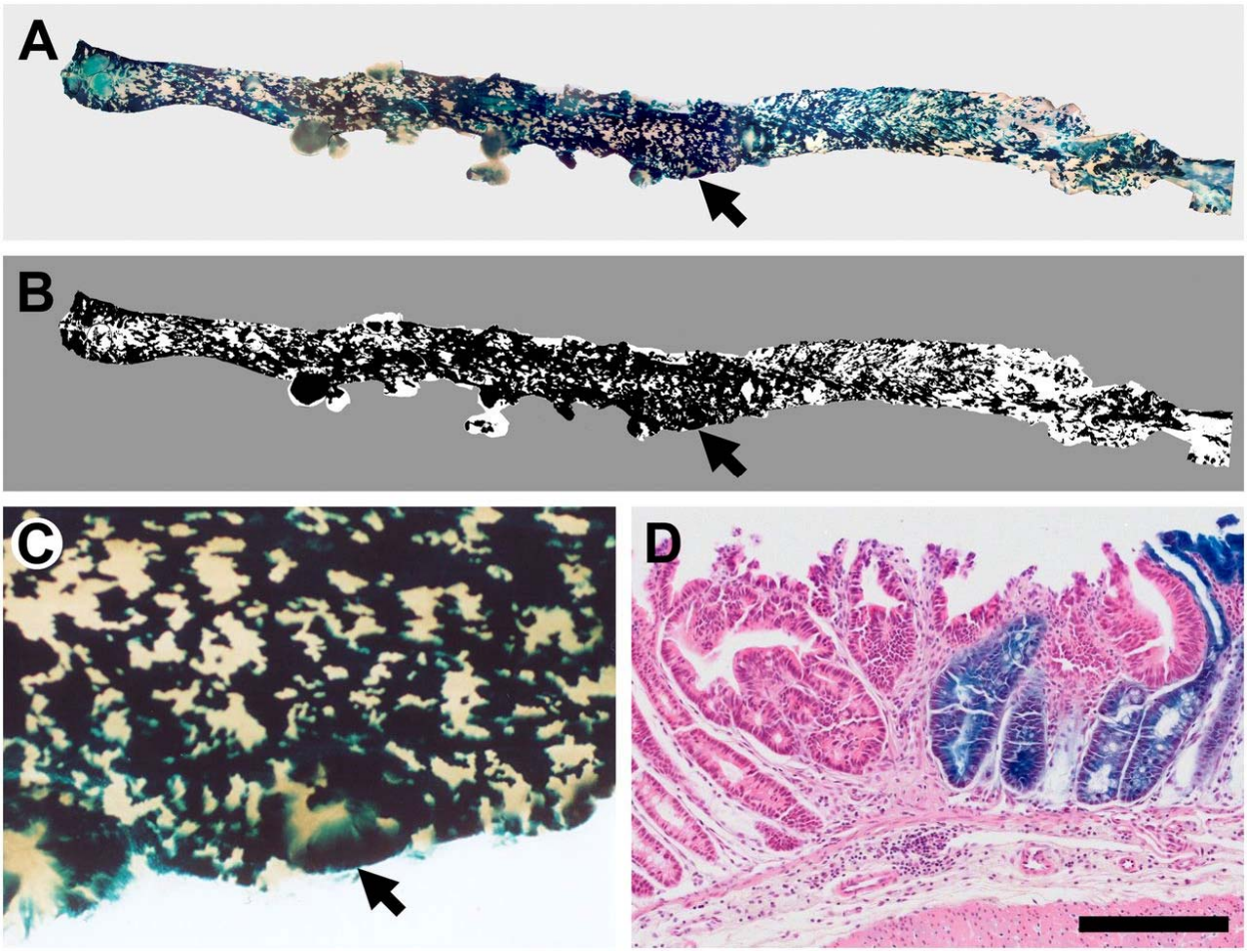
A
B
C
D

Appendix 7-3. Tumors from *Apc*$^{Min/+}$ ↔ *Apc*$^{1638N/+}$ LacZ+ aggregation chimeras can have a multi-ancestral origin. The mice were generated and killed when moribund. The intestinal tract was removed and stained with X-Gal. *Apc*$^{Min/+}$ cells are white, and *Apc*$^{1638N/+}$ cells carrying LacZ+ are blue. (A and B) The intestine was photographed (A) and digitized (B) for statistical analysis. (C) Tumors (wholemount) were then excised, embedded in paraffin, and sectioned. (D) Sections were stained with hematoxylin and eosin to determine whether a tumor was composed of white, blue, or a mixture of white and blue neoplastic cells. (Scale bar, 200 μm.)

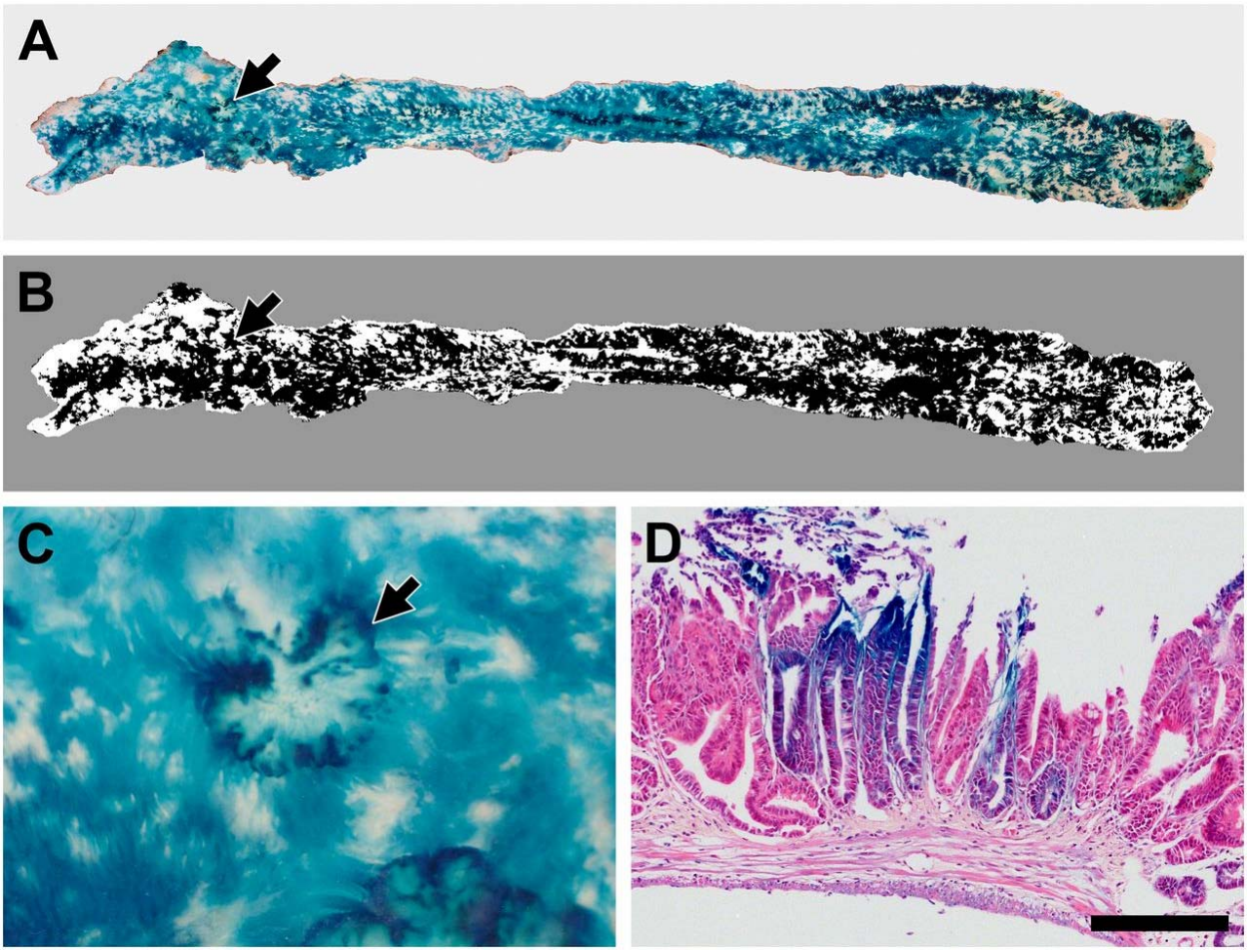
A
B
C
D

Appendix 7-4. Tumors from *Apc*$^{Min/+}$ ↔ *Apc*$^{+/+}$ LacZ+ aggregation chimeras can have a multi-ancestral origin. (A and B) The intestines from these chimeras are a patchwork of *Apc*$^{Min/+}$ cells (white) and *Apc*$^{+/+}$ LacZ+ cells (blue) as evidenced in this representative image, which was photographed (A) and digitized (B). (C and D) Several tumors were heterotypic, being composed of both cell types as indicated in the wholemount and verified by histology. (Scale bar, 200 μm.)

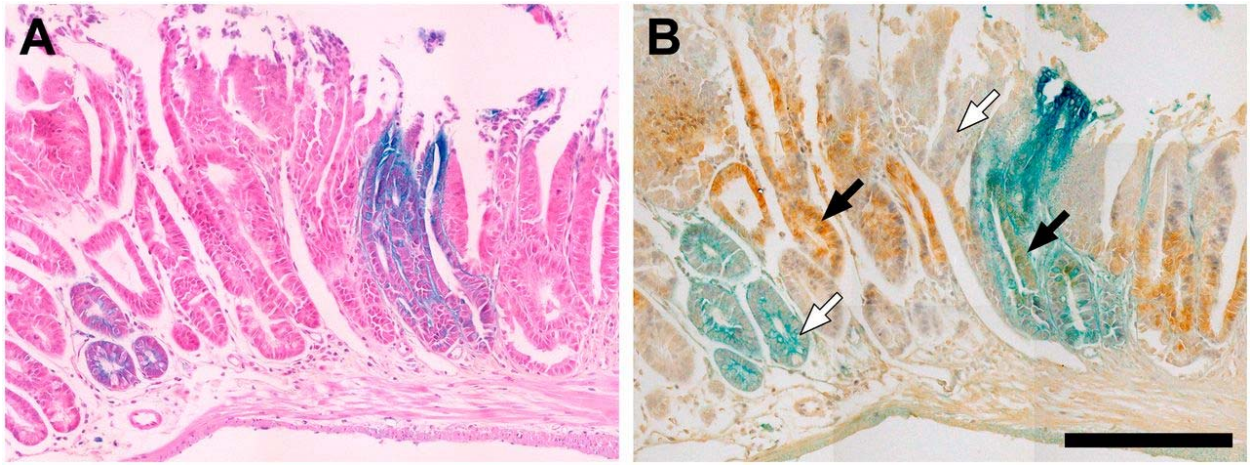
A
B

Appendix 7-5. Multi-ancestral tumors are composed of blue and white neoplastic cells. (A and B) To confirm the impression of two pathologists based on hematoxylin and eosin stained sections (A), immunohistochemistry was performed to assess the localization of β-catenin (B). Blue and white cells within the the tumor clearly have β-catenin localized to the nucleus (black arrows), which is a marker for neoplastic transformation, whereas histologically normal cells of either color do not (white arrows). (Note that A and B are composites to create the full images.)

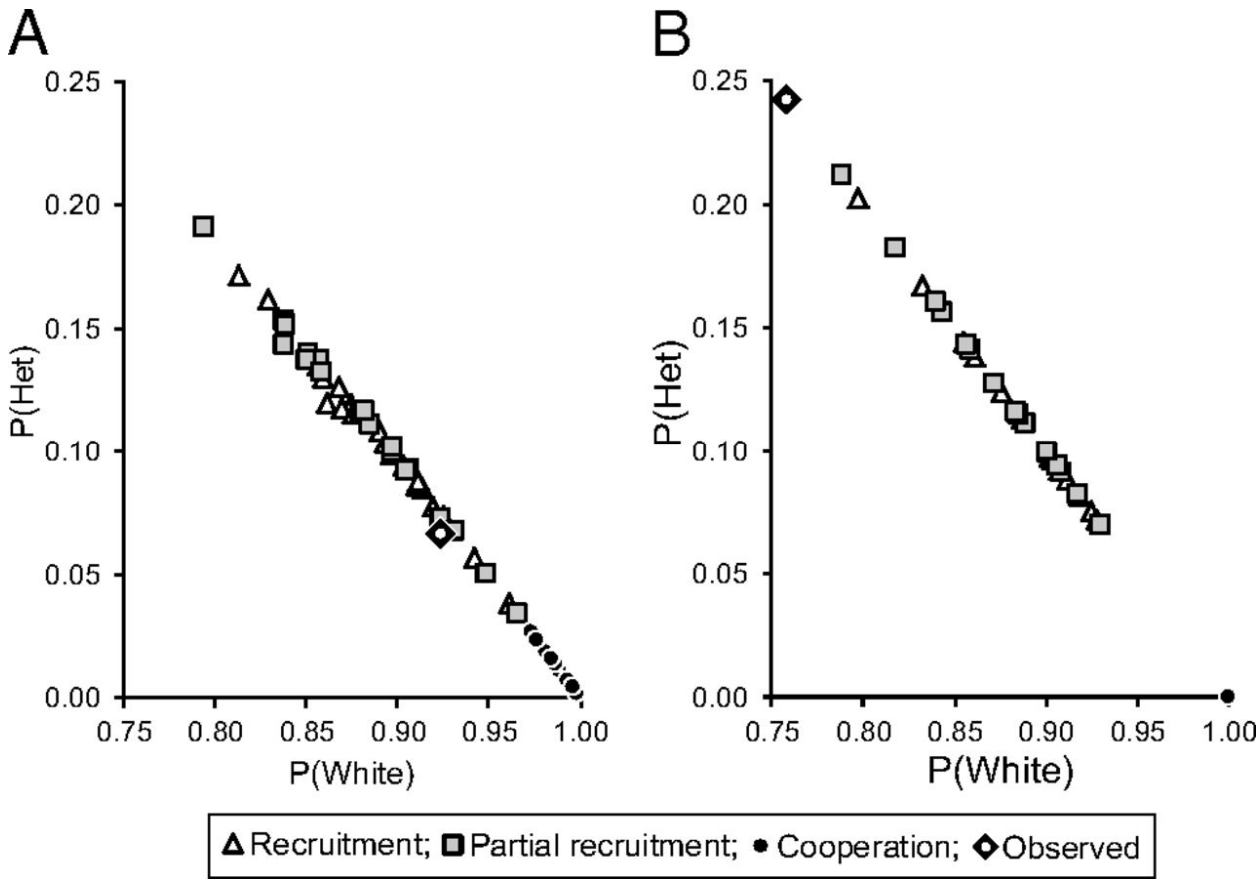
A
B
0.25
0.20
0.15
0.10
0.05
0.00
P(Het)
0.75
0.80
0.85
0.90
0.95
1.00
P(White)
Recruitment; Partial recruitment; Cooperation; Observed

Appendix 7-6. The probability that a tumor is heterotypic, homotypic blue, or homotypic white was determined using three different models. (A and B) Probabilities were calculated for each of the 20 intestinal sections from $Apc^{Min/+} \leftrightarrow Apc^{1638N/+}$ LacZ+ aggregation chimeras (A) and each of the 15 intestinal sections from $Apc^{Min/+} \leftrightarrow Apc^{+/+}$ LacZ+ aggregation chimeras (B). The values for heterotypic and homotypic white that were obtained considering recruitment in which all neighbors are transformed (white triangles), partial recruitment in which some neighbors are transformed (gray squares), and cooperation (black circles) were compared with the observed rate of heterotypic tumors (black diamonds with white centers). Some sections have a higher probability of forming heterotypic tumors (upper left quadrant) than others (lower right quadrant) because of the chimeric pattern. The probability that a tumor is homotypic blue is extremely low ($Apc^{1638N/+}$) or essentially zero ($Apc^{+/+}$) for all models, so these values are not shown.

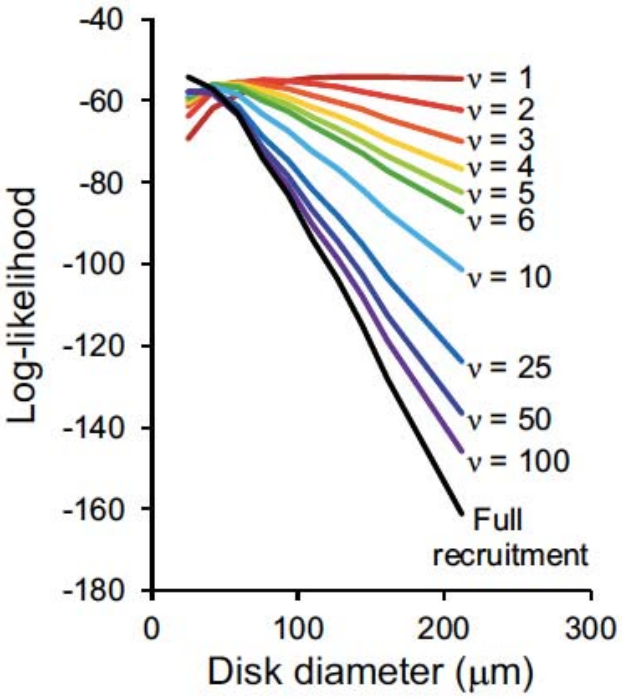
-40
-60
-80
-100
-120
-140
-160
-180
Log-likelihood
0
100
200
300
Disk diameter (μm)
ν = 1
ν = 2
ν = 3
ν = 4
ν = 5
ν = 6
ν = 10
ν = 25
ν = 50
ν = 100
Full
recruitment

Appendix 7-7. Formation of multi-ancestral tumors is best explained by the full or partial recruitment of neighboring cells over a relatively short distance. The maximum log likelihood was calculated at different interaction distances and with a different number of partners (v). Note the maximum log likelihood dropped quickly as the interaction distance increased. A simple explanation is that the calculations must account for homotypic tumors and as the interaction distance increases the affected area comes to include blue and white cells owing to the fine-grained pattern of chimerism.

Table

Appendix 7-8. Clonal structure of tumors in the aggregation chimeras.

Type	Mouse ID	Section	% Blue	Median distance to blue, μm	Median distance to white, μm	No. of tumors					
						Total	White	Blue	Heterotypic	Not scorable	Not studied
Apc$^{Min/+}$ ↔ *Apc*$^{1638N/+}$ *R26*$^{+}$	77	1	42	78	52	7	0	0	0	1	6
		2	40	68	43	14	0	0	0	2	12
		3	46	59	48	41	0	0	0	2	39
		4	36	78	42	59	0	0	1	1	57
		C	25	108	49	5	0	0	1	0	4
	124	1	50	60	54	7	1	0	1	5	0
		2	46	57	48	11	7	1	1	2	0
		3	30	59	31	31	29	0	0	2	0
		4	30	78	38	30	28	0	1	1	0
		C	51	43	57	11	11	0	0	0	0
	130	1	54	60	70	10	0	0	0	2	8
		2	57	42	51	13	2	0	0	3	8
		3	50	60	64	62	4	0	0	4	54
		4	52	54	57	27	1	0	0	1	25
		C	59	59	78	12	1	0	1	2	8
	136	1	38	88	57	7	2	0	1	1	3
		2	38	87	60	9	0	0	0	0	9
		3	28	86	42	53	8	0	0	1	44
		4	28	73	31	45	0	0	0	0	45
		C	18	167	51	20	3	0	0	0	17
Total						474	97	1	7	30	339
Apc$^{Min/+}$ ↔ *Apc*$^{+/+}$ *R26*$^{+}$	88	1	78	48	115	8	4	0	2	2	0
		2	61	54	68	16	6	0	0	10	0
		3	58	54	59	4	4	0	0	0	0
		4	54	34	42	0	0	0	0	0	0
		C	50	57	54	1	0	0	0	1	0
	111	1	48	78	66	4	1	0	1	2	0
		2	35	92	51	3	0	0	1	2	0
		3	30	97	42	7	6	0	0	1	0
		4	50	57	54	3	2	0	0	1	0
		C	42	60	42	0	0	0	0	0	0
	120	1	57	72	102	2	0	0	2	0	0
		2	42	85	68	2	0	0	1	1	0
		3	34	76	43	2	0	0	1	1	0
		4	41	66	51	2	2	0	0	0	0
		C	45	72	61	0	0	0	0	0	0
Total						54	25	0	8	21	0

References

1. Pietras, A. Cancer stem cells in tumor heterogeneity. *Adv Cancer Res* **112,** 255–281 (2011).

2. Parsons, B. L. Many different tumor types have polyclonal tumor origin: Evidence and implications. *Mutat Res Rev Mut Res* **659,** 232–247 (2008).

3. Merritt, A. J., Gould, K. A. & Dove, W. F. Polyclonal structure of intestinal adenomas in $Apc^{Min/+}$ mice with concomitant loss of Apc^{+} from all tumor lineages. *Proc Natl Acad Sci U S A* **94,** 13927 (1997).

4. Thliveris, A. T. *et al.* Clonal Structure of Carcinogen-Induced Intestinal Tumors in Mice. *Cancer Prev Res* **4,** 916–923 (2011).

5. Novelli, M. R. *et al.* Polyclonal Origin of Colonic Adenomas in an XO/XY Patient with FAP. *Science* **272,** 1187–1190 (1996).

6. Thirlwell, C. *et al.* Clonality Assessment and Clonal Ordering of Individual Neoplastic Crypts Shows Polyclonality of Colorectal Adenomas. *Gastroenterol* **138,** 1441–1454.e7 (2010).

7. Thliveris, A. T. *et al.* Polyclonality of familial murine adenomas: Analyses of mouse chimeras with low tumor multiplicity suggest short-range interactions. *Proc Natl Acad Sci U S A* **102,** 6960–6965 (2005).

8. Uronis, J. M. & Threadgill, D. W. Murine models of colorectal cancer. *Mamm Genome* **20,** 261–268 (2009).

9. Gould, K. A. & Dove, W. F. Localized gene action controlling intestinal neoplasia in mice. *Proc Natl Acad Sci U S A* **94,** 5848–5853 (1997).

10. Haigis, K. M. & Dove, W. F. A Robertsonian translocation suppresses a somatic recombination pathway to loss of heterozygosity. *Nat Genet* **33,** 33–39 (2003).

11. Kuraguchi, M. *et al.* The Distinct Spectra of Tumor-associated *Apc* Mutations in Mismatch Repair-deficient *Apc*^{1638N} Mice Define the Roles of MSH3 and MSH6 in DNA Repair and Intestinal Tumorigenesis. *Cancer Res* **61,** 7934–7942 (2001).

12. Roberts, R. B. *et al.* Importance of epidermal growth factor receptor signaling in establishment of adenomas and maintenance of carcinomas during intestinal tumorigenesis. *Proc Natl Acad Sci U S A* **99,** 1521–1526 (2002).

13. Zhang, Z. *et al.* Secreted frizzled related protein 2 protects cells from apoptosis by blocking the effect of canonical Wnt3a. *J Mol Cell Cardiol* **46,** 370–377 (2009).

14. Shimizu, H. *et al.* Transformation by Wnt family proteins correlates with regulation of beta-catenin. *Cell Growth Differ* **8,** 1349 (1997).

15. Mester, J., Wagenaar, E., Sluyser, M. & Nusse, R. Activation of int-1 and int-2 mammary oncogenes in hormone-dependent and -independent mammary tumors of GR mice. *J Viro.* **61,** 1073–1078 (1987).

16. Jue, S. F., Bradley, R. S., Rudnicki, J. A., Varmus, H. E. & Brown, A. M. The mouse Wnt-1 gene can act via a paracrine mechanism in transformation of mammary epithelial cells. *Mol Cell Biol* **12,** 321–328 (1992).

17. Vermeulen, L. *et al.* Wnt activity defines colon cancer stem cells and is regulated by the microenvironment. *Nature Cell Biol* **12,** 468–476 (2010).

18. Franco, O. E., Shaw, A. K., Strand, D. W. & Hayward, S. W. Cancer associated fibroblasts in cancer pathogenesis. *Cell Dev Biol* **21,** 33–39 (2010).

19. González-Sancho, J. M. *et al.* The Wnt antagonist DICKKOPF-1 gene is a downstream target of |[beta]|-catenin|[sol]|TCF and is downregulated in human colon cancer. *Oncogene* **24,** 1098–1103 (2005).

20. Fodde, R. *et al.* A targeted chain-termination mutation in the mouse Apc gene results in multiple intestinal tumors. *Proc Natl Acad Sci U S A* **91,** 8969–8973 (1994).

21. Skylar, O., Pau, G., M, S. & W, H. EBImage: Image processing toolbox for R. R package version 3.8.0. (2012). at <http://www.bioconductor.org/packages//2.7/bioc/html/EBImage.html>

22. Thliveris, A. T. *et al.* Transformation of epithelial cells through recruitment leads to polyclonal intestinal tumors. *Proc Natl Acad Sci U S A* **110,** 11523–11528 (2013).

Appendix 8. Colon cancer tumorigenesis initiated by the H1047R mutant PI3K.

This manuscript was included in the appendix as additional evidence that activation of PI3K is a driver of tumor initiation in the mammalian colon.

Alexander E. Yueh, Susan N. Payne, **Alyssa A. Leystra**, Dana R. Van De Hey, Tyler M. Foley, Cheri A. Pasch, Linda Clipson, Kristina A. Matkowskyj, Dustin A. Deming.

Abstract

The phosphoinositide 3-kinase (PI3K) signaling pathway is critical for multiple important cellular functions, and is one of the most commonly altered pathways in human cancers. We previously developed a mouse model in which colon cancers were initiated by a dominant active PI3K p110-p85 fusion protein. In that model, well-differentiated mucinous adenocarcinomas developed within the colon and initiated through a non-canonical mechanism that is not dependent on WNT signaling. To assess the potential relevance of PI3K mutations in human cancers, we sought to determine if one of the common mutations in the human disease could also initiate similar colon cancers. Mice were generated expressing the Pik3ca(H1047R) mutation, the analog of one of three human hotspot mutations in this gene. Mice expressing a constitutively active PI3K, as a result of this mutation, develop invasive adenocarcinomas strikingly similar to invasive adenocarcinomas found in human colon cancers. These tumors form without a polypoid intermediary and also lack nuclear CTNNB1 (β-catenin), indicating a non-canonical mechanism of tumor initiation mediated by the PI3K pathway. These cancers are sensitive to dual

PI3K/mTOR inhibition indicating dependence on the PI3K pathway. The tumor tissue remaining after treatment demonstrated reduction in cellular proliferation and inhibition of PI3K signaling.

Adapted from PLoS ONE; 11(2):e0148730. ©2016 Yueh et al.

In addition to reformatting, the following changes were made for the sake of consistency:

- Figures and references were renumbered
- "*Fc*$^{+}$" mice were renamed "Fabp1-Cre^{+}" mice
- "*Pik3ca*^{p110*}" mice were renamed "Pik3ca*$^{+}$" mice
- "*Pik3ca*^{H1047R}" mice were renamed "Pik3ca(H1047R)$^{+}$" mice

Authors' Contributions

A.E. Yueh, S.N. Payne, A.A. Leystra, and D.A. Deming designed, performed and analyzed experiments, and wrote the manuscript. D.R. Van De Hey, T.M. Foley, C.A. Pasch, and L. Clipson performed and analyzed experiments and wrote the manuscript. K.A. Matkowskyj analyzed experiments and wrote the manuscript. All authors discussed results and edited the manuscript.

Introduction

Colon cancer is a heterogeneous disease with multiple subtypes distinguished by their mutation profiles. Tumorigenesis is commonly thought to arise in the colon secondary to the sequential acquisition of mutations within the epithelial cells lining the base of the crypt.

Alterations in the *Adenomatous Polyposis Coli* (*APC*) tumor suppressor gene are thought to be the initiating event in the majority of sporadic human colorectal cancers with approximately 80–90% of human colon cancers harboring somatic mutations in *APC* [1-3]. Following loss of APC, tumors develop within the colon largely through the canonical adenoma-to-carcinoma sequence[4]. During this process the premalignant adenoma acquires mutations in other genes including *KRAS*, *TP53*, *PIK3CA*, and *BRAF* resulting in the eventual formation of an invasive adenocarcinoma and diversity in the molecular profile[5]. Non-canonical mechanisms of colon cancer initiation have also been described including the serrated polyp-carcinoma pathway[6].

The PIK3CA gene encodes for the p110 alpha catalytic subunit of PI3K and mutations occur in 20–30% of human colorectal cancers[7,8]. There are three hotspot mutations that occur inPIK3CA: E542K, E545K, and H1047R, all resulting in a constitutively active PI3K[9]. We previously developed a transgenic mouse model expressing a constitutively active PI3K throughout the distal small intestine and colon (Fabp1-Cre+ Pik3ca*$^{+}$)[10]. These mice developed invasive mucinous adenocarcinomas in the proximal colon. These cancers frequently invaded through the muscularis propria to the serosal surface. Cancer was also detected in regional lymph nodes and as satellite tumor deposits in the adjacent adipose tissue. Nuclear localization of CTNNBI (β-catenin) was not identified within these tumors, indicating that the WNT signaling cascade is not aberrant as would be expected if these cancers developed through the canonical adenoma-to-carcinoma pathway. These tumors also developed without an identifiable polypoid precursor lesion. While the Fabp1-Cre^{+} Pik3ca*$^{+}$ model results in a constitutively active PI3K, it uses a p85-p110 fusion protein not found in human cancers. Here we investigate whether tumorigenesis in the colon can be initiated secondary to the H1047R hotspot mutation in Pik3ca.

Results

Fabp1-Cre^{+} Pik3ca(H1047R)$^{+}$ mice develop invasive cancers in the colon:

To determine if the Pik3ca(H1047R) hotspot mutation could initiate colon tumorigenesis within the colon, a set of 33 (16 male and 17 female) Fabp1-Cre^{+} Pik3ca(H1047R)$^{+}$ mice was generated. These mice express the mutant PI3K in the distal small intestine and colon secondary to the FABP1-Cre. At necropsy, the mice had a median age of 165 days, ranging from 97 to 310 days. Six mice were moribund at a median age of 193 days (range 97–310). All Fabp1-Cre^{+} Pik3ca(H1047R)$^{+}$ mice demonstrated hyperplasia of the colon and small intestine. Tumors within the colon were identified in 20 of the 33 mice (61%). Of the mice with tumors, the median number of tumors was 2 (range 1–6). Multiple mice developed tumors over 1 cm in size (Appendix 8-1A and 1B). No metastatic disease or small intestinal cancers were identified in these mice. Appendix 8-8 compares the characteristics of the Fabp1-Cre^{+} Pik3ca(H1047R)$^{+}$ mice with those of the Fabp1-Cre^{+} Pik3ca*$^{+}$ and the *Apc$^{Min/+}$* mice. Following histological sectioning, these tumors were found to be invasive mucinous adenocarcinomas (Appendix 8-1C and 1D). They often penetrated through the muscularis propria and extended to the serosa. On histological examination the tumors were flat rather than polypoid in morphology.

The Fabp1-Cre^{+} Pik3ca(H1047R)$^{+}$ cancers are histologically similar to those in Fabp1-Cre^{+} Pik3ca*$^{+}$ mice (Appendix 8-2). The tumors from the Fabp1-Cre^{+} Pik3ca(H1047R)$^{+}$ and Fabp1-Cre^{+} Pik3ca*$^{+}$ animals exhibited deeply invasive mucinous adenocarcinomas without evidence of a precursor lesion. The tumors were not associated with epithelial surface dysplasia. In contrast, *Apc$^{Min/+}$* tumors developed from a dysplastic, polypoid precursor (tubular adenoma) and progressed to advanced adenomas (tubular adenoma with high-grade dysplasia) with rare progression to superficially invasive, well-differentiated adenocarcinomas.

Fabp1-Cre^{+} Pik3ca(H1047R)$^{+}$ cancers have increased cellular proliferation (Appendix 8-2). Immunohistochemistry showed an increased Ki67 proliferative index in Fabp1-Cre^{+} Pik3ca(H1047R)$^{+}$ compared to *Apc*$^{Min/+}$ tumors. Fabp1-Cre^{+} Pik3ca(H1047R)$^{+}$ tumors exhibited a proliferative index of >70% with most neoplastic nuclei exhibiting Ki67 nuclear expression. In contrast, *Apc*$^{Min/+}$ tumors had a low proliferative index as demonstrated by less than 25% nuclear expression of nuclear Ki67.

Pik3ca(H1047R)$^{+}$ results in activation of the PI3K/AKT/mTOR pathway and ERK 1/2 signaling

The epithelial cells in Fabp1-Cre^{+} Pik3ca(H1047R)$^{+}$ and Fabp1-Cre^{+} Pik3ca*$^{+}$ colon cancers demonstrate increased staining for phosphorylation of RPS6 compared to those in *Apc*$^{Min/+}$ colon tumors (Appendix 8-2). In addition, an increase in phosphorylated ERK1/2 was observed in thePik3ca mutant cancers (Appendix 8-2).

Immunoblotting demonstrated activation of the PI3K signaling cascade across tumor types (Appendix 8-3A). A trend towards an increase in phosphorylation of AKT, RPS6, and 4EBP1 was seen in the Fabp1-Cre^{+} Pik3ca(H1047R)$^{+}$ and Fabp1-Cre^{+} Pik3ca*$^{+}$ cancers (Appendix 8-3B). In comparison to Fabp1-Cre^{+} Pik3ca*$^{+}$ colon tumors, Fabp1-Cre^{+} Pik3ca(H1047R)$^{+}$ demonstrated a trend towards less phosphorylation of 4EBP1 (Appendix 8-3B).

Pik3ca(H1047R)$^{+}$ mutations initiate cancers through a non-canonical mechanism

The most common mutation in human colorectal adenocarcinomas results in a truncated APC protein. Truncation of the APC protein results in the loss of tumor suppression. A

commonly used marker for APC function is ß-catenin translocation to the nucleus of the colonic epithelial cells. Immunohistochemistry of the tumor cells showed that nuclear localization of ß-catenin was absent in both the Pik3ca(H1047R)$^{+}$ and Pik3ca*$^{+}$ cancers, but was abundantly present in the *Apc$^{Min/+}$* colon tumors (Appendix 8-4). The lack of nuclear ß-catenin indicates that APC loss has not occurred. If these cancers were arising though the canonical mechanism of tumorigenesis, loss of APC would be expected, thus these tumors are developing through a non-canonical mechanism.

Fabp1-Cre^{+} Pik3ca(H1047R)$^{+}$ cancers are sensitive to dual PI3K/mTOR inhibition

A second set of Fabp1-Cre^{+} Pik3ca(H1047R)$^{+}$ mice at 150 days of age was imaged with dual hybrid ^{18}F-FDG microPET/CT. After 24 hours, 11 mice (4 male and 7 female) were initiated on NVP-BEZ235 at 35mg/kg/day in 1% hydroxycellulose by oral gavage daily and 8 mice (4 male and 4 female) were administered vehicle-only control. After 14 days of treatment, the mice were imaged again with PET/CT 24 hours after the last dose of NVP-BEZ235 or control. Images were normalized to injected dose of ^{18}F-FDG, dose decay, activity, and mouse weight. Tumor volume was measured using the CT images acquired. The initial tumor volumes of treated and control mice were comparable (Appendix 8-9). The percent change in tumor volume was calculated for each tumor identified on baseline imaging (Appendix 8-5A and Appendix 8-6). A median increase in tumor volume of 11% was seen in the controls and a median reduction in tumor volume of 41% was observed in the cancers treated with NVP-BEZ235 ($p = 0.01$, two-sided Wilcoxon rank sum; Appendix 8-5B). In one control mouse two tumors were able to be identified on baseline imaging, but not detected on the second scan (Appendix 8-5B). The change in metabolic activity of each tumor was also assessed with ^{18}F-

FDG PET imaging. The median relative tumor avidity (avidity at day 15 divided by avidity at day 0) was 77% for cancers treated with NVP-BEZ235 compared to controls ($p = 0.13$, two-sided Wilcoxon rank sum test). The delay of 24 hours between NVP-BEZ235 dosing and PET scanning allows for the direct metabolic inhibition secondary to this agent to resolve. The changes in avidity are thus related to changes in tumor size and activity. These changes in avidity are also likely an underestimate of the change secondary to this treatment, as a tumor flare has been described following the withdrawal of mTOR inhibitors[11].

Following imaging, the mice were treated again with NVP-BEZ235 or control and necropsy performed 1 hour later. At necropsy, 18 tumors were identified in control mice compared to 12 in Fabp1-Cre^{+} Pik3ca$(H1047R)^{+}$ mice treated with NVP-BEZ235. No significant difference in median cancer size was observed (3.6 vs 3.2 mm, $p = 0.59$). Tumors were fixed in formalin and embedded in paraffin. H&E staining demonstrated a significant treatment response in those tumors treated with NVP-BEZ235, including a loss of epithelial cells surrounding the mucin lakes areas of cystic change/degeneration and areas of increased fibrosis, consistent with treatment effect (Appendix 8-7). Dual PI3K/mTOR inhibition resulted in decreased phosphorylation of AKT and RPS6 (Appendix 8-7). Decreased proliferation as measured by Ki67 staining was observed (Appendix 8-7). Additionally, the phosphorylated ERK1/2 is also diminished with NVP-BEZ235 treatment (Appendix 8-7).

Discussion

The PI3K pathway remains a target of interest for the development of novel therapeutic strategies for many cancers given the importance of this pathway for multiple vital cellular functions[12]. It is one of the most commonly aberrant pathways in cancer[7]. PI3K delta inhibitors, such as idelalisib, have been successfully applied to the treatment of hematologic malignancies[13]. In solid tumors, the alpha and beta isoforms are the predominant mediators of PI3K signaling, with minimal contributions from the gamma or delta isoforms. Response to PI3K alpha selective and pan inhibitors has been observed in certain settings[14]. Multiple early phase clinical studies are investigating the use of these agents in the setting of PIK3CA mutations[15-17]. Recently, in a phase I clinical trial a partial response was seen in a colorectal cancer patient treated with LY3023414, a dual PI3K/mTOR inhibitor[18]. However, the contribution of the PIK3CA mutation to the biology of these cancers has been under-investigated and the population of patients most likely to benefit from these agents has yet to be determined. This is especially true for colorectal cancer where PIK3CA mutations are most commonly thought to be a late event in tumorigenesis and the potential benefit from PI3K pathway inhibition is uncertain.

Only recently have the effects of a dominant active PI3K pathway been explored in the mammalian intestine. Our group was the first to describe the development of hyperplasia and invasive mucinous adenocarcinomas developing in the proximal colon as a result of expression of a dominant active PI3K (Pik3ca*$^{+}$)[10]. The cancers in this model developed through a non-canonical pathway without the identification of a polypoid intermediary and without activation of WNT signaling. To determine if similar tumors could be initiated in the setting of a hotspot mutation in PIK3CA commonly encountered in human cancers, we developed the Fabp1-Cre^{+} Pik3ca(H1047R)$^{+}$ murine model. Here we demonstrate that the Pik3ca(H1047R)$^{+}$ mutation

results in hyperplasia and the development of mucinous adenocarcinomas within the colon indistinguishable from the Fabp1-Cre^{+} Pik3ca*$^{+}$ mice. The predominant difference between these two models is the latency in which these tumors develop. In the Fabp1-Cre^{+} Pik3ca*$^{+}$ model, ~75% of mice had invasive cancers by 40 days of age[10], while in the Fabp1-Cre^{+} Pik3ca(H1047R)$^{+}$ mice no tumors were identified at 50 days of age and only 65% of mice had tumors at necropsy (age 97–310 days). These cancers appear to be developing through a similar mechanism with activation of the PI3K pathway and without activation of WNT signaling. The increased latency in cancer development in the Fabp1-Cre^{+} Pik3ca(H1047R)$^{+}$ mice appears related to a decreased level of activation of the PI3K pathway compared to the Fabp1-Cre^{+} Pik3ca*$^{+}$ mice.

Interestingly, increased ERK1/2 phosphorylation was observed in both the Fabp1-Cre^{+} Pik3ca*$^{+}$ and Fabp1-Cre^{+} Pik3ca(H1047R)$^{+}$ tumors compared to the *Apc$^{Min/+}$* colon tumors. In these cancers it does not appear to be a mechanism of resistance to PI3K pathway inhibition, though this has been demonstrated in some settings[19,20]. Activation of ERK1/2 signaling has been observed in other models with PIK3CA mutations including PIK3CA mutant breast and pancreatic cancers[21,22]. Activation of ERK1/2 seems to be largely independent of RAS in these Pik3ca mutant tumors[21]. It is instead potentially mediated by the RAC1/CRAF/MEK/ERK pathway. The phosphorylation of ERK1/2, in the models presented here, is likely downstream of PI3K signaling, as it is diminished with PI3K/mTOR inhibition.

We hypothesize that there is a subpopulation of patients that have cancers initiated by or dependent upon the PI3K signaling cascade. The cancers in this subpopulation may be extremely susceptible to many of the novel PI3K inhibitors similar to NVP-BEZ235. In a recent pathological series, activating mutations in PIK3CA were observed more commonly in mucinous

colon cancers in humans, similar to our model, and were associated with worsened prognosis[23]. Interestingly, in this same investigation, activating mutations in PIK3CA were inversely associated with the nuclear translocation of β-catenin[23]. Translocation of β-catenin would be expected if these tumors were initiated by aberrant WNT signaling as part of the previously described canonical mechanisms of tumorigenesis in colon cancers[24]. Together, these observations indicate that a subgroup of human colon cancers might arise in the setting of activated PI3K, as seen in our model.

Methods

Mouse Husbandry

All animal studies were conducted under protocols approved by the Institutional Animal Care and Use Committee at the University of Wisconsin–Madison, following the guidelines of the American Association for the Assessment and Accreditation of Laboratory Animal Care. Homozygous FVB.Fabp1-Cre^{+} female mice (NCI Mouse Repository; Strain Number 01XD8) were crossed to homozygous Pik3ca H1047R male mice (The Jackson Laboratory; Stock Number 016977) to generate Fabp1-Cre^{+} Pik3ca(H1047R)$^{+}$ mice used in this study. Mice were genotyped for Fabp1-Cre and Pik3ca(H1047R)$^{+}$ as described previously[25,26]. *Apc*$^{Min/+}$ mice (C57BL/6J *Apc*$^{Min/+}$/J; The Jackson Laboratory; Stock Number 002020) were maintained as previously described[27].

Histology and Immunohistochemistry

At necropsy, the colon was removed, flushed with PBS, opened lengthwise and fixed in 10% buffered formalin for 24 hours. Tissues were then stored in 70% ethanol, processed, embedded in paraffin, and cut into 5 μm sections. Every tenth section was stained with hematoxylin and eosin (H&E) for histological review. Immunohistochemistry was performed by dewaxing and rehydrating paraffin-embedded tissues before antigen unmasking was carried out by boiling the samples for 35 minutes in citrate buffer (pH 6.0). Next a peroxidase quench (Peroxidazed 1, PX9684, BioCare Medical, Concord, CA) and background block (Background Sniper, BS966H, BioCare Medical) were applied before the primary antibody was left on overnight. The secondary antibody (Mach 2 Rabbit HRP-Polymer, RHRP520H, BioCare Medical) was applied for 30 minutes followed by chromogen staining (Betazoid DAB Chromogen Kit, BDB2004H, BioCare Medical). Slides were counterstained with hematoxylin (CAT Hematoxylin, CATHE-H, BioCare Medical) and dehydrated for mounting. The primary antibodies included: anti-pAKT (Ser473) (D9E) (#4060, 1:100, Cell Signaling Technology, Beverly, MA), anti-pRPS6 (Ser 235/236) (#4858, 1:50, Cell Signaling Technology), anti-Ki67 (D3B5) (#12202, 1:400, Cell Signaling Technology) and mouse anti-β-catenin (D10A8) (#8480, 1:200, Cell Signaling Technology). The Ki67 proliferation index was measured as the percent of nuclei staining positive for Ki67 per tumor using ImmunoRatio, an ImageJ plugin (http://jvsmicroscope.uta.fi/sites/default/files/software/immunoratio-plugin/index.html).

Immunoblotting

Tissue samples were excised and flash frozen. After 24 hours, the samples were sonicated in T-PER tissue protein extraction reagent (Thermo Scientific, Pittsburg, PA), protease inhibitor

cocktail (Sigma-Aldrich, St. Louis, MO), and phenylmethylsulfonyl fluoride (PMSF, Sigma-Aldrich). Extracted protein was then run as previously described[28]. Primary antibodies against pAKT (Ser473) (D9E) (#4060, Cell Signaling Technology), AKT (#4691, Cell Signaling Technology), pRPS6 (Ser235/236) (#4858, Cell Signaling Technology), total RPS6 (5G10) (#2217, Cell Signaling Technology), p4EBP1 (Thr37/46) (236B4) (#2855, Cell Signaling Technology), 4EBP1 (53H11) (#9644 Cell Signaling Technology) were incubated in 5% bovine serum albumin (Sigma-Aldrich) at a 1:1000 ratio for 16 hours. Anti-β-actin (#5125, Cell Signaling Technology) was utilized as a loading control at a ratio of 1:1000.

Animal Treatment

Fabp1-Cre^{+} Pik3ca(H1047R)$^{+}$ mice over 150 days of age were selected and randomly assigned to the treatment and control groups. Baseline dual hybrid ^{18}F-FDG PET/CT scans were performed prior to and 15 days following treatment initiation. Animals in the control arm received hydroxyethyl cellulose dissolved in water to a 1% final concentration by oral gavage daily for 14 days. Animals randomized to the NVP-BEZ235 arm received 35 mg/kg of NVP-BEZ235 dissolved in 1% hydroxyethyl cellulose[29]. For therapeutic investigations, necropsy was performed following 14 days of treatment.

Dual hybrid ^{18}F-Fluorodeoxyglucose (FDG) Positron Emission Tomography (PET)/Computed Tomography (CT) Imaging

Animals were fasted for at least 6 hours prior to injection of ^{18}F-FDG (100 μCi; IBA Molecular, Romeoville, IL). After injection, the animals were kept under anesthesia for 60 minutes and then prepared for virtual colonography as described previously[30]. A PET acquisition

was performed, followed immediately by CT scanning. Maximum intensity projections were created in Siemens Inveon Research Workplace (Knoxville, TN). The PET images were reconstructed using OSEM3D/MAP (OSEM3D, 2 iterations; MAP 18, iterations 16 subsets). Attenuation correction was performed using the CT data. The CT images were reconstructed using standard conebeam reconstruction. Baseline and post-treatment PET scans were normalized to injected dose, dose decay, activity, and weight. Tumor volumes were estimated from measurements on the PET/CT scans. PET imaging was utilized to locate tumors prior to volume estimation. Tumor volumes can only be estimated, as delineating the exact tumor boundaries is difficult. This is because many of these cancers are not luminal and subtle FDG signal changes related to the hyperplastic normal epithelium surrounding the tumors exist. Tumor volumes in each cohort were compared using a two-sided Wilcoxon rank sum test. A p-value of less than 0.05 was considered statistically significant.

Disclosure of Potential Conflicts of Interest

No potential conflicts of interest were disclosed.

Aknowledgements

This project was supported by the National Institutes of Health (http://www.nih.gov/) P30 CA014520 (Core Grant, University of Wisconsin Carbone Cancer Center); start-up funds (D.A.D) from the UW Carbone Cancer Center, UW Department of Medicine, UW School of Medicine and Public Health, and the UW Graduate School through the Wisconsin Alumni Research Foundation; Funk Out Cancer (http://www.funkoutcancer.com/) and UW Carbone

Cancer Center Gastrointestinal Disease Oriented Working Group. The funders had no role in study design, data collection and analysis, decision to publish, or preparation of the manuscript.

Figures

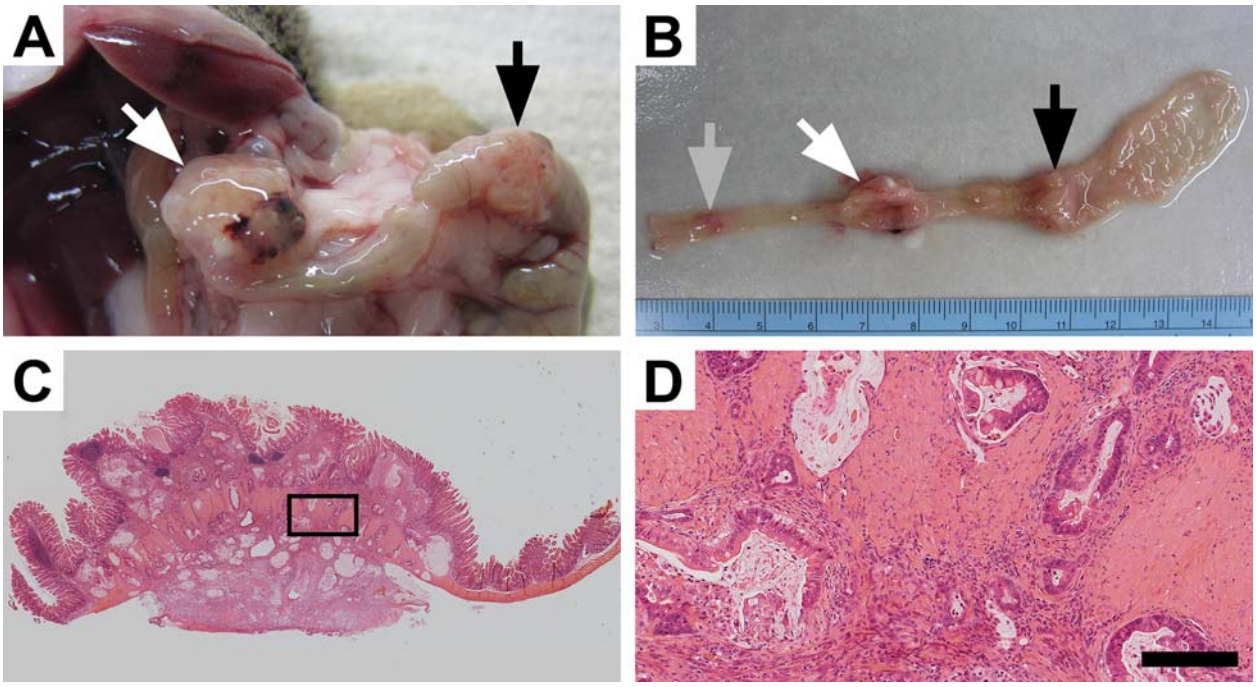

Appendix 8-1. Mutant PI3K can lead to colon cancer development. Approximately 60% of Fabp1-Cre^{+} Pik3ca(H1047R)$^{+}$ mice develop tumors within the colon which can result in these mice becoming moribund. At necropsy large colon tumors are found extending through the colonic wall (A). Upon resection, multiple lesions can be identified within the colon and can be over 1 cm in size (A and B). Following histological sectioning, H&E staining demonstrates that these lesions are invasive mucinous adenocarcinomas of the colon without a predominant intra-luminal component (C). Higher magnification demonstrates an abundant desmoplastic reaction with surrounding mucin lakes lined with epithelial cancer cells (D). D size bar = 200 μm.

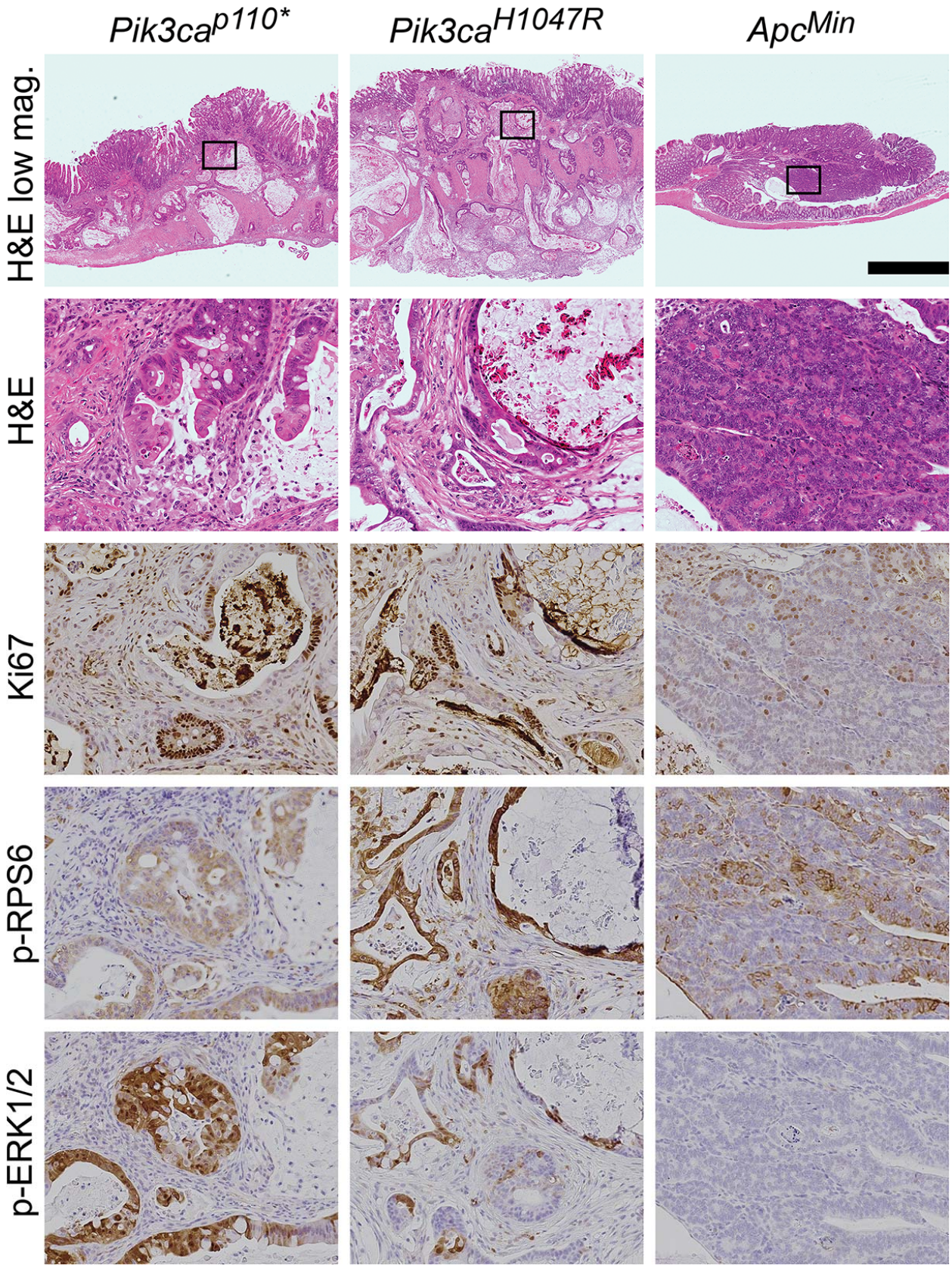
Pik3ca^p110*
Pik3ca^H1047R
Apc^Min
H&E low mag.
H&E
Ki67
p-RPS6
p-ERK1/2

Appendix 8-2. Fabp1-Cre^{+} Pik3ca(H1047R)$^{+}$ colon cancers are similar to those in Fabp1-Cre^{+} Pik3ca*$^{+}$ mice. In both of these Pik3ca mutant models, deeply invasive cancers are seen with the vast majority of the tumors having penetrated below the muscularis mucosa. This is in contrast to *Apc*$^{Min/+}$ colon tumors, which typically are adenomatous tumors with no or just superficial invasion. Abundant mucin is present within both the Fabp1-Cre^{+} Pik3ca(H1047R)$^{+}$ and Fabp1-Cre^{+} Pik3ca*$^{+}$ colon cancers. These Pik3ca mutant cancers also demonstrate increased proliferation, as measured by nuclear Ki67, in comparison to *Apc*$^{Min/+}$ tumors. In addition, phosphorylated RPS6 and ERK1/2 are increased above that seen in the *Apc*$^{Min/+}$ colon lesions. Scale bar for low magnification images = 1mm. Enlargements are 10x magnifications of the areas outlined in the low magnification images. Min, *Apc*$^{Min/+}$.

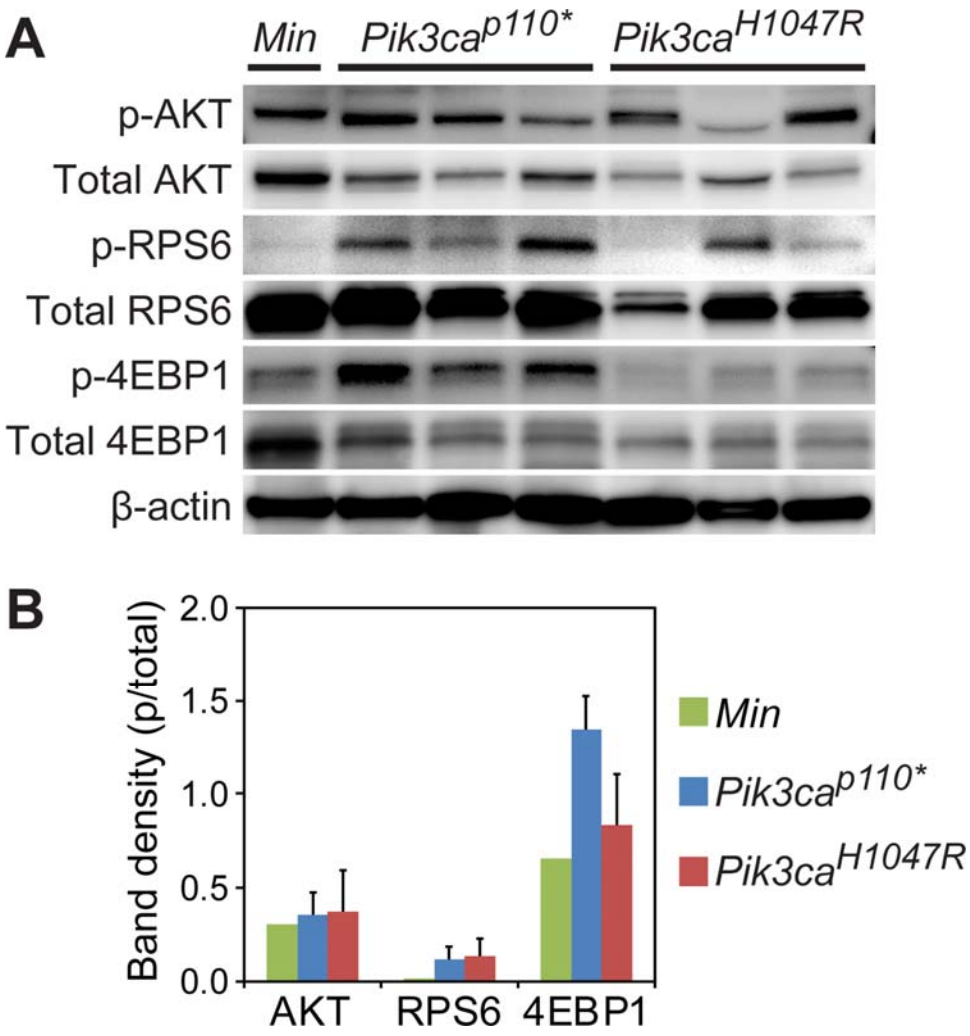
A
Min
Pik3ca^p110*
Pik3ca^H1047R
p-AKT
Total AKT
p-RPS6
Total RPS6
p-4EBP1
Total 4EBP1
β-actin
B
Band density (p/total)
2.0
1.5
1.0
0.5
0.0
AKT
RPS6
4EBP1
Min
Pik3ca^p110*
Pik3ca^H1047R

Appendix 8-3. The PI3K pathway is activated in *Apc*$^{Min/+}$, Fabp1-Cre^{+} Pik3ca*$^{+}$, and Fabp1-Cre^{+} Pik3ca(H1047R)$^{+}$ mice. Immunoblotting demonstrates robust phosphorylation of AKT in *Apc*$^{Min/+}$, Fabp1-Cre^{+} Pik3ca*$^{+}$ and Fabp1-Cre^{+} Pik3ca(H1047R)$^{+}$ colon tumors (A). Increased phosphorylation of RPS6 and 4EBP1 beyond that seen in the *Apc*$^{Min/+}$ lesions is observed in the Fabp1-Cre^{+} Pik3ca(H1047R)$^{+}$ and Fabp1-Cre^{+} Pik3ca*$^{+}$ colon tumors. The more aggressive phenotype seen in the Fabp1-Cre^{+} Pik3ca*$^{+}$ mice, with a greater number and decreased latency, is associated with an increased phosphorylation of 4EBP1 compared to Fabp1-Cre^{+} Pik3ca(H1047R)$^{+}$ tumors (B).

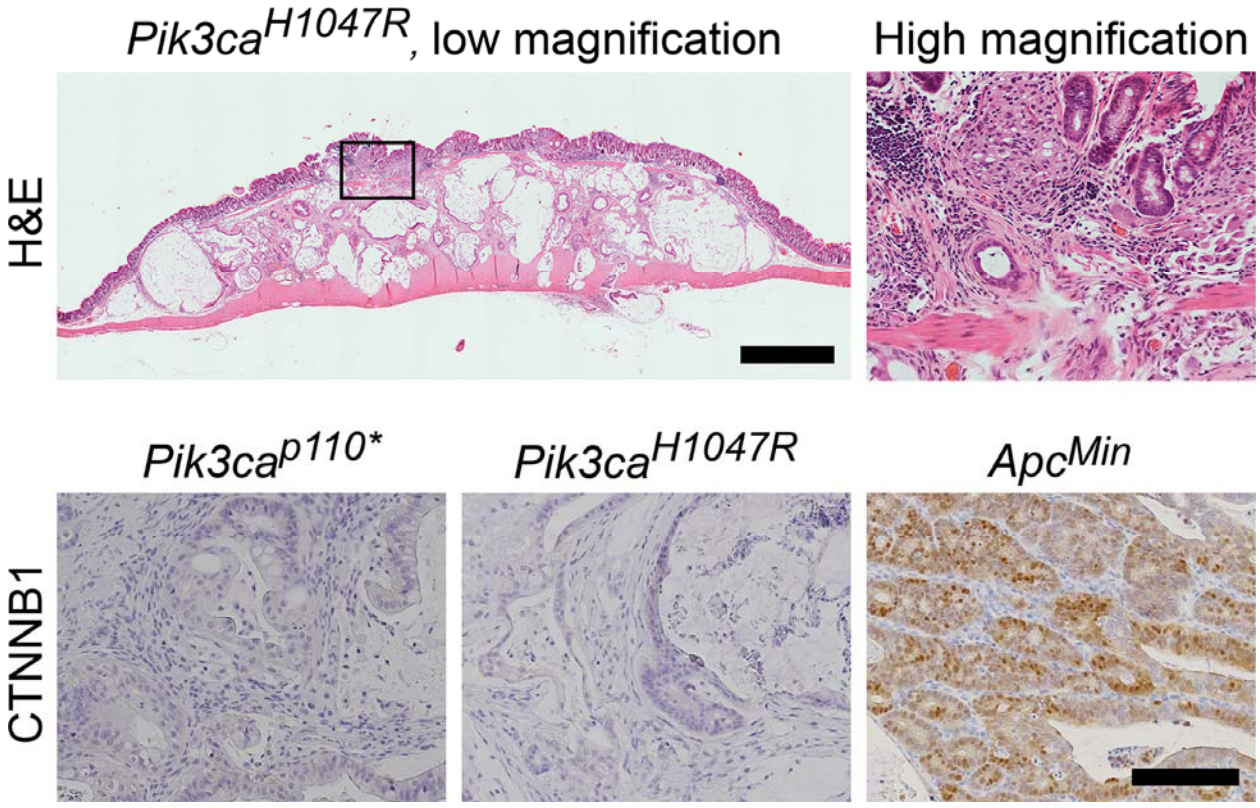
Pik3ca^H1047R, low magnification
High magnification
H&E
Pik3ca^p110*
Pik3ca^H1047R
Apc^Min
CTNNB1

Appendix 8-4. Fabp1-Cre^{+} Pik3ca(H1047R)$^{+}$ colon cancers develop through a non-canonical pathway. Histological examination demonstrates that these cancers are flat without a polypoid component. Low grade dysplasia (tubular adenoma) has not been identified in these or the Fabp1-Cre^{+} Pik3ca*$^{+}$ mice. At higher magnification, malignant glands above the muscularis mucosa can be identified which appear to be originating from the crypt bases without identification of surface low grade dysplasia. CTNNB1 staining demonstrates that nuclear CTNNB1 is absent in both of the Pik3ca mutant models, but is present in the *Apc*$^{Min/+}$ controls. Scale bar for low magnification image = 1mm. High magnification H&E image is a 6x magnification of the area indicated in the image to the left. Scale bar for CTNNB1 images = 100μm.

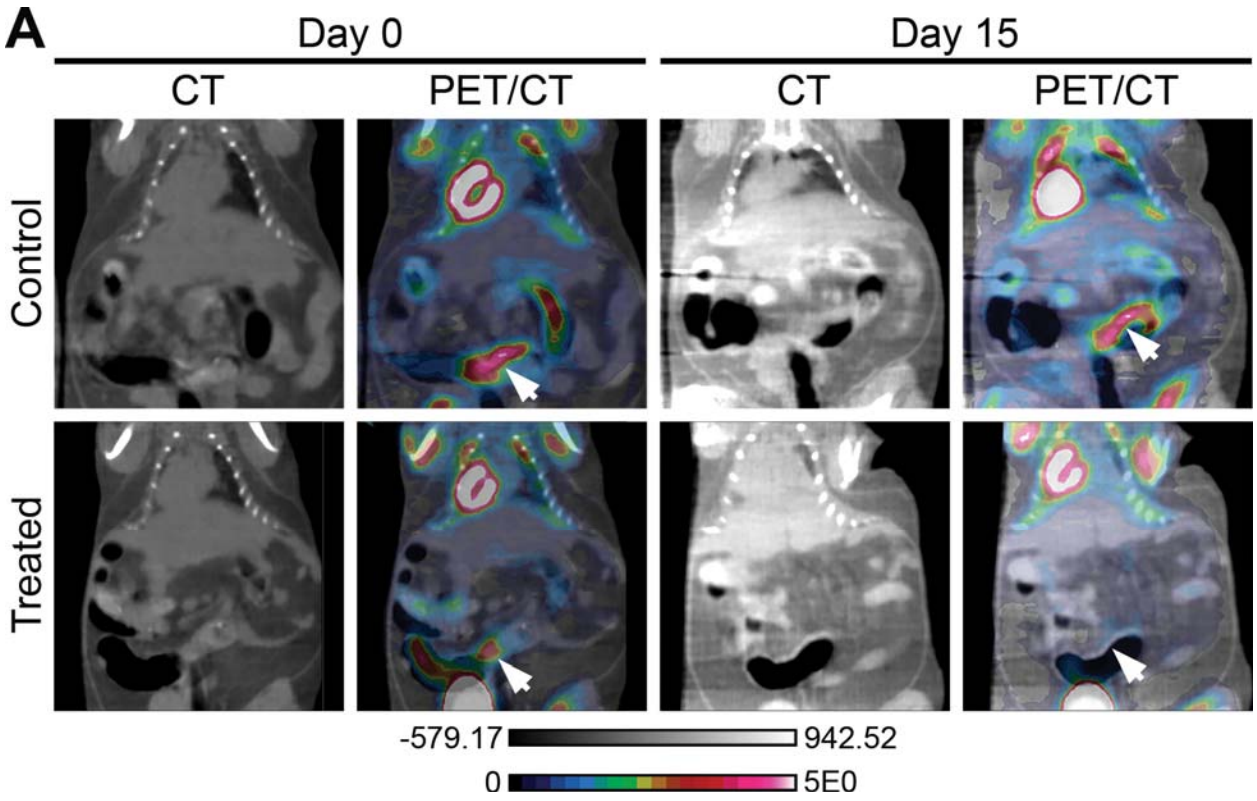
A
Day 0
Day 15
CT
PET/CT
CT
PET/CT
Control
Treated
-579.17
942.52
0
5E0

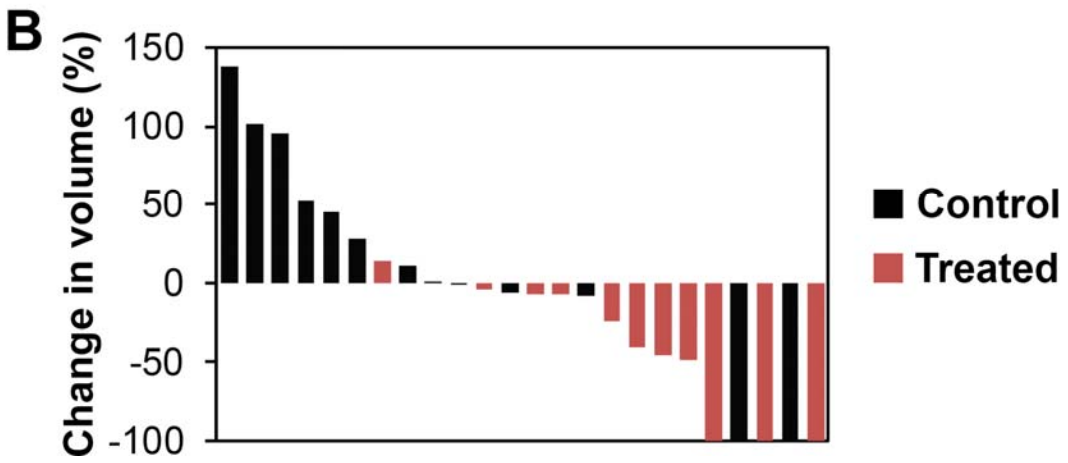
B
Change in volume (%)
150
100
50
0
-50
-100
Control
Treated

Appendix 8-5. Dual PI3K/mTOR inhibition induces treatment responses in Fabp1-Cre$^+$ Pik3ca(H1047R)$^+$ colon cancers. Fabp1-Cre$^+$ Pik3ca(H1047R)$^+$ mice were treated with NVP-BEZ235 (35mg/kg/day) or control once daily by oral gavage for 14 days. These mice underwent dual hybrid ^{18}F-FDG PET/CT imaging at baseline and then 24 hours following the last dose of study drug (A, arrows denote tumors pre- and post-treatment). A significant reduction in tumor volume, as measured on the CT images, was detected in the NVP-BEZ235 group ($p = 0.008$; B). In addition, there was a trend for a slight decrease in the median SUV for those cancers treated with the PI3K/mTOR inhibitor. In one control mouse, two tumors were observed on baseline imaging, but not detected on follow-up PET/CT imaging.

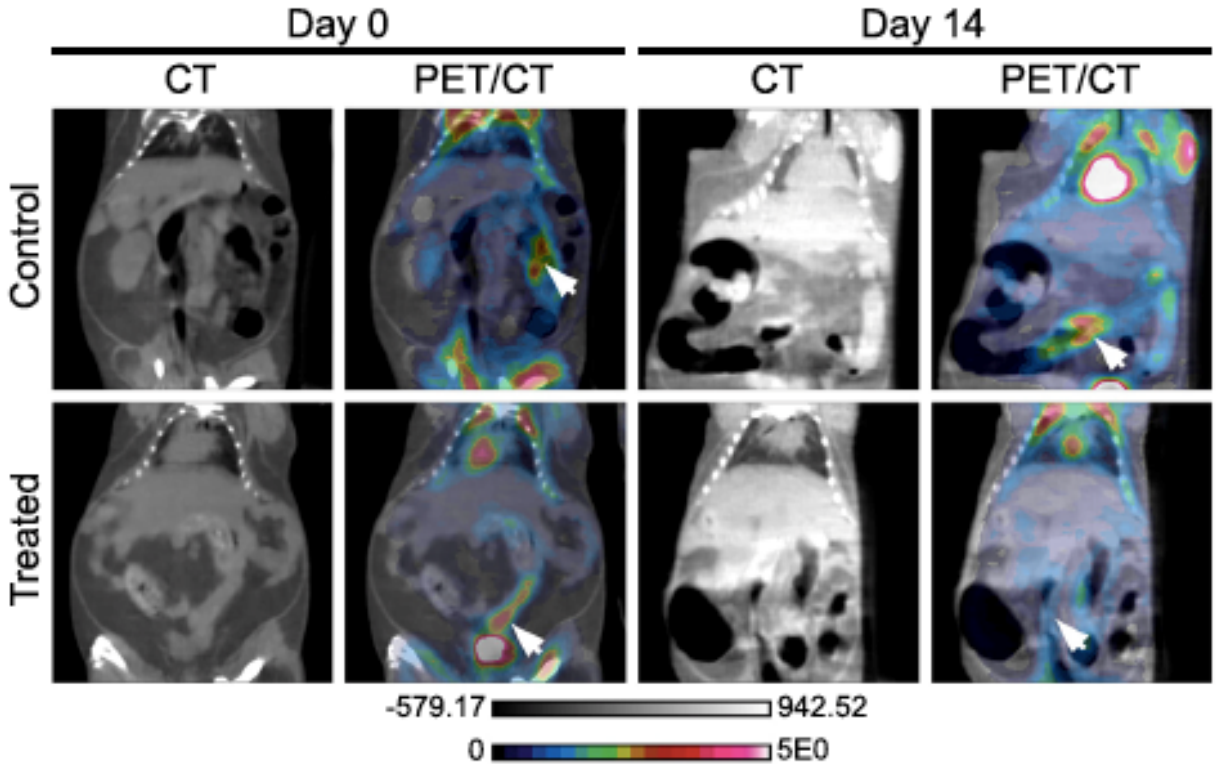
Day 0
Day 14
CT
PET/CT
CT
PET/CT
Control
Treated
-579.17
942.52
0
5E0

Appendix 8-6. Additional examples of baseline and post-treatment ^{18}F-FDG PET/CT scans of Fabp1-Cre^{+} Pik3ca(H1047R)$^{+}$ mice treated with NVP-BEZ235 (35mg/kg/day) or control once daily by oral gavage for 14 days. Arrows denote tumors pre- and post-treatment.

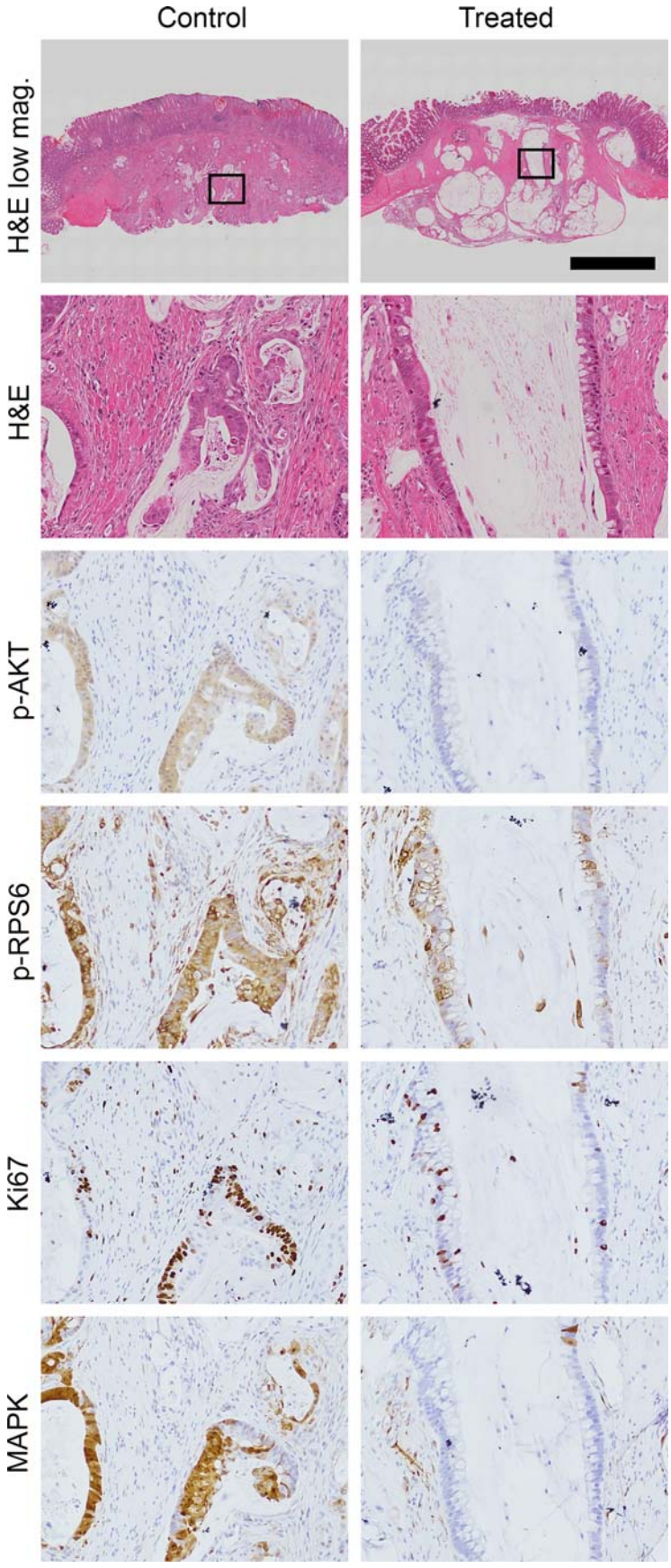
Control
Treated
H&E low mag.
H&E
p-AKT
p-RPS6
Ki67
MAPK

Appendix 8-7. Histological examination demonstrates a significant treatment effect following dual PI3K/mTOR inhibition of Fabp1-Cre^{+} Pik3ca(H1047R)$^{+}$ cancers. In comparison to controls, a dramatic treatment effect was identified on H&E staining: loss of epithelial cells surrounding the areas of cystic change/degeneration and areas of increased fibrosis. A decrease in Ki67 staining and phosphorylation of AKT, RPS6 and ERK1/2 are also seen. Scale bar for low magnification images = 1mm. High magnification panels are 10x magnifications of the areas indicated by the rectangles.

Tables

Appendix 8-8. Characteristics of *Apc*$^{Min/+}$, Fabp1-Cre^{+} Pik3ca*$^{+}$, and Fabp1-Cre^{+} Pik3ca(H1047R)$^{+}$ mice.

Mice	Small intestinal tumor count	Colon tumor count	Tumors progressing to cancer	Lifespan
C57BL/6J *Apc*$^{Min/+}$	92 ± 4 (males) 103 ± 4 (females)[a]	2.9 ± 0.2 (males) 1.6 ± 0.1 (females)[a]	0%[b]	Rarely survive beyond 120d[c]
(FVB x B6)F1 *Fc*$^{+}$ *Pik3ca*^{p110*}	None[d]	1.4[d]	100%[e]	Majority moribund at 40-60d[e]
FVB *Fc*$^{+}$ *Pik3ca*^{H1047R}	None[f]	1.2 ± 1.4[f]	100%[f]	>150d[f]

[a]Amos-Landgraf JM et al., Proc Natl Acac Sci USA 2014;111:16514-9. Data shown as mean ± SEM.

[b]Halberg RB et al., Cancer Res 2009;69:5768-75.

[c]Moser AR et al., Science 1990;247:322-4.

[d]Deming DA et al., Oncogene 2014;33:2245-54. Colon tumor count presented is the mean.

[e]Leystra AA et al., Cancer Res 2012;72:293106.

[f]This study. Colon tumor count shown as mean ± SD.

Appendix 8-9. Pretreatment volume of tumors imaged with PET/CT.

		Pretreatment tumor volume		
Treatment group	N of tumors	Mean	Median	Range
Control	13	30.6	21.6	3.2-106.9
Treated with NVP-BEZ235	11	42.3	30.4	3.9-88.0

References

1. Kinzler, K. W. & Vogelstein, B. Gatekeepers and caretakers. *Nature* **386,** 761–763 (1997).

2. Segditsas, S. & Tomlinson, I. Colorectal cancer and genetic alterations in the Wnt pathway. *Oncogene* **25,** 7531–7537 (2006).

3. Goss, K. H. & Groden, J. in *Encyclopedia of Cancer* 143–151 (Elsevier, 2002). doi:10.1016/B0-12-227555-1/00015-0

4. Fearon, E. R. & Vogelstein, B. A genetic model for colorectal tumorigenesis. *Cell* **61,** 759–767 (1990).

5. Markowitz, S. D. & Bertagnolli, M. M. Molecular Basis of Colorectal Cancer. *N Engl J Med* **361,** 2449–2460 (2009).

6. Vermeulen, L. *et al.* Wnt activity defines colon cancer stem cells and is regulated by the microenvironment. *Nature Cell Biol* **12,** 468–476 (2010).

7. Samuels, Y. High Frequency of Mutations of the *PIK3CA* Gene in Human Cancers. *Science* **304,** 554–554 (2004).

8. Vivanco, I. & Sawyers, C. L. The phosphatidylinositol 3-Kinase–AKT pathway in human cancer. *Nat Rev Cancer* **2,** 489–501 (2002).

9. Zhao, L. & Vogt, P. K. Hot-spot mutations in p110α of phosphatidylinositol 3-kinase (PI3K): Differential interactions with the regulatory subunit p85 and with RAS. *Cell Cycle* **9,** 596–600 (2014).

10. Leystra, A. A. *et al.* Mice expressing activated PI3K rapidly develop advanced colon cancer. *Cancer Res* **72,** 2931–2936 (2012).

11. Liu, G. *et al.* Pharmacodynamic Study Using FLT PET/CT in Patients with Renal Cell Cancer and Other Solid Malignancies Treated with Sunitinib Malate. *Clin Cancer Res* **17,** 7634–7644 (2011).

12. Yap, T. A., Bjerke, L., Clarke, P. A. & Workman, P. Drugging PI3K in cancer: refining targets and therapeutic strategies. - PubMed - NCBI. *Current Opinion in Pharmacology* **23,** 98–107 (2015).

13. Gopal, A. K. *et al.* PI3Kδ Inhibition by Idelalisib in Patients with Relapsed Indolent Lymphoma. *N Engl J Med* **370,** 1008–1018 (2014).

14. Janku, F. *et al.* PIK3CA Mutation H1047R Is Associated with Response to PI3K/AKT/mTOR Signaling Pathway Inhibitors in Early-Phase Clinical Trials. *Cancer Res* **73,** 276–284 (2013).

15. Rodon, J. *et al.* Abstract LB-65: Towards defining the genetic framework for clinical response to treatment with BYL719, a PI3Kalpha-specific inhibitor. *Cancer Res* **73,** LB–65–LB–65 (2013).

16. Pena, C. E. *et al.* Biomarker analysis from a Phase I study of copanlisib with expansion cohorts in solid tumors with and without *PIK3CA* mutations and NHL. *ASCO Meeting Abstracts* **33,** 2548 (2015).

17. Rodrigues, H. V. *et al.* Phase I combination of pazopanib and everolimus in *PIK3CA* mutation positive/PTEN loss patients with advanced solid tumors refractory to standard therapy. *Invest New Drugs* **33,** 700–709 (2015).

18. Moore, K. N. *et al.* A phase I, first-in-human dose study of the dual PI3K/mTOR inhibitor LY3023414 (LY) in patients (pts) with advanced cancer. *ASCO Meeting Abstracts* **33,** 11075 (2015).

19. Stelzer, M. K. *et al.* Rapamycin Inhibits Anal Carcinogenesis in Two Preclinical Animal Models. *Cancer Prev Res* **3,** 1542–1551 (2010).

20. Carracedo, A. *et al.* Inhibition of mTORC1 leads to MAPK pathway activation through a PI3K-dependent feedback loop in human cancer. *J Clin Invest* **118,** 3065–3074 (2008).

21. Ebi, H. *et al.* PI3K regulates MEK/ERK signaling in breast cancer via the Rac-GEF, P-Rex1. *Proc. Natl. Acad. Sci.* **110,** 21124–21129 (2013).

22. Payne, S. N. *et al.* PIK3CA mutations can initiate pancreatic tumorigenesis and are targetable with PI3K inhibitors. *Oncogenesis* **4,** e169 (2015).

23. Nosho, K. *et al.* PIK3CA Mutation in Colorectal Cancer: Relationship with Genetic and Epigenetic Alterations. *Neoplasia* **10,** 534–541 (2008).

24. Vogelstein, B. *et al.* Genetic Alterations during Colorectal-Tumor Development. *N Engl J Med* **319,** 525–532 (1988).

25. Wong, M. H., Saam, J. R., Stappenbeck, T. S., Rexer, C. H. & Gordon, J. I. Genetic mosaic analysis based on Cre recombinase and navigated laser capture microdissection. *Proc. Natl. Acad. Sci. U.S.A.* **97,** 12601–12606 (2000).

26. Adams, J. R. *et al.* Cooperation between Pik3ca and p53 Mutations in Mouse Mammary Tumor Formation. *Cancer Res.* **71,** 2706–2717 (2011).

27. Su, L. K. *et al.* Multiple intestinal neoplasia caused by a mutation in the murine homolog of the APC gene. *Science* **256,** 668–670 (1992).

28. Deming, D. A. *et al.* PIK3CA and APC mutations are synergistic in the development of intestinal cancers. *Oncogene* **33,** 2245–2254 (2014).

29. Engelman, J. A. *et al.* Effective use of PI3K and MEK inhibitors to treat mutant Kras G12D and PIK3CA H1047R murine lung cancers. *Nat Med* **14,** 1351–1356 (2008).

30. Deming, D. A. *et al.* mTOR inhibition elicits a dramatic response in PI3K-dependent colon cancers. *PLoS ONE* **8,** e60709 (2013).

APPENDIX 9. mTOR inhibition elicits a dramatic response in PI3K-dependent colon cancers.

This manuscript was included in the appendix as evidence for the incomplete response of tumors to therapy targeted against an actionable mutation present at tumor initiation.

Dustin A. Deming, **Alyssa A. Leystra**, Mohammed Farhoud, Laura Nettekoven, Linda Clipson, Dawn Albrecht, Mary Kay Washington, Ruth Sullivan, Jamey P. Weichert, and Richard B. Halberg.

Abstract

The phosphatidylinositide-3-kinase (PI3K) signaling pathway is critical for multiple cellular functions including metabolism, proliferation, angiogenesis, and apoptosis, and is the most commonly altered pathway in human cancers. Recently, we developed a novel mouse model of colon cancer in which tumors are initiated by a dominant active PI3K (Fabp1-Cre^{+} Pik3ca*$^{+}$). The cancers in these mice are moderately differentiated invasive mucinous adenocarcinomas of the proximal colon that develop by 50 days of age. Interestingly, these cancers form without a benign intermediary or aberrant WNT signaling, indicating a non-canonical mechanism of tumorigenesis. Since these tumors are dependent upon the PI3K pathway, we investigated the potential for tumor response by the targeting of this pathway with rapamycin, an mTOR inhibitor. A cohort of Fabp1-Cre^{+} Pik3ca*$^{+}$ mice were treated with rapamycin at a dose of 6 mg/kg/day or placebo for 14 days. FDG dual hybrid PET/CT imaging demonstrated a dramatic tumor response in the rapamycin arm and this was confirmed on necropsy. The tumor tissue

remaining after treatment with rapamycin demonstrated increased pERK1/2 or persistent phosphorylated ribosomal protein S6 (pS6), indicating potential resistance mechanisms. This unique model will further our understanding of human disease and facilitate the development of therapeutics through pharmacologic screening and biomarker identification.

Adapted from PLoS ONE; 8(4):e60709. ©2013 Deming et al.

In addition to reformatting, the following changes were made for the sake of consistency:

- Figures and references were renumbered
- "*FC"* mice were renamed "Fabp1-Cre^{+}" mice
- "*PIK3ca**" mice were renamed "Pik3ca*$^{+}$" mice

Authors' Contributions

Read and edited the manuscript: DAD AAL MF LN LC DA MKW RS JPW RBH. Conceived and designed the experiments: DAD RBH. Performed the experiments: DAD AAL MF LN RBH. Analyzed the data: DAD AAL MF LC DA MKW RS RBH. Contributed reagents/materials/analysis tools: MF JPW. Wrote the paper: DAD RBH.

Introduction

The development of targeted therapies for the treatment of cancer has been a subject of great interest and effort. Until recently, new directed therapies have been studied in largely unselected populations. Limited efficacy has been demonstrated using this approach. However, as we evolve closer to an era of personalized medicine, each histological subtype of cancer is

becoming better understood as a collection of rare cancers with each defined by its mutation profile. Therefore, the testing of targeted agents should be performed with a selected population carrying mutations known to activate the signaling pathways being targeted.

Human colonic tumors contain several possible oncogenic driver mutations which could potentially be targeted, including *KRAS*, *BRAF*, and *PIK3CA* These mutant kinases have been key targets for the continued development of therapeutic agents[1]. They have also been important in understanding the biology of resistance to the epidermal growth factor receptor directed therapies, cetuximab and panitumumab[2,3]. Despite significant advances in the treatment of this deadly disease, colorectal cancer remains the second leading cause of cancer related death in the United States[4]. To advance the treatment options for patients, further investigation regarding the biology of these mutations is necessary. This will provide an improved understanding of which patients are most likely to respond to particular therapies.

PIK3CA mutations occur in 20 to 30% of human colorectal cancers[5,6]. Three hotspot mutations are commonly found, including H1047R, E542K, and E545K, which result in a constitutively active form of the PI3K p110α catalytic subunit[7]. This dominant active PI3K then results in increased AKT/mTOR pathway signaling and increased cellular proliferation[8] (Appendix 9-1). While several investigators have examined the effects of these mutations in cell lines, our laboratory recently developed a murine model of colon cancer that is initiated by a dominant active PI3K (Fabp1-Cre^{+} Pik3ca*$^{+}$)[9]. In this model, large moderately differentiated mucinous invasive adenocarcinomas develop in the proximal colon by only 50 days of age. These tumors are initiated by a non-canonical pathway independent of aberrant WNT signaling. Since these tumors are initiated by activated PI3K, we aimed to determine if these tumors are dependent on this pathway. Here, we demonstrate that the treatment of Fabp1-Cre^{+} Pik3ca*$^{+}$

mice with the mTOR inhibitor, rapamycin, results in a dramatic response in advanced colon cancers. This indicates that human tumors dependent on the PI3K/AKT pathway are likely to be susceptible to inhibitors of downstream mediators.

Results

Fabp1-Cre^{+} Pik3ca^{+} Mice Develop Proximal Colon Cancers that can be Followed Longitudinally for Treatment Studies*

Fabp1-Cre^{+} Pik3ca*$^{+}$ mice rapidly develop moderately invasive mucinous adenocarcinomas[9]. Importantly for this study, the tumors in these mice can be detected by dual hybrid ^{18}F-FDG or ^{18}F-FLT PET/CT colonography (Appendix 9-2A and B, respectively). In our recent description of this model, we evaluated the development of tumors in the colon over time[9]. Invasive adenocarcinomas were identified in 75% of mice at just 40 days of age. The vast majority of mice become moribund by just 60 to 80 days of age. Given the goal of this study to measure the effect of rapamycin on pre-existing colon cancers with a dominantly active PI3K, we placed into our therapeutic study 22 Fabp1-Cre^{+} Pik3ca*$^{+}$ mice at 55 days of age, an age when most have pre-existing cancer, but have not yet become moribund. The mice were stratified into groups based on gender and pretreatment tumor size as estimated from baseline dual hybrid ^{18}F-FDG PET/CT colonography. A volume of 50 mm^3 was used as a cut-off to determine large versus small tumors. These mice were then randomized into two treatment arms, receiving either placebo or rapamycin by oral gavage. Baseline characteristics are displayed in Appendix 9-13.

Fabp1-Cre^{+} Pik3ca^{+} Mice Tolerate Rapamycin Treatment*

Rapamycin was administered to Fabp1-Cre^{+} Pik3ca*$^{+}$ mice at a dose of 6 mg/kg/day by oral gavage for a total of 14 consecutive days, which had been shown previously to be tolerable to mice[10]. The Fabp1-Cre^{+} Pik3ca*$^{+}$ mice also tolerated this treatment well (Appendix 9-13). No significant change in activity level or weight was noted between the placebo and treatment cohorts throughout the study period. Two mice in the placebo arm became moribund due to colonic obstruction from large proximal colon tumors and were sacrificed prior to completion of the intended treatment course. Both of these mice had large tumors on baseline imaging with volumes over 80 mm^3.

Rapamycin Induces a Significant Tumor Response in Fabp1-Cre^{+} Pik3ca*$^{+}$ Mice

After 14 days of treatment, the mice in both the placebo and rapamycin arms were imaged a second time to assess treatment efficacy. After normalization of the imaging data, a dramatic response was noted in the rapamycin-treated mice as compared to controls (Appendix 9-3, 4, and 14). In multiple animals, FDG activity consistent with tumor tissue could not be found following rapamycin treatment. The PET/CT images were used for tumor localization and the volumes were estimated based on measurements from these images (Appendix 9-5). In the placebo arm, tumor volume nearly doubled in size from baseline with an increase from baseline of 96%. This dramatic change was expected as these cancers grow quite quickly in this model. In the rapamycin cohort, there was a marked reduction in tumor volume, with only 16.9% of the baseline mass still being present on average (Appendix 9-3B and 14). Not all tumors responded to the same degree, albeit none of the cancers in the rapamycin arm were shown to increase in size while receiving treatment. Since these lesions are quite sensitive to inhibition of mTOR by

rapamycin, this further indicates that they are dependent on the PI3K/AKT/mTOR signaling cascade.

To confirm the response data acquired with the PET/CT colonography, necropsy was performed following imaging acquisition. A significant response was also seen at necropsy (Appendix 9-6). Using an intent-to-treat analysis, cecal and/or colon tumors were grossly present in 10 of 11 mice in the placebo arm, but were present in only 5 of 11 mice in the rapamycin arm (Appendix 9-6C, $p=0.021$), indicating a significant treatment effect with single agent rapamycin therapy. In the placebo arm, 8 of 11 mice had colon tumors, while cancers were present in only 3 of 11 rapamycin-treated mice (Appendix 9-6C, $p=0.034$). Both groups had an equal number of cecal tumors, with 2 of 11 mice having them in each arm. One of the Fabp1-Cre^{+} Pik3ca*$^{+}$ mice in the control group with a cecal tumor also developed metastatic disease with the spread of cancer to the mesenteric tissue abutting the spleen and pancreas (Appendix 9-6D and E). No evidence of metastatic disease was detected in any mice treated with rapamycin.

Fabp1-Cre^{+} Pik3ca^{+} Tumors Demonstrate p110* Expression and Activation of the PI3K Pathway that is Decreased with Rapamycin Treatment Resulting in Tumor Response and Reduced Proliferation*

Following necropsy, the colon tumors were isolated and prepared for histological sectioning. H&E staining demonstrated hyperplastic epithelial tissue and moderately differentiated invasive mucinous adenocarcinomas as expected in the placebo cohort (Appendix 9-7A, left). In the rapamycin-treated mice, a significant reduction in the hyperplasia of the epithelial tissue was noted, and the tumor size was reduced (Appendix 9-7A, right). The columnar malignant cells typically encircling the mucinous lakes were gone in the majority of

the tumors, resulting in fewer cells staining strongly for pAKT and pS6 in tumors from rapamycin-treated mice compared to controls (Appendix 9-7B and C, respectively). Diminished cellular proliferation was noted following rapamycin treatment as demonstrated by decreased Ki67 staining (Appendix 9-7D).

Following treatment with rapamycin, the upstream activation of the PI3K pathway remained unperturbed as expected (Appendix 9-8). At necropsy, some tumor tissue was flash frozen prior to protein preparation and quantification. The protein p110*, the dominant active form of PI3K used in this model, was expressed in the tumors and normal epithelium of the proximal colon in all animals regardless of treatment. Significant pAKT expression was also noted in the tumors and normal proximal colon tissue. The level of pAKT does not appear to be affected by rapamycin treatment. Proteins pmTOR, pSK61, and pS6 were reduced in response to rapamycin treatment in most tissues, though some tumors did clearly demonstrate continued activation of these proteins. The tumors with persistent pS6 signaling had less of a response to rapamycin treatment as noted on PET imaging.

Resistance to Rapamycin Treatment of Fabp1-Cre^{+} Pik3ca^{+} Mice Might be Mediated through pERK Up-regulation and Persistent pS6 Signaling Leading to Decreased Apoptosis*

Some tumors had a limited response to rapamycin treatment. We hypothesized that this might be related to up-regulation of the Raf/MEK/ERK signaling cascade or persistent pS6 signaling. ERK1/2 up-regulation has previously been described in response to rapamycin treatment[11,12]. Levels of pERK1/2 were evaluated in normal colon tissue, proximal colon tumors, and cecal tumors (Appendix 9-8). pERK1/2 was found to be dramatically up-regulated in one mouse from each treatment arm. In a group of ten tumors from untreated Fabp1-Cre^{+} Pik3ca*$^{+}$

mice, six demonstrated some degree of pERK1/2, indicating possible mechanism(s) for intrinsic resistance (Appendix 9-9A). In addition, all tissues treated with rapamycin did display an increase in pERK1/2 over controls. These data indicate that a subpopulation of Fabp1-Cre^{+} Pik3ca*$^{+}$ tumors possess activation of ERK signaling. This signaling might be responsible for some degree of resistance to mTOR inhibition, since the ERK pathway is not inhibited with this treatment strategy. This resistance may be intrinsic to the tumor or induced secondary to the treatment.

To confirm that WNT signaling is not aberrant in these tumors, as described previously, we performed histological analysis examining for evidence of nuclear β-catenin[9]. No nuclear β-catenin was seen in control tumors (Appendix 9-9B). In addition, the tumor remnants from rapamycin-treated mice were also examined for aberrant WNT signaling to determine if induction of this pathway may be a further mechanism decreasing the sensitivity of these tumors to rapamycin. No evidence of nuclear β-catenin was demonstrated in the tumors of rapamycin-treated mice (Appendix 9-9B).

Histological examination of a representative rapamycin-resistant Fabp1-Cre^{+} Pik3ca*$^{+}$ tumor demonstrated a similar morphology to cancers from controls (Appendix 9-10). In addition, no differences in cellular proliferation or levels of pAKT were noted (Appendix 9-10C). In a tumor from a control mouse, pS6 was noted in the mucosal hyperplasia as well as the tumor tissue, as expected (Appendix 9-10D, bottom). However, in the tumor from a rapamycin-treated mouse, a decrease in pS6 in the normal epithelial tissue was observed, but pS6 signal persisted in the remaining cancer tissue (Appendix 9-10D, top, Appendix 9-11). The amount of pS6 present in these resistant cancer cells exceeds what is seen in the responding cancer in Appendix 9-7.

This indicates a differential response in the normal tissue compared to the tumor tissue and might be a mechanism of resistance to mTOR inhibition in this setting.

Discussion

Targeting oncogenic pathways has led to recent exciting advances in multiple cancers, including vemurafenib in *BRAF* mutant melanoma, erlotinib in *EGFR* mutant non-small cell lung cancer, and crizotinib in lung cancer with the EMLA4-ALK translocation[13-15]. These agents are used in the setting of specific genetic alterations encoding oncogenic proteins. Targeting these driver proteins results in a high response rate to agents directed against them. This approach allowed for the expedient evaluation and FDA approval of these agents for these indications[16]. The development of these agents in specific molecular settings has led to realization that each histological type of cancer is actually a collection of numerous rare subtypes. These subtypes are each differentiated by their profile of mutations.

The PI3K/AKT pathway is the most common genetically altered signaling cascade in cancer. Significant clinical interest in targeting the PI3K/AKT/mTOR pathway continues to increase as novel inhibitors of this pathway continue to be developed. Inhibition of the PI3K pathway in cancers possessing *PIK3CA* mutations has demonstrated clinical benefit in breast and gynecologic malignancies, but the presence of these mutations alone does not predict sensitivity to these approaches[17]. The subpopulation of patients who are most likely to benefit from the continued development of novel inhibitors of the PI3K pathway remains unclear.

Until recently, the effects of an activated PI3K on the mammalian intestine had not been investigated. We were the first to describe the development of advanced invasive mucinous adenocarcinomas developing in the proximal colon as a result of expression of a dominant active

PI3K[9]. Interestingly, these tumors develop rapidly, without a significant luminal component or aberrations in WNT signaling, indicating a non-canonical mechanism of tumor initiation. Here, we demonstrate that the tumors forming in Fabp1-Cre^{+} Pik3ca*$^{+}$ mice are largely dependent upon the PI3K pathway. In this model, a dominant active PI3K is expressed in the colon resulting in tumor initiation. These cancers are very aggressive and are able to be followed longitudinally with dual hybrid ^{18}F-FDG PET/CT colonography. After just two weeks of rapamycin therapy a significant response was observed with imaging and confirmed at necropsy. These results indicate that Fabp1-Cre^{+} Pik3ca*$^{+}$ tumors are dependent on this pathway. If similar tumors are present in humans, inhibition of the PI3K pathway could result in significant clinical benefit for appropriate patients.

We hypothesize that a subpopulation of human tumors form as a consequence of a dominant active PI3K and that these tumors are dependent upon this pathway. In a recent pathological series, activating mutations in *PIK3CA* were observed more commonly in mucinous colon cancers in humans, similar to our model, and were associated with worsened prognosis[18]. Activating mutations in *PIK3CA* were inversely associated with the translocation of β-catenin[18]. Translocation of β-catenin would be expected if these tumors were initiated by aberrant WNT signaling as part of the previously described canonical mechanisms of tumorigenesis in colon cancers[19]. Together, these observations indicate that a subgroup of human colon cancers arise in the setting of activated PI3K, similar to what is seen in our model. Only a small number of tumors have been interrogated for aberrations in WNT signaling and mutations in *PIK3CA*, thus additional investigations are warranted to further characterize this patient population. Based on these prior studies, we believe that this likely represents 1–5% of all colon cancers.

Even with the significant responses seen in this study, resistance to rapamycin therapy was identified. Increased pERK1/2, pS6, or both were observed in tumors persisting despite rapamycin treatment. These resistance mechanisms may be intrinsic to the tumors or induced secondary to the rapamycin treatment. Rapamycin is known to inhibit ribosomal S6 kinases (S6K1 and S6K2) through its interaction with mTOR[20]. The inhibition of the S6Ks diminishes downstream phosphorylation of S6 at Ser240/244 and Ser235/236[21]. Studies in S6K1/S6K2-null mouse embryonic fibroblasts confirmed that these S6Ks were the major kinases affecting S6, but also demonstrated a MEK1/2 dependent mechanism of S6 phosphorylation at Ser235/236[22]. In addition, ERK1/2 has been demonstrated to activate the p90 ribosomal S6 kinase (RSK), which can subsequently phosphorylate S6 at Ser235/236 independent of mTOR signaling[23] (Appendix 9-12). In all tumors from Fabp1-Cre^{+} Pik3ca*$^{+}$ mice, we observe phosphorylation of S6 thought to be related to activation of the PI3K pathway. In a subset of tumors, we also observe increased pERK1/2 and persistent pS6. These data indicate that the alternate phosphorylation of S6 mediated by ERK1/2 activation of RSK might be a mechanism by which these tumors are resistant to rapamycin. Combinations of targeted therapies will probably be necessary in some circumstances to overcome these resistance mechanisms. PI3K and Raf/MEK/ERK pathway inhibitor combination regimens continue to be an active area of preclinical and clinical research[24-26].

Though rapamycin is a well known inhibitor of mTOR and the PI3K pathway, new agents continue to be developed to target this pathway. Agents targeting PI3K, AKT, and mTORC1/mTORC2 are in clinical development. We hypothesize that these agents would have significant response rates in our model system[27-29]. It is likely that each of these agents would, however, have different side-effect profiles and mechanisms of resistance. BYL719 (Novartis) is

the first alpha isomer specific PI3K inhibitor and may hold significant advantages over other agents with a hopefully improved safety profile compared to other pan inhibitors[30].

As we begin to expand our capabilities to personalize cancer treatments based on molecular features, this will necessitate subdivision of each histological type of cancer to collections of rare cancers defined by their mutation profiles. Acquiring genomic information as it relates to treatment response will be vital for the proper development of combinations of targeted therapies. Using murine models, we can control the mutation profile to quickly determine the best strategies to target these cancers. The findings can then be translated to the clinic, where patients can receive drugs dictated by the mutation profiles of their tumors. Preclinical testing of treatment strategies will be essential as the subtypes of each cancer become exceedingly rare and thus more difficult to study on a large scale in the clinic. *PIK3CA* mutations are a promising target in colorectal cancer, among others; now we need to optimize the administration of our therapies and identify the patient populations most likely to benefit.

Methods

Mouse Husbandry

All animal studies were conducted under protocols approved by the Institutional Animal Care and Use Committee at the University of Wisconsin-Madison, following the guidelines of the American Association for the Assessment and Accreditation of Laboratory Animal Care. Homozygous Fabp1-Cre^{+} female mice (FVB/N-Tg(Fabp1-Cre)1Jig; NCI Mouse Repository; Strain number - 01XD8) were crossed to homozygous Pik3ca*$^{+}$ male mice (C57BL/6-Gt(ROSA)26Sortm7(Pik3ca*,EGFP)Rsky/J; The Jackson Laboratory; Stock Number - 012343)

to generate Fabp1-Cre^{+} Pik3ca*$^{+}$ mice used in this study. Mice were genotyped for Fabp1-Cre and Pik3ca*$^{+}$ as described previously[31,32].

Animal Treatment

Fabp1-Cre^{+} Pik3ca*$^{+}$ mice between 50 and 60 days of age were selected for study enrollment as long as they were not moribund. Baseline dual hybrid ^{18}F-FDG PET/CT scans were performed prior to and 15 days following treatment initiation. The tumor size was subjectively determined from the pre-treatment raw images and used for stratification during randomization to the rapamycin and control arms. Animals in the control arm received ethanol dissolved in water to a 1% final concentration by oral gavage daily for 14 days. Animals randomized to the rapamycin arm received 6 mg/kg of rapamycin (LC Labs, Woburn, MA) by oral gavage per day for 14 consecutive days. Rapamycin was dissolved in ethanol to a concentration of 50 mg per ml prior to suspending in water to a final volume of 200 µl for administration.

Imaging

Animals were fasted for at least 6 hours prior to injection of ^{18}F-FDG (160 µCi; IBA Molecular, Romeoville, IL) or ^{18}F-FLT (140 µCi; University of Wisconsin Cyclotron, Madison WI). After injection, the animals were kept under anesthesia for 60 minutes and then prepared for virtual colonography as described previously[33]. A 10-minute PET acquisition was performed, followed immediately by CT scanning. Maximum intensity projections were created in Siemens Inveon Research Workplace (Knoxville, TN). The PET images were reconstructed using OSEM3D/MAP (OSEM3D, 2 iterations; MAP 18, iterations 16 subsets). Attenuation correction

was performed using the CT data. The CT images were reconstructed using standard conebeam reconstruction. Baseline and post-treatment PET scans were normalized to injected dose, dose decay, activity, and weight. Tumor volumes were estimated from measurements on the PET/CT scans (Appendix 9-5). PET imaging was utilized to locate tumors prior to volume estimation. Tumor volumes can only be estimated, as delineating the exact tumor boundaries is difficult. This is because these cancers are not luminal and subtle FDG signal changes related to the hyperplastic normal epithelium surrounding the tumors exist. Tumor volumes in each cohort were compared using a two-sided Student's exact t-test. A p value of less than 0.05 was considered statistically significant.

Histology and Immunohistochemistry

Mice were euthanized by CO2 asphyxiation following their post-treatment imaging. The small bowel and colon were removed, flushed with PBS, split lengthwise, splayed out, and fixed in 10% buffered formalin for 24 hours. Tissues were then stored in 70% ethanol, processed, embedded in paraffin, and cut into 5 μm sections. Every tenth section was stained with hematoxylin and eosin (H&E) for histological review. Immunohistochemistry was performed using the Histomouse™ Max Broad Spectrum (DAB) kit as instructed by the manufacturer (Invitrogen, Carlsbad, CA) and as previously described[9]. Immunofluorescence was performed using a similar protocol with the following changes: 5% milk in PBS was used to block tissues. All steps after incubation with the primary antibody and washing were omitted and replaced with the following: incubated with AlexaFluor 488 goat anti-rabbit IgG fluorescent secondary antibody (1∶1000, Invitrogen) for one hour, washed in PBS, and mounted using the ProlongGold Antifade Reagent with DAPI (Invitrogen). The primary antibodies included: anti-pAKT (Ser473,

1∶100, Cell Signaling Technology, Beverly, MA), anti-pS6 (1∶200, Cell Signaling Technology), anti-Ki67 (1∶1000, Cell Signaling Technology) and mouse anti-β-catenin (1∶200, BD Biosciences - Clone 14, San Diego, CA).

Western Blot Analysis

Tissue samples were excised and flash frozen. After 24 hours, the samples were sonicated in T-PER tissue protein extraction reagent (Thermo Scientific, Pittsburg, PA), proteasome inhibitor cocktail (Sigma-Aldrich, St. Louis, MO), and phenylmethylsulfonyl fluoride (PMSF, Sigma-Aldrich). Extracted protein was then run as previously described[9]. Primary antibodies against p110α, pAKT (Ser473), AKT (pan, 11E7), total Tuberin/TSC2 (D93F12), pmTOR (Ser2448), pS6K1 (p70 S6 kinase, Thr389), pS6 (Ser235/236), Total S6 (5G10), cleaved caspase 3, pERK1/2 (Thr202/Tyr 204) and total ERK 1/2 (Cell Signaling Technology) were incubated in bovine serum albumin (Sigma-Aldrich) at a 1∶1000 ratio for 16 hours. Anti-GAPDH antibody (Cell Signaling) was utilized as a loading control at a ratio of 1∶5000.

Conflict of Interest

No potential conflicts of interest were disclosed.

Grant Support

The project was supported by the Conquer Cancer Foundation of the American Society of Clinical Oncology through a Young Investigator Award (to DAD); the National Cancer Institute of the U.S. National Institutes of Health through T32 CA009614 (to DAD), P50 CA095103 Gastrointestinal Specialized Program of Research Excellence Grant, Vanderbilt Ingram Cancer

Center), R01 CA123438 (to RBH), P30 CA014520 (Core Grant, University of Wisconsin (UW) Carbone Cancer Center); and start-up funds (to RBH) from the UW Division of Gastroenterology and Hepatology, the UW Department of Medicine, and the UW School of Medicine and Public Health. The funders had no role in study design, data collection and analysis, decision to publish, or preparation of the manuscript.

Acknowledgements

We thank Ella Ward and Jane Weeks in Experimental Pathology at the UW Carbone Cancer Center for their technical assistance.

Figures

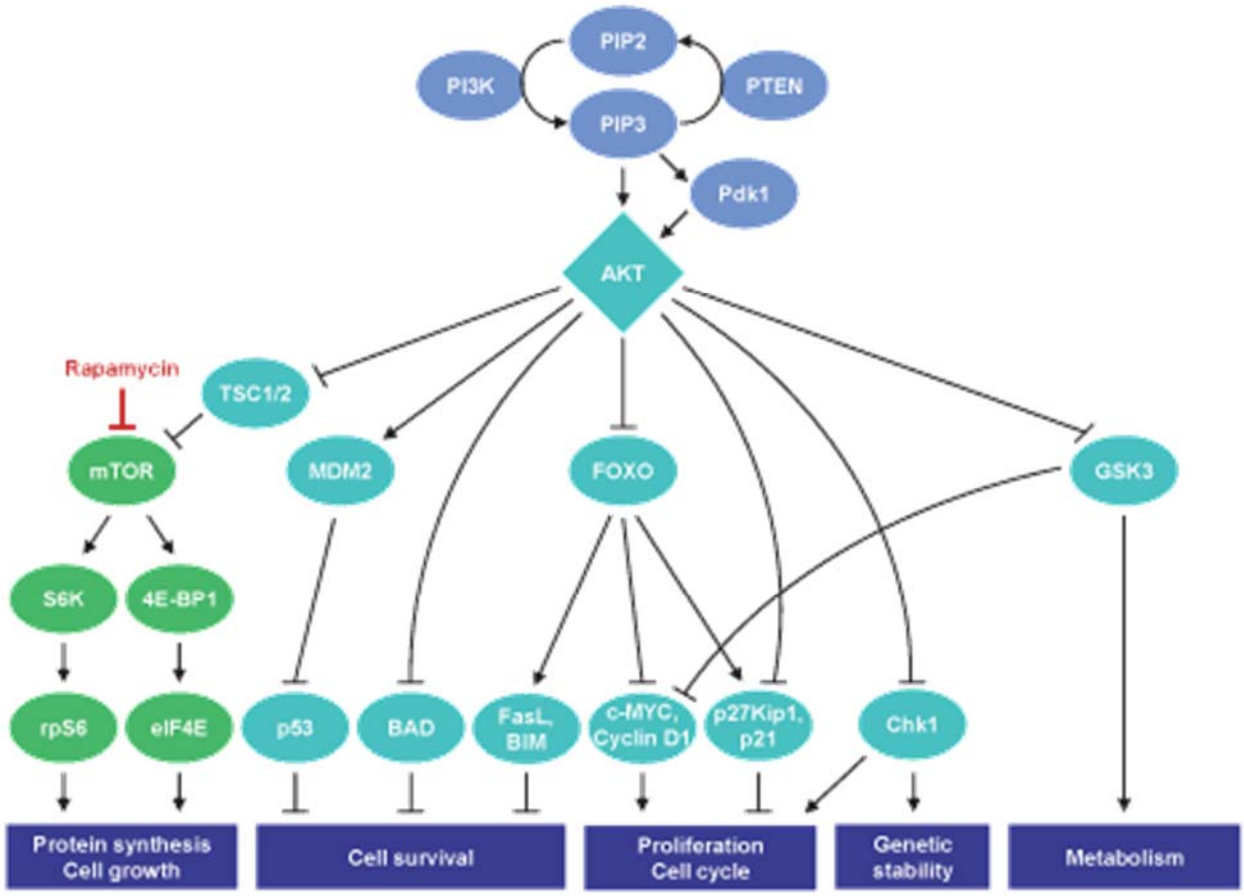
PIP2
PI3K
PTEN
PIP3
Pdk1
AKT
Rapamycin
TSC1/2
mTOR
MDM2
FOXO
GSK3
S6K
4E-BP1
rpS6
eIF4E
p53
BAD
FasL, BIM
c-MYC, Cyclin D1
p27Kip1, p21
Chk1
Protein synthesis Cell growth
Cell survival
Proliferation Cell cycle
Genetic stability
Metabolism

Appendix 9-1. The PI3K signaling pathway mediates vital cellular functions. The PI3K is commonly altered in human cancers and has been targeted for many new directed therapies.

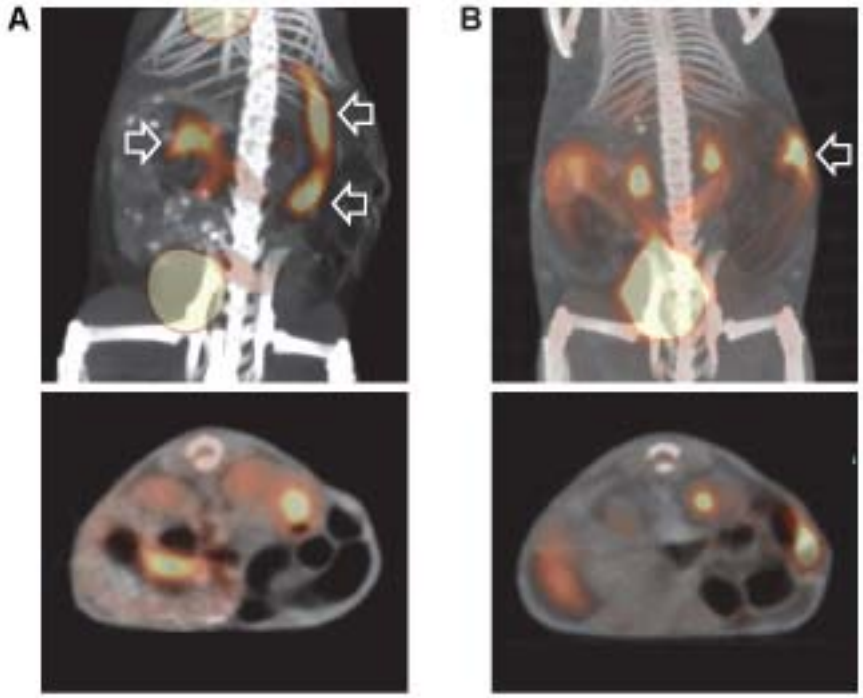
A
B

Appendix 9-2. Fabp1-Cre^{+} Pik3ca*$^{+}$ tumors can be identified by dual hybrid ^{18}F-FDG and ^{18}F-FLT PET/CT colonography for longitudinal treatment studies. Untreated Fabp1-Cre^{+} Pik3ca*$^{+}$ mice that were moribund were imaged with ^{18}F-FDG (A) and ^{18}F-FLT (B) PET/CT colonography. The PET avid areas correspond to invasive mucinous colonic adenocarcinomas. Three tumors were present in the untreated Fabp1-Cre^{+} Pik3ca*$^{+}$ mouse all three tumors were visualized with PET imaging (A). A single proximal colon tumor was visualized with ^{8}F-FLT PET/CT colonography in a separate untreated Fabp1-Cre^{+} Pik3ca*$^{+}$ mouse (B). Projections are shown on top and axial sections are displayed on the bottom.

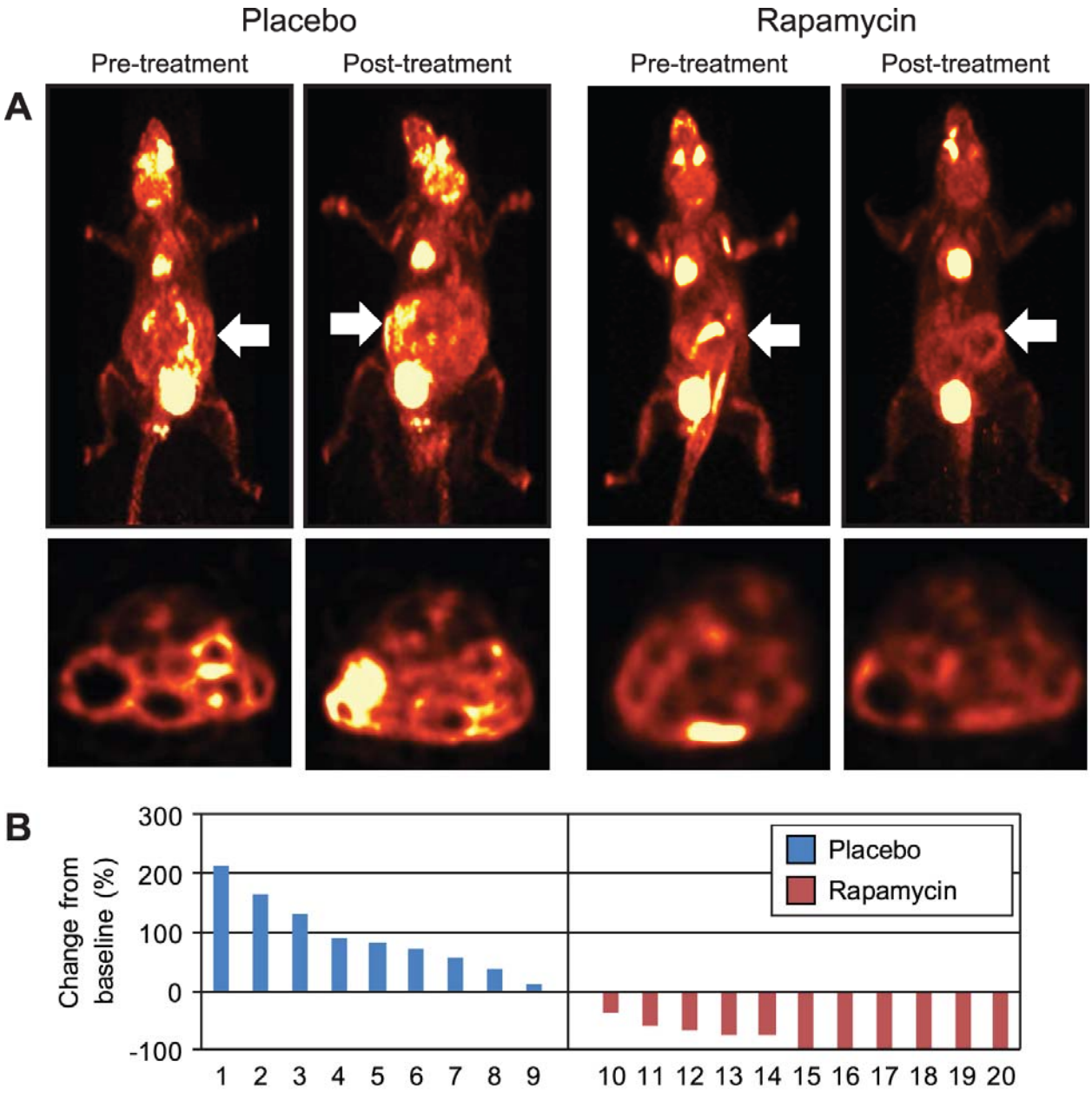
Placebo
Rapamycin
Pre-treatment
Post-treatment
Pre-treatment
Post-treatment
A
B
Change from baseline (%)
300
200
100
0
-100
1 2 3 4 5 6 7 8 9
10 11 12 13 14 15 16 17 18 19 20
Placebo
Rapamycin

Appendix 9-3. Longitudinal monitoring with dual hybrid 18F-FDG PET/CT colonography revealed a dramatic tumor response in Fabp1-Cre^{+} Pik3ca*$^{+}$ mice treated with rapamycin. A group of 22 Fabp1-Cre^{+} Pik3ca*$^{+}$ mice were imaged with dual hybrid 18F-FDG PET/CT colonography and stratified based on tumor size. Mice were then treated with a placebo (ethanol dissolved in drinking water) or rapamycin 6 mg/kg/day by oral gavage for 14 days. Following completion of the treatment course, PET/CT colonography was repeated to evaluate for tumor response. In the mice receiving placebo, the tumors increased in size during the 14 day treatment period (A, left). In the rapamycin arm a significant response was noted (A, right). Projection and axial views are presented on the top and bottoms, respectively. The tumors were located on PET images and volumes were measured from CT scans data. The percent change in tumor volume for each tumor is displayed in a waterfall plot (B).

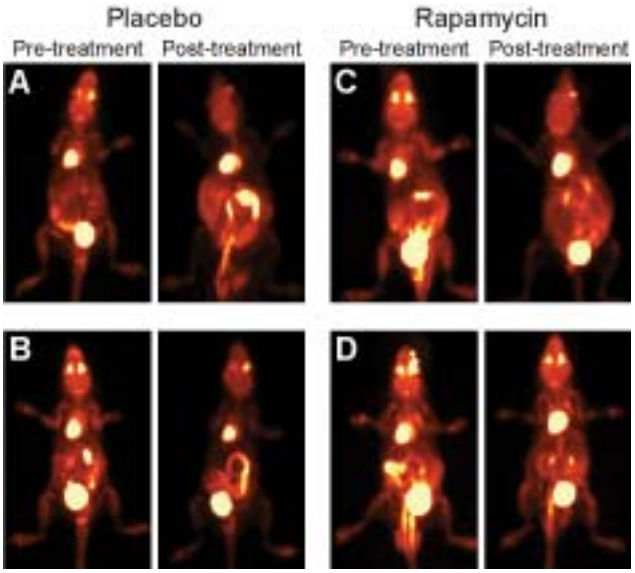
Placebo
Rapamycin
Pre-treatment
Post-treatment
Pre-treatment
Post-treatment
A
C
B
D

Appendix 9-4. Longitudinal monitoring with dual hybrid ^{18}F-FDG PET/CT colonography revealed a dramatic tumor response in Fabp1-Cre^{+} Pik3ca*$^{+}$ mice treated with rapamycin. Further examples of pre- and post-treatment PET imaging demonstrated tumor growth in the placebo-treated mice (A and B) and tumor response in the rapamycin-treated mice (C and D).

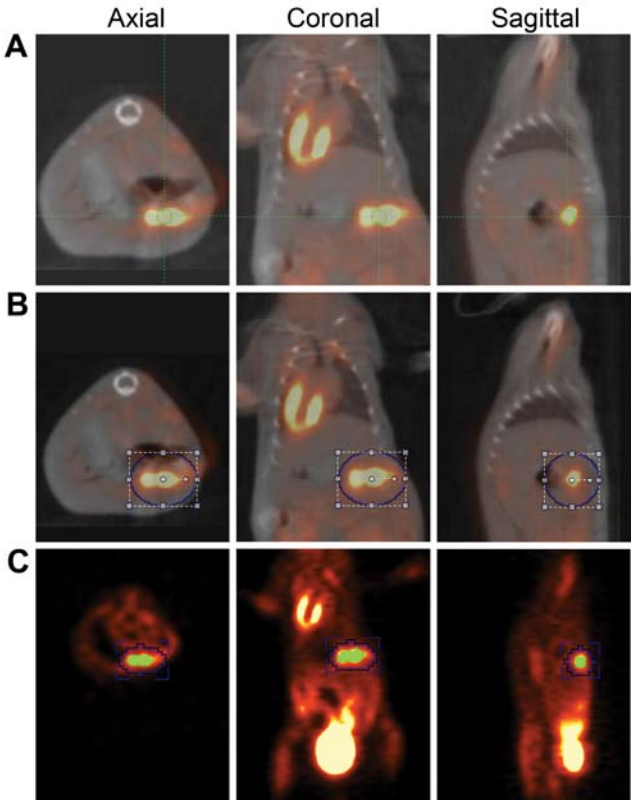
Axial
Coronal
Sagittal
A
B
C

Appendix 9-5. Volume estimation based on ^{18}F-FDG PET/CT. (A) PET/CT imaging was collected at baseline and following two weeks of rapamycin treatment. Tumors in Fabp1-Cre^{+} Pik3ca*$^{+}$ mice were identified based on PET avidity and tumor location was confirmed on CT in axial, coronal, and sagittal views. (B) To estimate tumor volume the area containing the tumor was encircled using Siemens Inveon Research Workplace. (C) The tumor was then highlighted based on voxel intensity in the region of interest and a software-generated tumor volume was estimated.

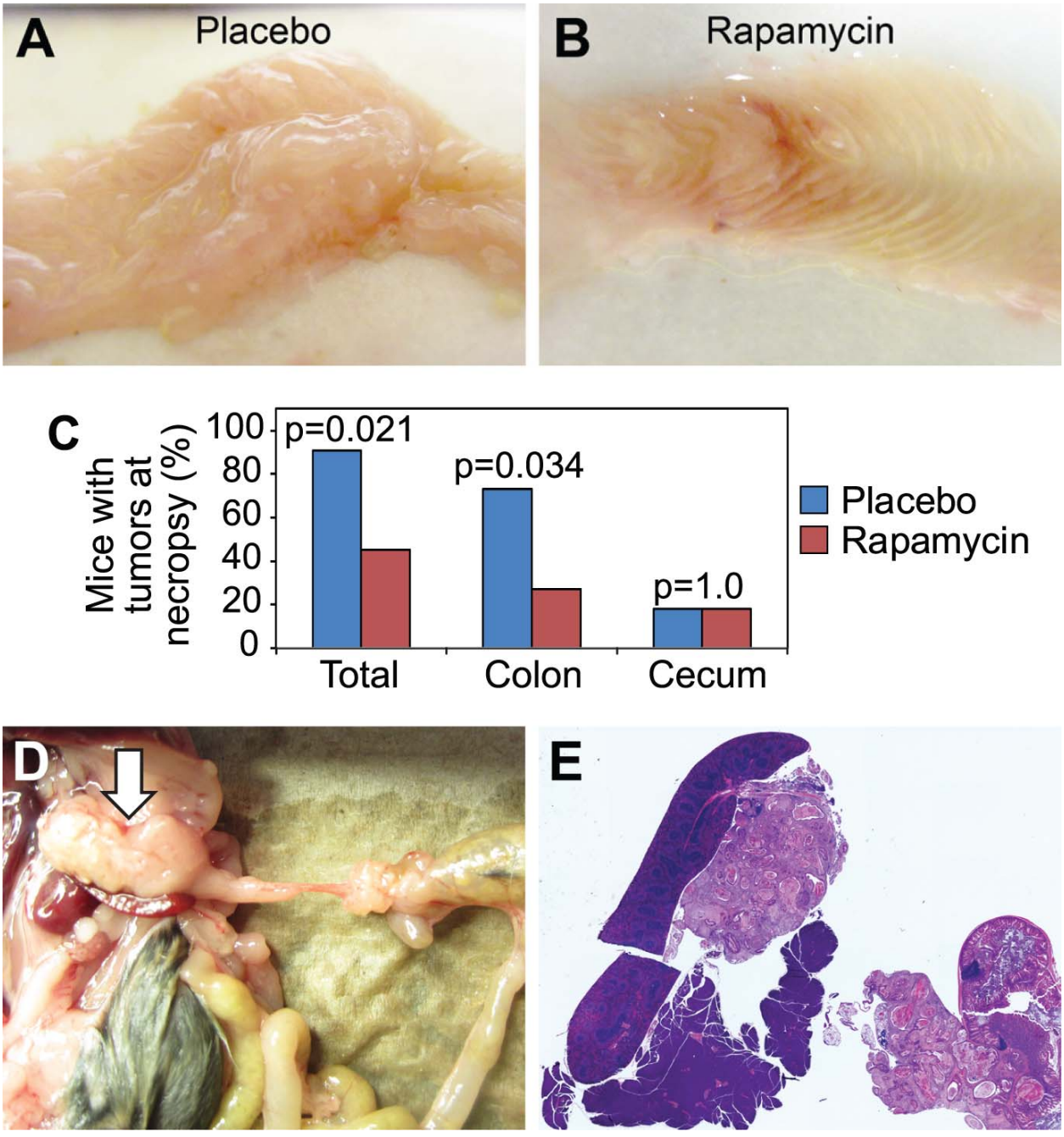
A
Placebo
B
Rapamycin
C
Mice with tumors at necropsy (%)
100
80
60
40
20
0
p=0.021
p=0.034
p=1.0
Total
Colon
Cecum
Placebo
Rapamycin
D
E

Appendix 9-6. Tumor response in Fabp1-Cre^{+} Pik3ca*$^{+}$ mice was confirmed at necropsy and metastatic disease was identified in the control arm. Following post-treatment imaging, necropsy was performed. The colon was excised and split lengthwise. Large submucosal tumors were seen in mice treated with placebo (A). A dramatic response was observed at necropsy in the rapamycin-treated cohort (B). Hyperproliferation was diminished in the normal proximal colon and minimal residual tumor was identified. 10 of 11 Fabp1-Cre^{+} Pik3ca*$^{+}$ mice in the placebo cohort had identifiable tumors while only 5 of 11 mice in the rapamycin arm had identifiable tumors (C). One mouse in the placebo cohort was found to have metastatic disease from a cecal tumor (D). A large lesion within the mesentery was identified abutting the spleen and pancreas (D, arrow). On histological sectioning a similar morphology was noted between the metastatic deposit and the primary tumor within the cecum (E).

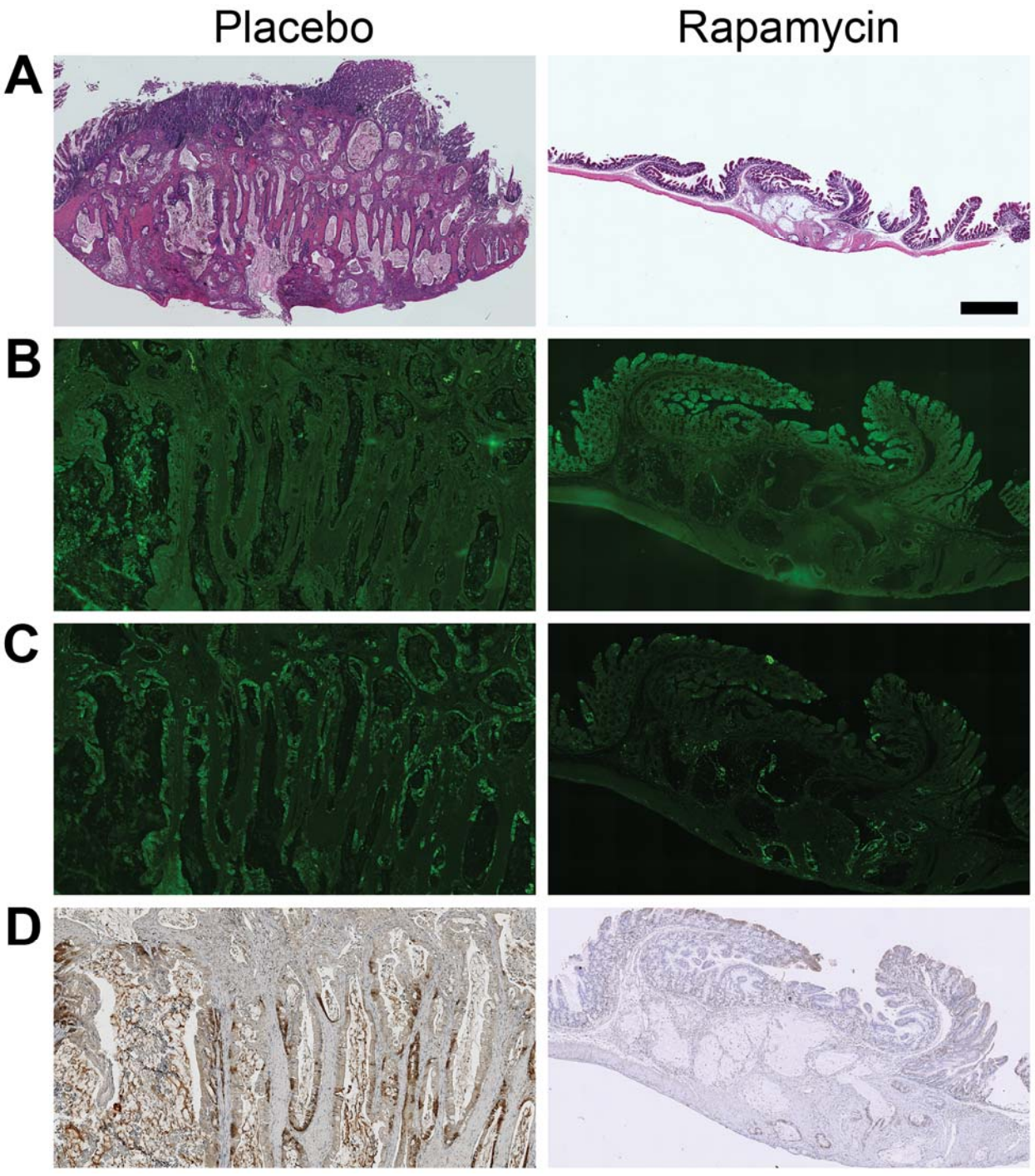
Placebo
Rapamycin
A
B
C
D

Appendix 9-7. Staining of histological sections demonstrates tumor response, decreased PI3K signaling, and decreased cell proliferation following rapamycin treatment. Following necropsy, colonic tumor tissue with adjacent colon epithelial tissue was formalin-fixed, paraffin-embedded, and underwent histological sectioning. Tissue was stained with H&E (A). Compared to placebo, a dramatic decrease in size was noted in the tumors from rapamycin-treated mice. The tumor pictured in A, rapamycin is from a Fabp1-Cre^{+} 3K mouse treated in a pilot of this study and chosen for this figure due to the observed dramatic partial response. In addition, the malignant columnar epithelium surrounding the mucinous lakes was diminished following rapamycin treatment as compared to control. Fewer pAKT and pS6-positive cells were observed in the tumors from mice treated with rapamycin as compared to tumors from mice given placebo (B and C*,* respectively). Tumor proliferation, as measured by Ki67, was also reduced in tumors from mice treated with rapamycin compared to those treated with placebo (D). Size bar: *A*, 1 mm. B–D are ~3× enlargements.

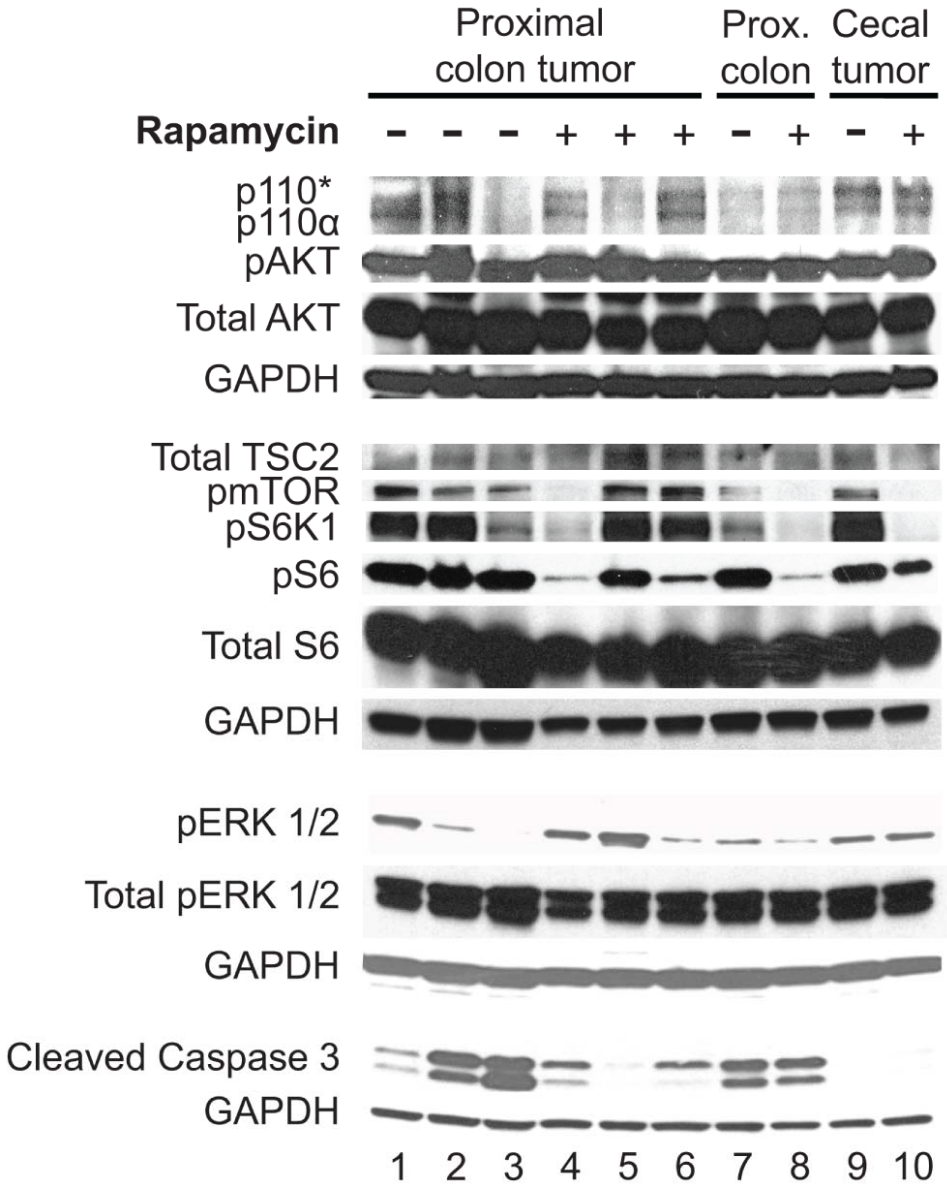
Proximal colon tumor
Prox. colon
Cecal tumor
Rapamycin
- - - + + + - + - +
p110*
p110α
pAKT
Total AKT
GAPDH
Total TSC2
pmTOR
pS6K1
pS6
Total S6
GAPDH
pERK 1/2
Total pERK 1/2
GAPDH
Cleaved Caspase 3
GAPDH
1 2 3 4 5 6 7 8 9 10

Appendix 9-8. Upstream activation of the PI3K pathway was unperturbed, but downstream signaling varied with response to rapamycin treatment. All Fabp1-Cre^{+} Pik3ca*$^{+}$ tumors and hyperplastic colon tissue demonstrated expression of p110*, the dominant active catalytic subunit of PI3K in this model. This resulted in increased phosphorylation of AKT9. The levels of pAKT and total AKT were not altered in response to rapamycin treatment. TSC2 total levels also did not vary. The levels of pmTOR, pSK1, and pS6, however, varied with rapamycin treatment. In tumors from the placebo cohort (−), high levels of pS6 were observed. In tumors that were treated with rapamycin (+), decreased levels of pS6 were seen in the majority of tumors and correlated with increased response on PET imaging. Increased pERK1/2 was observed in some placebo-treated cancers and also the rapamycin-treated tumor with persistent pS6 signaling. Fabp1-Cre^{+} Pik3ca*$^{+}$ tumor and hyperplastic tissue had increased cleaved caspase 3 due to increased cell turnover. A reduction in cleaved caspase 3 was identified in tumors possessing increased pERK1/2 signaling indicating that tumors with increased pERK may be resistant to rapamycin treatment through decreased apoptosis. GAPDH was used as a loading control.

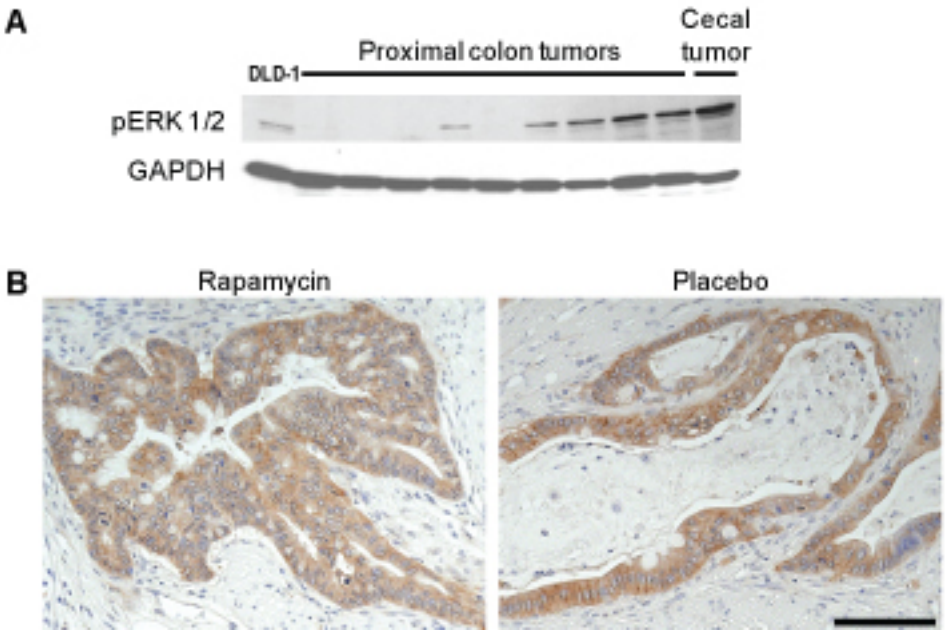
A
Proximal colon tumors
Cecal tumor
DLD-1
pERK 1/2
GAPDH
B
Rapamycin
Placebo

Appendix 9-9. pERK1/2 was increased in some untreated Fabp1-Cre^{+} Pik3ca*$^{+}$ tumors. (A) A group of ten Fabp1-Cre^{+} Pik3ca*$^{+}$ mice were dissected and the colon and cecal tumors were flash frozen. 5 of 9 proximal colon tumors demonstrated some degree of pERK1/2 signaling. The one cecal tumor identified also demonstrated increased pERK1/2. **(**B) β-catenin staining was performed on multiple rapamycin- and placebo-treated tumors. In all instances no nuclear localization of β-catenin was identified, indicating that aberrant WNT signaling is not playing a role in tumorigenesis or resistance to mTOR inhibition. Scale bar: (B), 100μm.

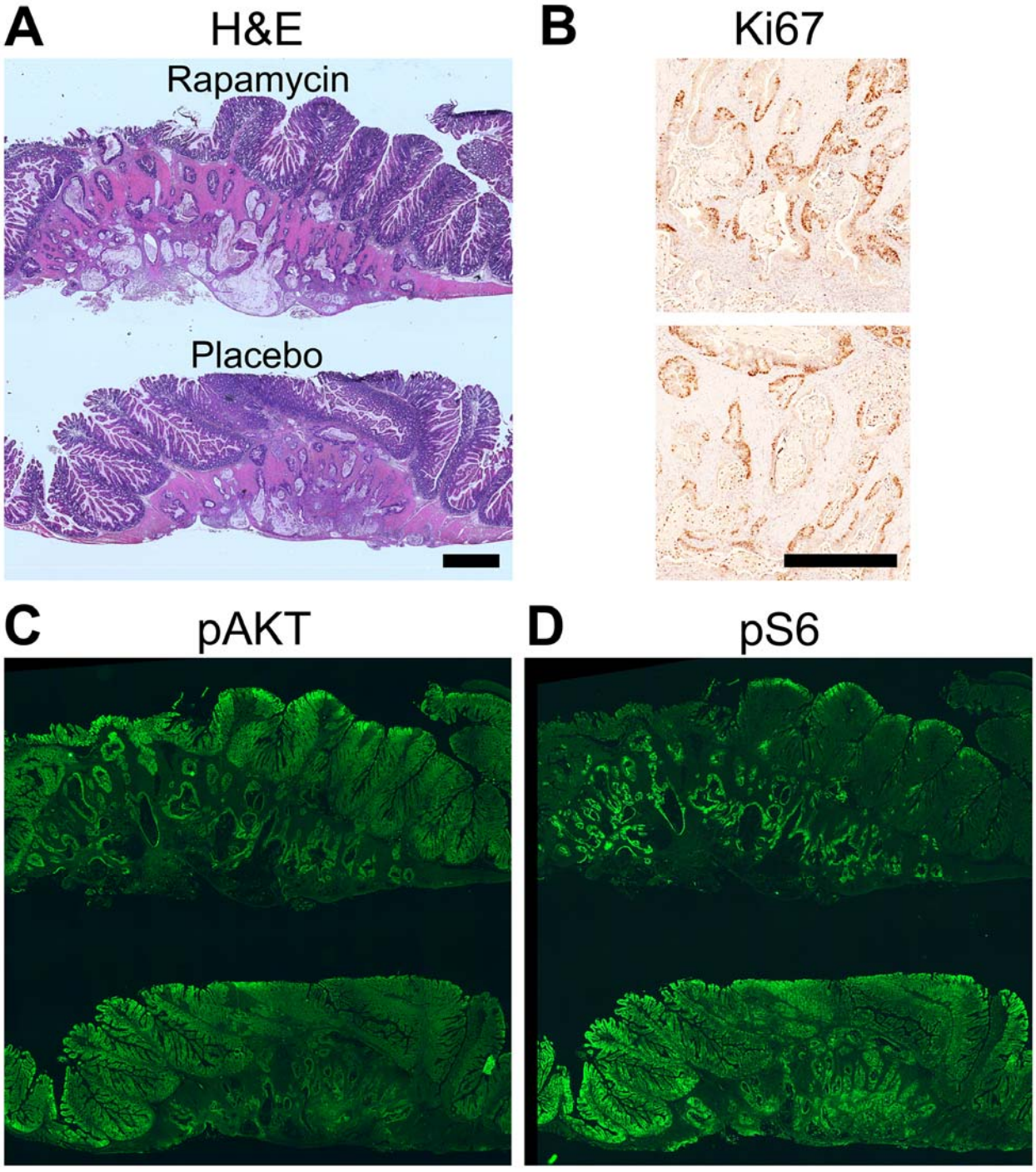
A
H&E
Rapamycin
Placebo
B
Ki67
C
pAKT
D
pS6

Appendix 9-10. Persistent Fabp1-Cre^{+} Pik3ca*$^{+}$ tumors demonstrated a differential response in pS6 in the hyperplastic and tumor tissue following rapamycin treatment. (A) A tumor resistant to rapamycin (top in each panel) and a tumor from a placebo-treated Fabp1-Cre^{+} Pik3ca*$^{+}$ mouse (bottom in each panel) were embedded in the same histological block. A similar phenotype and proliferation rate were noted on H&E and Ki67 staining, respectively (A and B). No significant difference in pAKT was seen between the tumors from the placebo and rapamycin treated mice (C). In the tissue from the placebo-treated mouse, increased pS6 was seen in the tumor tissue and overlying hyperplastic tissue as expected (D). Interestingly, in the tissue from the rapamycin-treated Fabp1-Cre^{+} Pik3ca*$^{+}$ mouse, decreased pS6 is noted in the hyperplastic tissue, but increased pS6 signaling remains in the resistant tumor tissue despite rapamycin treatment. This indicates that persistent pS6 setting within the tumors may be the mechanism of tumor resistance. This same staining pattern was observed in all tumors (3/3) with some neoplastic cells remaining after treatment with rapamycin that were examined. Size bars: A, C and D, 1 mm; B, 500 μm.

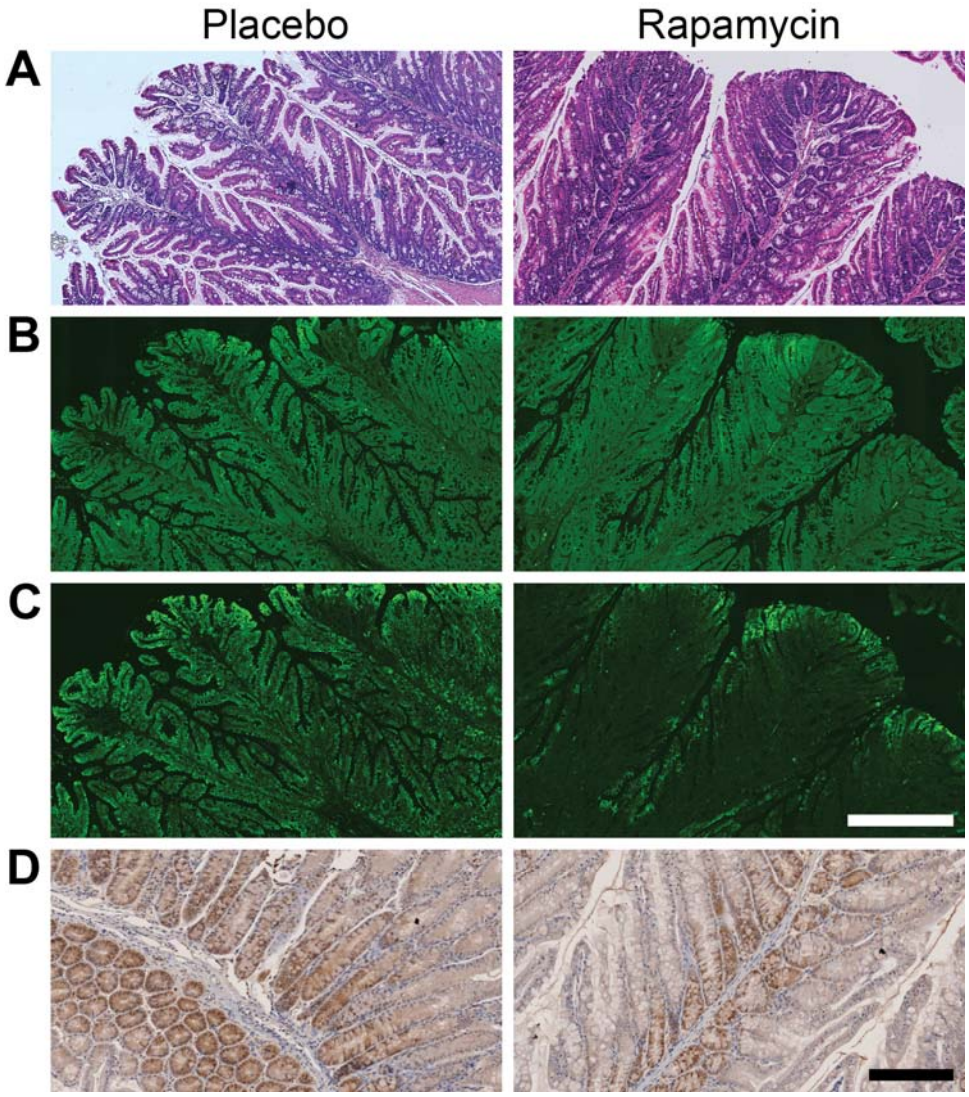
Placebo
Rapamycin
A
B
C
D

Appendix 9-11. Rapamycin treatment resulted in decreased pS6 and proliferation in the hyperplastic tissue from the colon of Fabp1-Cre^{+} Pik3ca*$^{+}$ mice. (A) In the colon of Fabp1-Cre^{+} Pik3ca*$^{+}$ mice, hyperplastic tissue was identified. In the placebo-treated mice, increased pAKT (B), pS6 (C), and Ki67 (D) staining were noted in the hyperplastic epithelium. In the rapamycin-treated mice increased pAKT is observed similar to that in the control, but as expected a decrease in pS6 is seen in response to rapamycin treatment. This reduction in pS6 is associated with a decrease in cell proliferation as determined by Ki67 staining. Size bars: A-C, 500μm; D, 200 μm.

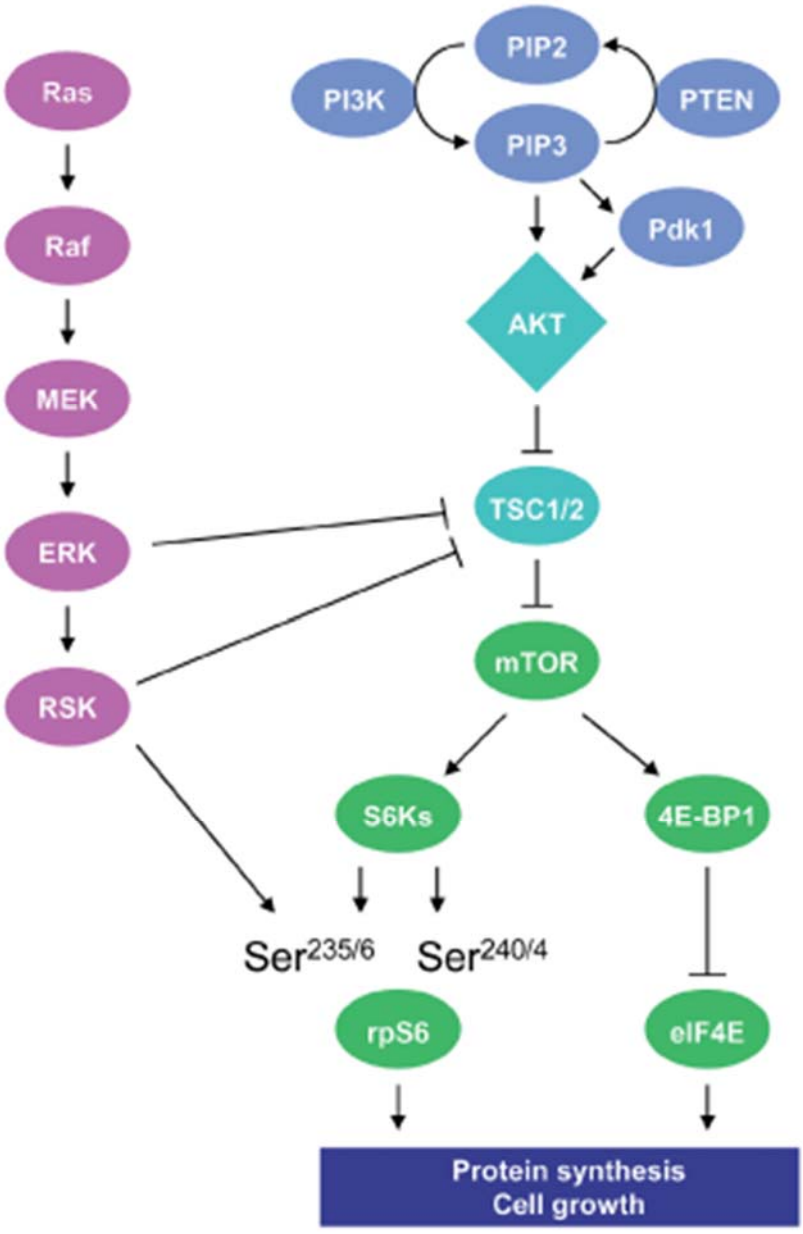
Ras
Raf
MEK
ERK
RSK
PIP2
PI3K
PTEN
PIP3
Pdk1
AKT
TSC1/2
mTOR
S6Ks
4E-BP1
Ser235/6
Ser240/4
rpS6
eIF4E
Protein synthesis
Cell growth

Appendix 9-12. ERK1/2 signaling is able to phosphorylate S6 on Ser$^{235/236}$ through RSK mediated signaling. ERK1/2 has been demonstrated to activate RSK signaling which results in site-specific phosphorylation of S6 at the Ser$^{235/236}$ site. S6K mediated phosphorylation of S6 can take place at either Ser$^{235/236}$ or Ser$^{240/244}$. (Adapted from Roux, et al., 2007)[23].

Tables

Appendix 9-13. Fabp1-Cre^{+} Pik3ca*$^{+}$ mice baseline characteristics and tolerability of rapamycin versus placebo.

			Pre-Tx tumors, N by size		Mouse weight, mean (g)			
Treatment arm	Sex	N	Large (>50 mm^3)	Small (<50 mm^3)	Pre-Tx	Post-Tx	Deaths on study	Received all doses
Placebo	Male	6	4	2	24.9	23.7	2	4/6
	Female	5	1	4	20.1	21.3	0	5/5
Rapamycin	Male	7	2	5	24.8	23.9	0	7/7
	Female	4	2	2	19.2	20.1	0	4/4

Twenty-two mice at 55 days of age were randomized 1:1 to rapamycin or placebo treatment arms. Mice were stratified based on gender and pretreatment tumor size. These mice tolerated the treatment well as demonstrated by minimal change in weight from baseline. In the placebo cohort, two mice became moribund prior to study completion. In both instances, large proximal colon tumors caused obstructive enteropathy. All mice in the rapamycin treated cohort completed the treatment course as intended. Tx, treatment.

doi:10.1371/journal.pone.0060709.t001

Appendix 9-14. Dual hybrid ^{18}F-FDG PET/CT colonography allows for longitudinal monitoring of tumor response and estimation of tumor volumes.

Treatment arm	Mouse#	Tumor volume (mm^3)		% Change in volume	Finding on necropsy
		Baseline	Post-Tx		
Placebo	1	51.8	162.2	213	Colon tumor
	2	32.6	86.8	166	Cecal tumor/metastatic disease
	3	45.1	104.1	131	Colon tumor
	4	29.3	56.1	91	Colon tumor
	5	41.3	74.8	81	No tumor
	6	37.4	63.8	71	Colon tumor
	7	23.5	36.9	57	Colon tumor
	8	61.9	84.9	37	Colon tumor
	9	65.7	73.9	12	Cecal tumor
	21*	90.2	NA	NA	Colon tumor
	22*	81.6	NA	NA	Colon tumor
Rapamycin	10	86.8	55.2	-36	Cecal tumor
	11	16.8	6.7	-60	No tumor
	12	37.4	11.5	-69	Colon tumor
	13	185.2	48.0	-74	Colon tumor
	14	114.7	28.8	-75	Cecal tumor
	15	26.9	0	-100	No tumor
	16	15.8	0	-100	No tumor
	17	35.5	0	-100	No tumor
	18	27.3	0	-100	Colon tumor
	19	95.0	0	-100	No tumor
	20	19.7	0	-100	No tumor

Twenty-two mice were enrolled and randomized to treatment with placebo or rapamycin. Dual hybrid ^{18}F-FDG PET/CT colonography was performed at baseline and following 14 days of treatment. Baseline and post-treatment tumor volume estimates for each mouse are listed. A strong concordance was noted with the PET/CT imaging data and the necropsy results. All of the tumors in the placebo-treated mice grew, while a reduction in tumor volume was noted in all the rapamycin-treated mice. Tx, treatment. *Mice became moribund owing to intestinal obstruction prior to completion of treatment course.

References

1. Markowitz, S. D. & Bertagnolli, M. M. Molecular Basis of Colorectal Cancer. *N Engl J Med* **361,** 2449–2460 (2009).

2. Allegra, C. J. *et al.* American Society of Clinical Oncology Provisional Clinical Opinion: Testing for KRAS Gene Mutations in Patients With Metastatic Colorectal Carcinoma to Predict Response to Anti–Epidermal Growth Factor Receptor Monoclonal Antibody Therapy. *JCO* **27,** 2091–2096 (2009).

3. Sartore-Bianchi, A. *et al.* Integrated molecular dissection of the epidermal growth factor receptor (EFGR) oncogenic pathway to predict response to EGFR-targeted monoclonal antibodies in metastatic colorectal cancer. *Targ Oncol* **5,** 19–28 (2010).

4. American Cancer Society. Cancer Facts & Figures 2011. (2011). at <http://www.cancer.org/acs/groups/content/@epidemiologysurveilance/documents/document/acspc-029771.pdf>

5. Samuels, Y. High Frequency of Mutations of the *PIK3CA* Gene in Human Cancers. *Science* **304,** 554–554 (2004).

6. Ligresti, G. *et al.* PIK3CA mutations in human solid tumors: Role in sensitivity to various therapeutic approaches. *Cell Cycle* **8,** 1352–1358 (2009).

7. Zhao, L. & Vogt, P. K. Hot-spot mutations in p110α of phosphatidylinositol 3-kinase (PI3K): Differential interactions with the regulatory subunit p85 and with RAS. *Cell Cycle* **9,** 596–600 (2014).

8. Vivanco, I. & Sawyers, C. L. The phosphatidylinositol 3-Kinase–AKT pathway in human cancer. *Nat Rev Cancer* **2,** 489–501 (2002).

9. Leystra, A. A. *et al.* Mice expressing activated PI3K rapidly develop advanced colon cancer. *Cancer Res* **72,** 2931–2936 (2012).

10. Engelman, J. A. *et al.* Effective use of PI3K and MEK inhibitors to treat mutant Kras G12D and PIK3CA H1047R murine lung cancers. *Nat Med* **14,** 1351–1356 (2008).

11. Stelzer, M. K. *et al.* Rapamycin Inhibits Anal Carcinogenesis in Two Preclinical Animal Models. *Cancer Prev Res* **3,** 1542–1551 (2010).

12. Carracedo, A. *et al.* Inhibition of mTORC1 leads to MAPK pathway activation through a PI3K-dependent feedback loop in human cancer. *J Clin Invest* **118,** 3065–3074 (2008).

13. Flaherty, K. T. *et al.* Inhibition of Mutated, Activated BRAF in Metastatic Melanoma. *N Engl J Med* **363,** 809–819 (2010).

14. Pal, S. K., Figlin, R. A. & Reckamp, K. Targeted Therapies for Non–Small Cell Lung Cancer: An Evolving Landscape. *Mol Cancer Ther* **9,** 1931–1944 (2010).

15. Kwak, E. L. *et al.* Anaplastic Lymphoma Kinase Inhibition in Non–Small-Cell Lung Cancer. *N Engl J Med* **363,** 1693–1703 (2010).

16. Chabner, B. A. Early Accelerated Approval for Highly Targeted Cancer Drugs. *N Engl J Med* **364,** 1087–1089 (2011).

17. Janku, F. *et al.* PI3K/AKT/mTOR Inhibitors in Patients With Breast and Gynecologic Malignancies Harboring PIK3CA Mutations. *JCO* **30,** 777–782 (2012).

18. Nosho, K. *et al.* PIK3CA Mutation in Colorectal Cancer: Relationship with Genetic and Epigenetic Alterations. *Neoplasia* **10,** 534–541 (2008).

19. Vogelstein, B. *et al.* Genetic Alterations during Colorectal-Tumor Development. *N Engl J Med* **319,** 525–532 (1988).

20. Chung, J., Kuo, C. J., Crabtree, G. R. & Blenis, J. Rapamycin-FKBP specifically blocks growth-dependent activation of and signaling by the 70 kd S6 protein kinases. *Cell* **69,** 1227–1236 (1992).

21. Hauge, C. & Frödin, M. RSK and MSK in MAP kinase signalling. *Journal of Cell Science* **119,** 3021–3023 (2006).

22. Pende, M. *et al.* S6K1$^{-/-}$/S6K2$^{-/-}$ Mice Exhibit Perinatal Lethality and Rapamycin-Sensitive 5′-Terminal Oligopyrimidine mRNA Translation and Reveal a Mitogen-Activated Protein Kinase-Dependent S6 Kinase Pathway. *Mol Cell Biol* **24,** 3112–3124 (2004).

23. Roux, P. P. *et al.* RAS/ERK Signaling Promotes Site-specific Ribosomal Protein S6 Phosphorylation via RSK and Stimulates Cap-dependent Translation. *J Biol Chem* **282,** 14056–14064 (2007).

24. Haagensen, E. J., Kyle, S., Beale, G. S., Maxwell, R. J. & Newell, D. R. The synergistic interaction of MEK and PI3K inhibitors is modulated by mTOR inhibition. *Br J Cancer* **106,** 1386–1394 (2012).

25. Migliardi, G. *et al.* Inhibition of MEK and PI3K/mTOR Suppresses Tumor Growth but Does Not Cause Tumor Regression in Patient-Derived Xenografts of RAS-Mutant Colorectal Carcinomas. *Clin Cancer Res* **18,** 2515–2525 (2012).

26. Shimizu, T. *et al.* The Clinical Effect of the Dual-Targeting Strategy Involving PI3K/AKT/mTOR and RAS/MEK/ERK Pathways in Patients with Advanced Cancer. *Clin Cancer Res* **18,** 2316–2325 (2012).

27. Hernandez-Aya, L. F. & Gonzalez-Angulo, A. M. Targeting the Phosphatidylinositol 3-Kinase Signaling Pathway in Breast Cancer. *The Oncologist* **16,** 404–414 (2011).

28. Schmidt-Kittler, O. *et al.* PI3Kα Inhibitors That Inhibit Metastasis. *Oncotarget* **1,** 339–348 (2010).

29. Wong, K.-K., Engelman, J. A. & Cantley, L. C. Targeting the PI3K signaling pathway in cancer. *Curr Opin Genet Dev* **20,** 87–90 (2010).

30. Juric, D. *et al.* Abstract CT-01: BYL719, a next generation PI3K alpha specific inhibitor: Preliminary safety, PK, and efficacy results from the first-in-human study. *Cancer Res.* **72,** CT–01–CT–01 (2012).

31. Saam, J. R. & Gordon, J. I. Inducible gene knockouts in the small intestinal and colonic epithelium. *J Biol Chem* **274,** 38071–38082 (1999).

32. Srinivasan, L. *et al.* PI3 Kinase Signals BCR-Dependent Mature B Cell Survival. *Cell* **139,** 573–586 (2009).

33. Durkee, B. Y. *et al.* Reproducibility of Tumor Volume Measurement at MicroCT Colonography in Living Mice. *Acad Radiol* **15,** 334–341 (2008).